Traitement de signaux RF à l'aide de dispositifs optoélectroniques ultra-rapides et travaux complémentaires de spectroscopie térahertz. RF signal processing using ultrafast optoelectronics devices and related terahertz spectroscopy experiments.

Mohan Babu Kuppam

UNIVERSITÉ DE GRENOBLE

THÈSE

Pour obtenir le grade de

DOCTEUR DE L'UNIVERSITÉ DE GRENOBLE

Spécialité : **Optique et Radiofréquences**

Arrêté ministériel : 7 août 2006

Présentée par

Mohan Babu KUPPAM

Thèse dirigée par **Jean-Louis COUTAZ** et
codirigée par **Jean-François ROUX**
préparée au sein du **Laboratoire IMEP-LAHC**
dans **l'École Doctorale EEATS**

Traitement de signaux RF à l'aide de dispositifs opto-électroniques ultra-rapides et travaux complémentaires de spectroscopie térahertz

Thèse soutenue publiquement le **13 décembre 2013**,
devant le jury composé de :

Guy VITRANT
Directeur de recherches au CNRS, IMEP-LAHC, Université de Grenoble, président
Laurent CHUSSEAU
Directeur de recherches au CNRS, IES, Université de Montpellier 2, rapporteur
Didier DECOSTER
Professeur, IEMN, Université de Lille 1, rapporteur
Jean-François LAMPIN
Chargé de recherches au CNRS, HDR, IEMN, Université de Lille 1, examinateur
Jean-François ROUX
Maitre de conférences HDR, IMEP-LAHC, Université de Savoie, co-directeur de thèse
Jean-Louis COUTAZ
Professeur, IMEP-LAHC, Université de Savoie, directeur de thèse

TABLE OF CONTENT

CHAPTER 3: OPTOELECTRONIC DEMODULATION OF INFORMATION SIGNAL USING LTG-GaAs PHOTOSWITCH

***CHAPTER 4:* CHARACTERIZATION OF LTG-GaBiAs PHOTOSWITCH**

CHAPTER 5: APPLICATIONS OF THz SPECTROSCOPY

Résumé

Ce travail a été consacré à l'étude de composants optoélectroniques ultra-rapides pour le traitement de signaux RF jusqu'au domaine THz, ainsi qu'à l'étude de composants pour les faisceaux THz. Tout d'abord, le travail a porté sur des photo-commutateurs optoélectroniques fabriqués avec des semi-conducteurs ultrarapides. Le dispositif, éclairé par le battement de 2 faisceaux optiques et polarisé par une tension RF, réalise le mélange de ces fréquences. Les propriétés du dispositif (bande passante, efficacité, génération de fréquences…) ont été modélisées et les simulations ont été validées par des mesures expérimentales. Quand le signal RF est modulé par un signal « information », cette information peut être directement extraite en égalant fréquences RF et de battement optique. Le signal démodulé est très pur : ainsi nous avons mesuré une largeur spectrale à -3 dB de 11 Hz. D'autres matériaux pour la génération THz et la photo-commutation ultrarapide furent aussi étudiés, comme des boîtes quantiques en InAs. Enfin, nous avons réalisé une étude par spectroscopie THz dans le domaine temporel des propriétés de dispositifs métalliques sous-longueur d'onde pour la manipulation de faisceaux THz, comme des réseaux de trous dans une plaque métallique ou de filtres à grille, ainsi que de films nanométriques de graphène ou de nanotubes de carbone.

Mots clefs: Optoélectronique, térahertz (THz), GaAs basse température, battement optique, génération de bandes latérales, mélange de fréquences, démodulation, spectroscopie dans le domaine temporel.

Abstract

This PhD work was devoted to the study of ultrafast optoelectronic components for processing RF signals up to the THz range, and of related THz devices. First, we used a photoconductive switch, made of low-temperature grown GaAs, excited by the optical beating of two CW laser beams and biased by a RF signal. The switch serves as a frequency mixer, whose properties (bandwidth, efficiency, sideband generation…) were modeled and the simulation results were experimentally validated. When the RF signal is modulated by information, this information can be directly extracted by setting the beating frequency equal to the RF one. The demodulated signal exhibits a high spectral purity, 11 Hz bandwidth at -3 dB. Other materials for THz generation and fast photo-switching were also studied, like InAs quantum dots. Finally, we performed a THz time-domain spectroscopy study of metallic sub-wavelength devices for THz beam processing, like hole arrays and mesh filters, as well as nanometric thin films of graphene and carbon nanotubes.

Key words: Optoelectronics, terahertz (THz), low temperature grown GaAs, optical beating, side band generation, frequency mixer, demodulation, time domain spectroscopy.

ACKNOLEDGEMENT

First of all, I would like to express my sincere gratitude to my supervisor Professor Jean-Louis Coutaz for supervising my research and discussing the problems that came into my research journey. This thesis could not be completed without his continuous instruction, support and encouragement. I also thank full to my co-supervisor Dr. Jean-Francois Roux for his instructions and help.

During my PhD degree, I received assistance from a number of people. Firstly, I would like to thank Dr. Jean-Francois Lampin, Professor Arunas Krotkus for their significant support in terms of devices, experimental setup, valuable suggestions and discussions which helped to my thesis work. I also thank to Dr. Frederic Garet for his very useful support and suggestions for all THz-TDS related works. I thank also to Mitepho partners, namely Professor Lamela, Professor Reithmaier, and Vitalii, Fabio, Philipp and Ehsan for their collaboration.

I especially acknowledge the deep debt of gratitude owed to my parents Penchalaiah and Saraswathi, and to my brothers Narasimhulu, Subramanyam and Chandraiah for their support and love throughout my personal and education carrier.

I thank to my friends Maher, Mohammod, Furat, Benjamin, Andrius and colleagues who supported me during my degree. I also thank to secretaries Fernanda and Cindy in the laboratory and to administrative staff in the University.

Finally, I thank to the Marie-Curie funded MITEPHO project, which gave me an opportunity to improve my scientific skills and to achieve the doctoral degree.

Mohan Babu K.

CHAPTER 1: *INTRODUCTION*

INTRODUCTION

I. Motivation of this work

Bandwidth demand in optical telecommunications is continuously increasing and requires optoelectronic devices operating at a bit rate beyond 100 Gbits/s. As existing electronic devices hardly operate at this speed due to long lifetime and transit time of electrons in conventional semiconductor materials and devices, new ultrafast light sources and optical switches are required for the development of ultra-high bit rate optical systems. Modern ultrafast techniques lead the performance of the optoelectronic devices to the requested level. For example, a low temperature grown GaAs metal-semiconductor-metal (MSM) photo detector has been reported to have a band width of 500 GHz [1], ultrafast p-i-n photodiodes with a 100 GHz bandwidth are demonstrated in [2], InP–InGaAs Uni-Travelling-Carrier (UTC) photodiodes exhibits a 3-dB bandwidth of 150 GHz [3,4], InGaAs photoconductor showed an optical band width of 300 GHz [5], LTG-GaAs travelling wave photo detector exhibits a 3-dB electrical bandwidth of 234 GHz [6]. Due to the rapidly increasing in signal bandwidths and the involved of digital techniques, the need for higher speed analog-to-digital (A/D) conversion arises in order to interface between the analog and digital signals. A variety of applications for A/D conversion at tens of gigahertz sampling rates exist in optical communications, wireless communications, radar, etc. [7-12]. Semiconductor photo-switches are among the fastest devices that can be precisely triggered. When manufactured with ultrafast semiconductor materials, switching times much shorter than one picosecond can be achieved, leading to effective bandwidths exceeding the THz threshold.

The main part of this work was devoted to the mixing, using an ultrafast semiconductor photoconductive switch, in between radio-frequency (RF) signals in the CW regime and optical signals modulated at RF frequencies. Also we performed related studies on the THz response of structured artificial materials such as mesh filters and holes arrays, of graphene and carbon nanotube films, and of quantum dots (QD).

II. Organization of thesis

The whole thesis work is categorized into four chapters:

In chapter 2, we study the mixing of a radio frequency (RF) signal and a modulated optical beam, resulting from the beating of two CW lasers, using an inter-digitated photoconductive switch as the mixer. The mixing process leads to the generation of sideband frequencies in the RF transmitted signal. We developed a theoretical model for mixing and side band generation, and this model is nicely validated by experimental work using a low-temperature grown GaAs device excited by two laser diodes at 0.8-μm wavelength.

In chapter 3, we present optoelectronic direct demodulation results performed with the same ultrafast device as studied in chapter 2. In this case, the beating signal plays a dual role, i.e. to both excite the switch and to generate the RF signal through opto-electrical conversion in a photodiode. Thus both RF and photonic signals exhibit the same frequency and allow for heterodyne detection of the RF signal. As a consequence, any modulation of the RF signal can be directly extracted from the RF carrier frequency. The experiment was demonstrated for a demodulated signal at 10 MHz with a band width of 11 Hz. We also present the scattering parameters results of the device. The LTG-GaAs switch used for this study was grown and processed at IEMN Lille.

In chapter4, we present a similar study as performed in earlier chapters, but at ~1 μm of optical wavelength. Here, for this purpose, we used a GaBiAs epitaxial layer grown by the team of A. Krotkus in Vilnius. This material was processed at IEMN Lille. And the mixing experiment was performed at IMEP-LAHC Grenoble using a home-made two-color Nd-doped vanadate laser.

Finally in chapter 5, we first study the ultrafast carrier dynamics in InAs QD layers in order to know whether they could be used as ultrafast device for THz generation and photo-switching at 1.5 μm wavelength. This carrier dynamics was evaluated by means of 3 different time-resolved experiments, namely optical pump-and-probe, optical pump and THz probe, and photoluminescence. We also performed classical THz time-domain spectroscopy. Secondly, we study the electrical behavior of carbon nanotube (CNT) layers and graphene layers through THz time-domain spectroscopy. Refractive index and the DC conductivity of those layers was extrapolated from broadband THz time-domain measured data. The advantage of this method is to obtain the DC conductivity without any need of electrical contacts, which are rather difficult to attach to these nanometer-thick films.

Finally, we study the THz electromagnetic response of some diffractive structures. The first ones were arrays of holes designed and manufactured in a slab of steel. HFSS and REM codes were used to calculate the THz transmission of such devices. Above the hole cut-off frequency, some spectral pattern were expected as resulting from both surface plasmon excitation and from Wood-Rayleigh anomalies (energy repartition at the appearance of new diffracted orders). Unfortunately, certainly because of the ohmic losses and roughness scattering in the steel foil, surface plasmons were not definitively observed. Later on, we measured the THz transmission of metallic meshes deposited over thin cyclic olen copolymer films, which could be used to perform photo-lithography process without altering their properties and shapes due to their good transparency, small thickness, and good mechanical robustness while showing a flexible character.

References

[1] S. Y. Chou, Y. Liu, W. Khalil, T. Y. Hsiang, and S. Alexandrou, *"Ultrafast nanoscale metal-semiconductor-metal photodetectors on bulk and low-temperature grown GaAs,*" Appl. Phys. Lett., **61**, 819 (1992)

[2] Y. -G. Wey *et al, "l108-GHz GaInAs/InP p-i-n photodiodes with integrated bias tees and matched resistors,"* IEEE Photon. Technol. Lett., **5**, 82 (1993)

[3] Naofumi Shimizu, *"InP–InGaAs Uni-Traveling-Carrier Photodiode With Improved 3-dB Bandwidth of Over 150 GHz,"* IEEE Photon. Technol. Lett., **10**, 412 (1998).

[4] S. Giboney *et al, "Travelling-Wave Photo detectors with 172-GHz Bandwidth and 76-GHz Bandwidth-Efficiency Product,"* IEEE Photon. Technol. Lett., **7**, 412 (1995).

[5] Ho-Jin SONG *"Microwave Photonics Mixer Utilizing an InGaAs Photoconductor for Radio over Fiber Application,"* IEICE Trans. Electron., 90-C, 457(2007).

[6] Jin-Wei Shi et al, *"High-Speed and High-Power Performances of LTG-GaAs Based Metal–Semiconductor–Metal Traveling-Wave-Photo detectors in 1.3-μm Wavelength Regime,"* IEEE Photonics Technology Letters, 14, 363 (2002).

[7] Pascal Febvre *et al, "Superconducting Photosensitive Interfaces for Triggering RSFQ Circuits,"* IEEE transactions on applied superconductivity, **17**, 530 (2007).

[8] Delord, Roux, Coutaz, and Breuil, "*Study of Optoelectronic Sampler Linearity for Analog-to-Digital Conversion of RF Signals,"* IEEE photonics technology letters, **21**, 1369 (2009).

[9] P.W. Juodawlkis, "*Impact of photo detector nonlinearities on photonic analog-to-digital converters,"* and also see Jin-Wei Shi "*High speed and high power performances of LTG-GaAs based TWPDs in telecommunication wavelength (/spl sim/1.3 /spl mu/m),"* Lasers and Electro-Optics, CLEO '02, (2002).

[10] Jae-Young Kim et al, "*Characteristics of InP–InGaAs HPT-Based Optically Injection-Locked Self-Oscillating Optoelectronic Mixers and Their Influence on Radio-Over-Fiber System Performance,"* IEEE Photonics Technology Letters, **19**,155 (2007).

[11] Jun-Hyuk Seo *"Conversion Efficiency Characteristics of Cascaded SOA-EAM Frequency Up/Down-Converters,"* Microwave Photonics, 107 (2005).

[12] Masahiro Tsuchiya et al, *"Nonlinear Photodetection Scheme and Its SystemApplications to Fiber-Optic Millimeter-Wave Wireless Down-Links,"* IEEE Transactions Microwave Theory and Technique, **47**, 1342 (1999).

CHAPTER 2: OPTOELECTRONIC RF SIGNAL PROCESSING USING LTG-GaAs PHOTOSWITCH

OPTOELECTRONIC RF SIGNAL PROCESSING USING LTG-GaAs PHOTOSWITCH

I. INTRODUCTION

In this chapter, we are providing the details of photoconductive switches, i.e. the optical characterization of low temperature grown (LTG) GaAs semiconductor material, and the current-voltage characteristics of LTG-GaAs photoconductive switches. We also give more details on optoelectronic sampling and generation of sideband frequencies in the radio frequency (RF) region using the LTG-GaAs photoconductive switch excited at 0.78 μm. We present a theoretical and experimental study of the mixing of a RF electrical signal whose frequency is f_ω and a modulated optical beam at frequency f_Ω resulting from the beating of two CW lasers, using an inter-digitated LTG-GaAs photoconductive switch as the mixer. The non-linear mixing process leads to the generation of sideband frequencies in the transmitted RF signal. We report on the generation of side band frequencies to the RF signal in the range of 10 to 28 GHz. Moreover the device delivers a signal at frequency f_Ω when DC biased. The analysis shows that this optoelectronic device exhibits a low pass band behavior.

II. PHOTOCONDUCTIVE SWITCH

A photoconductive semiconductor switch is an electrical switch, which is based on the photoconductivity of a semiconductor material, i.e. its electrical conductivity increases when light impinging on its surface. All semiconductor materials generate free charge carriers when light with energy above the band gap falls on its surface, which then contribute to the electrical conductivity. In general, all conventional semiconductor materials exhibit longer carrier relaxation time, and are not useful for ultrafast optoelectronic applications. In order to reduce the recovery time of the switch (determined partly by the life time of the photo excited carriers), traps that quickly capture the free changes must be incorporated in the material. This is achieved through a low-temperature growth (often followed by rapid thermal annealing), some doping (e.g. chromium in GaAs), or ion bombardment for producing crystal defects [1, 2, 3, 4]. Commonly used materials are LTG-GaAs, chromium-doped gallium arsenide (Cr-GaAs), LTG gallium bismuth arsenide (LTG-GaBiAs), indium phosphide (InP), amorphous

silicon, etc. In addition to the carrier life time, the bandgap energy, dark resistivity, and electrical break down resistance are also important. The art of different kinds of photoswitches are presented below. In Fig. 2.1a, d is the thickness, w is width, L is the length of the semiconductor material and d_0 is the depth of the semiconductor in which electron-hole are generated by the light. And in Fig. 2.1b, w is the width, L is the length of the gap of the switch.

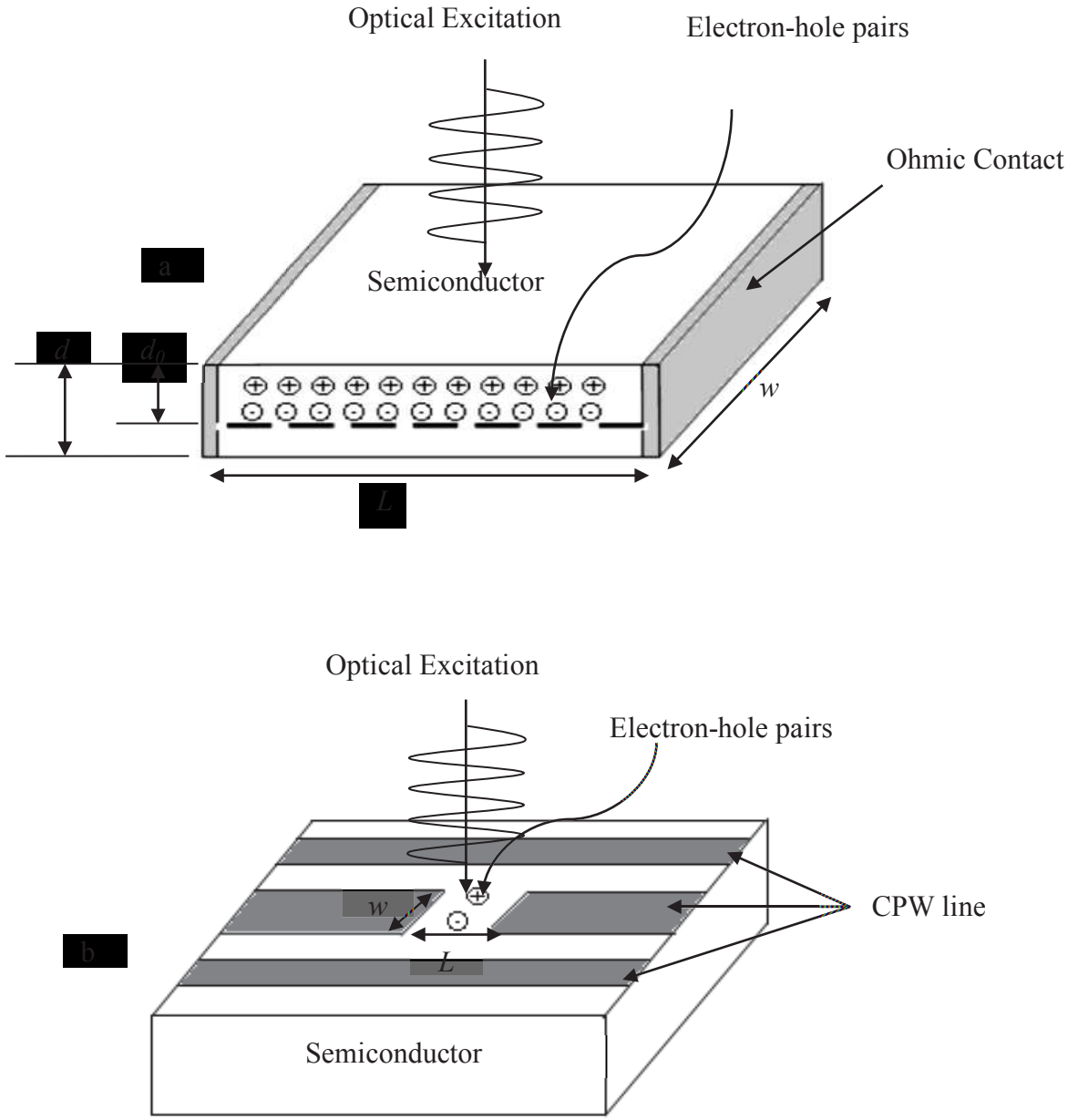

Fig. 2.1: Device representation for a) High voltage photoswitch, and b) High speed photoswitch

There are different designs of photoconductive switches applicable:

II.1. High voltage photoconductive switches

Bulk semiconductor devices with electrical contacts on its end faces are used for switching at very high voltage (Fig. 2.1a). The device length is within the millimeter or centimeter range. The semiconductor device parameters are: length L, width w and thickness d. The optical absorption depth (d_0) is equal or less than the thickness of the semiconductor block. The dark resistance of the device is:

$$R_{dark} = \frac{\rho_0}{w}\frac{L}{d} \tag{II-1}$$

Where ρ_0 is the dark resistivity of the semiconductor material and is given by:

$$\rho_0 = \frac{1}{q\left(n_0\mu_{n0} + p_0\mu_{p0}\right)} \tag{II-1a}$$

Where n_0 and p_0 are the free electron and hole densities and μ_{n0} and μ_{p0} are the electron and hole motilities.

II.2. High speed photoconductive switches

Devices (Fig. 2.1b) with a small gap in a microwave line (CPW or microstrip). The gap can be straight or a more complicated inter-digitated structure. The gap width is about few microns; such kinds of switches are used for low-power applications at very high speed switching. The switch geometrical parameters are its width w, its length l (i.e. gap between two electrodes) and its thickness d (penetration depth of the incident light). When the light falls on the switch, the resistance of the switch is:

$$R = \frac{V_S}{I} = \frac{l}{w\,d\,Nq\left(\mu_p + \mu_n\right)} \tag{II-2}$$

where μ_n *and* μ_p are electron and hole mobilities respectively, q is the carrier charge and N is the carrier density in the switch after optical excitation.

Photoconductive semiconductor switches are used in a variety of applications:

- ✓ For photoconductive sampling, particularly for testing of high-speed integrated electronic circuits [5,6,7];
- ✓ For the generation and detection of terahertz pulses [8,9];

- ✓ For the generation of microwaves and millimeter waves via direct DC to RF conversion, in both continuous-wave and pulsed as high-speed photo detectors in optical fiber communications [10];
- ✓ Very fast analog-to-digital converters [10a];

In our present study, we have used LTG-GaAs photoconductive antennas (discussed in chapter- 2 and 3). This molecular beam epitaxy grown LTG-GaAs is the most efficient material for high speed optoelectronic applications due to its low dark current and short relaxation time. LTG-GaAs photoconductive switches have one major drawback, i.e. the optical band gap of 1.43 eV. This prevents LTG-GaAs photo switches to operate at common optical communication wavelengths of 1.3 and 1.55 μm. So, we also used LTG-GaBiAs devices at higher wavelengths, i.e. above 1μm.

III. OPTICAL CHARACTERIZATION OF LTG-GaAs SEMICONDUCTOR MATERIAL

III.1. Principle of optical pump-probe technique

Optical pump-probe spectroscopy is a dominant technique to study carrier dynamics in material science research. In this spectroscopic system, when the material absorbs high energy photons from the pump beam, its transmissivity and reflectivity are modified [11, 11a, 11b, 11c, 11d]. The changes in optical properties are due to the contribution of thermal relaxation, electron-phonon relaxation and Fermi level shifting, etc. The probe beam falls on the sample and its transmitted or reflected part is collected by a photo detector. When the transmissivity or the reflectivity is changed due to the excitation pulses, the intensity of the transmission or reflection of the probe pulse changes accordingly. The time analysis of these changes allows one to monitor the transient response of the material to the optical excitation. In the case of semiconductors excited with above band gap photon energies, the analysis of the experiment is usually complex as numerous physical phenomenon have to be taken into account. Nevertheless, under certain hypothesis, one can simplify the approach and can considered that the time evolution of the reflected optical probe is a direct signature of the electrons and holes that have been photo-generated by the pump pulse [11c, 11d].

III.2. Numerical data analysis approach

The measured *ΔR/R* or $\Delta T/T$ curves exhibit different relaxation rates due to the contribution of different processes simultaneously, so making data analysis is difficult. To simplify this difficulty, the total response is taken as a superposition of many processes, and each of them has a single relaxation rate [11d]. Each relaxation process is exponential and follows the solution of the below equation (written here for *ΔR/R*).

$$\frac{d\left(\Delta R/R\right)}{dt} = \eta I\left(t\right) - \frac{\Delta R/R}{\tau_R}, \tag{II-3}$$

where $I\left(t\right) = I_0 \exp\left(-4\ln 2 \frac{t^2}{\tau_p{}^2}\right)$ is the Gaussian excitation due to the laser pulse with FWHM of τ_p and amplitude of I_0. τ_R is the single relaxation time, and η is the proportional constant.

When the optical probe energy is above band gap, we measure the change in reflection (as the sample is too thick to transmit any portion of the probe beam). Usually (under experimental condition where angles are close to normal incidence) we can considered that the change in the reflection coefficient of the illuminated semiconductor is mainly depending onto the change of the real part of its refraction index [11b, 11d]. On the other hand, in the case of below band gap probe, one can use transmission experiment, and the pump induced variation of the transmission coefficient would be mainly governed by the variation of the absorption coefficient which directly depends on the photo-excited carrier density.

Moreover, in the case of moderate pump power we can assume that both changes (in refractive index and absorption) are linearly proportional to the pump intensity.

In our case, we will perform a degenerate pump-probe experiment in which the photon energy falls above the bandgap so we will record the change in the reflection coefficient:

$$\frac{\Delta R}{R} \propto \frac{\Delta n}{n} \propto I_{laser}.$$

The solution of equation (II-3) is written as

$$\Delta R/R = k \exp\left(-\frac{t}{\tau_R}\right) \tag{II-3c}$$

Where *k* is a normalization constant that is related to the amplitude of the signal. For double exponential decay process, there will be two terms in the right side of the equation (II-3a) with different amplitude constants k_1 and k_2, and relaxation times τ_{R1} and τ_{R2} and given as:

$$\Delta R/R = k_1 \exp\left(-\frac{t}{\tau_{R1}}\right) + k_2 \exp\left(-\frac{t}{\tau_{R2}}\right) \quad \text{(II-3d)}$$

And, also for triple exponential decay, there will be three terms in the right hand side of the equation (II-3a).

$$\Delta R/R = k_1 \exp\left(-\frac{t}{\tau_{R1}}\right) + k_2 \exp\left(-\frac{t}{\tau_{R2}}\right) + k_3 \exp\left(-\frac{t}{\tau_{R3}}\right) \quad \text{(II-3e)}$$

,

and so on. Similarly, the same expressions are used for *ΔT/T* data analysis. Similar approach has been used in many works [11a, 11b] and carrier dynamics will be examined in the following section III.3

III.3. Optical pump-probe system

In a typical optical pump–probe technique that measures time-dependent changes in reflectivity, photons with above-band-gap energy are used to create electron-hole pairs near the surface of the GaAs. These photo generated carriers contribute to changes in the refractive index of the material, Δn, and thus to changes in the reflectivity, through a combination of mechanisms. The three principal mechanisms that lead to refractive index changes are free-carrier absorption, band filling, and bandgap renormalization [11c]. The Δn factor for each of these three depends on the pump–photon energy and photo carrier density. For photo carrier densities that are typically involved in our reflectivity measurements ($\leq 10^{18}$ cm^{-3}), electron band filling tends to control the refractive index changes at photon energies greater than the band gap in GaAs. Since the changes in reflectivity are directly proportional to changes in refractive index, the measured quantity ΔR will also be controlled principally by band filling effects.

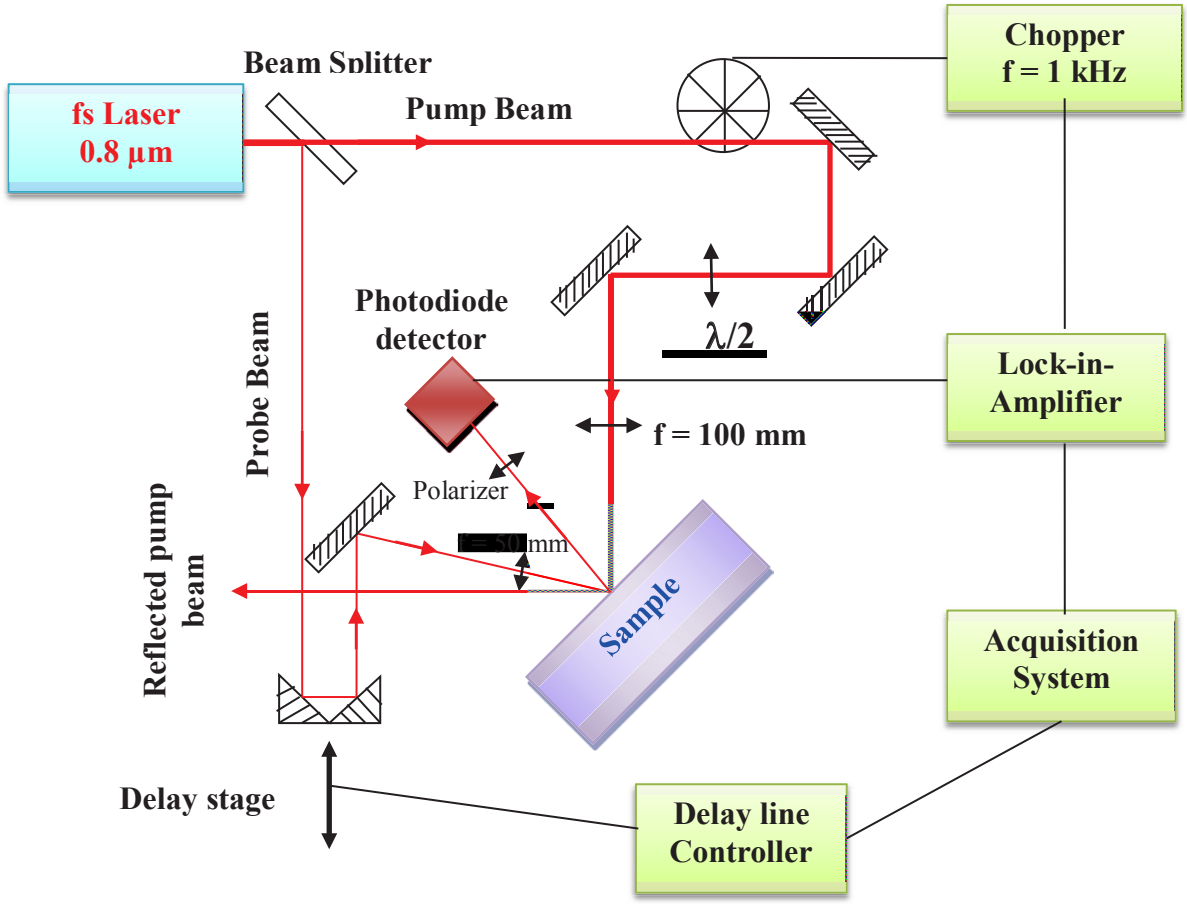

Fig. 2.2: The schematic representation of optical pump-probe reflectivity experimental set up.

Initial time dependent changes in the reflectivity will, therefore, be controlled by the rate at which photo generated electrons fill up the lowest available states near the band edge. The subsequent decay time will be an indication of the rate at which these photo generated electrons are then trapped or recombine at lower energy states below the conduction band edge. This decay time is typically referred simply as the photo carrier relaxation time, and is ultimately the time that limits the speed of response of the material photo conductance.

III.3.1. Carrier life time measurement in LTG-GaAs

Standard femtosecond optical pump-probe reflectivity measurement is performed on LTG-GaAs material in order to determine the carrier relaxation or trapping time. The schematic of experimental set up is presented in Fig. 2.2. This experimental setup is driven by a mode-locked Ti:sapphire laser (wavelength 800 nm, pulse duration 50 fs and repetition rate 85 MHz). A beam-splitter divides the laser beam into two components, one is the probe beam and the another one is the pump beam. These pump and probe beams are orthogonally polarized using a λ/2 wave-plate in order to minimize interference effects. A computer controlled delay stage is used to introduce a time delay between pump and probe pulses. The pump beam is chopped at around 1 kHz and focused on the sample.

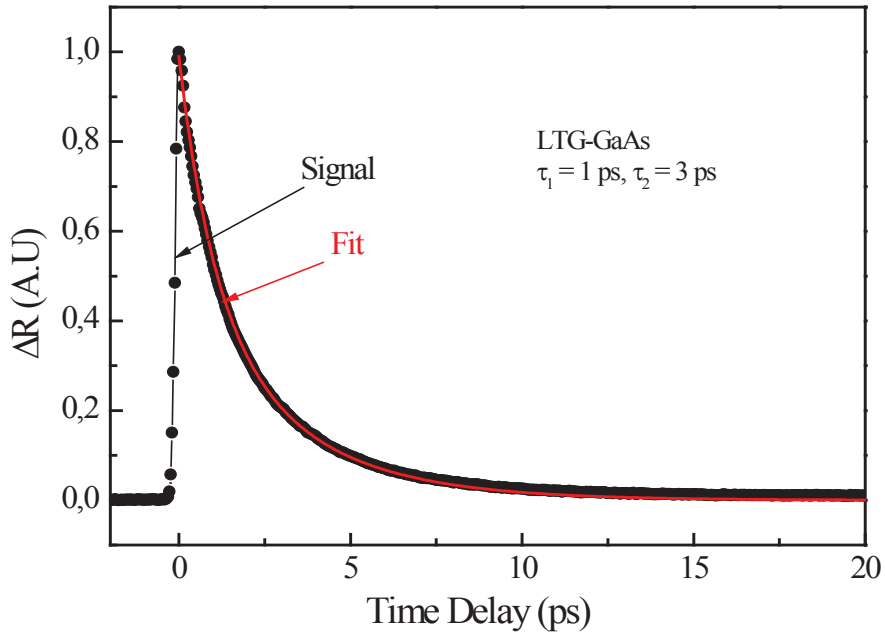

Fig. 2.3: Transient reflectivity signal measured at 800 nm wavelength for LTG-GaAs material. Experiment performed at IEMN, University of Lille.

The probe beam is more focused inside the pump spot. The probe beam reflected from the surface of the LTG-GaAs is measured with a photo detector (photo diode). The signal from the photo detector is sent to a lock-in-amplifier which is locked to the chopper frequency. The changes in the reflected probe beam power that are caused by the presence of the photo generated carriers generated by the pump beam are recorded as a function of the time delay between the pump-probe beams. The pump and probe average powers are typically 100 and 10 mW respectively.

Fig. 2.3 shows the transient reflectivity data measured with typical pump-probe technique for the LTG-GaAs material which is grown at IEMN, University of Lille. Our present LTG-GaAs device was grown with a substrate temperature of 250° and then annealed at 620° during 1 min. First, ΔR signal rises rapidly near to zero delay time and then it decreases exponentially. The rise time for the reflected signal is about 290 fs (Fig. 2.3). The exponential fitting process (see in section III.2) gives two time constants: one is $\tau_1 = 1$ ps and the second one is $\tau_2 = 3$ ps. Since we excite the carriers with 800 nm (1.55 eV), the photo generated carriers acquire an excess energy around 130 meV with respect to the band gap of GaAs (1.42 eV). So, the fast time decay corresponds to the free electron life time. The second delay time is attributed to the holes. Indeed, free electrons are trapped by a defect level in the band gap. The percentage of filled traps limits the free electron capture. Traps are later made empty by recombination with holes.

IV. LTG-GaAs Device demonstration

The microscopic picture of the LTG-GaAs photoconductive switch (top view) is shown in Fig. 2.4a. A coplanar waveguide (CPW) is deposited on a 2-µm thick low-temperature grown (LTG) GaAs layer. This 2-µm thick LTG-GaAs layer is grown by gas-source molecular beam epitaxy (MBE) on a semi-insulating GaAs substrate at 250°C, and then annealed at 620°C for a period of 1 min. Between the GaAs substrate and the LTG-GaAs layer, a 20 nm AlGaAs barrier layer prevents the photo generated carriers to escaping from the LTG-GaAs layer into the substrate. The CPW is made of parallel 0.5-µm thick evaporated Ti/Au strips, the width of the central strip is 20 µm and the widths of two grand strips are the same with 80 µm for each. The gold strips are separated by 14.5 µm, resulting in a 50-Ω impedance. The photoswitch is located in the central strip of the CPW. The switch structure is an inter-digitated one, including 10 fingers (length 19 µm, width 1 µm) separated by a 1-µm gap. These devices are very sensitive to the photo light because of the short distance between the fingers and hence the enhancement of the electric field even at low bias voltage. The capacity of the switch, when not illuminated, is deduced from microwave S-parameters measurements and is equal to $C = 26$ fF.

a)

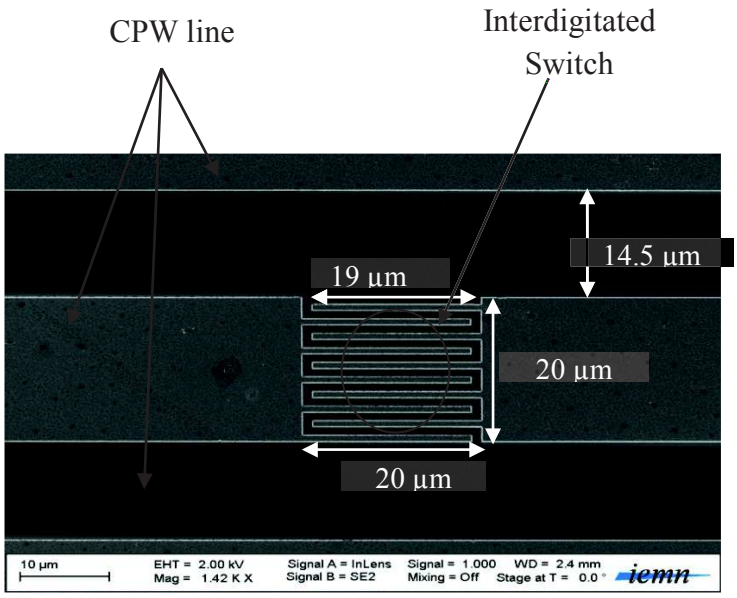

b)

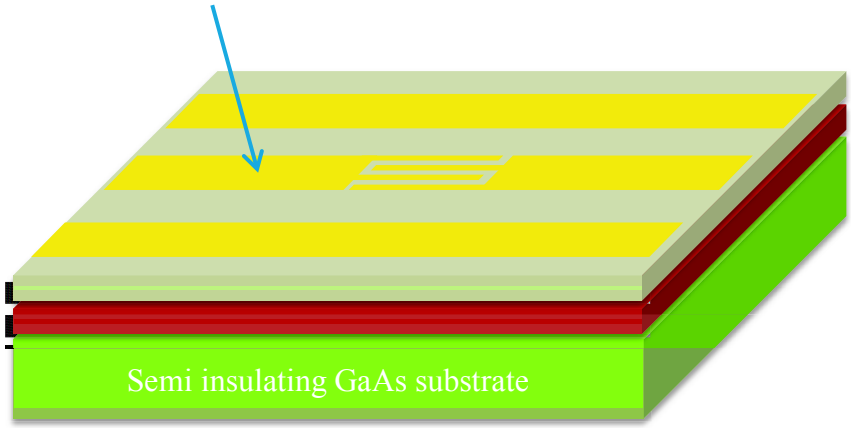

Fig. 2.4: Microscopic picture of low temperature grown GaAs top view (Picture taken at IEMN, Lille) (a) and Classical representation of LTG-GaAs photoconductive switch growth mechanism (b)

V. I-V characteristics of LTG-GaAs photoswitch

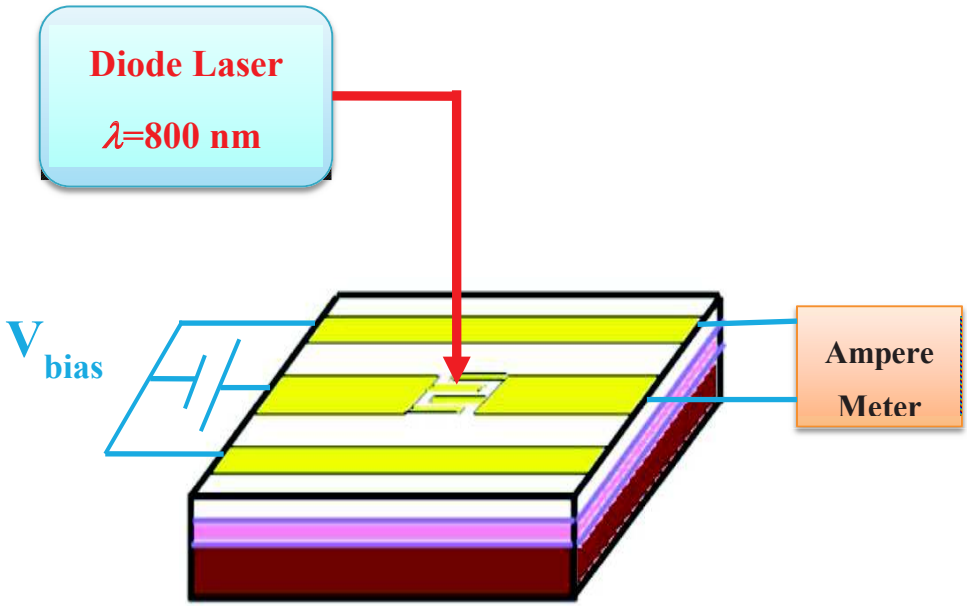

Fig. 2.5a: Experimental set up for photocurrent measurement with respect to bias voltage under the illumination.

In this section, we study the electrical behavior of the photoswitch by measuring its current-voltage characteristics under different optical powers. The measurements were done at IEMN. The experimental set up is shown in Fig. 2.5a. Our present device is a LTG-GaAs photoconductive switch with inter-digitated electrodes. Here, the device is biased with DC voltage and illuminated with a continuous wave (CW) laser light (λ=800 nm). Each absorbed photon of the laser light contributes to create carriers in the semiconductor material, which induces a photocurrent. The photo generated current as function of the DC bias voltage is recorded with a computer. We sweep the DC bias voltage from -1 V to +1 V for two different CW optical powers, namely 11 and 22 mW and the recorded curves are presented in Fig. 2.5b. These curves exhibit an usual S-shape, as already reported in the literature [12], i.e. the current shows first a sub-linear behavior versus the bias voltage, and then tends to saturate at higher voltages. This is explained by the saturation of the drift velocity of the photo-generated carriers [13, 14].

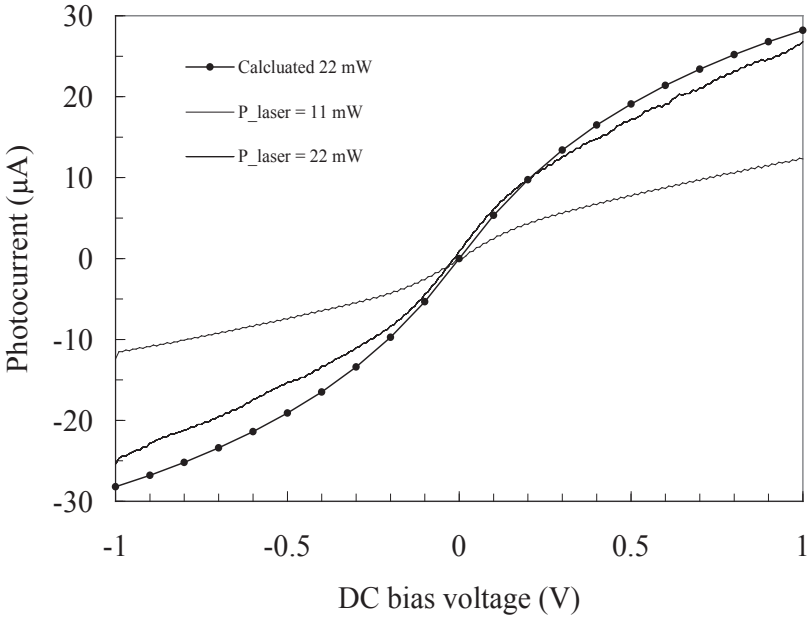

Fig. 2.5b: I-V characteristics of the photoswitch under CW illumination (continuous line P_o=11 mW, dashed line P_o =22 mW). Dots are calculated with P_o =22 mW.

This hypothesis is validated by modeling the photoswitch response. We take into account the photo-carrier dynamics in the semiconductor by solving the rate equation, based on the Shockley-Read-Hall approach. As already mentioned above (eq. II.3d) we assume exponential decay of the photo-generated carriers. From the time evolution of the carrier density N(t) we evaluate the current generated in the device. For that, we assume that the contribution of the holes to the current is negligible as their mobility is usually 2 order of magnitude lower than the electrons one in GaAs or LT-GaAs. Then the current density is $J(t) = q \cdot N(t) \cdot \mu \cdot E$ from which we deduce the current I(t) by considering that the electrical filed is uniformly equal to E=V/l along all dimensions (lateral, longitudinal and vertical) in the region where photoelectrons are generated.

The photo switch geometrical parameters are its width *w* (total length of the fingers), its length *l* (i.e. gap between two fingers) and its thickness

When the photoswitch is biased under large electrical field, the carriers experiment strong acceleration and different effects can lead to carrier velocity saturation. Usually, in GaAs the main phenomena is due to excitation of the carriers up to secondary conduction band where their mobility is lower. Before that, the velocity experiences an overshoot and then saturates to a saturation of 1.2×10^7 cm/s. The overshoot is appearing typically for electric field of few kV/cm. In LT-GaAs, the mobility of the carriers is reduced because of less homogeneity of the semiconductor crystal and the previous overshoot phenomenon is consequently shifted toward very high electrical fields. Before reaching a secondary conduction valley, the photo-generated carrier start to collide in between each other. They also interact with some arsenic cluster that are present in such layers. Following Arifin *et al.* [14a], we have thus introduced the saturation of the carrier mobility as:

$$\mu(E) = \frac{\mu_0}{1+\frac{\mu_0 E}{v_{sat}}} \qquad \text{(II-4b)}$$

where μ_0 is the low-field mobility and v_{sat} is the photo-carrier saturation velocity. The parameters used in fitting process are carrier concentration in semiconductor before excitation is $N_0=1.16\times10^{28}$ m^{-3}, optical power 22 mW, mobility is 0.012 $m^2/V/s$. Now we can see a good fit (see Fig. 2.4b) with experimental curve for $v_{sat} = 5\times10^6$ m/s, in agreement with values already reported for LTG-GaAs [13, 14, 15].

VI. OPTOELECTRONIC SAMPLING AND GENERATION OF SIDEBAND FREQUENCIES

Semiconductor materials with an ultrafast response in the near infrared frequency region have attracted much attention because of their applications as ultrafast photo detectors for optical communication systems and optoelectronic emitters and detectors of terahertz radiation. Ultrafast photoconductive switches are widely used for picosecond electrical pulse generation [16]. Recently, our team used photoconductive switches under pulsed operation and demonstrated [17] that radio frequency (RF) electrical signals are smartly sampled with a photoconductive switch designed in a coplanar waveguide (CPW) and excited by a comb of femtosecond laser pulses. The RF bandwidth of these devices is determined by the photo response time of semiconductor material and the electrical circuit. When employing an ultrafast semiconductor like LTG-GaAs [18], this RF bandwidth exceeds several hundreds of

GHz. Moreover, these devices show linear response to the RF bias voltage and also exhibit a spurious free dynamic range better than 40 dB at 10 GHz, allowing the design of high-resolution optoelectronic ADC [13]. Another signal processing operation that can be performed with metal-semiconductor-metal structure is the generation of sub-carrier signals that are obtained by simultaneously illuminating the device with a modulated optical beam and biasing it with an AC electrical signal considered as the carrier [19]. This has been used in the processing of amplitude [20] or frequency modulated signals in the MHz range [21]. In this section, we present the development of a model for optoelectronic mixing of RF signal (f_ω) and optical beating signal (f_Ω) which is obtained from two CW lasers, using a LTG-GaAs photo-switch to generate sideband frequencies in the transmitted RF signal. The validation of this model is checked by comparison with the experimental results.

VI. 1. Model of a photoconductive switch

VI. 1.1. General Expression

The photoconductive switch consists in a gap made in the central line of a coplanar wave guide (CPW), deposited over an ultrafast semiconductor material. In the present study, the gap exhibits more complicated inter-digitated structure (see Fig. 2.6a). The device is biased by a RF voltage $V(t)$ and the gap is illuminated by optical beating which comes from two CW lasers, whose optical angular frequencies are respectively ω_1 and ω_2, such as $\omega_1 - \omega_2 = \Omega$, with $\Omega << \omega_1, \omega_2$. We suppose the two lasers exhibit the same power P_0 thus the mean optical power at the gap is $P_{laser}(t) = 2P_0(1 + m\cos(\Omega t))$. Here we introduce a modulation factor *m* which is equal to 1 for the case of two beams that are perfectly overlapping in space; in any other case, it will be smaller than 1. We use a simple analytical model [17], in which the device is described by lumped elements, to determine the optoelectronic response of the device. The switch is represented by a photo-varying resistance $R(t)$ in parallel with a capacitance *C (*Fig. 2.6b*)*.

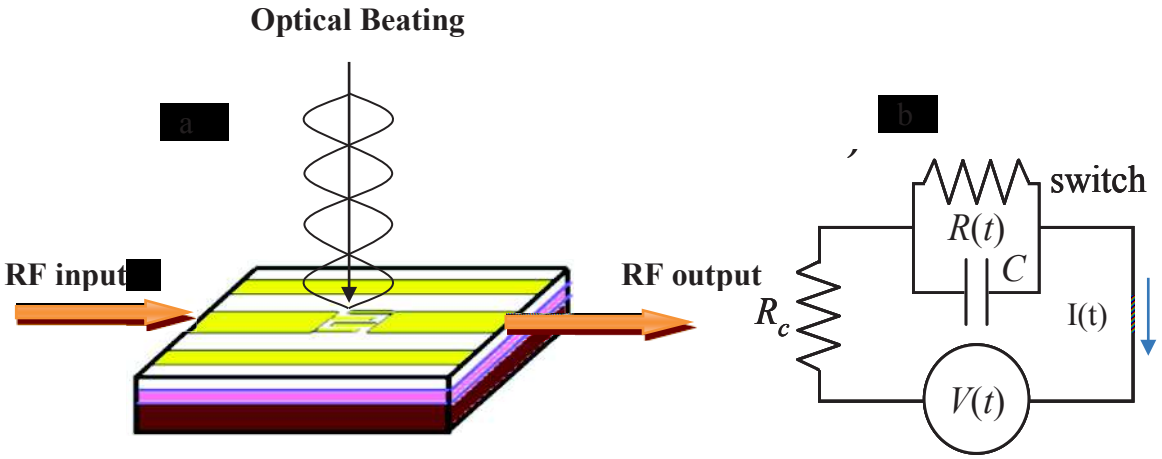

Fig. 2.6: CPW line with the interdigitated switch excited by the optical beating (a), and equivalent electrical circuit (b).

We do not treat the propagation of the RF signal along the CPW, but we assume the impedance of this CPW together with the resistance of the feeding circuit is included in the circuit resistance R_c. Thus the differential equation for the current $I(t)$ in the circuit can be written as

$$R_c C \frac{dI(t)}{dt} + \left(1 + \frac{R_c}{R(t)}\right) I(t) = \frac{V(t)}{R(t)} + C\frac{dV(t)}{dt} \qquad \text{(II-5)}$$

The switch resistance is inversely proportional to the carrier density $N(t)$ in the semiconductor material. When the light illuminates the gap of the switch, electron–hole pairs are generated by absorbing the incident light. Thus, the electrical signal can spread across the gap, and then it becomes conductor. So, the resistance decreases with increasing the number of charge carriers:

$$\frac{1}{R(t)} = A\,N(t) = A\left(N_{dark} + \Delta N(t)\right) = \frac{1}{R_{dark}} + A\,\Delta N(t) \qquad \text{(II-6)}$$

where A is a proportionality constant, and R_{dark} and N_{dark} are the dark resistance and the dark carrier density respectively. $\Delta N(t)$ is the photo-carrier density when the switch illuminated by optical beating.

Let us now derive the expression for the A coefficient. The photo switch geometrical parameters are its w (total length of the fingers), its length l (i.e. gap between two fingers) and its thickness

switch results only from the conduction contribution (the displacement contribution is assumed to be weak), the photocurrent in the switch is:

$$R = \frac{V_s}{I} = \frac{l}{w\,\delta\,Nq\mu} \tag{II-7}$$

where μ is the free carrier mobility that is supposed to be independent of electric field and q is the carrier charge. From equations (II-6) and (II-7), the coefficient A can be written as:

$$A = \frac{1}{R\,N} = \frac{w\,\delta}{l} q\mu \tag{II-7a}$$

Here, we should point out that because we treat the case of semiconductor with an ultrafast carrier lifetime τ shorter than a few ps, the dynamics of the photo generated carriers is assumed to be fully governed by this trapping time and any diffusion or drift process can be neglected. As a consequence, the thickness of the current sheet is equal to the penetration depth

$$E_1(t) = E_1 e^{j\omega_1 t}$$
$$E_2(t) = E_2 e^{j\omega_2 t} \quad \text{(II-10)}$$

Where E_1 and E_2 are the amplitude of the signals and the resultant signal is:

$$E(t) = E_1 e^{j\omega_1 t} + E_2 e^{j\omega_2 t} \quad \text{(II-11)}$$

The intensity of optical signal is expressed as:

$$I_{laser}(t) = |E(t)|^2 \quad \text{(II-12)}$$

From equations (II-11) and (II-12), the optical intensity can be simplified as

$$I_{laser}(t) = I_1 + I_2 + 2m\sqrt{I_1 I_2}\cos(\Omega t) \qquad \text{with } \Omega \equiv \omega_2 - \omega_1 \quad \text{(II-13)}$$

If the two laser beams are of equal intensity, the preceding equation leads to the simplified relation in terms of power:

$$P_{laser}(t) = 2mP_o\left(1+\cos(\Omega t)\right), \quad \text{(II-14)}$$

Thus, the carrier density including expressions (II-14) writes:

$$N(t) = N_{dark} + 2mP_o\beta\frac{1}{V}\frac{\lambda}{hc}\int_{-\infty}^{t}\left(1+\cos(\Omega t')\right)f(t-t')dt' = N_{dark} + \Delta N(t) \quad \text{(II-15)}$$

Equation (II-15) can be solved and simplified as follows for a single exponential decay time of the carrier population:

$$\Delta N(t) = 2P_o\beta\frac{\tau}{V}\frac{\lambda}{hc}\left(1+mG^2\left(\cos(\Omega t)+X\sin(\Omega t)\right)\right) \quad \text{(II-16)}$$

Using equations (II-7a) and (II-16), the differential equation (II-8) can be written as:

$$R_c C\frac{dI(t)}{dt} + \left(1+R_c\left(\frac{1}{R_{dark}}+G_{opt}\right)+R_c G_{opt} m\frac{\cos\Omega t + X\sin\Omega t}{1+X^2}\right)I(t)$$
$$= V(t)\left(\left(\frac{1}{R_{dark}}+G_{opt}\right)+\left(G_{opt}m\frac{\cos\Omega t + X\sin\Omega t}{1+X^2}\right)\right)+C\frac{dV(t)}{dt} \quad \text{(II-17)}$$

with $G_{opt} = 2\frac{q\mu}{l^2} P_o \beta \frac{\lambda}{hc} \tau$. Let us notice that G_{opt} corresponds to an optically-induced conductance.

VI.1.2. Harmonic bias field

Let us now introduce the RF bias voltage; we suppose the bias voltage is an harmonic signal at RF frequency ω defined by:

$$V(t) = V_o \cos(\omega t + \varphi) = \frac{1}{2} V_o \left(e^{j(\omega t+\varphi)} + e^{-j(\omega t+\varphi)} \right) \tag{II-18}$$

where φ is the phase between optical and RF signals and V_0 is the amplitude of the RF signal. Substituting equation (II-18) in equation (II-17) and making use of complex exponential functions, we get:

$$\begin{aligned} R_c C \frac{dI(t)}{dt} + \left(1 + R_c \left(\frac{1}{R_{dark}} + G_{opt} \right) + \frac{1}{2} R_c G_{opt} m \left(\frac{e^{j\Omega t}}{(1+jX)} + \frac{e^{-j\Omega t}}{(1-jX)} \right) \right) I(t) \\ = \frac{1}{2} V_o \left(e^{j(\omega t+\varphi)} + e^{-j(\omega t+\varphi)} \right) \left(\begin{array}{l} \left(\frac{1}{R_{dark}} + G_{opt} \right) + \\ G_{opt} m \frac{1}{2} \left(\frac{e^{j\Omega t}}{(1+jX)} + \frac{e^{-j\Omega t}}{(1-jX)} \right) \end{array} \right) \\ + C \frac{1}{2} V_o j\omega \left(e^{j(\omega t+\varphi)} - e^{-j(\omega t+\varphi)} \right) \end{aligned} \tag{II-19}$$

For simplicity, we substitute $Z = \frac{R_c G_{opt} m}{2(1+jX)}$ and $G = \frac{1}{R_{dark}} + G_{opt}$ in the above equation and the simplified equation is written as

$$R_c C\frac{dI(t)}{dt}+\left(1+R_c G+Ze^{j\Omega t}+Z^* e^{-j\Omega t}\right)I(t) = \frac{1}{2}V_o\begin{pmatrix}(G+jC\omega)e^{j(\omega t+\varphi)}+(G-jC\omega)e^{-j(\omega t+\varphi)}\\ +\frac{Z}{R_c}\left(e^{j((\omega+\Omega)t+\varphi)}+e^{-j((\omega-\Omega)t+\varphi)}\right)\\ +\frac{Z^*}{R_c}\left(e^{j((\omega-\Omega)t+\varphi)}+e^{-j((\omega+\Omega)t+\varphi)}\right)\end{pmatrix} \quad \text{(II-20)}$$

Let assume that the solution of the equation (II-20) is a series of harmonic functions oscillating at frequency $\omega+n\Omega$ (n is an integer):

$$I(t)=\sum_{n=-\infty}^{n=+\infty} a_n e^{j((\omega+n\Omega)t-\phi)}+b_n e^{-j((\omega+n\Omega)t-\phi)}$$
$$\frac{dI(t)}{dt}=\sum_{n=-\infty}^{+\infty} j(\omega+n\Omega)a_n e^{j((\omega+n\Omega)t+\varphi)}-j(\omega+n\Omega)b_n e^{-j((\omega+n\Omega)t+\varphi)} \quad \text{(II-21)}$$

We introduce this solution in equation (II-20) and, as the complex exponential functions form a basis, and we equalize the terms of same frequency. We get

$$\frac{a_n}{f_n}+Za_{n-1}+Z^*a_{n+1}=\frac{1}{2}V_o\left[(G+jC\omega)\delta_{n=0}+\left(\frac{Z}{R_c}\right)\delta_{n=1}+\left(\frac{Z^*}{R_c}\right)\delta_{n=-1}\right]$$
$$\frac{b_n}{f^*_n}+Zb_{n+1}+Z^*b_{n-1}=\frac{1}{2}V_o\left[(G-jC\omega)\delta_{n=0}+\left(\frac{Z}{R_c}\right)\delta_{n=-1}+\left(\frac{Z^*}{R_c}\right)\delta_{n=1}\right] \quad \text{(II-22)}$$

With $f_n=\dfrac{1}{\left(1+R_c G+jR_c C(\omega+n\Omega)\right)}$

where * superscript indicates the complex conjugate value. $\delta_{n=m}$ is the Kronecker's delta ($\delta_{n=n}=1, \delta_{n\neq m}=0$). Solving the equation (II-22) is easy when we assume that the higher order harmonics are much weaker than the preceding ones, i.e. $a_{|0|}>>a_{|1|}>>...a_{|n|}>>a_{|n+1|}...$ and $b_{|0|}>>b_{|1|}>>...b_{|n|}>>b_{|n+1|}...$:

For n>1

$$\begin{aligned} &\frac{a_n}{f_n} + Za_{n-1} = 0 && \frac{b_n}{f^*_n} + Z^* b_{n-1} = 0 \\ &\Rightarrow a_n = -f_n Z a_{n-1} && \Rightarrow b_n = -f^*_n Z^* b_{n-1} \end{aligned} \qquad \text{(II-23)}$$

Similarly we write the expressions for n=1, 0, -1, <1 values as

$$\begin{aligned} &a_1 = Z\left(\frac{V_o}{2R_c} - a_0\right) f_1; \quad (n=1) && b_1 = Z^*\left(\frac{V_o}{2R_c} - b_0\right) f_1^*; \quad (n=1) \\ &a_0 = \frac{1}{2} V_o \left(G + jC\omega\right) f_0; \ (n=0) && b_0 = \frac{1}{2} V_o \left(G - jC\omega\right) f_0^*; \ (n=0) \\ &a_{-1} = Z^*\left(\frac{V_o}{2R_c} - a_0\right) f_{-1}; \ (n=-1) && b_{-1} = Z\left(\frac{V_o}{2R_c} - b_0\right) f_{-1}^*; \quad (n=-1) \\ &a_n = -Z^* a_{n+1} f_n; \quad (n<1) && b_n = -Z b_{n+1} f_n^*; \quad (n<1) \end{aligned} \qquad \text{(II-24)}$$

Note that for the photoswitch current at RF frequency ω, the $\pm jC\omega$ terms in the expression of a_0 and b_0 correspond to the contribution of the direct capacitive coupling, while the G term is related to conductive coupling including both dark and illuminated conductance.

VI.1.3. Expression for the harmonic powers

Let us now determine the expressions of the instantaneous electrical power $P(\omega+n\Omega)$ dissipated in the load resistance Rc at frequency $\omega+n\Omega$ using expressions (II-21) and (II-24).

$$P\left(\omega + n\Omega\right) = R_c I^2 \left(\omega + n\Omega\right) \qquad \text{(II-25)}$$

From (II-25), it is easy to show that the mean power $\overline{P\left(\omega + n\Omega\right)}$ at frequency $\omega + n\Omega$ is expressed as:

$$\overline{P\left(\omega + n\Omega\right)} = 2R_c a_n b_n \qquad \text{(II-26)}$$

Therefore the active power $P_{\omega+n\Omega}$ delivered by the circuit at frequency $\omega + n\Omega$ is:

$$P_{\omega+n\Omega} = 2R_c \,\mathrm{Re}\left(a_n b_n\right) \tag{II-27}$$

where $\mathrm{Re}(...)$ denotes the real part of $(...)$. From equation (II-24), we get

$$\begin{aligned} a_0 b_0 &= \frac{1}{4}\left(G^2 + (C\omega)^2\right)\left|f_0\right|^2 V_0^2 \\ a_{\pm1} b_{\pm1} &= \frac{\left(G_{opt} m\right)^2}{4\left(1+X^2\right)}\frac{1}{4}\left(\frac{1}{\left(\left(1+R_c G\right)^2 + \left(R_c C\omega\right)^2\right)}\right) V_0^2 \left|f_{\pm1}\right|^2 \\ a_{\pm n} b_{\pm n} &= \frac{\left(R_c G_{opt} m\right)^2}{4\left(1+X^2\right)} a_{n\pm1} b_{n\pm1} \left|f_{\pm n}\right|^2 \end{aligned} \tag{II-28}$$

We derive the harmonic power expression at ω (n=0):

$$\begin{aligned} P_\omega &= 2R_c \,\mathrm{Re}\left(a_0 b_0\right) \\ P_\omega &= 2R_c \frac{1}{4}\left(G^2 + (C\omega)^2\right)\left|f_0\right|^2 V_0^2 \end{aligned} \tag{II-29}$$

Because the source and the CPW line exhibit a 50-Ω impedance while the resistance of the switch is much larger, the switch can be considered as an open circuit, and thus $V_{source} = \frac{V_0}{2}$.

As the RF input power is $P_{RF} = \frac{V_{source}^2}{2R_c} = \frac{V_0^2}{8R_c}$, we finally obtain:

$$P_{\omega,dBm} = 20\log\left(\left|f_0\right|\sqrt{\left(R^2{}_c G^2 + \left(R_c C\omega\right)^2\right)}\right) + P_{RF,\,dBm} + 6 \tag{II-30}$$

Similarly, we obtain the power equation at $\omega+n\Omega$ (n: …..-1, +1…..)

$$P_{\omega\pm\Omega,dBm} = 20\log\left(\frac{R_c G_{opt} m}{2\sqrt{1+X^2}}\left|f_0\right|\left|f_{\pm1}\right|\right) + P_{RF,dBm} + 6 \tag{II-31}$$

$$P_{(\omega+n\Omega),\,dBm} = 20\log\left(\frac{R_c G_{opt} m}{2\sqrt{1+X^2}}\left|f_n\right|\right) + P_{\omega+(n\mp1)\Omega,dBm} \quad (|n|>1) \tag{II-32}$$

In (II -32), the "$\mp$" sign takes the value "$-$" for $n>1$, and "$+$" for $n<-1$. Relations (II-30-II-32) indicate that under illumination, the efficiency of the sideband generation is limited by the low pass band behavior of the device, related to either the RF or optical beat frequencies. Indeed, $|f_n|$ and $1/\sqrt{1+X^2} = 1/\sqrt{1+\Omega^2\tau^2}$ terms are the modulus of first order low pass filters whose cutoff angular frequencies are respectively $(1+R_cG)/R_cC$ and $1/\tau$. At first order, the sideband powers vary linearly with G_{opt}, i.e. with the optical power P_o, the carrier mobility μ and lifetime τ. On the contrary, the powers depend inversely on the square of the distance l between the electrodes of the switch. In the low frequency limit, i.e. below the cutoff frequencies, relations (II-30- II-32) may be approximated by:

$$P_{\omega,dBm} \approx 20\log\left(\frac{R_cG}{1+R_cG}\right) + P_{RF,\,dBm} + 6 \tag{II-33}$$

$$P_{\omega\pm\Omega} \approx 20\log\left(\frac{(R_cG_{opt}m)}{2(1+R_cG)^2}\right) + P_{RF,dBm} + 6 \tag{II-34}$$

$$P_{(\omega+n\Omega),\,dBm} \approx 20\log\left(\frac{R_cG_{opt}m}{2(1+R_cG)}\right) + P_{\omega+(n\mp1)\Omega,dBm} \quad (|n|>1) \tag{II-35}$$

These relations point out that the sideband signals are generated by the optical excitation through the conductance *G*.

VI.1.4. Expression for the dark signal

We write again equation (II-30) i.e.

$$P_{\omega,dBm} = 20\log\left(\frac{\sqrt{\left(R^2{}_cG^2 + (R_cC\omega)^2\right)}}{1+R_CG+R_CC(\omega+n\Omega)}\right) + P_{RF,\,dBm} + 6 \tag{II-36}$$

For the dark case, there is no optical excitation, therefore $G_{opt}=0$. In addition, and for LTG-GaAs photoswitch, $R_{dark}>>Rc$, so we can neglect the R_cG term in the above equation and re-writes as:

$$P_{dark,dBm} = 20\log\left(\frac{R_C C\omega}{1+R_C C\omega}\right) + P_{RF,\,dBm} + 6 \qquad \text{(II -37)}$$

Equation (II-37) represents the power of transmitted RF signal under no laser illumination. This transmission without light excitation arises only from a capacitance effect in the switch, as we suppose that R_{dark} is large.

VI.1.5. Numerical results

We have numerically calculated the dependence of the harmonic powers on the different parameters of the sideband generation. Our modeling is performed for a LTG-GaAs inter-digitated photoswitch, with a 1-μm distance in between the 1-μm width electrodes, which is used in the experimental part of this work. The device capacity is 26 fF, and the access line has a 50-Ω impedance. We suppose that the switch is illuminated at λ=0.8 μm by a P_o = 10 mW laser beam. In fact, because of the inter-digitated structure, only half of the LTG-GaAs material is not covered by metal, thus 50 % of the impinging photons reach the bare LTG-GaAs material, where about 30 % are reflected by the LTG-GaAs surface. Thus only 35% (b = 0.35) of the incoming photons are transformed into photo carriers. Mobility in LTG-GaAs is taken as μ = 285 $cm^2/V/s$. This value is the average of different reported data [20] deduced from photoswitch characterization (it should be noted that analysis of THz emission leads to higher mobility values, maybe due to the contribution of displacement currents [18]). We choose τ = 4 ps, which corresponds to the carrier lifetime in the sample used in the experimental part of this work, as measured by pump and-probe reflectivity experiment. All these values lead to $G_{opt} = 2.54 \times 10^{-4}\ \Omega^{-1}$.

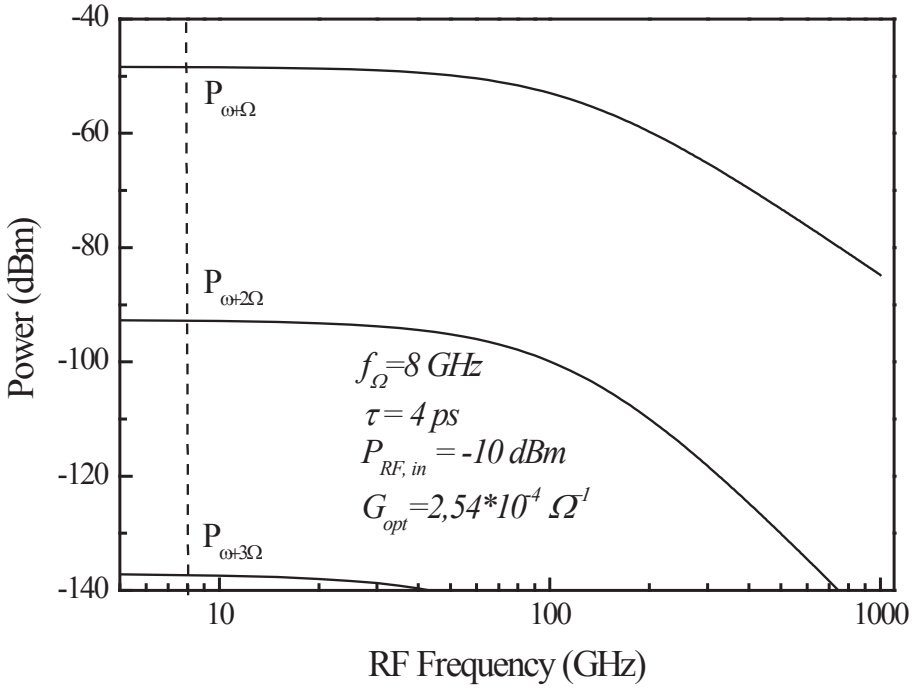

Fig. 2.7: Harmonic powers versus RF frequency when f_Ω = 8 GHz (dashed line). The harmonic numbers are given in the legend. P_{RF} is set to -10 dBm.

Fig. 2.7 shows the harmonic signals (from n = +1 to n = +3) as function the RF frequency for the beat frequency $f_\Omega = 8$ GHz and the RF input power P_{RF} = -10 dBm. The low-pass filter behavior of the device, originating in the function $|f_n|$, is clearly seen. Here, with the device parameters given after, RcG is almost negligible and thus the cutoff frequency for the sideband generation is, $f_{cutoff,n} = \frac{2}{2\pi R_c C} - n f_\Omega$. Thanks to the low value of the circuit response time R_cC, the bandwidth of the device, in terms of sideband generation, exceeds 80 GHz for the first harmonic and 50 GHz for the second harmonic. The power $P_{\omega+n\Omega}$ is larger by about 50 dB as compared to the next harmonic $P_{\omega+(n+1)\Omega}$. $P_{\omega+n\Omega}$ and $P_{\omega-n\Omega}$ (not drawn here) are almost equal. The harmonic power dependence on the beating frequency is presented in Fig. 2.8. Here the RF frequency and power are set to 20 GHz and P_{RF}= -10 dBm respectively. The curves resemble the ones versus RF frequency, but the cutoff frequency appears at a lower value because of the $1/\sqrt{1+X^2} = 1/\sqrt{1+\Omega^2\tau^2}$ term.

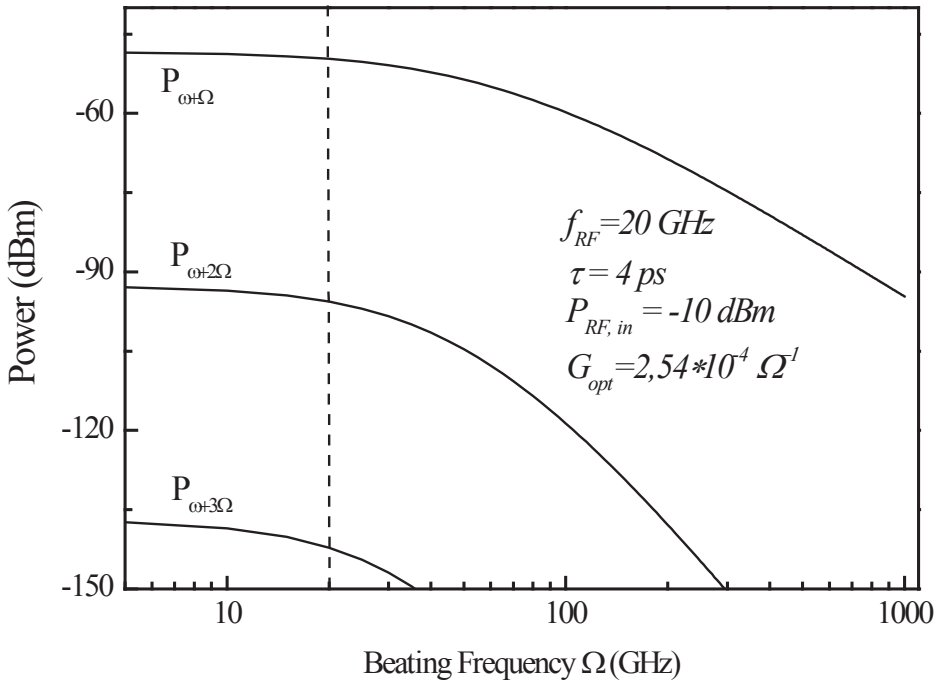

Fig. 2.8: Harmonic powers versus beat frequency. The RF frequency is 20 GHz (dashed line). P_{RF} is set to -10 dBm.

To study the effect of semiconductor material properties (carrier mobility and lifetime) and of the optical excitation (power P_o), we plot (Fig. 2.9) the value of G_{opt} versus P_o for the parameters given above ($\tau = 4$ ps, μ = 250 cm^2/V/s). For common optical powers (mW range), G_{opt} is rather small.

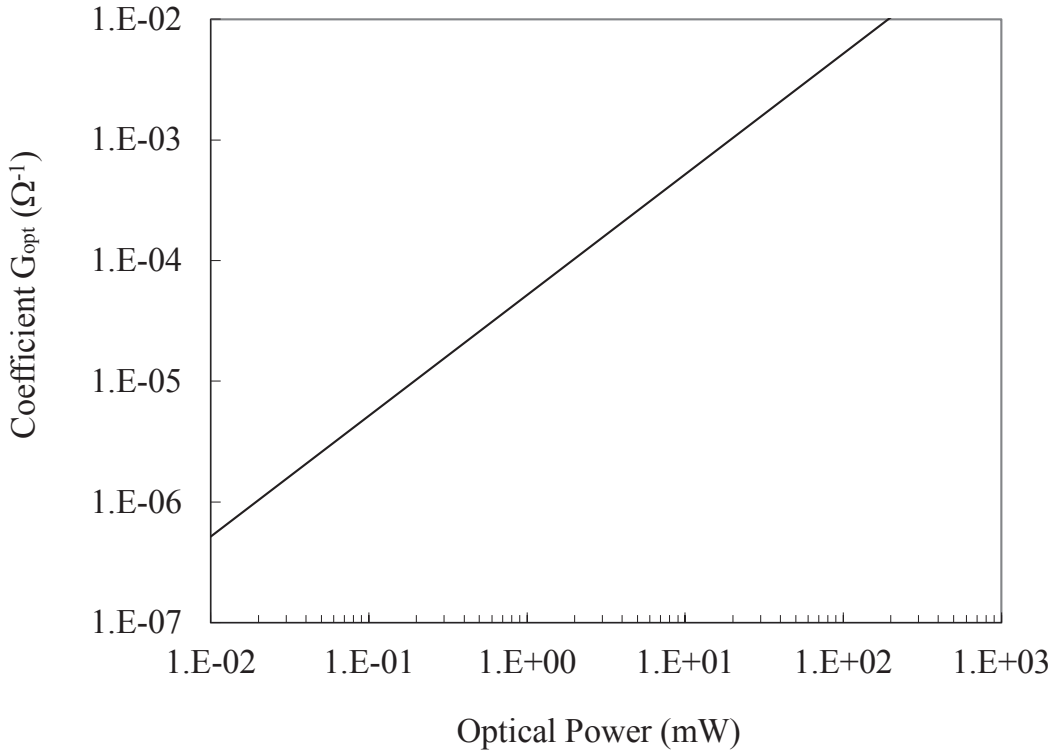

Fig. 2.9: G_{opt} coefficient versus the optical power P_o calculated for τ = 4 ps and μ = 250 $cm^2/V/s$. As G_{opt} varies as the product $P_o \times \tau \times \mu$, similar curves are obtained versus τ or μ, while the other parameters are kept constant.

The dependence of the harmonic powers on G_{opt} is given in Fig. 2.10 for the case of $f_{RF} = 20$ GHz and $f_\Omega = 10$ GHz. As expected from relations (II-30- II-32), for small values of G_{opt}, i.e. shorter lifetime and weaker optical power, the harmonic powers vary almost linearly with G_{opt}. At higher values of G_{opt} , $P_{\omega+n\Omega}$ increases strongly with G_{opt} . This change of regime appears for $G_{opt} \approx 5\times10^{-3}\ \Omega^{-1}$, i.e. for a P_o power of ~ 100 mW with τ = 4 ps, or for τ~ 400 ps with P_o = 1 mW. Below this threshold value, the switch behaves as a capacitance, because $C\omega > G_{opt}$ while, over the threshold, the optical excitation decreases the switch resistance and makes the switch conducting (see equation (II-30)).As already explained, changing G_{opt}, i.e. varying either P_o or τ, affects strongly the power of the generated sideband signals, but not the low pass filter behavior of the device. This is observed in Fig. 2.11, where the first harmonic power $P_{\omega+n\Omega,\ dBm,}$ is plotted versus f_{RF} for different values of G_{opt}. The cutoff frequency increases with G_{opt} i.e., when P_o is kept constant, it decreases when the carrier lifetime τ increases.

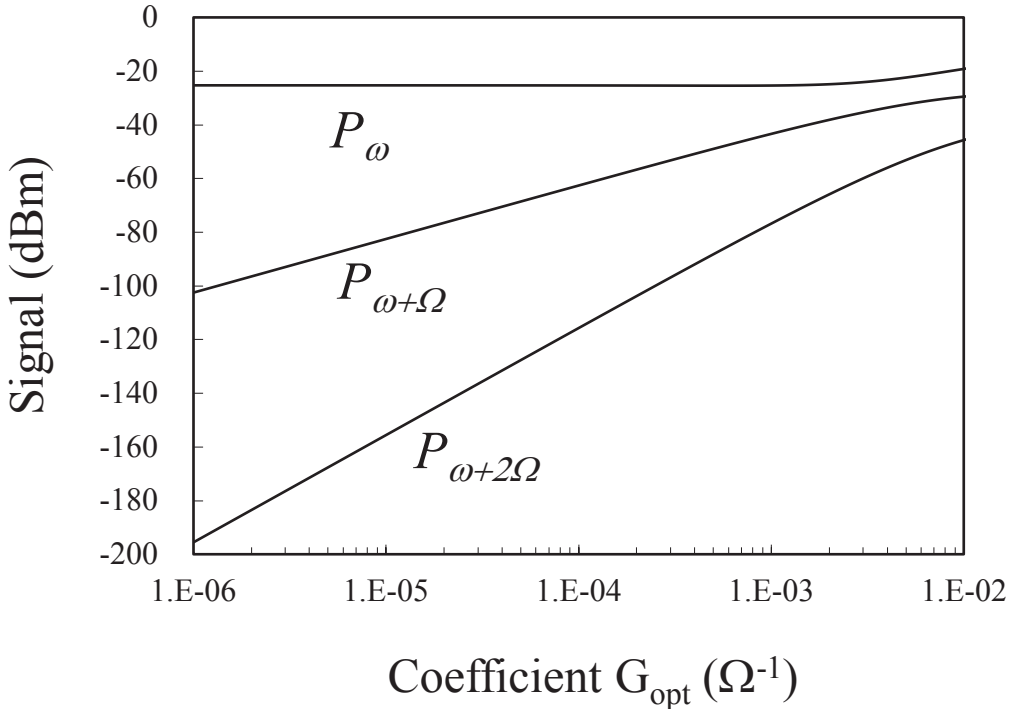

Fig. 2.10: Harmonic powers versus the G_{opt} coefficient. The RF frequency is 20 GHz and the optical beat frequency is 10 GHz. P_{RF} is set to 0 dBm.

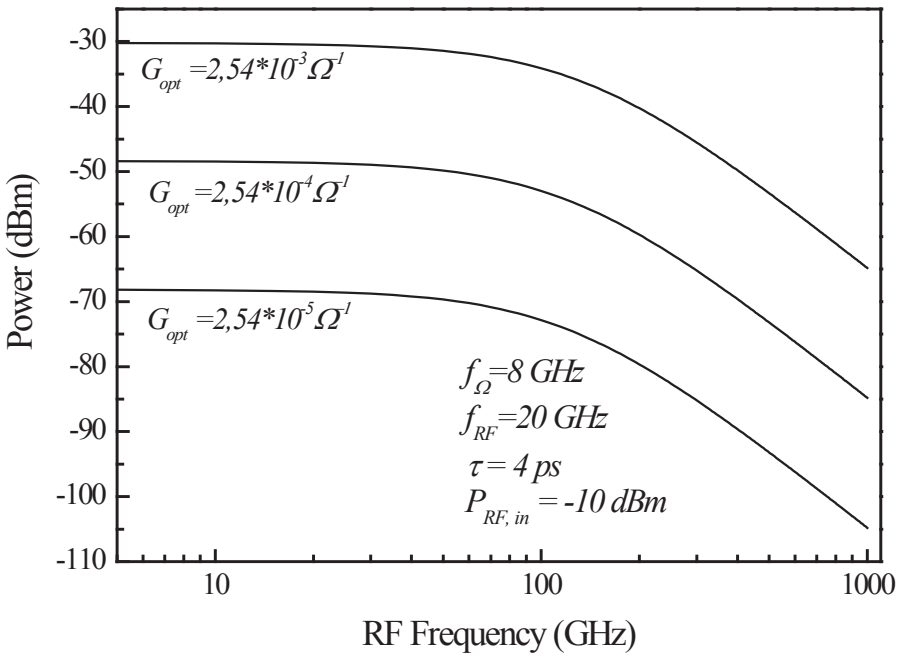

Fig. 2.11: First harmonic power $P_{\omega+\Omega,dBm}$ versus f_{RF}. The optical beat frequency is 8 GHz and P_{RF} is set to -10 dBm.

VI.2. Experimental work

VI.2.1. Experimental setup for frequency sideband generation

The sketch of heterodyne experimental setup used for generation of sideband frequencies is presented in Fig. 2.12. The ultrafast device is RF biased by a microwave signal generator (Rohde & Schwarz SMR 40) that delivers a signal in the 0.1-40 GHz RF frequency range. The RF power P_{RF} can be varied from -25 dBm up to +5 dBm. The transmitted RF signal is recorded in a spectrum analyzer (Rohde & Schwarz FSU 67). The microwave signals are applied and measured at the device thanks to 40 GHz coplanar probes. Two bias-T are also used to allow the dc bias of the device. The photo switch is illuminated by a light beam delivered by 2 CW DFB laser diodes (Eagleyard EYP-DFB-0785-00040-1500-BFY02-0000) at $\lambda \approx 0.78$ µm.

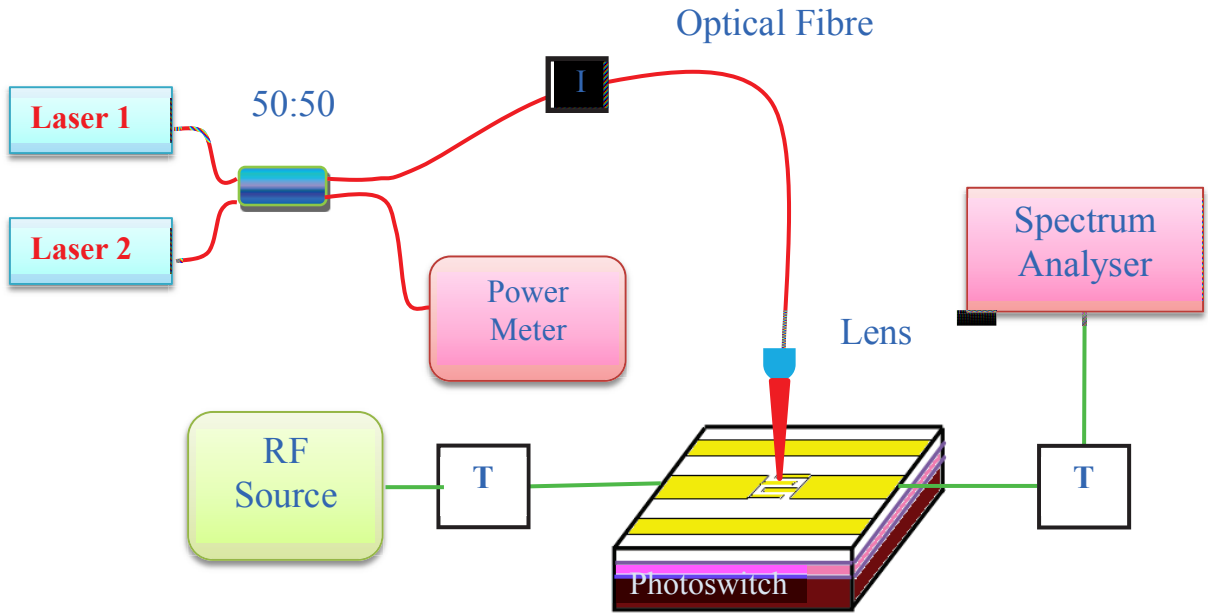

Fig. 2.12: Hetero-dyne experimental setup for harmonic generation. I is isolator, T is Bias-T.

A 50/50 fiber coupler is used to couple the light of the two lasers into one fiber and a Faraday isolator prevents back reflection in the two laser diodes. The output of the isolator is then coupled to a lensed fiber that focuses the beam in the plane of the switch with a waist diameter of about 8-10 µm. The difference between the two laser frequencies is continuously tuned from a few GHz up to 40 GHz (maximum of the spectrum analyzer bandwidth) by varying the temperature of the laser diodes which are finely controlled and stabilized.

VI.2.2. Sideband generation experimental results

In this section, we present the experimental results obtained using the heterodyne experimental setup (Fig. 2.12). First, we measured the dark response of the device and the recorded transmitted RF power as function of RF frequency under no light illumination is presented in Fig. 2.13 (open circles). Here, the RF input power is -10 dBm and the transmitted power is less than -30 dBm. The data are well fitted by relation (II-28) with R_c = 50 Ω and C = 26 fF, up to 15 GHz for which a resonance is clearly seen. This last one could be attributed to an impedance mismatch at the input/output connections of the device. The dark resistance R_{dark} of the switch is at least larger than 100 MΩ.

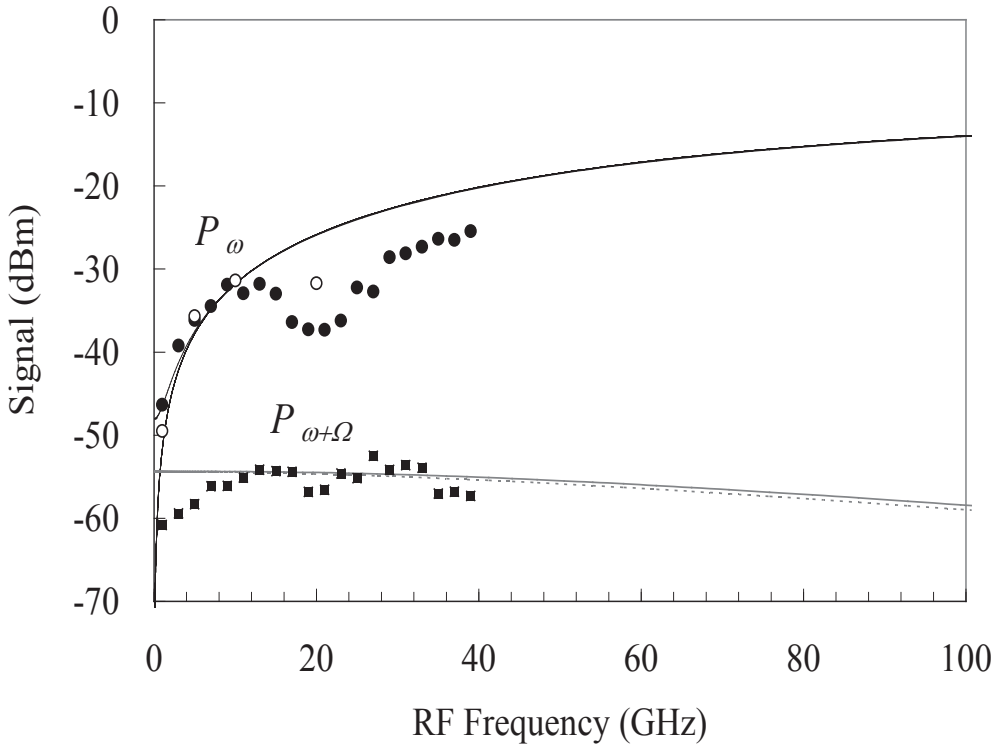

Fig. 2.13: Powers at ω and ω+Ω delivered by the device. f_Ω = 5 GHz, P_{RF} = *-10* dBm, P_o = 10 mW. The lines are calculated with (II-23-II-24). The upper dashed line is the dark power at ω, while the upper continuous line is P_ω under illumination. The continuous and dashed lines below are $P_{\omega+\Omega}$ are $P_{\omega-\Omega}$.

The measured powers P_ω and $P_{\omega+\Omega}$ are plotted versus f_{RF} on Fig. 2.13. Because of the low value of G_{opt}, P_ω under illumination is almost close to the dark value, excepted at low frequency for which the capacitive behavior is strongly perturbed by the optically induced conductivity. Both measured powers are well estimated by the modeling, at least up to the resonance frequency for P_ω.

A typical sideband generation signal is plotted on Fig. 2.14. In this example, the RF frequency

is 20 GHz, while the optical beat frequency is 5 GHz and P_{RF} = 5 dBm. The harmonic lines from n = -3 to n = +2 are clearly observed over the ~ –80 dBm noise level. The transmitted power at ω is about –17 dBm, in good agreement with the calculated value using relation (II-30). The difference between ω and $\omega \pm \Omega$ lines is –22 dBm, here again as expected from theory. The variation of the ω and $\omega + \Omega$ peak amplitude with the RF frequency is shown on Fig. 2.13 (full squares and circles). The order of magnitude of the recorded signals corresponds to the calculated one. With the experimental parameters used in this study and especially the short lifetime τ = 4 ps, the sideband signal at $\omega + \Omega$ is weakly varying with f_{RF}. The signal P_{ω} is almost equal to the dark power P_{ω}^{dark}.

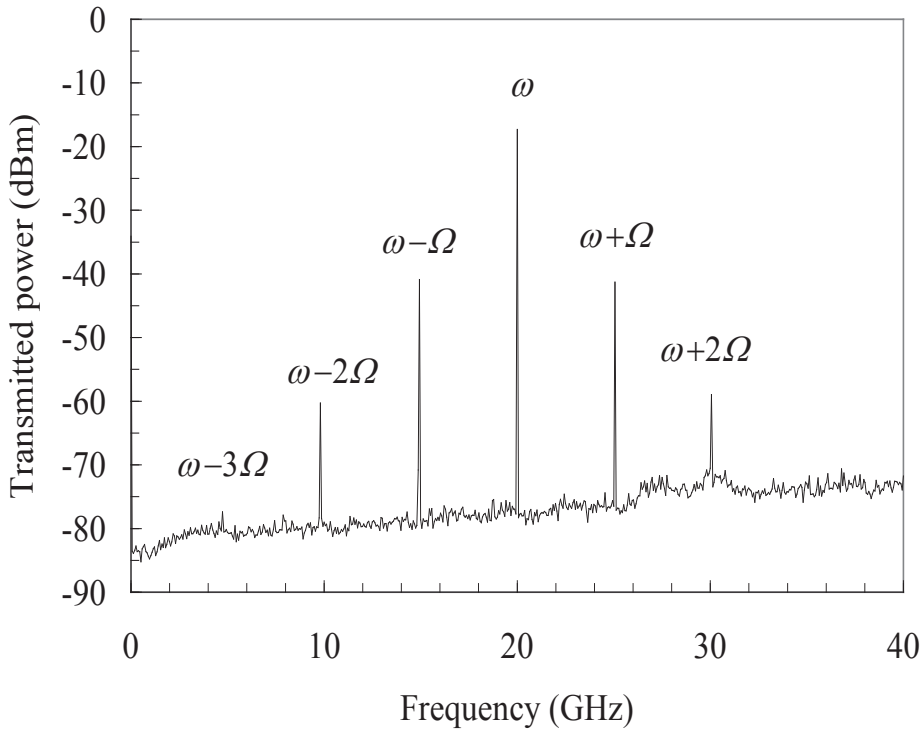

Fig. 2.14: Transmitted spectrum by the switch biased with a 5-dBm signal at 20 GHz and illuminated by the optical beat beam (P_o = 10 mW) at 5 GHz.

It means that the change of the device resistance induced by illumination is not strong enough to perturb the capacitance-like response of the switch. Nevertheless, the effect is more pronounced at lower frequencies. At f_{RF} = 1 GHz, the difference $P_{\omega} - P_{\omega}^{dark}$ is 3 dBm. This effect is also observed for the calculated curves. As already reported above, the resonance effect is clearly seen for both ω and $\omega + \Omega$ signals.

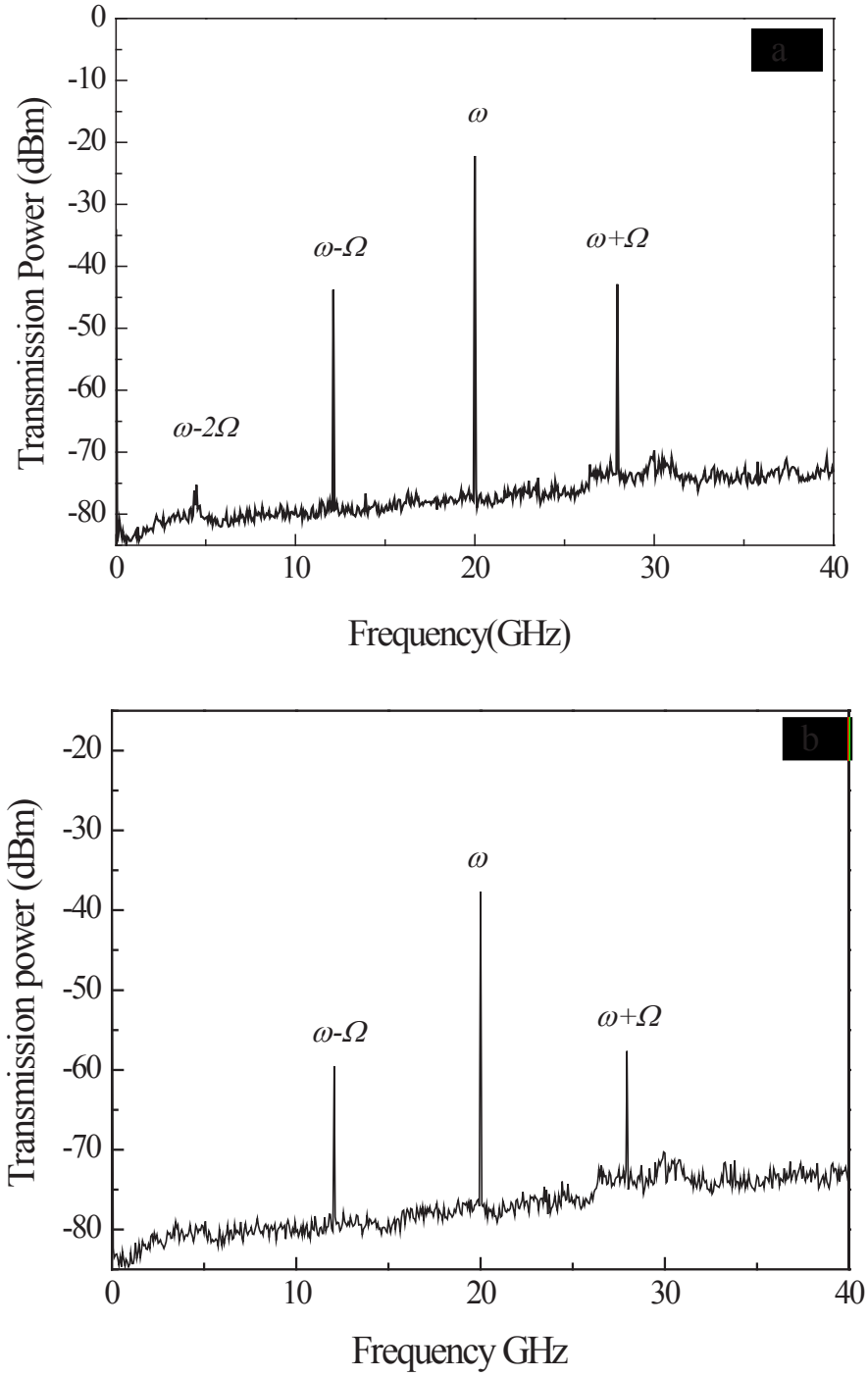

Fig. 2.15: Transmitted spectrum by the switch biased with a 0-dBm signal (a), and with a -15-dBm signal (b) at 20 GHz and illuminated by the optical beat beam (P_o = 10 mW) at 8 GHz.

The measured powers at $\omega \pm 2\Omega$ (~ –40 dBm) and $\omega \pm 3\Omega$ (~ –78 dBm) are much bigger than the calculated values (respectively –77 and –122 dBm). This can be explained by the nonlinear response of the switch with the bias voltage (Fig. 2.4). This nonlinear behavior is known [10, 14] to alter the sinusoidal shape of the harmonic bias, resulting in generation of harmonics that are added to the signal generated through the optical beating excitation.

Similarly, we do the same measurement to generate side band signals at different RF input powers and the recoded spectra are presented in Fig. 2.15. For these two examples, we keep the RF frequency 20 GHz and the optical beating frequency 8 GHz, and vary the input RF power P_{RF}=0 dBm (Fig. 2.15a) and P_{RF}=-15 dBm (Fig. 2.15b). The harmonic lines from n = -2 to n = +1 and from n = -1 to n = +1 with noise level~ –80 dBm are clearly observed in Fig.15 (a & b) respectively. Because of low input RF power, the higher order peaks are not detected.

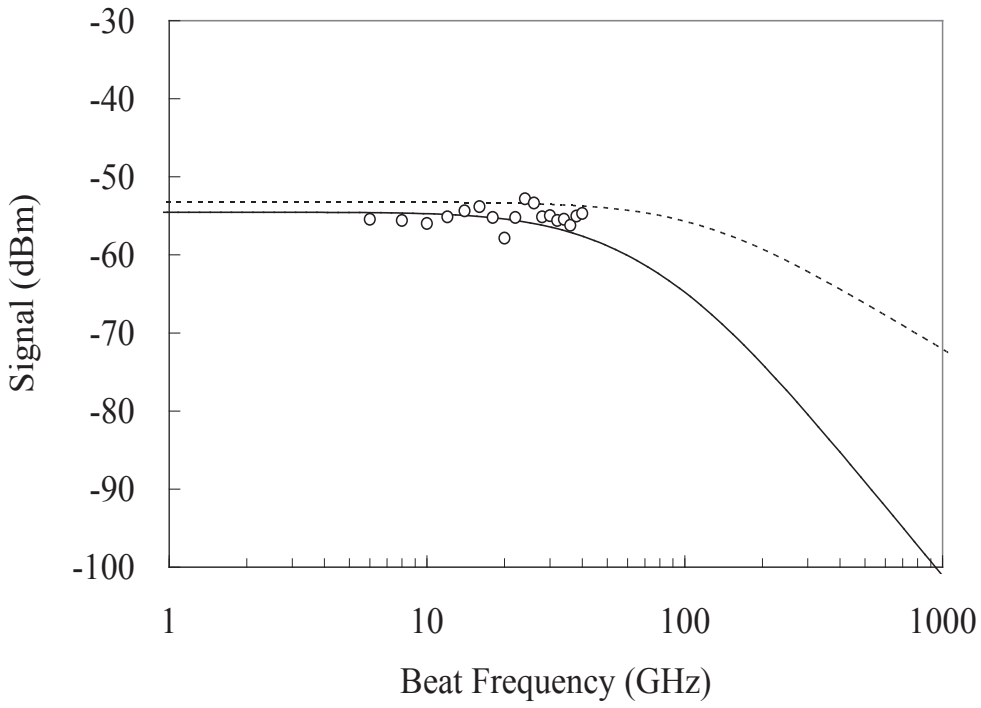

Fig. 2.16: Powers at ω-Ω delivered by the device versus the optical beat frequency f_Ω. . f_ω = 20 GHz, P_{RF} = -10 dBm, P_o = 22 mW. The line is calculated with (II-31). Open circles are measured data. The dashed line is the power P_Ω generated when a DC voltage (V_{DC} = 1 V) is applied to the device.

The signal at $\omega - \Omega$ versus the beat frequency f_Ω is plotted on Fig. 2.16. In the experimental range, the $\omega - \Omega$ power is almost constant. Nevertheless, the resonance dip at 20 GHz is observed. The agreement between model and measured data is good.

Finally, we check the dependence of the signals on the RF power. As given by (II-23-II-25), this dependence is expected to be linear, as we did not introduce the saturation of the carrier velocity in our model. The experiment is performed with f_{RF} = 20 GHz and f_Ω = 21 GHz. The bias power P_{RF} is -10 dBm and P_o = 10 mW. The results are given on Fig. 2.17. In the studied range, i.e. $-25\ \text{dBm} < P_{RF} < 5\ \text{dBm}$, the device response is linear and the measured values are well fitted by the model (corrected from the resonance effect at 20 GHz). At higher powers, the $\omega - \Omega$ signal starts to saturate.

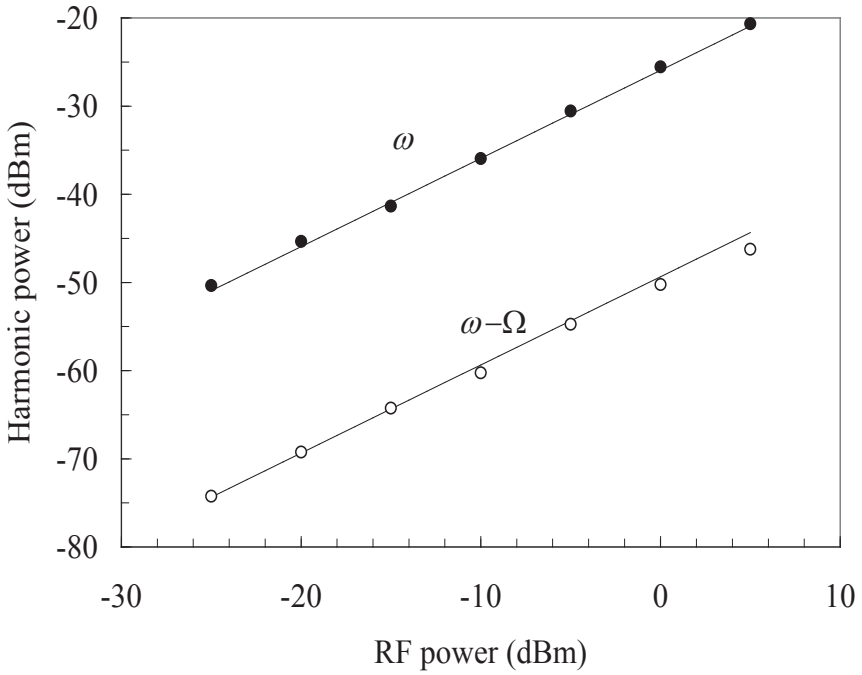

Fig. 2.17: Transmitted signal versus the RF bias power. Open circles are measured data at ω, full circles are for the ω–Ω signal. The continuous lines are calculated with relations (II-23-II-25).

VII. RF OPTOELECTRONIC FREQUENCY GENERATION

In this section, we are interested in using the photoswitch as a RF generator when DC biased and excited by an optical beam beating at the RF frequency. We first give the description of

an analytical model based on lumped element circuit. Then we present experimental results to validate the analytical model.

VII. 1. Theoretical expression

When we apply a DC bias voltage, the device becomes a generator of RF signal when illuminated by an optical beating beam, whose beating frequency ranges in the RF domain. Let us now rewrite the equation (II-20) with an additional DC voltage:

$$V(t) = V_{DC} + V_o \cos(\omega t + \varphi) \tag{II-38}$$

This equation is substituted in the circuit differential equation (II-17) and we get an additional right-hand side term, namely $\left(G + \frac{Z}{R_c} e^{j\Omega t} + \frac{Z^*}{R_c} e^{-j\Omega t} \right) V_{DC}$, to equation (II-19) i.e.

$$R_c C \frac{dI(t)}{dt} + \left(1 + R_c G + Z e^{j\Omega t} + Z^* e^{-j\Omega t}\right) I(t) = \frac{1}{2} V_o \left(\begin{array}{l} (G + jC\omega) e^{j(\omega t + \varphi)} \\ + (G - jC\omega) e^{-j(\omega t + \varphi)} \\ + \frac{Z}{R_c} \left(e^{j((\omega + \Omega)t + \varphi)} + e^{-j((\omega - \Omega)t + \varphi)} \right) \\ + \frac{Z^*}{R_c} \left(e^{j((\omega - \Omega)t + \varphi)} + e^{-j((\omega + \Omega)t + \varphi)} \right) \end{array} \right) + \left(G + \frac{Z}{R_c} e^{j\Omega t} + \frac{Z^*}{R_c} e^{-j\Omega t} \right) V_{DC} \tag{II-40}$$

The solution of this equation is the sum of first term and second term in right hand side of the above equation. The solution for the first right hand term is already obtained in section V.1.2, and let us now derives the solution of:

$$R_c C \frac{dI(t)}{dt} + \left((1 + R_c G) + Z e^{j\Omega t} + Z^* e^{-j\Omega t} \right) I(t) = \left(G + \frac{Z}{R_c} e^{j\Omega t} + \frac{Z^*}{R_c} e^{-j\Omega t} \right) V_{DC} \tag{II-41}$$

We express this solution $I_{DC}(t)$ as a series of harmonics at frequencies $n\Omega$:

$$I_{DC}(t) = \sum_{n=-\infty}^{n=+\infty} g_n e^{jn\Omega t} \tag{II-42}$$

We get:

$$\frac{g_n}{F_n} + Z\, g_{n-1} + Z^*\, g_{n+1} = \left(G\delta_{n=0} + \frac{Z}{R_c}\delta_{n=1} + \frac{Z^*}{R_c}\delta_{n=-1} \right) V_{DC} \tag{II-43}$$

with $F_n = \dfrac{1}{(1+R_cG) + jR_cCn\Omega}$

By applying the same procedure as in section V.1.2, we obtain:

$$\begin{cases} g_n = -ZF_n\, g_{n-1} \quad (n>1); \quad g_n = -Z^* F_n\, g_{n+1} \quad (n<-1), \\ \left(\dfrac{1}{F_1} - |Z|^2 F_2 \right) g_1 + Z\, g_0 = \dfrac{Z}{R_c} V_{DC}, (n=1) \\ \dfrac{g_0}{F_0} + Z\, g_{-1} + Z^*\, g_1 = GV_{DC}, (n=0) \\ \left(\dfrac{1}{F_1^*} - |Z|^2 F_2^* \right) g_{-1} + Z^*\, g_0 = \dfrac{Z^*}{R_c} V_{DC}\,(n=-1). \end{cases} \tag{II-44}$$

The set of equations leads to quite huge and complicated expressions of g_1, g_{-1} and g_0. However, this system can be simplified as $|Z|^2 << 1$ ($Z = \dfrac{RcG_{opt}m}{2(1+jX)}$ and $G_{opt}<10^{-2}\ \Omega^{-1}$, see in Fig. 2.9):

$$\begin{cases} g_n = -ZF_n\, g_{n-1} \quad (n>1) \\ g_1 \approx \dfrac{ZF_1}{R_c} V_{DC}, \\ g_0 \approx \dfrac{R_cG}{R_c(1+R_cG)} V_{DC}, \\ g_{-1} \approx \dfrac{Z^* F_1^*}{R_c} V_{DC} m \\ g_n = -Z^* F_n\, g_{n+1} \quad (n<-1) \end{cases} \tag{II-45}$$

The power generated at Ω is:

$$P_\Omega = R_c \overline{I_\Omega{}^2} = \frac{R_c \left(G_{opt} m V_{DC} \right)^2}{2\left(1+X^2\right)\left((1+R_cG)^2 + (R_cC\Omega)^2 \right)} \tag{II-46}$$

This is the final expression to evaluate the power of the DC signal. The band width of the device is controlled by the $(1+X^2)$, $(1+R_cG)$, $R_cC\Omega$ terms in (III-46) as it can be seen in the following figures.

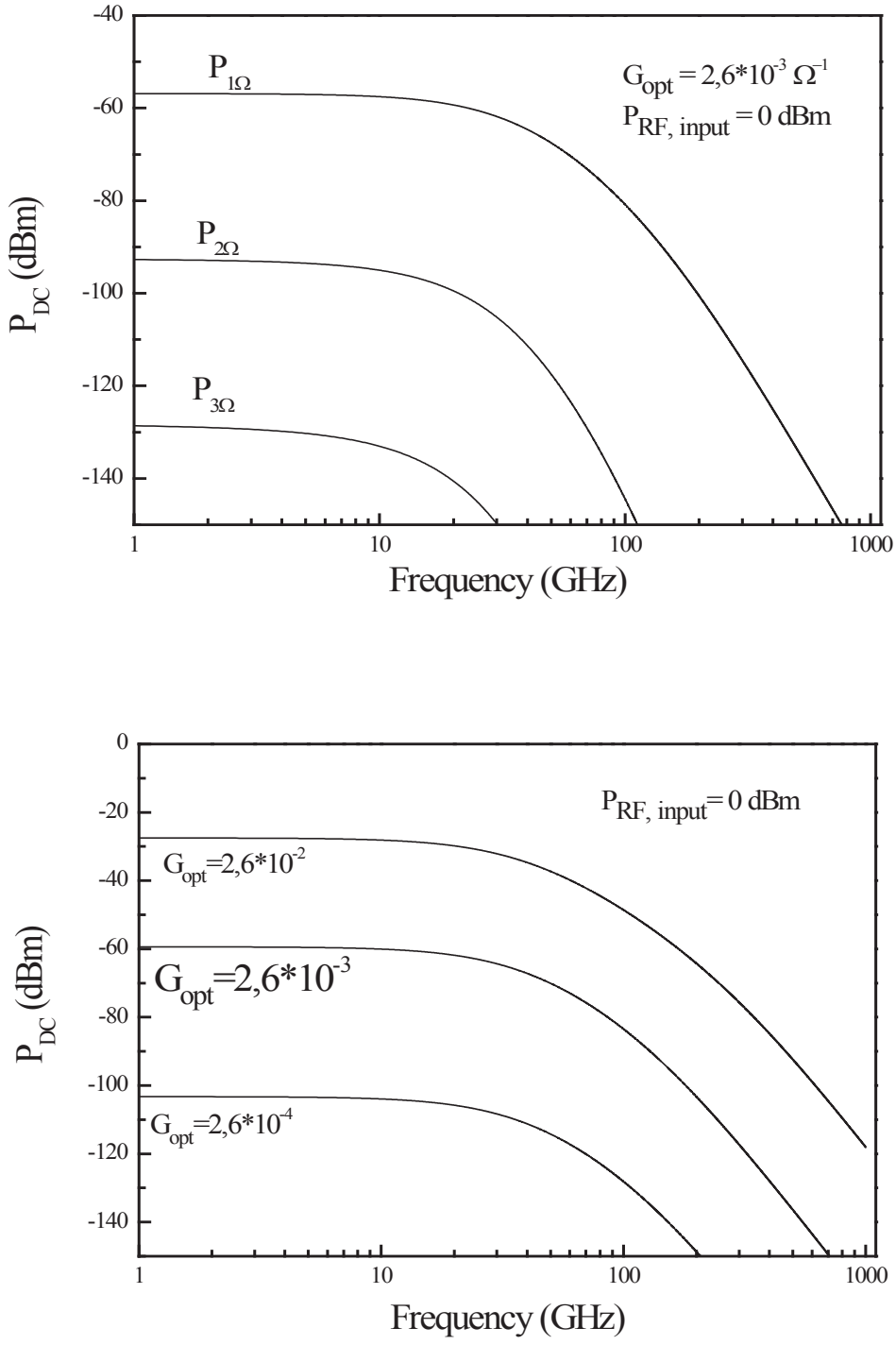

Fig. 2.18: (a), DC signal powers versus f_Ω, G_{opt} is set to 2.6×10^{-3} Ω^{-1}, and (b) first harmonic power $P_{\Omega,,dBm}$ versus f_Ω, for different G_{opt}, i.e. for different optical pump powers. The input RF power is set to 0 dBm.

Fig. 2.18a represents the DC signal powers (from n = +1 to n = +3) as function of the beating

frequency for G_{opt}= 3×10^{-3} Ω^{-1} and P_{RF} = *0* dBm. The curves exhibit the low pass filter behavior of the device as mentioned earlier. $P_{1\Omega}$ is higher about 37 dBm than the followed signal $P_{2\Omega}$ and the device bandwidth is higher for $P_{1\Omega}$ than the preceding ones $P_{2\Omega}$, $P_{3\Omega}$ due to the term $1/\sqrt{1+X^2}$ in equation (II-46). Changing G_{opt}, i.e. varying either P_o or τ, affects strongly the power of DC signal, but the low pass filter behavior of the device remains same (see in Fig. 2.18b, where the first DC signal power $P_{1\Omega}$ is plotted versus beating frequency for different values of G_{opt}). The cutoff frequency increases with G_{opt} i.e., when P_o is kept constant, it decreases when the carrier lifetime τ increases.

VII. 2. Experimental results and discussion

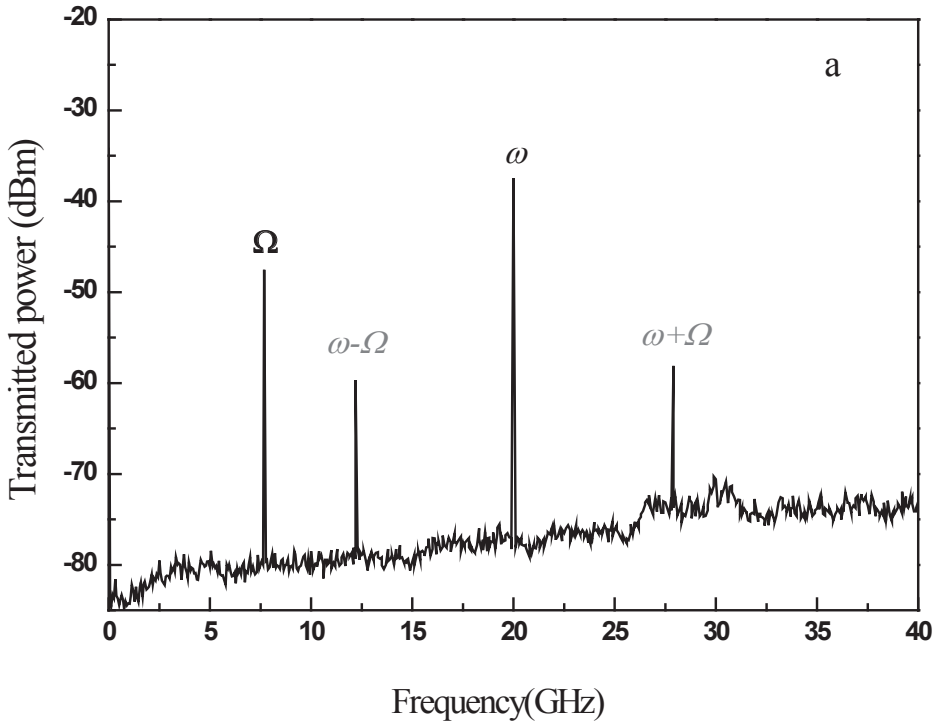

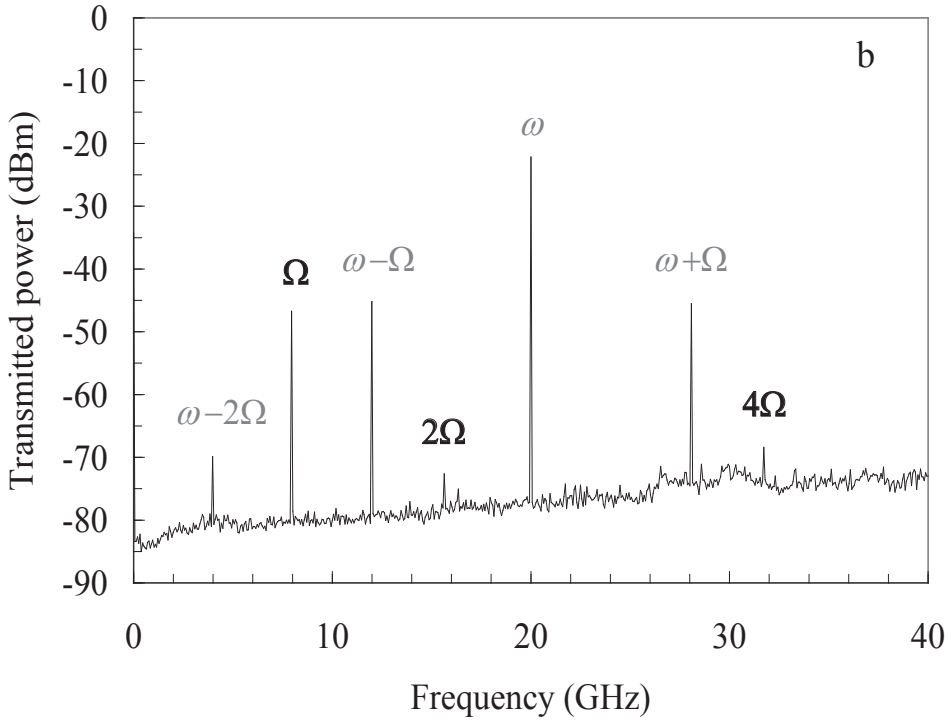

Fig. 2.19: Generated spectrum when the device is biased with a RF 20 GHz signal and a DC voltage (V_{DC} = 1 V). The optical beat power at 8 GHz is 10 mW with RF power P_{RF}=-15 dBm (a), and with RF power P_{RF}=0 dBm (b). The lines generated thanks to the DC bias are indicated with bold values, while the sideband generation is labeled with grey values.

In Fig. 2.19, we presents the spectrum recorded when the device is simultaneously biased with a RF signal at f_{RF} = 20 GHz and a DC voltage V_{DC}= 1 V. The optical beat frequency is f_Ω = 8 GHz and the laser power is 22 mW. In Fig. 2.19a, one clearly sees the signal at ω, together with the harmonic peaks at $\omega+n\Omega$, and a peak at Ω (8 GHz) for input RF power P_{RF}=-15 dBm. Due to this weak input RF power we do not see peaks at 2Ω (16 GHz), 3Ω (24 GHz) etc. No signal is expected at 2w unless the PSW acts as a rectifying circuit, which is not the case here. For a higher input RF power P_{RF}=0 dBm (Fig. 2.19b), we can see the peaks at Ω (8 GHz), 2Ω (16 GHz) and 4Ω (32 GHz) in addition to the signal at ω, together with the harmonic peaks at $\omega+n\Omega$. The signal at 3Ω is not detected. The Ω signal is of the order of what is calculated using relation (II-46). This calculated signal is plotted on Fig. 2.16 (dashed curve) versus f_Ω. It shows a plateau (-53 dBm) up to 100 GHz, over which it strongly decreases with f_Ω. The cut off frequency (-3 dBm) can be derived from (II-46):

$$f_{\Omega,cutoff} \approx \min\left(\frac{1}{2\pi\tau}, \frac{1+R_c G_{opt}}{2R_c C}\right) \qquad \text{(II-47)}$$

Here, the bandwidth is limited by the carrier lifetime (τ = 4 ps) in the semiconductor, as the R_cC circuit response time is of the order of 1.4 ps. The calculated value of the power (-53 dBm) at f_Ω = 8 GHz is a bit smaller than the recorded one (-48 dBm). As proposed previously, this larger experimental signal may be explained by the contribution to the non linearity of the saturation of the photo-carrier mobility in the semiconductor.

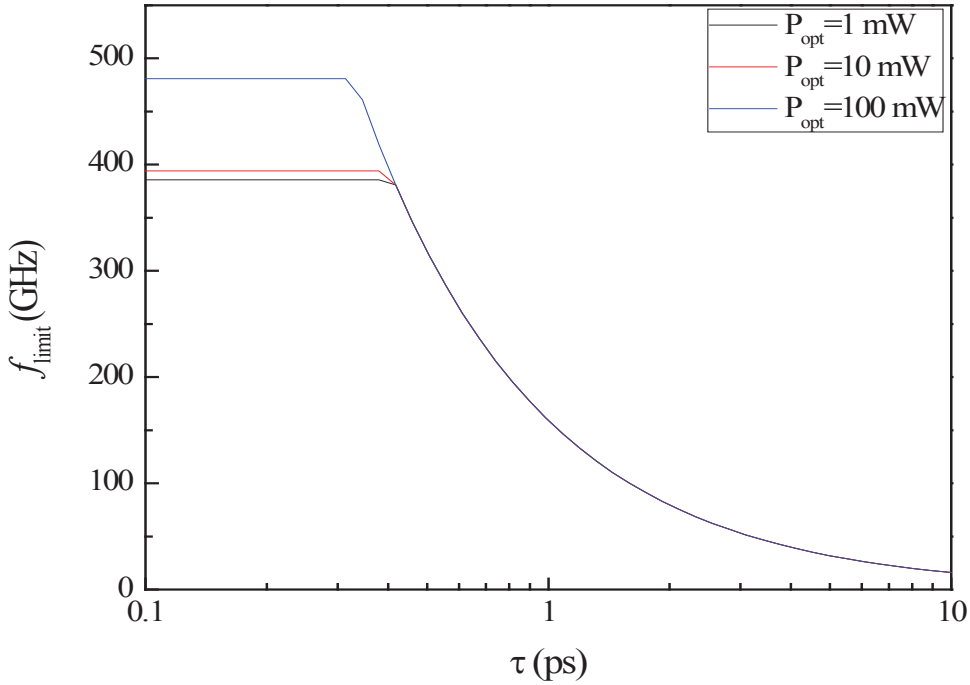

Fig. 2.20: $f_{\Omega,\,cutoff}$ versus τ for different optical powers

To evaluate the upper limit of the bandwidth of this device as RF frequency generator, we plot $f_{\Omega,\,cutoff}$ versus τ on Fig. 2.20, for different optical powers. With sub-*ps* carrier life times, the bandwidth is circuit limited, and reaches typically 400 GHz at low excitation power. For longer life times, the bandwidth decreases exponentially with τ.

VIII. CONCLUSION

We have studied the voltage-current characteristics of the device and the results show the device exhibits non-linear behavior. The nonlinear behavior of light detection in ultrafast optoelectronic switches is used to perform mixing between a RF signal and the optical beating exciting beam. Our analysis shows that this opto-microwave interaction is practically limited in terms of bandwidth by the carrier lifetime in the switch semiconductor material. Employing ultrafast semiconductors with a sub-picosecond carrier lifetime lead to bandwidths exceeding several hundreds of GHz. This analysis is here experimentally validated with a LTG-GaAs switch and its bandwidth is 100 GHz achieved. We are continuing to present the extended study of opto-microwaves phenomena, like the demodulation of information signal carried by the RF signal, in the following chapter-3.

References

[1] John F. Whitaker**, "***Optoelectronic applications of LTMBE III-V materials*" Materials Science and Engineering: *B, **22**,* 61 (1993).

[2] J. Lochtefeld, M. R. Melloch, and J. C. P. Chang ; "*The role of point defects and arsenic precipitates in carrier trapping and recombination in low-temperature grown GaAs";* Appl. Phys. Lett., **69**, 1465 (1996).

[3] F. W. Smith*,* A. R. Calawa*,* C. L. Chen*,* M. J. Manfra*, and* L. J. Mahoney*, "New MBE buffer used to eliminate back gating in GaAs MESFETs,"* IEEE Electron Device Lett*.,* **9***,* 77 *(1988).*

[4] David D. Nolte *"Semi-insulating semiconductor heterostructures: Optoelectronic properties and applications"* J. Appl. Phys., **85**, 6259 (1999).

[5] Jiun-Ren Hwang, Heng-Ju Cheng, and John F. Whitaker, *"Photoconductive sampling with an integrated source follower/amplifier,"* Appl. Phys. Lett., **68**, 1464(1996).

[6] G. Sargsjan, K. Hempel, B. Altmann, H. Bergner, "*On-wafer testing of ICs using free-running optoelectronic sampling and capacitive coupling*"; Microelectronic Engineering, **34**, 187(1997).

[7] B. Kolner, D. Bloom, *"Electro-optic sampling in GaAs Integrated Circuits,*" *IEEE Journal of Selected Topics in Quantum Electronics,* **22**, *765* (1985).

[8] D. Krökel, D. Grischkowsky, and M. B. Ketchen, "*Subpicosecond electrical pulse generation using photoconductive switches with long carrier lifetimes"* Appl. Phys. Lett., **54**, 1046 (1989).

[9] F. W. Smith, H. Q. Le, V. Diadiuk, M. A. Hollis, A. R. Calawa, S. Gupta, M. Frankel, D. R. Dykaar, G. A. Mourou, and T. Y. Hsiang, "*Picosecond GaAs-based photoconductive optoelectronic detectors"* Appl. Phys. Lett., **54**, 890 (1989).

[10] H. Lee, "*Picosecond optics and microwave technology"*, IEEE Trans. Microwave Theory Technol., **38**, 596 (1990).

[10a] Jin- Wei Shi et al, *"High Speed and High Power Performances of LTG-GaAs Based TWPDs in Telecommunication Wavelength (-1.3 μm),"* CLEO, 10 (2002). See also P. W.

Juodawlkis et al, *"Impact of Photo detector Nonlinearities on Photonic Analog-to Digital Converters,"* CLEO, 11 (2002).

[11] S. B. Fleischer, B. Pevzner, D. J. Dougherty, H. J. Zeiger, G. Dresselhaus, M. S. Dresselhaus, E. P. Ippen and A. F. Hebard, *"Ultrafast dynamics of superconducting K_3C_{60} and Rb_3C_{60}"* Phys. Rev. B, **62**, 1366 (2000).

[11a] S. B. Fleischer, B. Pevzner, D. J. Dougherty, H. J. Zeiger, G. Dresselhaus, M. S. Dresselhaus, E. P. Ippen, and A. F. Hebard, Phys. Rev. B, 62, 1366 (2000).

[11b] G. L. Eesley, J. Heremans, and M. S. Meyerand, Phys. Rev. Lett., 65, 3445 (1990).

[11c] B. R. Bennett, R. A. Soref "*Carrier-Induced Change in Refractive GaAs, and InGaAsP*," IEEE Journal Quantum Electronics, **26**, 113 (1990).

[11d] J.-F. Roux, J.-L. Coutaz and A. Krotkus. "Time-resolved reflectivity characterization of polycrystalline low-temperature-grown GaAs", Appl. Phys. Lett., 74, 2462,(1999).

[12] S. Cho and J. Lyou, *"Generation of Ultrafast Electrical Pulses on Semiconductor Photoconductive Switches,"* Journal of the Korean Physical Society, **42**, 272 (2003).

[13] J.-M. Delord, J.-F. Roux, J.-L. Coutaz, and N. Breuil, *"Study of optoelectronic sampler linearity for analog-to-digital conversion of RF signals,"* IEEE Photon. Technol. Lett., **21**, 1369 (2009).

[14] J.-F. Roux, J.-M. Delord, J.-L. Coutaz, *"High speed photoswitching: from material properties to device performances,"* Phys. Status Solidi C6, 2843 (2009).

[14-a] P. Arifin, E. Goldys, and T. L. Tansley, "Monte-Carlo simulation of electron-drift velocity in low-temperature grown GaAs in a Schottky-barrier model", Phys. Rev. B, vol. 52, pp. 5708- 5713, Aug. 1995.

[15] N. Zamdmer, Q. Hu, K. A. McIntosh, and S. Verghese, *Appl. Phys. Lett.,* **75**, 2313 (1999).

[16] M. Bieler, M. Spitzer, K. Pierz, and U. Siegner, *"Improved Optoelectronic Technique for the Time-Domain Characterization of Sampling Oscilloscopes,"* IEEE Trans. Instrum. Meas., **58**, 1065 (2009); and also see M. Ma, H. Ma, P. Gong, C. Yang, and K. Feng, *"Ultrafast optoelectronic technology for radio metrology applications",* Journal of Systems Engineering and Electronics, **21**, 461 (2010); O. Wada, *"Recent Progress in*

Semiconductor-Based Photonic Signal-Processing Devices," IEEE Journal of Selected Topics in Quantum Electronics, **17**, 309 (2011).

[17] J.-F. Roux, J.-M. Delord, and J.-L. Coutaz, *"RF Frequency Response of Photoconductive Samplers,"* IEEE Journal of Quantum Electronics, **47**, 223 (2011).

[18] A. Krotkus and J.-L. Coutaz, *"Non-stochiometric semiconductor materials for terahertz optoelectronics applications,"* Semicond. Sci. Technol., ***20,*** 142 *(2005).*

[19] A Krotkus, *"Semiconductors for terahertz photonics applications,"* Journal of Physics D: Applied Physics, **43**, 273001 (2010).

[20] Q. Z. Liu and R. I. MacDonald, IEEE Photonics Technol. Lett., **5**, 1403 (1993).

[21] H. Shen and K. Aliberti, *"Theoretical analysis of an anisotropic metal–semiconductor–metal optoelectronic mixer",* J. Appl. Phys., **91**, 3880 (2002).

[22] K. Aliberti, H. Shen, M. Stead, W. Ruff, and B. Stann, *"Frequency-Dependent Rectification Current in Metal–Semiconductor–Metal Detectors,"* IEEE Photon. Technol. Lett., **14**, 381 (2002).

CHAPTER 3: OPTOELECTRONIC DEMODULATION OF INFORMATION SIGNAL USING LTG-GaAs PHOTOSWITCH

OPTOELECTRONIC DEMODULATION OF INFORMATION SIGNAL USING LTG-GaAs PHOTOSWITCH

I. Introduction

In chapter-2, we discussed theoretical and experimental studies on optoelectronic sampling and side band frequency generation using an ultrafast optoelectronic sampler. The continuation of this study is given in the present chapter-3. Here we show how ultrafast photoconductive switches can perform a direct demodulation of an information signal carried by a RF signal. First, following the analytical approach of chap. 2, we present how the device performs as a demodulator. Then, we experimentally show the demodulation of a 10-MHz information signal that modulates a 2.5-GHz carrier signal. Based on this proof of concept, operation up to several hundreds of GHz is possible.

II. Principle of optoelectronic demodulation

As shown above the experiment is very similar to the one described before excepted that the switch is biased with a radio frequency (RF) signal, oscillating at angular frequency ω_{RF}, which is modulated by a low frequency $(\Delta\omega)$ signal. Thus ω_{RF} plays the role of the carrier signal frequency, while $\Delta\omega$ corresponds the information signal frequency. Therefore, the bias voltage frequency writes $\omega_{RF} \pm \Delta\omega$. As previously, the switch is simultaneously illuminated by 2 CW laser beams, whose optical frequencies are respectively ω_1 and ω_2:

$$P_{laser}(t) = 2P_{laser}\left(1 + m\cos(\Omega t)\right) \qquad \text{(III-1)}$$

where $\Omega = \omega_1 - \omega_2$ is the beating frequency, P_{laser} is the power of each laser beam and m is a modulation factor that accounts for an unbalanced photo-excitation. As the carrier population is accelerated by the bias voltage at frequency $\omega_{RF} \pm \Delta\omega$, the photocurrent flowing through the switch includes harmonics at $\omega_{RF} \pm \Delta\omega \pm n\Omega$, where n is an integer. If the beating frequency Ω is adjusted to be equal to the RF frequency ω_{RF}, the frequency of the first harmonic $(n = \pm 1)$ will be $\pm\Delta\omega$. Thus the photoswitch directly demodulates the low frequency signal, i.e. it extracts the information signal out of the carrier frequency signal.

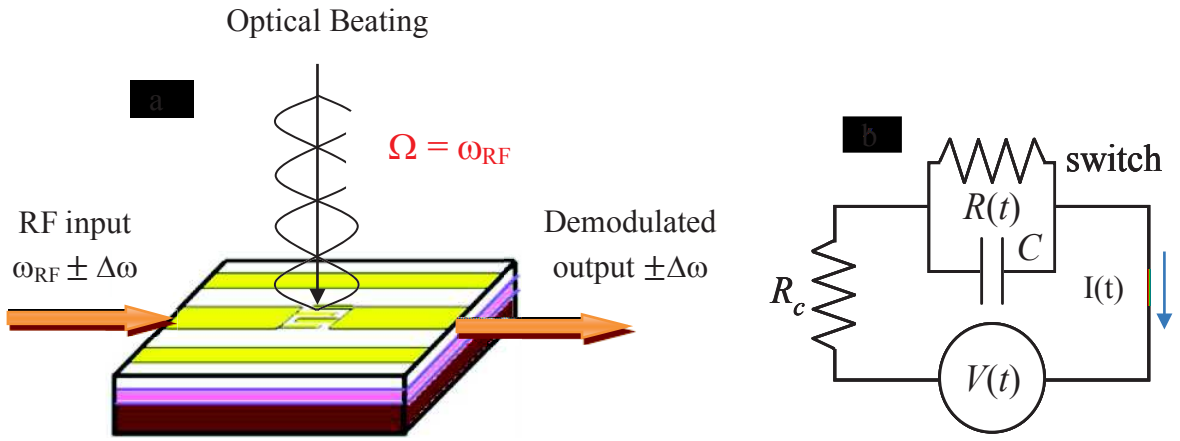

Fig. 3.1: a) Scheme of the photoconductive switch; b) Lumped element model

III. Model of a photoswitch for optoelectronic demodulation

III. 1. Expression for Harmonics

In this section, we derive an expression for the power of demodulated signal using lumped element model. As already discussed in previous chapter, the switch is represented by a photo-varying resistance $R(t)$ in parallel with a capacitance C (Fig. 3.1b). The differential equation (II-5) for the current $I(t)$ is kept valid and we start with $\Delta N(t)$ the photo carrier density in switch after optical excitation as given by relation (II-16):

$$\Delta N(t) = \frac{G_{opt}}{A}\left(1 + m\frac{\cos(\Omega t) + \Omega\tau\sin(\Omega t)}{1+\Omega^2\tau^2}\right) \qquad \text{(III-1)}$$

$G_{opt} = 2\frac{q\mu}{l^2}P_{laser}\beta\frac{\lambda}{hc}\tau$ is the photo-induced conductance.

We introduce the bias voltage, which includes now the modulation at frequency $\Delta\omega$ of the carrier frequency $\omega_{RF} = \Omega$, and it writes:

$$V(t) = V_o \cos(\Omega t + \varphi)\cos(\Delta\omega t)$$
$$= \frac{V_o}{4}\left(e^{j((\Delta\omega+\Omega)t+\varphi)} + e^{j((\Delta\omega-\Omega)t-\varphi)} + e^{-j((\Delta\omega+\Omega)t+\varphi)} + e^{-j((\Delta\omega-\Omega)t-\varphi)}\right). \quad \text{(III-2)}$$

φ is the phase difference between RF and modulation signals. The complete differential equation for the current $I(t)$ in the circuit is obtained by inserting expressions (II-6) (III-4) and (III-2) in equation (III-1) and writes as:

$$R_c C\frac{dI(t)}{dt} + \left(\left(1 + R_c G_{opt}\right) + Ze^{j\Omega t} + Z^* e^{-j\Omega t}\right)I(t)$$
$$= \frac{1}{4}V_o \left(\begin{array}{l} \left(\left(G_{opt} + Cj(\omega-\Delta\omega)\right)e^{j((\omega-\Delta\omega)t-\varphi)} + \left(G_{opt} - Cj(\omega-\Delta\omega)\right)e^{-j((\omega-\Delta\omega)t-\varphi)}\right. \\ \left. + \left(G_{opt} + Cj(\omega+\Delta\omega)\right)e^{j((\omega+\Delta\omega)t-\varphi)} + \left(G_{opt} - Cj(\omega+\Delta\omega)\right)e^{-j((\omega+\Delta\omega)t-\varphi)}\right) \\ + \frac{Z}{R_c}\left(e^{j(\Delta\omega t-\varphi)} + e^{-j((\Delta\omega-2\Omega)t-\varphi)} + e^{j((\Delta\omega+2\Omega)t-\varphi)} + e^{-j(\Delta\omega t-\varphi)}\right) \\ + \frac{Z^*}{R_c}\left(e^{j((\Delta\omega-2\Omega)t-\varphi)} + e^{-j(\Delta\omega t-\varphi)} + e^{j(\Delta\omega t-\varphi)} + e^{-j((\Delta\omega+2\Omega)t-\varphi)}\right) \\ \end{array} \right) \quad \text{(III-3)}$$

with $Z = \frac{1}{2}\frac{R_c G_{opt} m}{1 + j\Omega\tau}$; $G = G_{opt} + 1/R_{dark}$

This is the final equation which we need to solve. We now chose the solution of the above differential equation, as a series of harmonic functions oscillating at frequency $\Delta\omega + n\Omega$ (n is an integer):

$$I(t) = \sum_{n=-\infty}^{n=+\infty} a_n e^{j((\Delta\omega+n\Omega)t-\phi)} + b_n e^{-j((\Delta\omega+n\Omega)t-\phi)}$$
$$\frac{dI(t)}{dt} = \sum_{n=-\infty}^{+\infty} j(\Delta\omega + n\Omega)a_n e^{j((\Delta\omega+n\Omega)t+\varphi)} - j(\Delta\omega + n\Omega)b_n e^{-j((\Delta\omega+n\Omega)t+\varphi)} \quad \text{(III-4)}$$

We substitute the expression (III-4) in to equation (III-3). As the harmonic functions are a mathematical basis, we obtain for the positive and negative frequencies:

$$\begin{aligned}
&\left(1+R_cG_{opt}+R_cCj\left(\Delta\omega+n\Omega\right)\right)a_n+Za_{n-1}+Z^*a_{n+1}\\
&\quad=\frac{1}{4}V_o\left[\left(\frac{Z}{R_c}\right)_{n=2}+\left(G_{opt}+Cj\left(\Delta\omega+\Omega\right)\right)_{n=1}+\left(\frac{Z+Z^*}{R_c}\right)_{n=0}+\left(G_{opt}+Cj\left(\Delta\omega-\Omega\right)\right)_{n=-1}+\left(\frac{Z^*}{R_c}\right)_{n=-2}\right]\\
&\left(1+R_cG_{opt}-R_cCj\left(\Delta\omega+n\Omega\right)\right)b_n\ +Zb_{n+1}+Z^*b_{n-1}\\
&\quad=\frac{1}{4}V_o\left[\left(\frac{Z^*}{R_c}\right)_{n=2}+\left(G_{opt}-Cj\left(\Delta\omega+\Omega\right)\right)_{n=1}+\left(\frac{Z+Z^*}{R_c}\right)_{n=0}+\left(G_{opt}-Cj\left(\Delta\omega-\Omega\right)\right)_{n=-1}+\left(\frac{Z}{R_c}\right)_{n=-2}\right]
\end{aligned} \tag{III-5}$$

We simplify the above equations as:

$$\begin{aligned}
&a_nf_n^{-1}+Za_{n-1}+Z^*a_{n+1}\\
&\qquad=\frac{V_o}{4R_c}\left[\begin{array}{l}Z\delta_{n=2}+Z^*\delta_{n=-2}+\left(Z+Z^*\right)\delta_{n=0}\\+\left(f_1^{-1}-1\right)\delta_{n=1}+\left(f_{-1}{}^{-1}-1\right)\delta_{n=-1}\end{array}\right],
\end{aligned} \tag{III-6}$$

$$\begin{aligned}
&b_nf_n^{*-1}+Zb_{n+1}+Z^*b_{n-1}\\
&\qquad=\frac{V_o}{4R_c}\left[\begin{array}{l}Z^*\delta_{n=2}+Z\delta_{n=-2}+\left(Z+Z^*\right)\delta_{n=0}\\+\left(f_1^{*-1}-1\right)\delta_{n=1}+\left(f_{-1}^{*}{}^{-1}-1\right)\delta_{n=-1}\end{array}\right]
\end{aligned} \tag{III-7}$$

with $f_n=\left(1+R_cG+jR_cC\left(\Delta\omega+n\Omega\right)\right)^{-1}$ and $\delta_{n=p}$ is the Kronecker symbol ($\delta_{n=p}=1$ if $n=p$, $\delta_{n=p}=0$ if $n\neq p$). Now we write the coefficients a_n and b_n from (III-6) and (III-7), by making the assumption that the harmonic signal amplitude strongly decreases with n ($|n|\geq 2$; let us notice that the largest coefficients are a_1 and a_{-1}, as they correspond to the non-mixed transmitted signal that exists even without optical excitation):

$$
\begin{aligned}
&a_n = -f_n Z a_{n-1}\ ; && b_n = -f_n^* Z^* b_{n-1}; && (n>2)\\
&a_2 = f_2\left(\frac{V_o}{4R_c} - a_1\right) Z; && b_2 = f_2^*\left(\frac{V_o}{4R_c} - b_1\right) Z^*; && (n=2)\\
&a_1 = f_1\left(\frac{V_o}{4R_c}\left(f_1^{-1}-1\right) - Z a_0\right); && b_1 = f_1^*\left(\frac{V_o}{4R_c}\left(f_1^{*-1}-1\right) - Z^* b_0\right); && (n=1)\\
&a_0 = f_0\left(\frac{V_o}{4R_c}\left(Z+Z^*\right) - \left(Z a_{-1} + Z^* a_1\right)\right); && b_0 = f_0^*\left(\frac{V_o}{4R_c}\left(Z+Z^*\right) - \left(Z b_1 + Z^* b_{-1}\right)\right); && (n=0)\\
&a_{-1} = f_{-1}\left(\frac{V_o}{4R_c}\left({f_{-1}}^{-1}-1\right) - Z^* a_0\right); && b_{-1} = f_{-1}^*\left(\frac{V_o}{4R_c}\left(f_{-1}^{*-1}-1\right) - Z b_0\right); && (n=-1)\\
&a_{-2} = f_{-2}\left(\frac{V_o}{4R_c} - a_{-1}\right) Z^*; && b_{-2} = f_{-2}^*\left(\frac{V_o}{4R_c} - b_{-1}\right) Z; && (n=-2)\\
&a_n = -f_n Z^* a_{n+1}\ ; && b_n = -f_n^* Z b_{n+1}; && (n<2)
\end{aligned}
\qquad \text{(III-8)}
$$

Now we write the mean power $P_n = P(\Delta\omega + n\Omega)$ of the current at frequency $\Delta\omega + n\Omega$ dissipated in the R_c load calculated from (III-7):

$$P_n = 2R_c\,\mathrm{Re}(a_n b_n) \qquad \text{(III-9)}$$

where $\mathrm{Re}(...)$ denotes the real part of $(...)$. Using the coefficients a_n and b_n from (III-11), we obtain:

$$P_{\pm n} = |Z|^2 |f_{\pm n}|^2 P_{\pm(n-1)} \quad (|n|>2) \qquad \text{(III-10)}$$

$$P_{\pm 2} = |f_{\pm 2}|^2 |Z|^2 P_{RF}\,\mathrm{Re}\left(\frac{\left(Z^2 - |Z|^2 + f_0^{-1} f_{\mp 1}^{-1}\right)\left(Z^{*2} - |Z|^2 + f_0^{*-1} f_{\mp 1}^{*-1}\right)}{2D_a D_b}\right) \qquad \text{(III-11)}$$

$$P_{\pm 1} = \frac{P_{RF}}{2}\mathrm{Re}\left(\frac{1}{D_a D_b}\left(D_a + |Z|^2 - Z^2 - f_0^{-1} f_{\mp 1}^{-1}\right)\times\left(D_b + |Z|^2 - Z^{*2} - f_0^{*-1} f_{\mp 1}^{*-1}\right)\right) \qquad \text{(III-12)}$$

$$P_0 = \mathrm{Re}\left(\frac{\left(f_1^{-1} Z + Z^* f_{-1}^{-1} \right)\left(Z f_{-1}^{*-1} + Z^* f_1^{*-1} \right)}{2 D_a D_b} \right) P_{RF} \tag{III-13}$$

$$\begin{cases} D_a = f_0^{-1} f_1^{-1} f_{-1}^{-1} - |Z|^2 \left(f_1^{-1} + f_{-1}^{-1} \right), \\ D_b = f_0^{*-1} f_1^{*-1} f_{-1}^{*-1} - |Z|^2 \left(f_1^{*-1} + f_{-1}^{*-1} \right). \end{cases} \tag{III-14}$$

In relations (III-13) and (III-14), make the substitution $Z \leftrightarrow Z^*$ when calculating P_{-1} and P_{-2}. The RF power delivered by the source and the bias voltage at the switch, taking account the impedance mismatch at the switch, are related by:

$$P_{RF} = V_o^{\,2} / 16 R_c \tag{III-15}$$

Usually, the Z coefficient remains small when dealing with GHz frequencies and picosecond carrier lifetimes in the semiconductor material. Therefore, (III-12- III-15) relations simplify into:

$$P_{\pm n} = |Z|^2 \, |f_{\pm n}|^2 \, P_{\pm(n-1)}, \qquad (|n| > 2) \tag{III-16}$$

$$P_{\pm 2} = \frac{1}{2} |f_{\pm 1}|^2 \, |f_{\pm 2}|^2 \, |Z|^2 \, P_{RF}, \tag{III-17}$$

$$P_{\pm 1} = \frac{1}{2} \mathrm{Re}\left((1 - f_{\pm 1}) \left(1 - f_{\pm 1}^{\,*} \right) \right) P_{RF}, \tag{III-18}$$

$$P_0 = \frac{1}{2} \mathrm{Re}\left(\frac{\left(f_1^{-1} Z + Z^* f_{-1}^{-1} \right)\left(Z f_{-1}^{*-1} + Z^* f_1^{*-1} \right)}{\left| f_0^{-1} \right|^2 \left| f_1^{-1} \right|^2 \left| f_{-1}^{-1} \right|^2} \right) P_{RF}. \tag{III-19}$$

III. 2: Numerical Results

In this section, we are presenting the calculated results using the lumped element model and we study the dependence of harmonic power for different values of the carrier lifetime and of the optical power. The demodulated power P_0 (III-16, III-22) varies linearly with P_{RF}, and as the square of the power P_{laser} of the optical beams: without light excitation (P_{laser}=0), this signal does not exist. Its spectral behavior is dominated by those of the coefficients $f_{\pm 1}$ and Z.

Both behave as low pass filters with -3 dB cutoff frequencies respectively equal to $f_{circuit} \approx (1+R_cG)/2R_cC$ and $f_{SC} \approx 1/2\pi\tau$. Practically, $R_cG << 1$ thus $f_{circuit} \approx 1/2R_cC$. For $R_c = 50\,\Omega$ circuits, inter-digitated switch capacities are of the order of a few tens of fF, resulting in $f_{circuit}$ ranging between 100 and 1000 GHz. Dipole switches exhibit capacities one order of magnitude smaller, thus in this case the circuit response is not a limiting factor, but the device efficiency is weak. For ultrafast semiconductors like LTG-GaAs, the available sub-picosecond lifetime makes f_{SC} passing the THz limit. However, this is at the expense of efficiency, as G_{opt} and thus Z are proportional to τ.

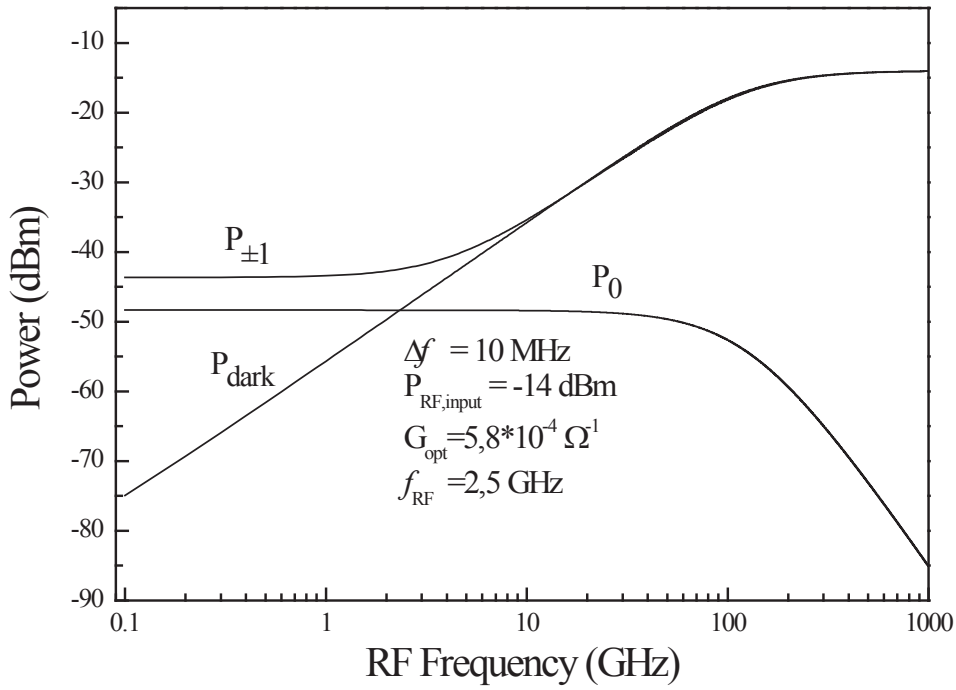

Fig. 3.2: Calculated powers P_0, $P_{\pm1}$ and $P_{\pm1,dark}$ v.s. RF frequency, with $\Delta f = \Delta\omega / 2\pi = 10$ MHz, G_{opt} = $5.8\times10^{-4}\ \Omega^{-1}$ and R_{dark} = 100 MΩ.

The power $P_{\pm1}$ at the incoming RF frequency (III-15, III-21) varies as the bias RF power. Even without optical excitation, $P_{\pm1}$ is not null because the input signal flows through the switch. As the dark resistivity of the semiconductor material is large, at least at 0.8-μm wavelength, the dark switch response is mostly capacitor-like, i.e. it behaves as a high pass filter. The influence of the photo-excitation is thus mainly effective at the lower frequencies.

These behaviors are clearly observed on Fig. 3.2, where we plot P_0, $P_{\pm1}$ and the dark value of $P_{\pm1}$ versus $f_{RF} = \Omega/2\pi$. We take $\Delta f = \Delta\omega / 2\pi = 10$ MHz, τ = 4 ps, C = 26 fF, l = 1 µm, μ = 250 cm^2/V/s and R_{dark} = 100 MΩ, which correspond to our experimental parameters. For P_{laser} = 13.5 mW, this leads to G_{opt} = 5.8×10^{-4} Ω^{-1}. Because of the small value of Δf as compared to f_{RF}, the P_1 and P_{-1} curves are superimposed. The dark $P_{\pm1}$ curve exhibits a high pass behavior, as explained previously. The cutoff of this curve is limited by the material response, as $f_{SC} = 125$ GHz, while $f_{circuit} \approx 384$ GHz. When the switch is illuminated, the $P_{\pm1}$ deviates from its dark value only at lower frequencies. In contrast, the demodulated power P_0 shows a low pass filter behavior, with a 100 GHz cutoff frequency. This cutoff value cannot be analytically derived from (III-16) or even from (III-22).

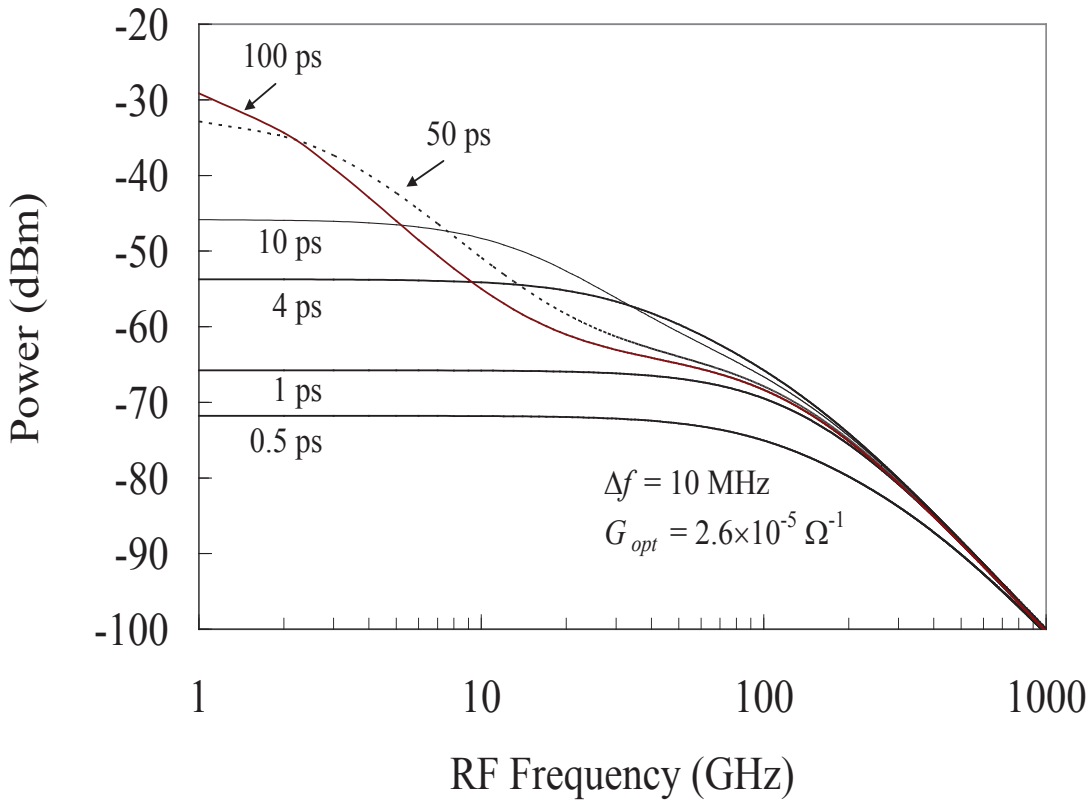

Fig. 3.3: Calculated power P_0 v.s. RF frequency for different carrier lifetimes τ, with $\Delta f = \Delta\omega / 2\pi = 10$ MHz, G_{opt} = 2.6×10^{-5} Ω^{1}, $P_{RF,input}$ =0 dBm and R_{dark} = 100 MΩ.

Fig. 3.3 presents the power P_0 of the demodulated signal versus f_{RF}, for different carrier lifetimes τ spreading from 0.5 up to 100 fs, and for P_{laser} = 1 mW (G_{opt} = 2.6×10^{-5} Ω^{-1}). The

low pass filter behavior of the device response is clearly observed. When τ is short (here below 10 ps), the bandwidth is mostly limited by the circuit response time. When τ becomes larger, the device response is more complex. The bandwidth is first limited by the carrier lifetime, and at higher frequencies, the circuit response contributes to the decay of the signal. Below the bandwidth cutoff, the demodulated signal power depends strongly with τ.

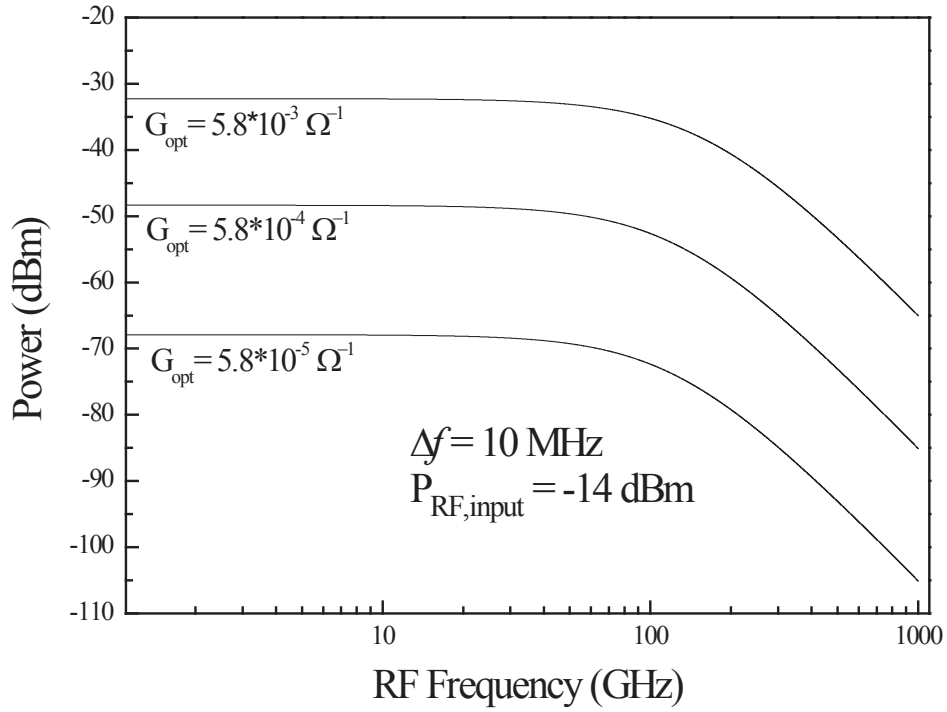

Fig. 3.4: Demodulated signal power as function of RF frequency f_{RF}. The modulation frequency and input RF power is set to be $f_{\Delta\omega}$ =10 MHz and $P_{RF,input}$ = -14 dBm respectively.

Fig. 3.4 shows the influence of the optical pump power that excites the switch. The parameter of the curves is G_{opt} that depends linearly on P_{laser}. In our model, no saturation of photo carrier generation occurs in the semiconductor, thus the power of the demodulated signal varies linearly with P_{laser}.

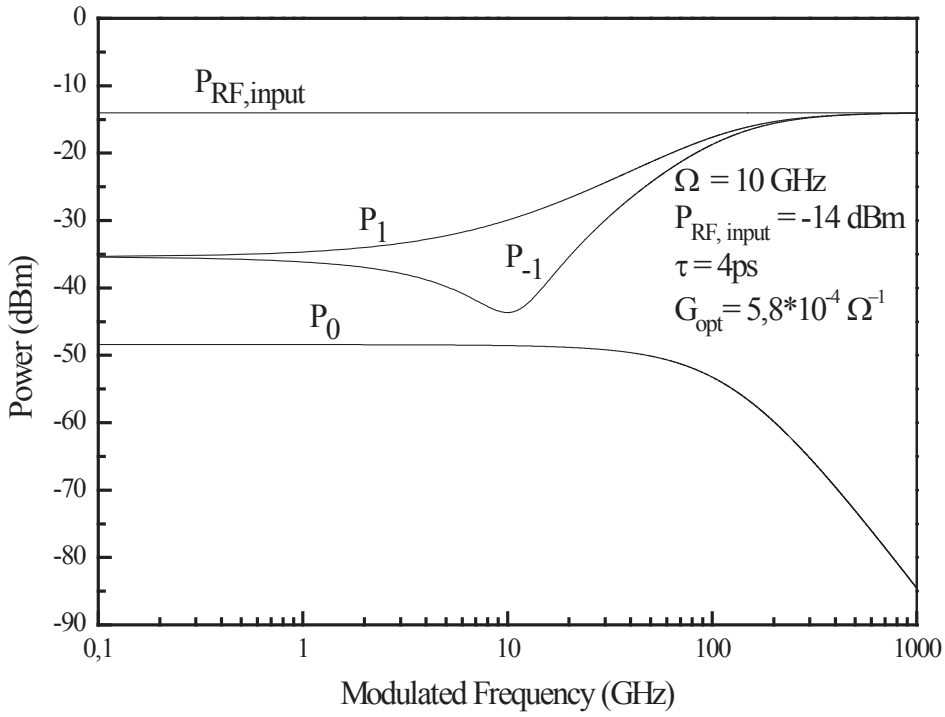

Fig. 3.5: Harmonic power as function of demodulated frequency Δf. The RF frequency and carrier life time are set to be f_{RF} =10 GHz and τ =4 ps respectively.

Finally, Fig. 3.5 shows harmonics power P_0, P_{+1} and P_{-1} versus the modulation frequency Δf when the RF frequency f_{RF} is set equal to 10 GHz. The P_0 curve exhibits low pass band behavior and P_{+1} and P_{-1} curves exhibit high pass band behavior as mentioned earlier. With 4 ps carrier life time, demodulation upto 100 GHz is possible.

IV. EXPERIMENTAL WORK

In this section we discuss about the transmission characteristics of the LTG-GaAs device and the description of the homodyne experimental setup for optoelectronic demodulation experiment, including frequency mixer, photodiode, bias-T, etc. Finally, we present the demodulation experimental results together with numerical results.

IV.1. Photoconductive Device

The microscopic picture of LTG-GaAs photoconductive switch is presented in Fig. 2.5a and also the fabrication steps of the device are presented in section V of chapter 2.

IV.2. S-parameters of the LTG-GaAs device

In this section, we present a detailed study of photoconductive switch with respect to microwave signal to be analyzed. As discussed in earlier chapter 2, the photoswitch is a fairly simple device since it consists of an electrical circuit whose conduction line is interrupted by a gap of semiconductor material. When the gap is not illuminated with light, the circuit becomes open because its dark resistance is very high and the electrical signal is not propagated to the output, thus the photoswitch is in OFF state. When the gap is subjected to light, the gap becomes conductive, "ON" state. Indeed, its resistance decreases due to the generation of electron-hole pairs by absorbing the incident light. Therefore, the electrical signal can spread across the gap and becomes conductor, and as the resistivity of the semiconductor (substrate) is low. In our present study, we use a LTG-GaAs photoconductive switch with a gap that is a more complicated interdigitated structure. The interdigitated structure consists of 10 metal fingers, and the spacing between the fingers is 1 μm and the length each finger is 19 μm. These devices are very sensitive to the photo light because of the short distance between the fingers and hence increase the electric field even at low bias voltage. The carriers life time of LTG-GaAs is about 4 ps, which will allow us at least to cover the radio frequency bandwidth from 1 to 40 GHz.

IV.2.1. Equivalent electrical circuit

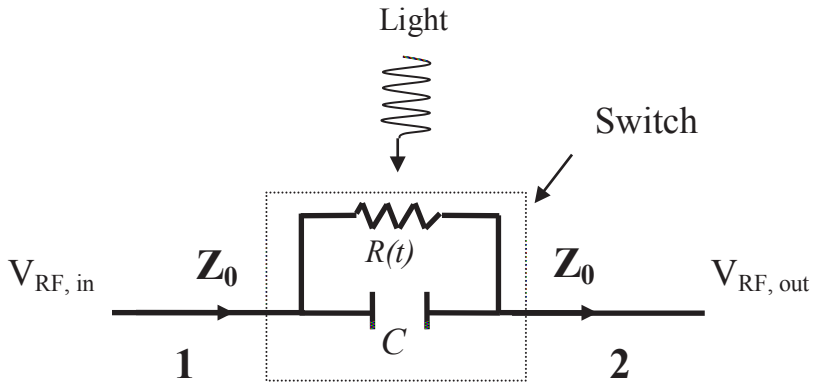

Fig. 3.6a: Equivalent circuit of the switch

As already discussed in the earlier chapter, the photo switch is time varying resistance with parallel capacitance and its equivalent circuit is presented in Fig. 3.6 (a). The notation of the variable resistance is *R(t)* and capacitance *C* and the conductance *G(=1/R(t))* are used in our model. The electrodes facing each other being on each side of the gap, leads to a capacitance, whose value depends on the geometrical parameters of the structure. This effect is taken into account by setting parallel with a capacitor *C* to variable resistance.

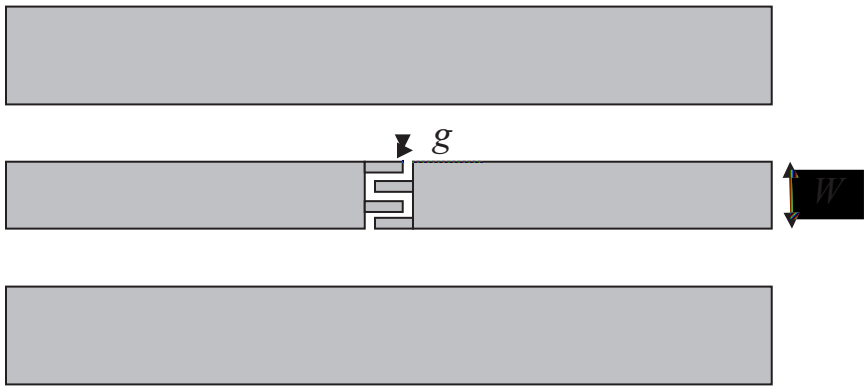

Fig. 3.6b: Schematic of the coplanar line and the gap

Several theoretical models made [1, 2, 3] for coplanar structure (Fig. 3.6b) and the expressions for the capacity and the modulus of S21 are give as:

$$C = \frac{2\varepsilon_r \varepsilon_0 W}{\pi}\left(p - \sqrt{1+p^2}\right) + \ln\left(\frac{p+\sqrt{1+p^2}}{p}\right) \qquad \text{(III-23a)}$$

where $p = \frac{g}{4W}$,and *g, W<<λ* while g is the gap distance in between the fingers.

The modules of the S parameters of the switch inserted in the CPW line are:

$$|S_{11}| = 20Log\left(\frac{1}{\sqrt{(1+2Z_0G)^2 + (2Z_0C\omega)}}\right) \qquad \text{(III-23b)}$$

$$|S_{21}| = 20Log\left(2\sqrt{\frac{(Z_0G)^2 + (Z_0C\omega)^2}{(1+2Z_0G)^2 + (2Z_0C\omega)^2}}\right) \qquad \text{(III-23c)}$$

For our present case, g = 1 µm, W = 20 µm and Z_0 = 50 Ω.

IV.2.2. Experimental results

The S-parameter measurement of the LTG-GaAs device is performed using a vectorial network analyzer to study the resistive power of the semiconductor material under different optical powers. Neglecting the dark resistance of the device which is larger than 1 MΩ, the impedance $Z(\omega)$ of the switch is inversely proportional to the capacitance and applied frequency.

$$Z(\omega) = \frac{1}{jC\omega}. \qquad \text{(III-23c)}$$

The experimental setup used for studying the scattering parameter of the LTG-GaAs device is shown in Fig. 3.6(d). Here, we use a vector network analyzer (E8361A, 10 MHz- 67 GHz) as microwave source and detector, and an external cavity diode laser operating at 800 nm is illuminates the switch. In this experiment, we bias the switch with the microwave through the VNA, and the reflected and transmitted signals of the switch are collected by the VNA. The same measurement is done while the switch is or not illuminated with light.

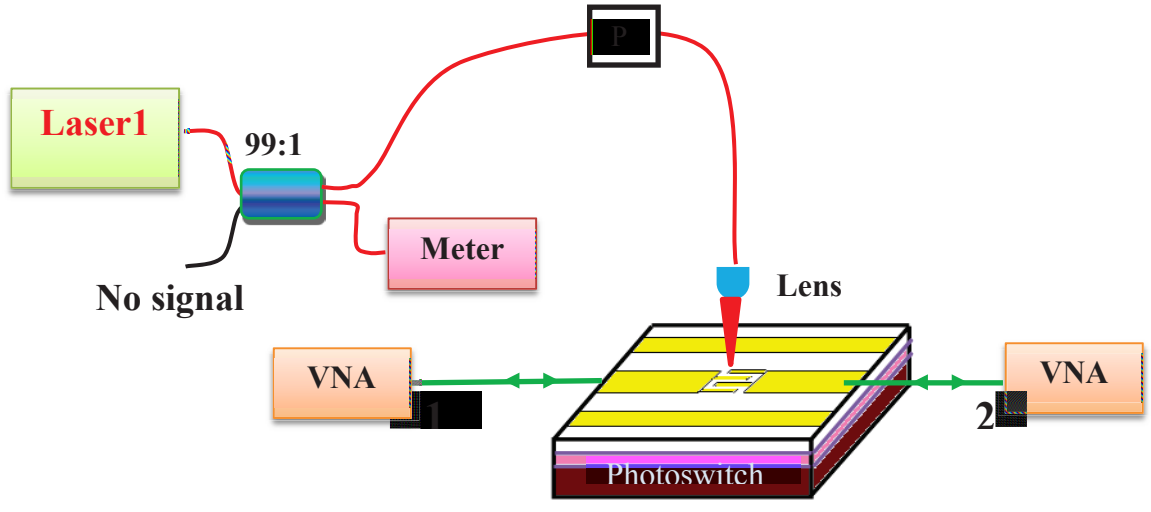

Fig. 3.6c: Experimental setup for S-parameters measurement. VNA is vector network analyzer, P is polarization controller, 1 and 2 are the ports of VNA.

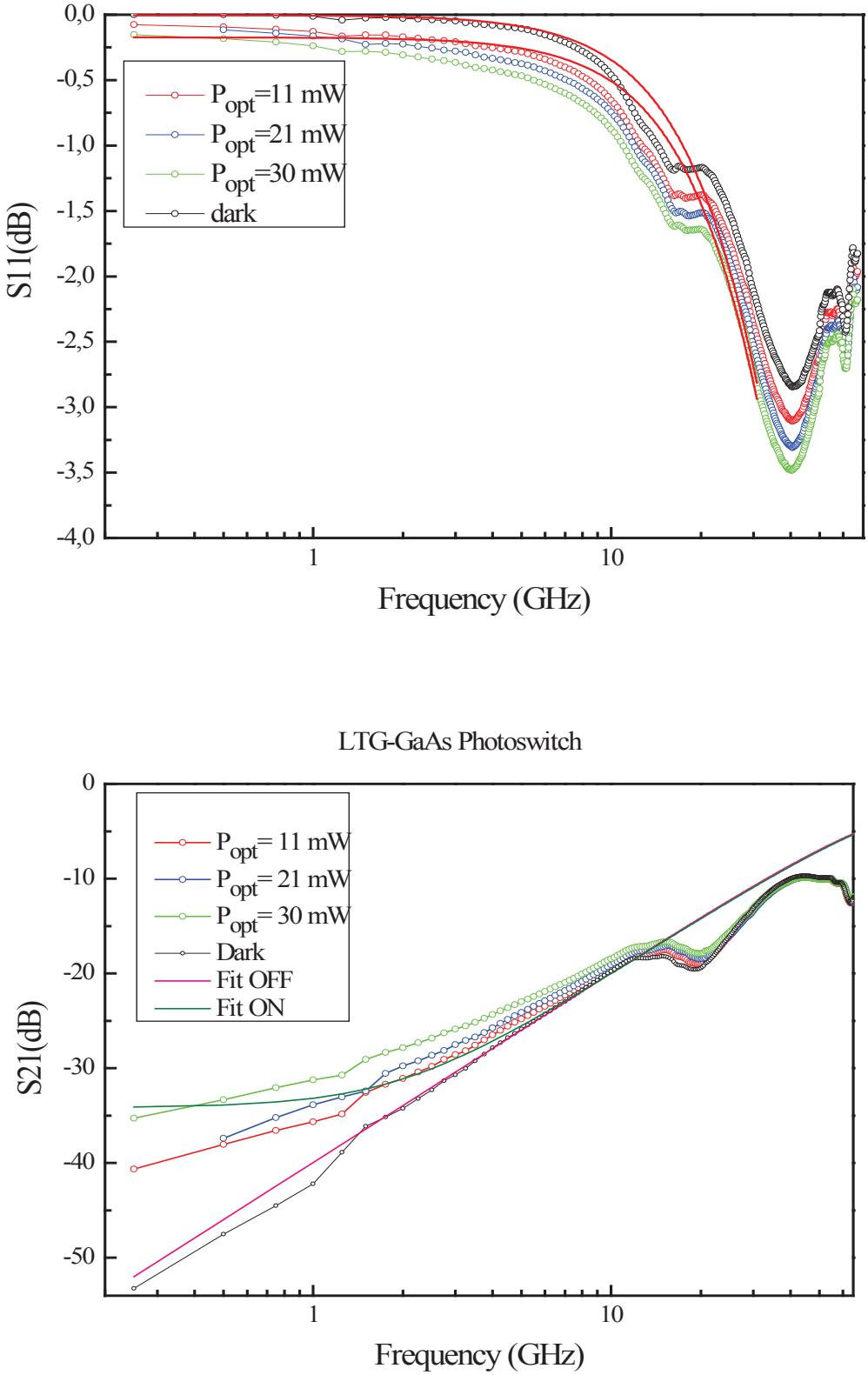

Fig. 3.7: a) Reflection (S11), and b) transmission (S21) characteristics of LTG-GaAs device for different optical powers.

The reflection and transmission experimental spectra of the LTG-GaAs photoswitch for different optical powers are presented in Fig. 3.7. As we see in Fig. 3.7, at low frequency around 0.5 GHz, the microwave transmission through the switch is very low (-53 dB) and the reflection is low (≈0.1 dB) under dark condition (no light on the switch). This is because of the capacity behavior of the switch at lower frequencies (see relation III-23d). The transmission increases with frequency up to 20 GHz. At 20 GHz, as already reported, we observe a resonance, maybe due to the impedance mismatch at the device input and output. Similarly, a second resonance is observed at the second harmonic of 20 GHz, i.e. 40 GHz. When the switch is illuminated, it becomes conductive, thus the transmission increases even at low frequency. The transmission difference between on-off conditions is approximately 18 dB at 0.5 GHz and 1.3 dB at 20 GHz. We fit the experimental data with theory using the relation III-23b & c for the present device for dark and illumination conditions, and the fitting parameter are $C=16\,fF$, $Z_0=50\,\Omega$, $R_{dark}=1\,M\Omega$. For dark condition, theoretical data is well fit with experimental data in lower frequency region up to 20GHz for both S11 and S21. For the illumination case, fitting is good only in the frequency region of 3-10 GHz.

IV.3. Optoelectronic Demodulation

IV.3.1. Description of the experimental setup

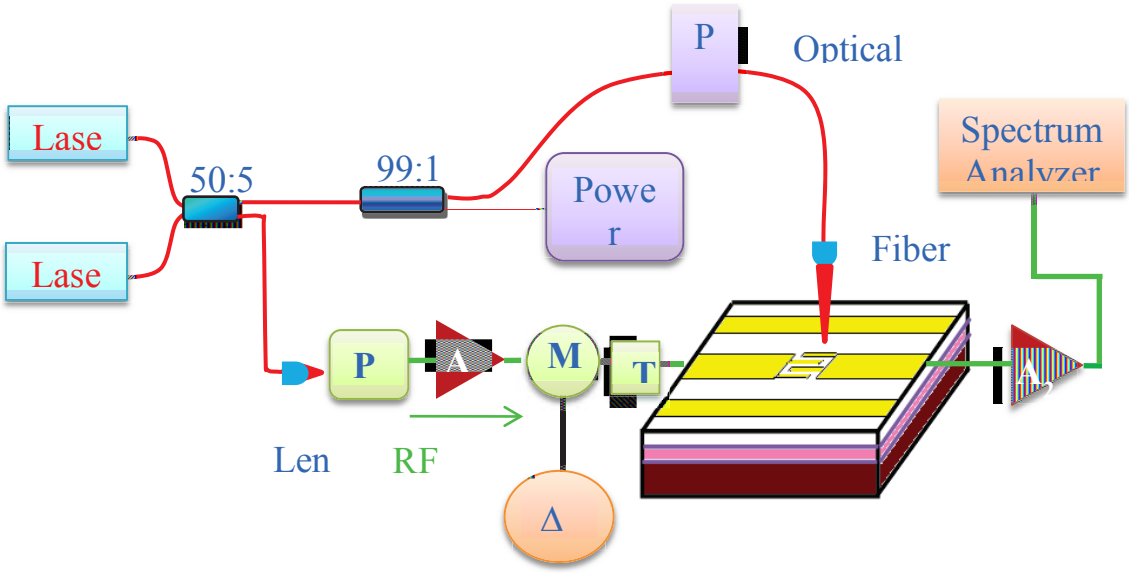

Fig. 3.8: Homodyne experimental scheme for demodulation. P is polarization controller, M is Mixer, T is bias-T, A_1 and A_2 are amplifiers, PD is photo diode.

The classical homodyne experimental setup used for demodulation is shown in the Fig. 3.8, Here the photo switch is illuminated by the optical beating signal, which is delivered from two external cavity CW diode lasers (TLB6700) at 0.78 μm. A 50/50 fiber coupler (coupler 1) splits the beam into 2 fibers. One output excites a Si PIN photodiode (Hamamatsu S7911) that converts the optical signal into a RF signal. This RF signal biases the photo switch. Here we note that, due to instability of laser diodes for the lower beating frequencies (ω_2-$\omega_1 = \Omega \leq 2.5$ GHz), we used the optical signal itself as the RF signal after conversion with the photo diode. One bias-T is used to allow the dc bias of the device. This carrier signal is modulated at a lower frequency using a minicircuit-ZX05-43-s+.

The other output of coupler 1 is connected to another 99/1 coupler (coupler 2). The output of the coupler 2 is connected to a lensed fiber that focuses the light on the switch with a waist diameter about 4 μm. The other output of coupler 2 is connected to the power meter to monitor the optical power. The transmitted signal is recorded with a spectrum analyzer whose bandwidth is 20 Hz - 67 GHz (Rohde & Schwarz FSU 67) and an oscilloscope (Rohde & Schwarz RTM 1054). The electrical contacts between coplanar probes and the photoswitch are monitored by using a high resolution video camera.

IV.3.1.1. Frequency Mixer

A frequency mixer is a non-linear electrical circuit that produces new frequencies when two frequency signals are applied. This device is used in a variety of RF applications. A mixer converts RF power at one frequency to another are usually at a smaller frequency to make signal processing easier and also inexpensive.

The ideal mixer, represented by Fig. 3.9, for notation clarity is a device which multiplies two input frequency signals. Let us consider processing a signal $V_{RF}(t)$ through analog multiplication with a sinusoidal signal generated by local oscillator $V_{LO}(t)$ and we get the output signal $V_{IF}(t)$:

$$V_{IF}(t) = kV_{RF}(t)V_{LO}(t), \qquad \text{(III-24)}$$

where k is the conversion factor.

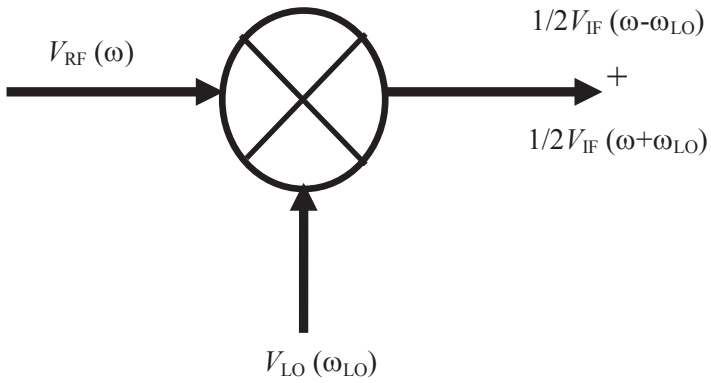

Fig. 3.9: Circuit symbol for a frequency mixer

Let us write the expressions for radio frequency (RF) and local oscillator (LO) signals:

$$V_{RF}(t) = a(t)\cos\left(\omega_{RF} + \Phi(t)\right) \tag{III-25}$$

And $V_{LO}(t) = V_{LO}\cos\omega_{LO}t$ (III-26)

where ω_{RF} is RF angular frequency, $a(t)$ and $\Phi(t)$ are the amplitude and phase of the RF signal, ω_{LO} and V_{LO} are the frequency and the amplitude of LO signal. Inserting equations (III-25) and (III-26) in equation (III-24), we obtain:

$$\begin{aligned} V_{IF}(t) &= ka(t)\cos\left(\omega_{RF} + \Phi(t)\right) \times V_{LO}\cos\omega_{LO}t \\ &= \frac{kV_{LO}}{2}a(t)\cos\left[\left(\omega_{RF} - \omega_{LO}\right) + \Phi(t)\right] + \frac{kV_{LO}}{2}a(t)\cos\left[\left(\omega_{RF} + \omega_{LO}\right) + \Phi(t)\right] \end{aligned} \tag{III-27}$$

We generate two outputs IF (intermediate frequency) signals, one at frequency $\omega_{RF} - \omega_{LO}$ and the other at frequency $\omega_{RF} + \omega_{LO}$ shown in Fig 3.10a. The two IF signals are nearly identical to the RF signal and the only difference is the magnitude (smaller magnitude) and the frequency (much lower frequency). Therefore, the modulation information has been preserved in the mixing process and we can recover the information of amplitude *a*(t) and phase $\phi(t)$ from the IF signal. In our present work we are taking into consideration only down

converted signal $\omega_{RF} - \omega_{LO}$ because the recovering process of $a(t)$ and $\phi(t)$ is more accurate and easy at lower frequency.

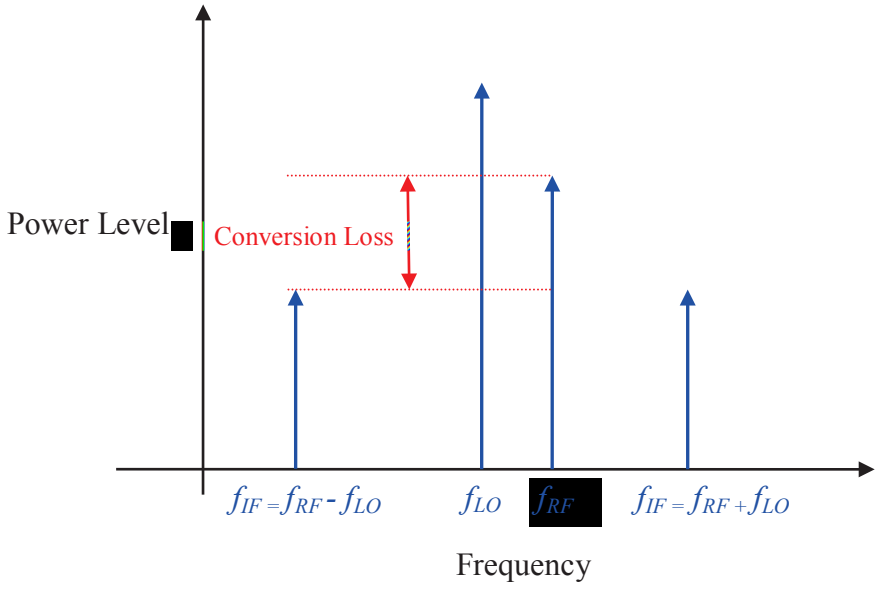

Fig. 3.10a: Sketch for generation of down and up converted signal in a mixer.

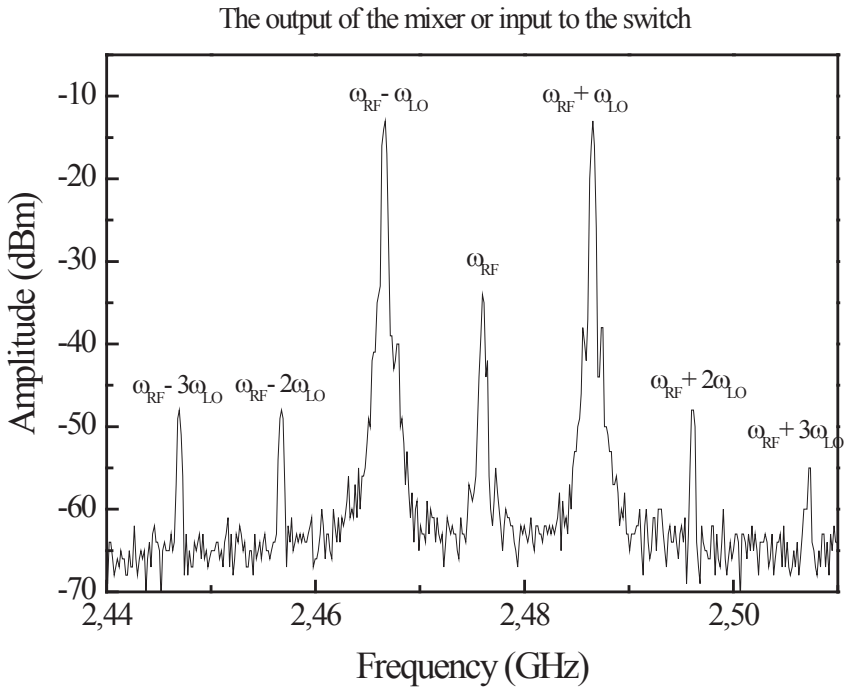

Fig. 3.10b: Up and down converted signals generated by frequency mixer for RF and LO signal frequencies 2.46 GHz and 10 MHz respectively. The output signal is recorded using 12 dB gain amplifier after the mixer as shown in Fig. 3.8.

The conversion loss of the mixer is defined as the ratio between the unconverted (RF signal) and the converted signal (IF signal) signal:

$$\text{Conversion Loss} = -10\log_{10}\left(\frac{P_{RF}}{P_{IF}}\right) \qquad \text{(III-28)}$$

In our present work, we use a mixer as modulator. RF signal frequency is $f_{RF} \approx 2.476$ GHz and the LO (modulation) signal frequency is 10 MHz. The output of the mixer (with 12 dB gain amplifier) is shown in Fig. 3.10c. We can see the 1, 2 and 3 up-converted signals respectively at 2.486, 2.496, 2.506 GHz and the down converted signals are seen at 2.465, 2.456 and 2.446 GHz. This signal is fed to the photoswitch to perform the demodulation process. Here, in our demodulation experiment, we are considering only the down converted signal ω_{RF}-ω_{LO} which is having the amplitude about ≈-14 dBm as shown in Fig. 3.10b.

IV.3.2. Demodulation Experimental results and discussion

The main idea of this homodyne experiment is to demodulate the information signal from the RF carrier signal using the LTG-GaAs photoconductive switch. Here, the LTG-GaAs photoconductive switch is biased with RF signal, oscillating at angular frequency $\omega_{RF,}$ which is modulated by an information signal ($\Delta\omega$) and simultaneously the switch is illuminated with optical beating (Ω), which results from the difference of two laser frequencies coming from two CW lasers. This non-linear mixing of modulated RF signal $(\omega_{RF} \pm \Delta\omega)$ with optical signal (Ω) leads generation of new RF frequencies at $(\omega_{RF} \pm \Delta\omega) \pm n\Omega$ (n-integer). If we set the RF signal frequency ω_{RF} equal to the optical beating frequency, the frequency of the first harmonic ($n=\pm 1$) will be $\pm\Delta\omega$. Thus the photoswitch directly demodulates the information signal from the carrier (RF) signal and this demodulated signal is received by an oscilloscope or a spectrum analyzer. We set RF signal frequency $\omega_{RF} = 2\pi\times 2.5$ GHz, information signal frequency $\Delta\omega = 2\pi\times 10$ MHz and optical beating frequency $\Omega = 2\pi\times 2.5$ GHz. The demodulated signal at 10 MHz is recorded on both oscilloscope and spectrum analyzer and are presented in Fig. 3.11 and Fig. 3.12.

The measured amplitude of the demodulated signal is about -65 dBm (not shown in figure) when no amplifiers are used and this value is close to the noise level. So we are taking amplifiers to increase the amplitude of the demodulated signal. For the first trial, we used only one low noise RF amplifier (ZX60-14012L) with the gain about 12 dB and we get the demodulated signal amplitude ≈ -53 dBm with a noise level of -70 dBm. Then we used two amplifiers RF and IF (MITEQ with 40 dB gain), with a total gain about 62 dB and we obtain the amplitude of the demodulated signal of about -14 dBm with same noise level as in the one amplifier case. This is because of the RF attenuation effect in the spectrum analyzer: when the amplitude of the signal is higher than a reference level, then the attenuation effect is introduced to avoid overload, gain compression and distortion. In our present case, we set 35 dB as reference level. These experimental amplitude values of the demodulated signal are very close to the numerical values in both the cases (RF amplifier and RF+IF amplifiers). These two measurements (one amplifier and two amplifies) were done with a resolution bandwidth (RBW) and video band width (VBW) of about 10 KHz and 30 KHz respectively.

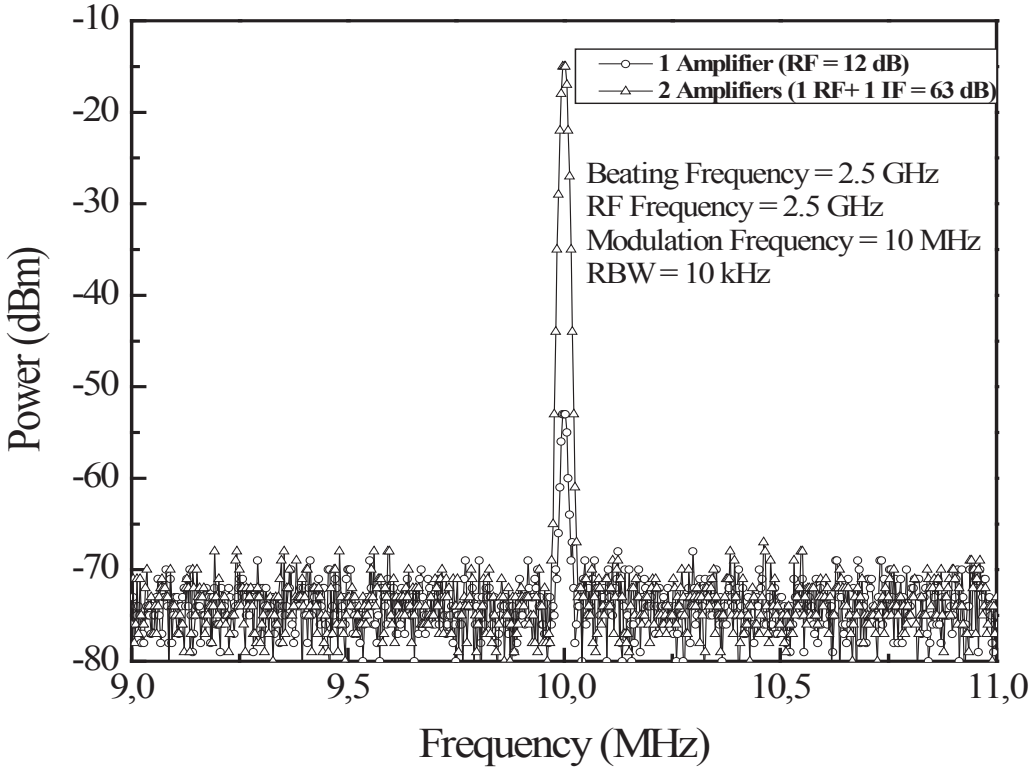

Fig. 3.11a: Demodulated signal power vs RF frequency recorded on network (line with open circles corresponds signal with 12 gain and line with open triangles represents the signal with 62 dB gain).

The RF and optical beating signal frequencies are set to be $f_{RF} = f_{\Omega} = 2.5$ GHz and the information signal frequency $\Delta\omega = 10$ MHz.

	Input RF power to the switch (dBm)	Amplitude (dBm)		FWHM (kHz)
		Theory	Experiment	
Demodulated signal with RF amplifier	-14	-48.35	-53	22
Demodulated signal with RF+IF amplifiers	-14	-8.35	-14	38

Table 3.1: Theoretical and experimental values of demodulated signal amplitude

The numerical values of the demodulated signal amplitude are -48.35 dBm (see Fig. 3.5) for the one RF amplifier case and -8.35 dBm for the two amplifiers case. These values are presented in table 3.1 together with experimental values. This numerical values are calculated using the relation (III-22) by taking P_{laser}= 13.65 mW (at the photoswitch), and a carrier life time τ= 4 ps.

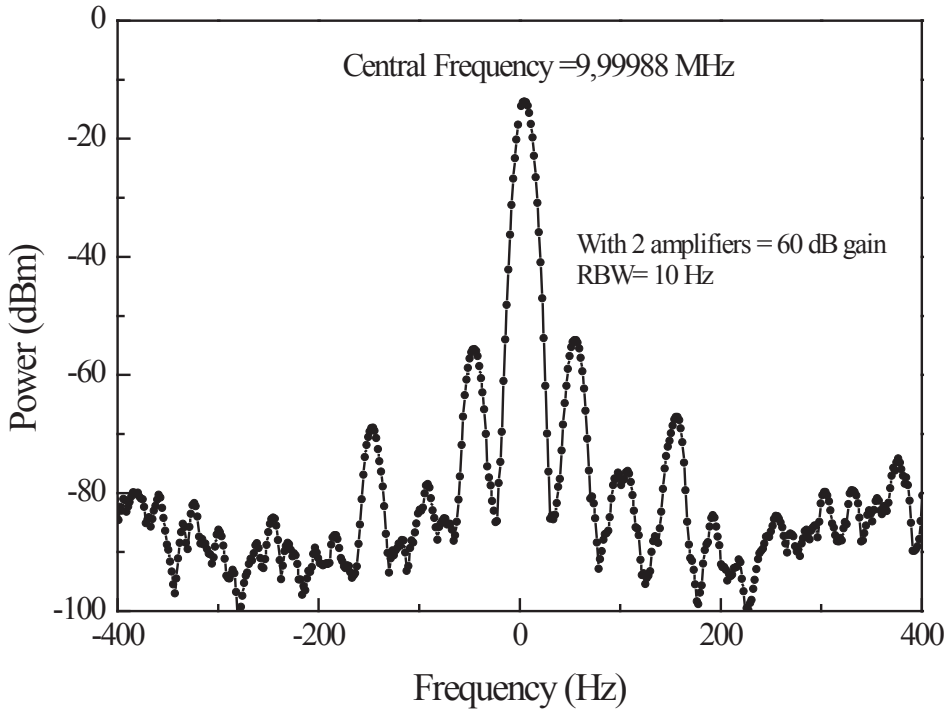

Fig. 3.11b: Demodulated signal recorded on spectrum analyze at high resolution.

Now we would like to concentrate on the band width of the demodulation signal. So, we repeat the demodulation experiment with the same experimental setup as before (Fig. 3.8). Here also, the beating and RF signal frequencies are 3 GHz and the modulation frequency is 10 MHz. In this measurement, we set RBW and VBW to 10 Hz and 30 Hz respectively, so that the resolution measurement is increased. The spectrum for the demodulated signal recorded with the spectrum analyzer is presented in Fig. 3.11b. For good visibility, we set the demodulation frequency 9.99988 MHz as 0 Hz in Fig. 3.11b. The amplitude of the demodulated signal is about -11 dBm and is close to the numerical value. The width of demodulated signal is very narrow and its -3 dB band width is 11 Hz. Thus the bandwidth is only limited by the RF local oscillator and by the spectrum analyzer, i.e. by the electronics. The opto-electric conversion, and the device do not degrade the signal bandwidth. By decreasing the RBW, the noise floor also decreased, because at high RBW, more frequency components pass the detector.

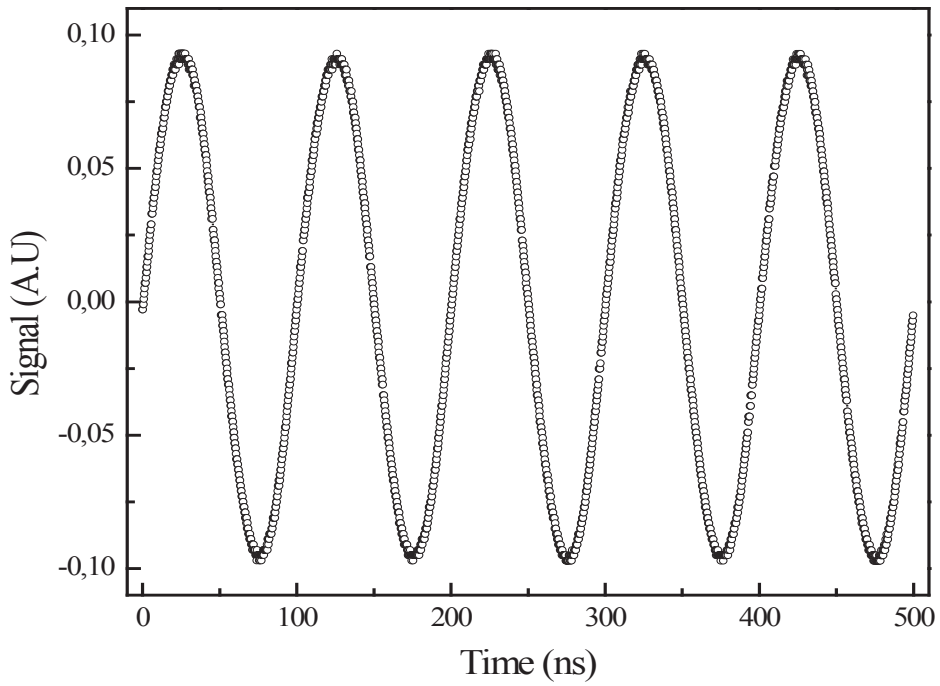

Fig. 3.12: Demodulated signal at 10 MHz recorded an oscilloscope.

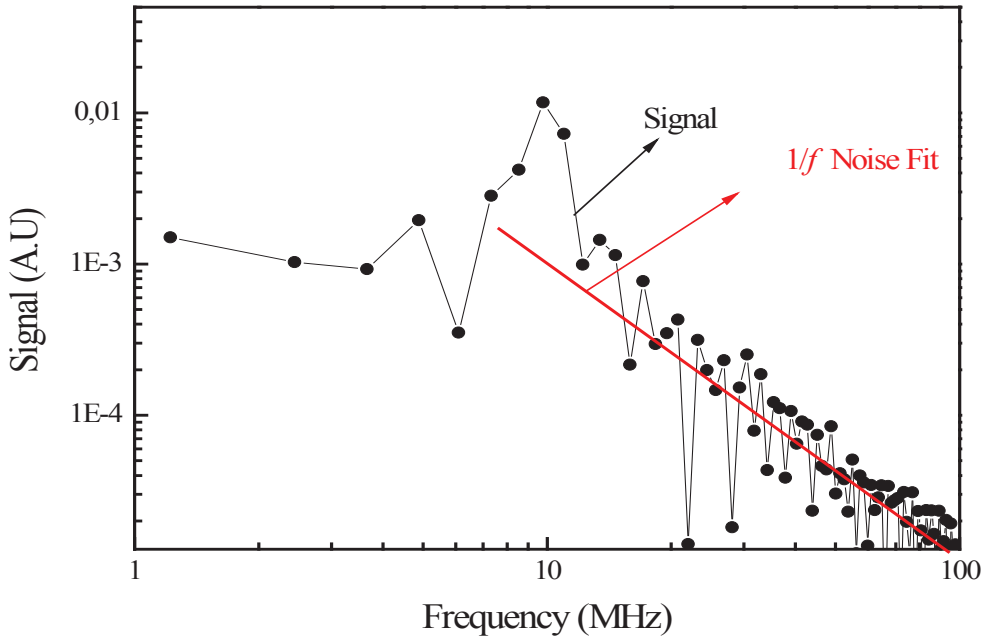

Fig. 3.13: Fast Fourier Transform of the demodulated signal (Fig. 3.12)

The time domain demodulated signal at 10 MHz observed with an oscilloscope is presented in Fig. 3.12. We make the Fast Fourier Transform of this recorded temporal signal and the spectrum is plotted in Fig. 3.13. The demodulated spectrum shows a peak at 10 MHz as expected and the spectrum exhibits a $1/f$ noise due to the electronics used in the experiment. The FWHM of the FFT signal is bigger than the original signal, because the resolution is limited by the time window of the oscilloscope record. The FFT spectrum does not exhibit signals at n×10 MHz (n-integer) frequencies, which implies that the demodulated signal recorded on oscilloscope is almost perfectly sinusoidal.

V. CONCLUSION

It has been shown that the homodyne scheme using LTG-GaAs photoconductive switch biased with information signal carried by a RF signal and illuminated simultaneously by a CW optical beating is capable of demodulating the information signal directly without using any external electronic device under the condition $\omega_{RF} = \Omega$. The band width of the recorded demodulated signal is about 11 Hz, which is very good for high resolution applications. We study the dependence of harmonics power versus many factors like RF, modulation frequencies and optical parameter G_{opt} (i.e. carrier relaxation time τ, optical power P_0 etc.) using a lumped element model. Numerical results show that the device exhibits low pass filter behavior (P_0 curve) and device band width is strongly depends on carrier life time. With ultrafast semiconductors, the device may operate at frequencies exceeding 100 GHz.

REFERENCES

[1] D. H. Auston, "*Impulse response of photoconductors in transmission lines*". IEEE Journal of Quant. Electro., **19**, 639 (1983).

[2] W. J. Getsinger. "*Circuit Duals on Planar Transmission Media*". IEEE MTT-S International Microwave Symposium Digest. 154 (1983).

[3] Jean-Marie Delord doctoral thesis *"Echantillonnage photoconductif de signaux Radio-Fréquence",* University of Savoie (2010).

[4] Bahaa E. A. Saleh, Malvin C. Teich, "*Fundamentals of Photonics"*. John Wiley & Sons, 660 (1991).

CHAPTER 4: CHARACTERIZATION OF LTG-GaBiAs MATERIAL AND PHOTOSWITCH

CHARACTERIZATION OF LTG-GaBiAs MATERIAL AND PHOTOSWITCH

I. Introduction

Semiconductor materials with ultrafast response are useful in many applications, like for ultrafast detectors in optical communications and as optoelectronic emitters and detectors of THz radiation. The most employed material is low temperature grown GaAs (LTG-GaAs), which is compatible with the photon quantum energy of Ti:Sa lasers. Nowadays, bulk Ti-Sa laser systems are replaced more and more by compact fiber lasers emitting in the 1-μm or 1.55-μm wavelength range. Several studies have been performed to find the best material to work at these higher wavelengths [1-5]. A good candidate could be LTG GaBiAs, with its ultrashort carrier lifetime and relatively small lattice mismatch with the GaAs substrate. This material is achieved just by the substitution of some As by Bi in GaAs [6-10] resulting in a dramatic decrease in the band gap, about 90 meV per percent of Bi. For this reason GaBiAs is attracting attention for long wavelength (>1μm) photonics applications including THz optoelectronics such as THz antennas [11].

In this chapter, we propose two LTG-GaBiAs devices named as B261 and B263 for opto-micro wave studies. Here, we first characterize the material properties of LTG-GaBiAs, such as carrier lifetime and energy gap, and then the voltage-current characteristics of LTG-GaBiAs photo conductive switch. We will also study the opto-microwave mixing in such switches at 1-μm excitation wavelength soon and the results will be discussed in the following sections.

II. FTIR absorption spectroscopy for band gap measurement in LTG-GaAs

II.1. Working principle of FTIR

Fourier transforms infrared (FTIR) spectroscopy is a technique based on the Michelson interferometer. FTIR spectroscopy allows us to determine the optical properties material over a broad spectral region. The schematic representation of FTIR experimental setup is presented in Fig.4.1, which consists of a beam splitter, a fixed mirror and a moving mirror (scanning mirror). As shown in Fig. 4.1, light from the source is split into two beams, one towards the fixed mirror and the other to the moving mirror. The two reflected beams by the two mirrors are recombines at the beam splitter and then go towards the detector through the sample. As the two beams originate from the same source, therefore these two beams interfere constructively or destructively for a particular frequency depending on the position of the moving mirror. If the moving mirror is scanned over a distance x, a sinusoidal signal is detected at that frequency. When a broad band source is used, all the sinusoidal signals corresponding to each frequency of the source are added, resulting in a particular signal versus x, namely the Interferogram, which is nothing but the Fourier transform of the source. Let us call δ the optical path difference between the two arms of the interferometer:

$$\delta=2\left(x_1-x_2\right) \tag{IV-1}$$

Where x_1, x_2 are the distances between the beam splitter to moving mirror and fixed mirror respectively. For a given frequency ω, the detected interference is:

$$f\left(\omega,x\right)=f\left(\omega\right)e^{j\omega\delta} \tag{IV-2}$$

where *f(ω)* is the spectral density of the source. The whole signal is:

$$F\left(x\right)=\int_0^\infty f\left(\omega\right)e^{j\omega\delta}d\omega\,. \tag{IV-3}$$

This is the inverse Fourier transform of *f(ω)*. *f(ω)* is simply obtain by taking the Fourier transform of the Interferogram *F(x)*

$$f\left(\omega\right)=\int_0^\infty F\left(x\right)e^{j\omega\delta}dx \tag{IV-4}$$

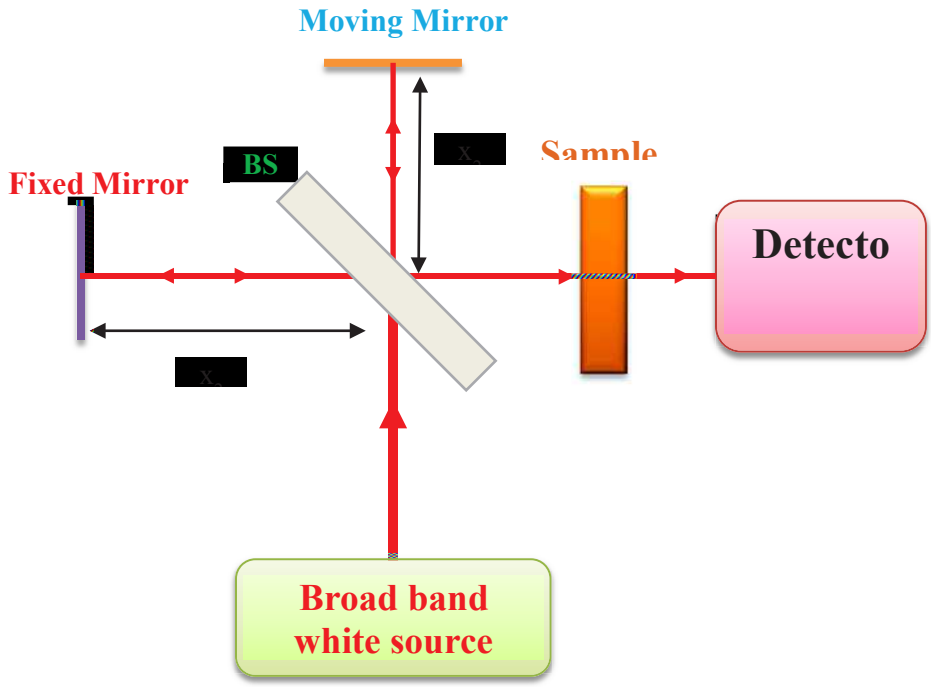

Fig. 4.1: Schematic diagram of FTIR setup. BS is Beam Splitter.

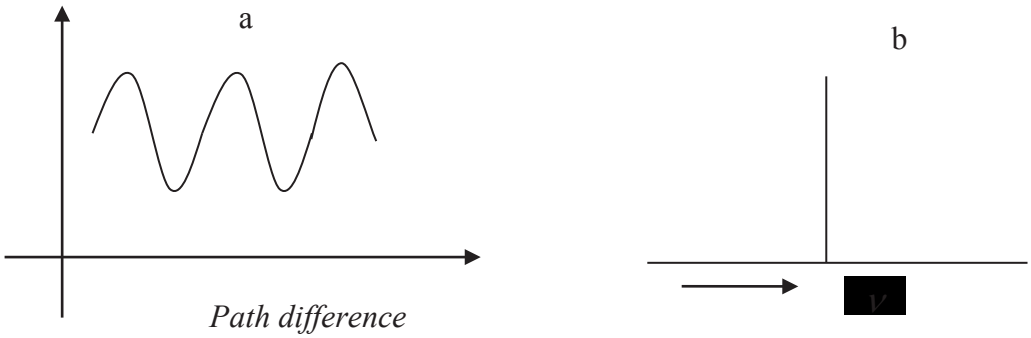

Fig. 4.2: Interferogram (a), FT of Interferogram (a), for monochromatic light.

II.2. Transmission spectrum of LTG-GaBiAs and results

When putting a sample before the detector and recording the waveforms without and with the sample, the ratio of their FFT give the transmittance of the sample defined as follows

$$T = \frac{I}{I_0} \qquad \text{(IV-5)}$$

If reflection at the sample surfaces can be neglected, T is simply $e^{-\alpha d}$, where d is the thickness and α is absorption coefficient.

Here, we use FTIR spectroscopy to determine the energy band of the LTG-GaBi$_x$As$_{1-x}$ alloy (B261 and B263). The measurement was done by taking air as the reference. The measured IR transmission spectrum for two LTG-GaBiAs samples is presented in Fig 4.3. We determine the band gap energies of two samples B261 and B263, as the edge of IR transmission spectrum, and we get 1.033 and 0.97 eV respectively. These energy band gap values are close to the reported values [6-10, 12].

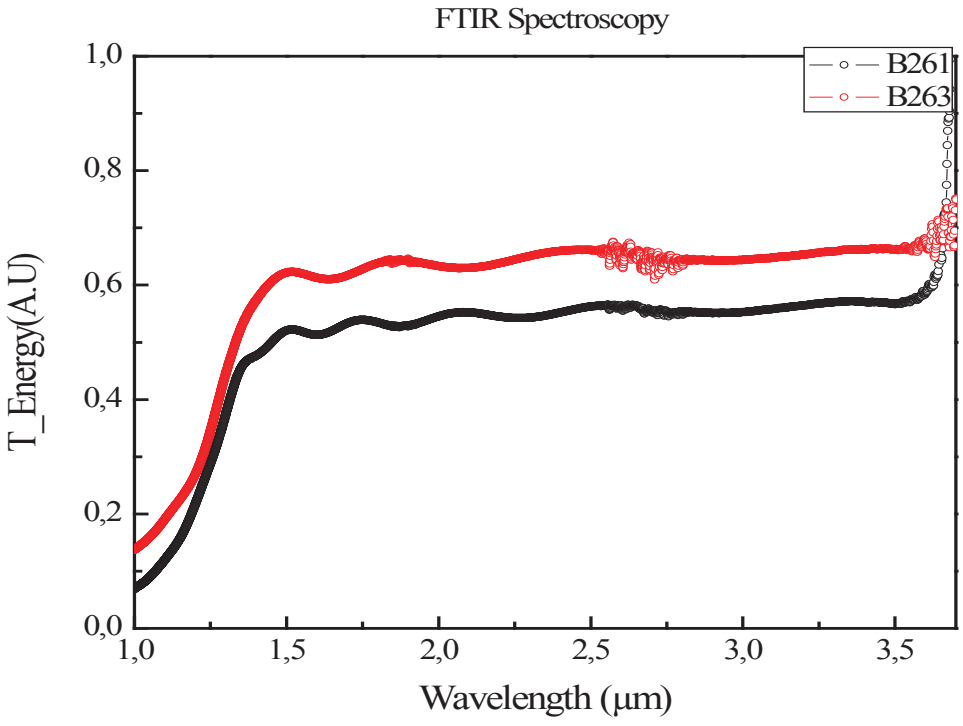

Fig. 4.3: FTIR transmission spectrum of LTG-GaBiAs

LTG-GaBiAs Device	Bi concentration (% of As)	Energy gap (eV)
B261	6	1.033
B263	7	0.97

Table 4.1: Details of LTG-GaBiAs devices

III. Carrier Life time measurement by Optical pump-probe technique

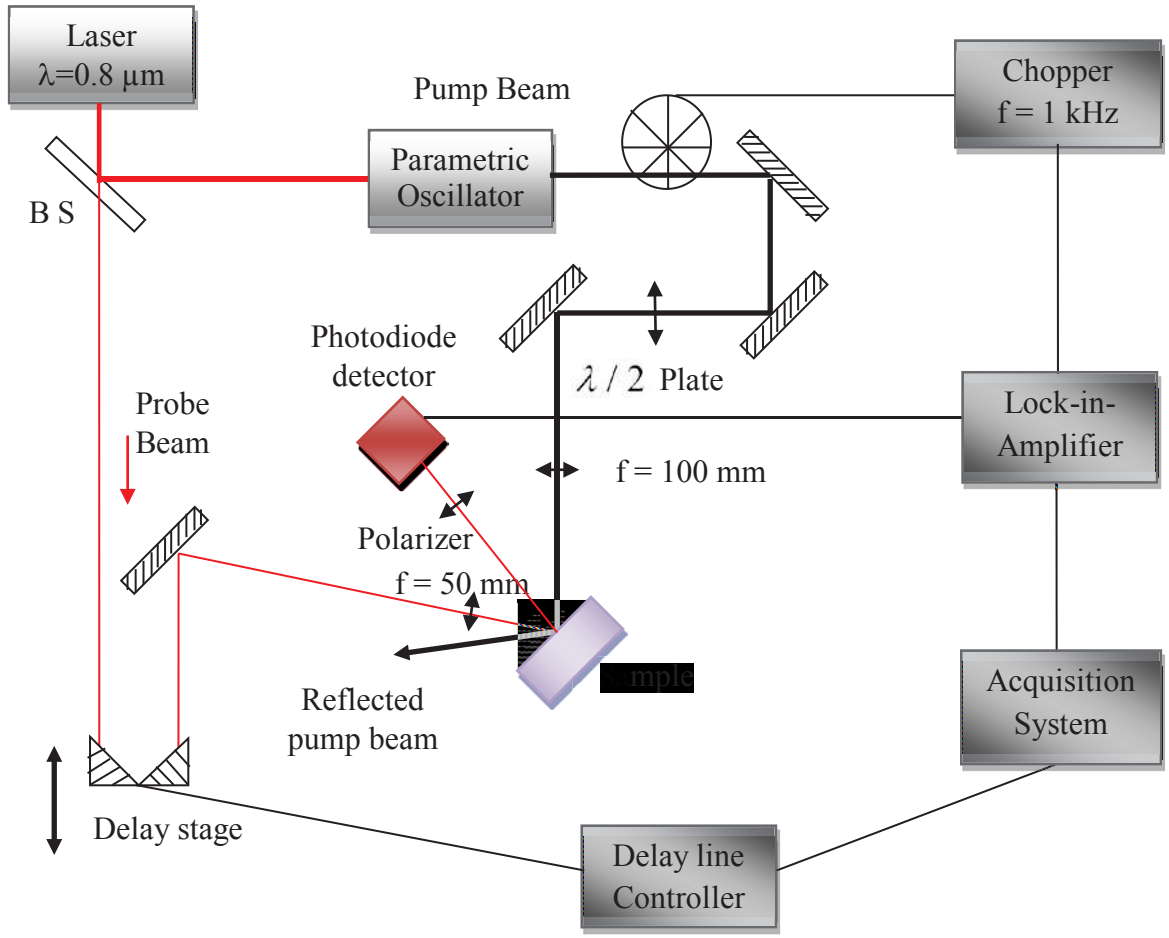

Fig. 4.4: Optical pump-probe experimental setup for carrier life time measurement.

Standard femtosecond optical pump-probe reflectivity measurement was performed on LTG-GaBiAs material in order to determine the carrier trapping time. The schematic representation

of optical pump-probe experimental set up is presented in Fig. 4.4. This set-up includes a mode locked Ti:Sa laser system which is operating at 0.8 µm with a pulse repetition rate of 85 MHz and a pulse duration of 150 fs. A beam splitter divides the laser beam into two, one is the probe beam and the other inputs an optical parametric oscillator (OPO) that generates tunable wavelengths from 1000 to 1650 nm using $LiNbO_3$. Here, the beam which is coming out of the OPO is used as the pump beam to excite the sample. These pump and probe beams are orthogonally polarized using a λ/2 wave-plate in order to minimize interference effects. A computer controlled delay stage is used to introduce a time delay between pump and probe pulses. The pump beam from OPO is chopped at around 1 kHz. The probe beam is focused at the centre of the pump beam on the sample surface (size of the probe beam is much smaller than pump beam) and then focused on the photo detector (photo diode). The signal from the detector is connected to a lock-in-amplifier which is locked to the chopper frequency.

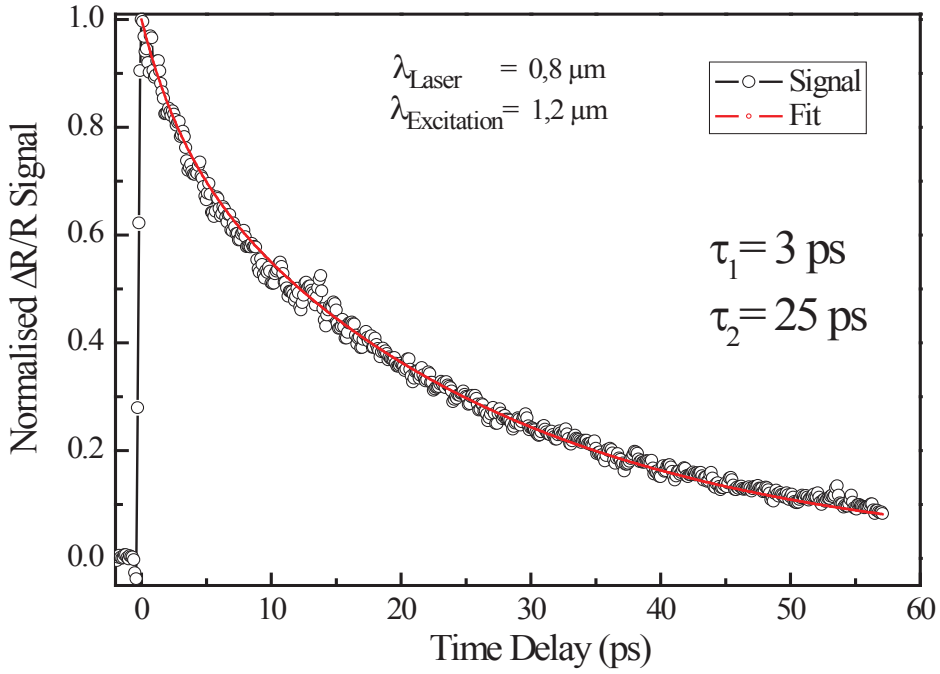

Fig. 4.5a: Normalized reflectivity signal measured at 1.2 µm wavelength for LTG-GaBiAs (B261) material. Experiment performed at IEMN, University of Lille.

We have done a series of pump-probe measurements at different excitation wavelengths to study carrier dynamics in two different LTG-GaBiAs (B2621 and B263) layers grown at 240 °C temperature. First, we present the normalized transient reflectivity data for B261 and B263

samples measured at 1.2 μm excitation wavelength in Fig. 4.5a and 4.5b respectively. The ΔR/R signal rises rapidly near to zero delay time and then decreased exponentially. We used a double exponential decay process to describe the carrier dynamics in the semiconductor material as discussed in section III.2 of chapter 2. The double exponential fitting process gives two characteristic time constants, τ_1 = 3 ps and τ_2 = 25 ps for B261, and τ_1 = 7 ps and τ_2 = 21 ps for B263. The shortest time constant corresponds to the carrier trapping time and the longer time corresponds to the trap emptying time, i.e. the time for the trapped electrons to recombine with the holes [12-13].

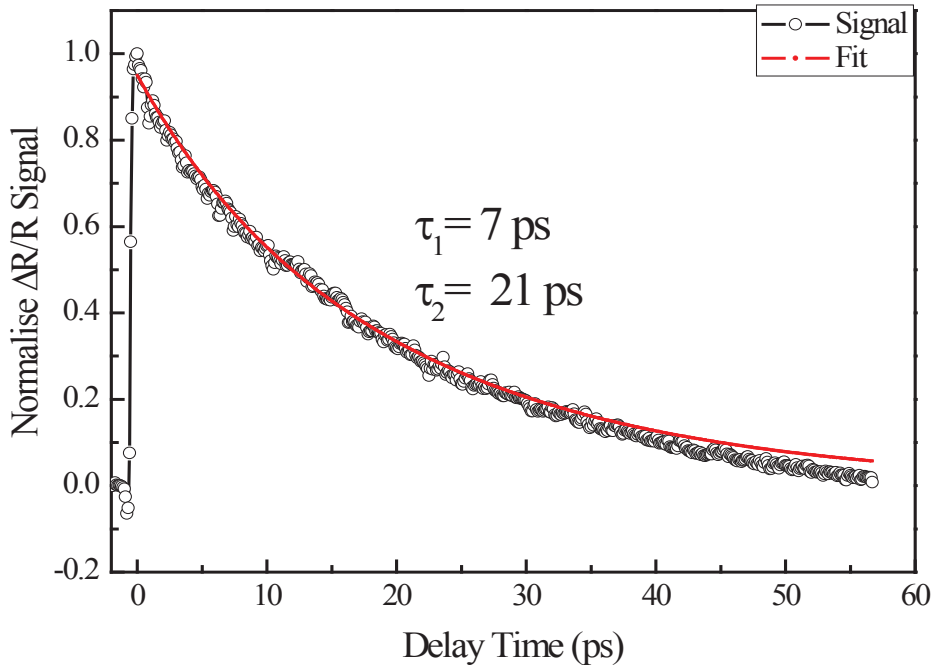

Fig. 4.5b: Normalized reflectivity signal measured at 1.2 μm wavelength for B263.

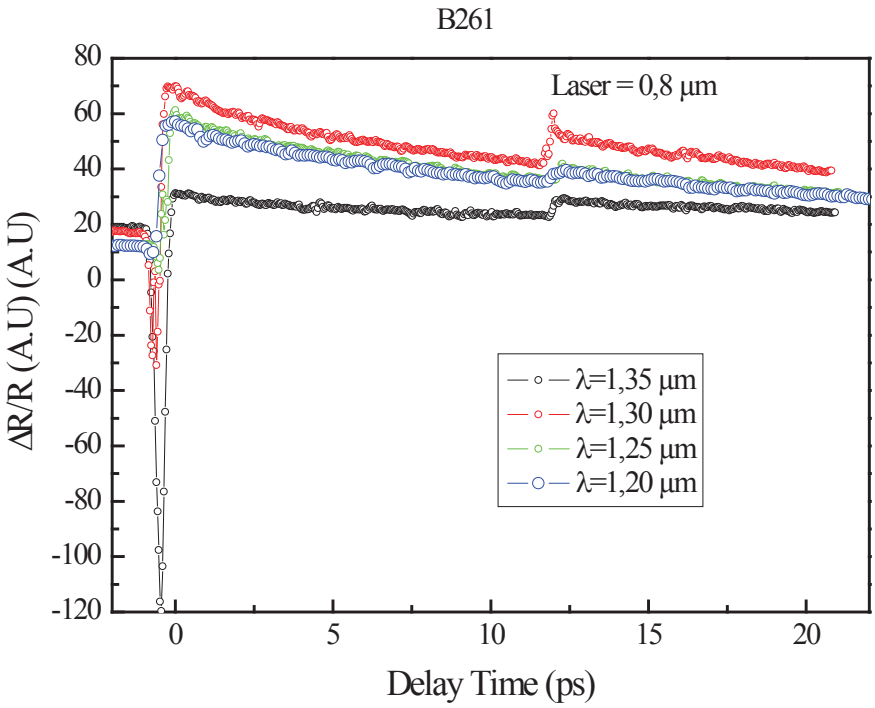

Fig. 4.6: Transient reflectivity data measure at different excitation wavelengths for B261.

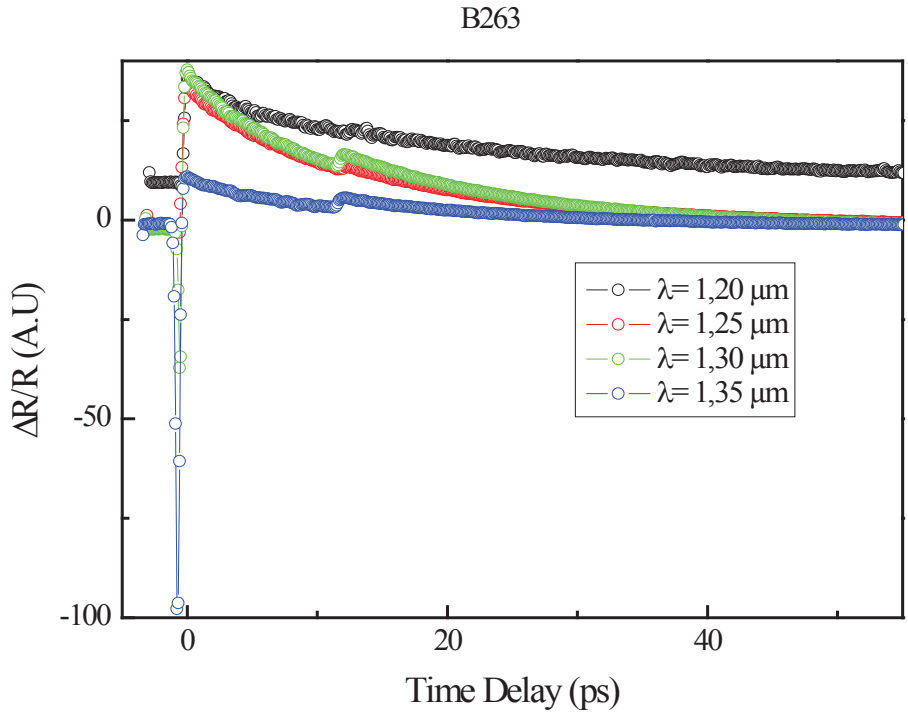

Fig. 4.7: Transient reflectivity data measured at different excitation wavelengths for B263.

Transient reflectivity curves measured at different excitation wavelengths (just above the band gap energy of the semiconductor material) for B261 and B263 are presented in Fig. 4.6 and Fig. 4.7. All the measured curves at 1.2, 1.25, 1.23 and 1.35 µm excitation wavelengths

exhibit exponential behavior and we observed a dip at 12.5 ps in all the curves which corresponds to the reflection in substrate, because the substrate is transparent at these wavelengths due to its larger band gap. At zero pump-probe delay, there is an instantaneous reflection decrease which can be attributed to two-photon absorption (TPA). Its shape closely matches the autocorrelation trace of the laser pulses while its amplitude depends on the pump wavelength. This latter effect might be due to a resonant effect in the GaBiAs layer whose refractive index is slightly different from that of GaAs. Fig. 4.7a shows the normalized transient reflectivity data for the B263 sample. This figure show, that when the excitation wavelength is increased (photon energy is larger and closer to the bandgap of the GaBiAs), the carrier capture time (fast decay curve) is reduced. The fact that the optical probe experienced some reflection variation clearly indicates that the optical pump beam is partially absorbed despite the photon energy is below the band gap (<0.97 eV). This can be explained by the presence of defects in the gap of the semiconductor material. Finally, we conclude that, the carrier life of B261 is lower than the B263, so B261 will be a more efficient material than B263 for ultrafast optoelectronics application, particularly for high band width applications.

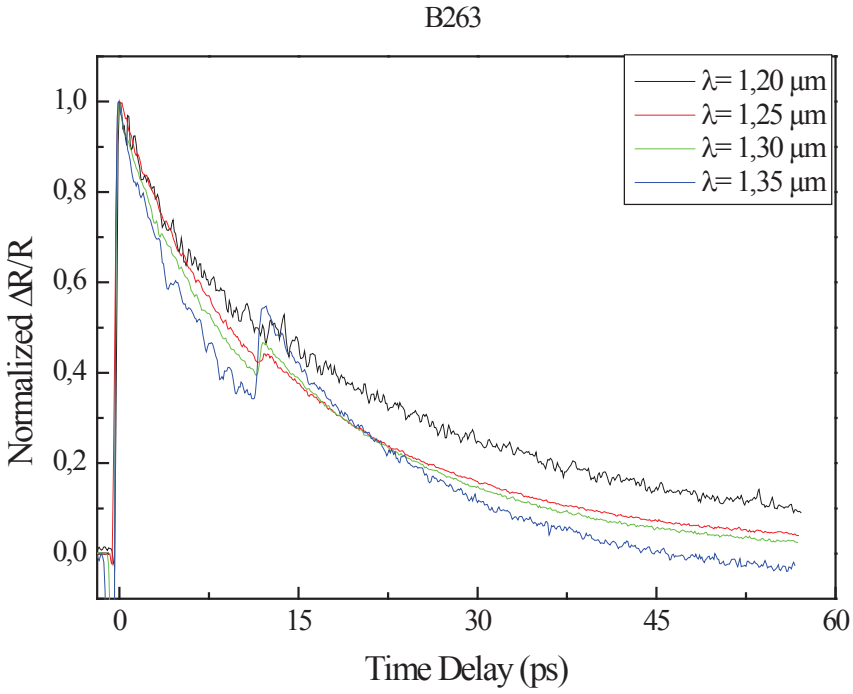

Fig. 4.7a: Normalized ΔR/R curves at different excitation wavelengths for B263.

IV. LTG-GaBiAs Device demonstration

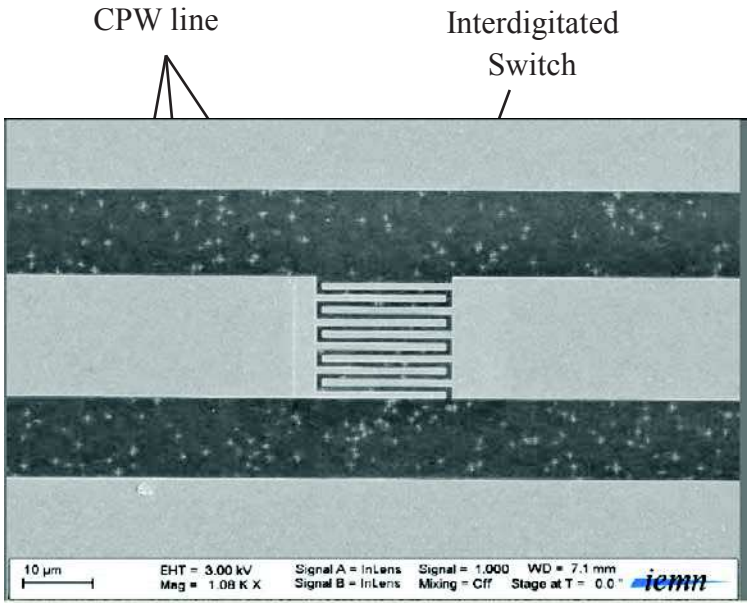

Fig. 4.8: Microscopic picture of low temperature grown GaAs top view (Picture taken at IEMN, Lille).

Here we used the two different LTG-GaBiAs photo switches (B261 and B263) for opto-micro wave characterization. LTG-GaBiAs semiconductor layers are fabricated at SPI, Vilnius whereas the CPW design on LTG-GaBiAs material was done at IEMN, Lille.

The 1.5 µm GaBiAs layers were grown on semi-insulating (100)-oriented GaAs substrate. by a molecular-beam-epitaxy system at 240 °C temperature, at a growth rate of 2 µm/h and for different Bi/As beam ratio. After cleaning the substrate surface, a 500 nm GaAs buffer layer was grown at 600°C substrate temperature, and then cooled to 270 °C in order to grow 400 nm thick LTG GaAs layer. The concentration of Bi element is determined by X-ray diffraction technique. The percentages of Bi in B261 and B263 are 6% and 7% of As respectively. The carrier mobility μ_n of such layers is generally found to be about 2000 $cm^2/V/s$ [12].

The CPW structure is made of parallel 0.5-µm thick evaporated Ti/Au strips, the width of the central strip is 20 µm and the widths of two grand strips are the same, with 80 µm for each. The gold strips are separated by 14.5 µm, resulting in 50-Ω impedance. The photoswitch is located in the central strip of the CPW. The switch structure is an interdigitated one, including 10 fingers (length 19 µm, width 1 µm) separated by a 1-µm gap. The microscopic picture of the LTG-GaBiAs (B263) photoconductive switch (top view) is shown in Fig. 4.8.

V. I-V Characterization of LTG-GaBiAs Photoswitch

In this section, we studied the electrical behavior of photoswitch by measuring its current-voltage characteristics of photoswitch devices at 1.06 µm excitation wavelength. The schematic of present experimental set up is presented in Fig. 2.8. The setup includes a Nd:YAG laser operating at 1.06 µm with maximum 0.9 W power, voltages source and an ampere meter.

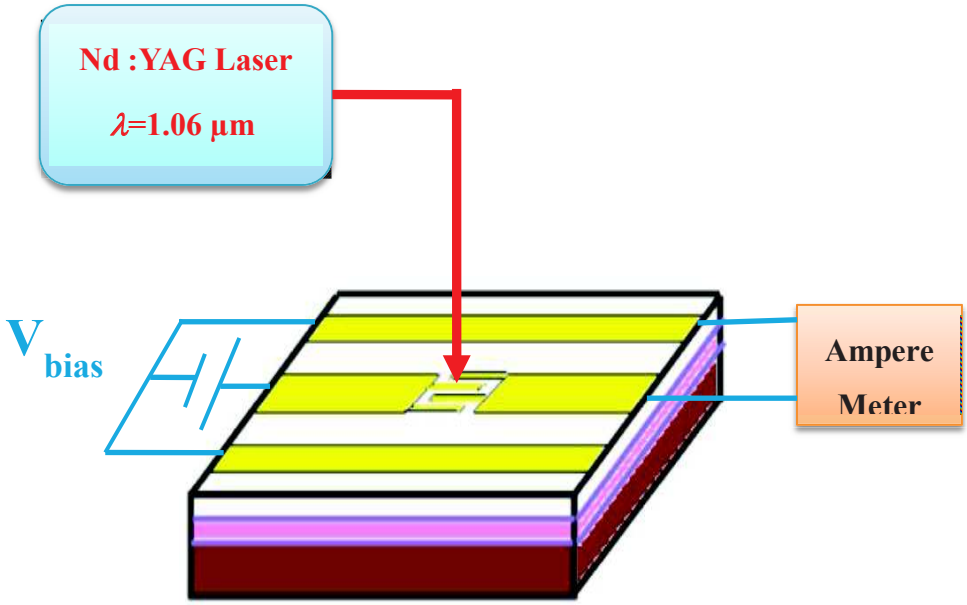

Fig. 4.8: Experimental set up for current-voltage measurement.

Here, the device is biased with a DC voltage and is illuminated with the laser light. We assume that each absorbed photon in the laser light contributes to create carriers in the semiconductor material, which induces a photocurrent. The photo generated current and dark current (no light) as function of DC bias voltage are recorded with a computer. We measured the photocurrent for optical power of 380 µW and dark current by sweeping the bias voltage from -10 to +10 V as presented in the Fig. 4.9. The measured curves exhibit a Schottky diode behavior for lower bias voltages around 0 V. When we increase the bias voltage, the free carrier density in the depletion region increases, which implies a higher photo current. Let us notice that the sample B263 show a lower dark current as compared to sample B261.

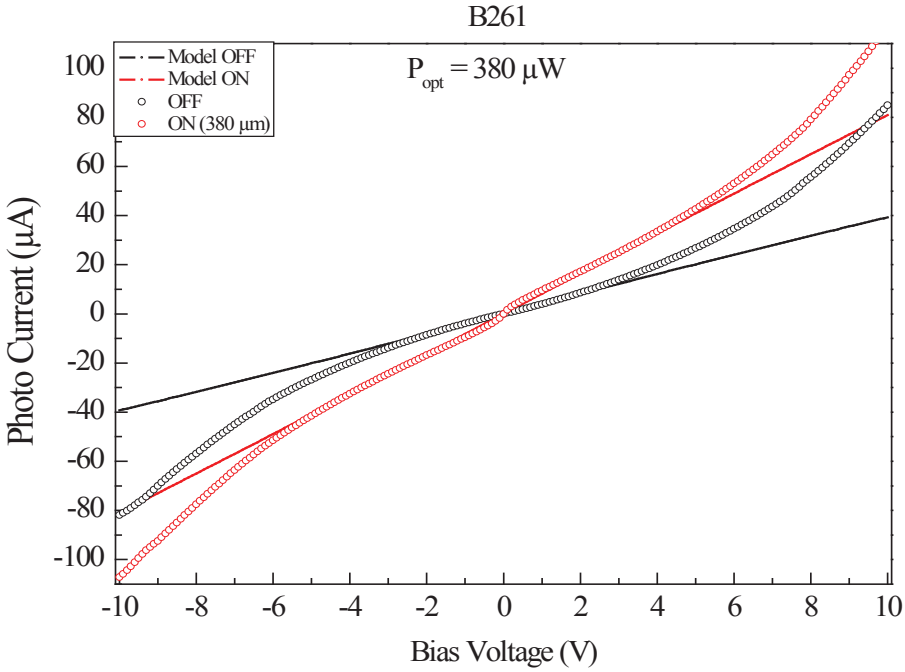

Fig. 4.9 a: I-V characteristics of B261 under illumination (red line) and dark conations (black line).

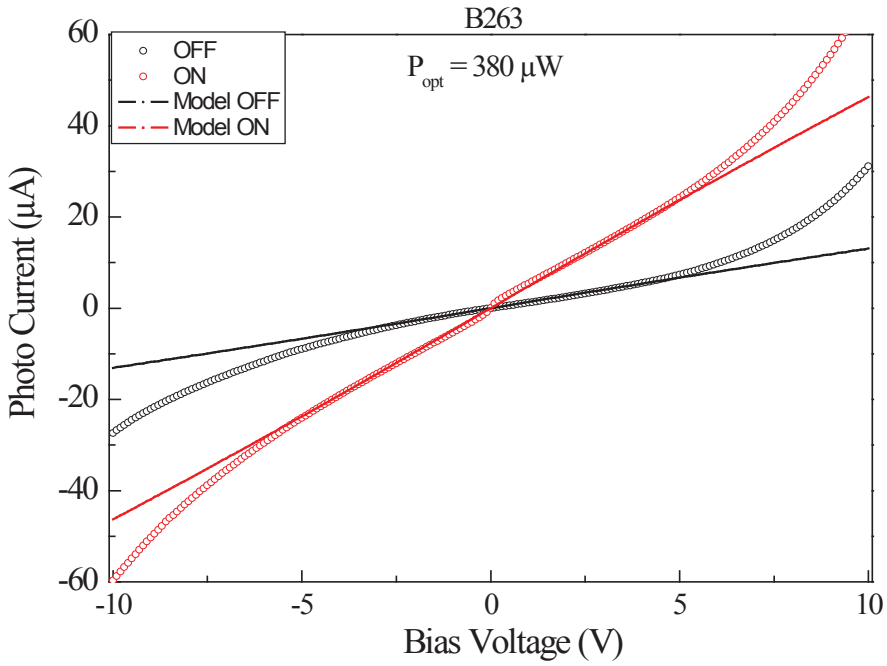

Fig. 4.9b: I-V characteristics of the photoswitch under illumination (red line) and dark conations (black line).

For higher voltage regime (after 5 V in Fig. 4.9), the photo current strongly dominates due to the space charge effect. The saturation voltages for such devices are very high and no velocity saturation is observed as compared to what has been observed for the devices made from LT-GaAs (see chapter II). The photocurrent in B261 is higher than in B263.

In order to deduce the carrier mobility from the I-V curve, we simply use a linear variation of the current density versus the applied voltage:

$$J = nq\mu E \qquad \text{(IV-5)}$$

With $\mu = \mu_0$, where μ_0 is the low-field mobility. This model works for only low bias voltages as we do not introduce the any saturation. We can see a good fit (see Fig. 4.9) with experimental curve upto 3 V for dark curve and 5 V for curves with light. The parameters used for the fit are: carrier concentration in semiconductor before excitation is $N_0=2.5\times10^{28}$ m^{-3}, optical power 380 µW, mobility is 0.2 $m^2/V/s$ and diameter of the optical beam on switch is 15 µm confirming the good value of the carrier mobility. Because of longer carrier trapping time (7 ps) the sample B263 shows a larger photocurrent than B261 whose carrier trapping time is 3 ps : together with a lower dark current this behavior results in a better ON/OFF ratio for sample B263.

VI. Conclusion

The GaBiAs materials, and thus the manufactured photoswitch, shown attractive performances to perform opto-micro wave experiment at $\lambda \sim 1\,\mu m$. These experiments are still under way at IMEP-LAHC in Grenoble. We hope to perform measurement in coming months.

References:

[1] Takazato, M. Kamakura, T. Matsui, J. Kitagawa, and Y. Kadoya: Appl. Phys. Lett., **90**, 101119 (2007).

[2] M. Suzuki and M. Tonouchi: Appl. Phys. Lett., **86**, 163504 (2005).

[3] O. Hatem, J. Cunningham, E. H. Linfield, C. D. Wood, A. G. Davies, P. J. Cannard, M. J. Robertson, and D. G. Moodie: Appl. Phys. Lett., **98**, 121107 (2011).

[4] J. Sigmund, C. Sydlo, H. L. Hartnagel, N. Benker, H. Fuess, F. Rutz, T. Kleine-Ostmann, and M. Koch: Appl. Phys. Lett., **87**, 252103 (2005).

[5] J. Mangeney, T. Laurent, M. Martin, J. C. Harmand, L. Travers, and O. Mauguin: Appl. Phys. Lett., **99**, 141902 (2011).

[6] K. Oe: J. Appl. Phys., Part 1, **41**, 2801 (2002).

[7] M. Yoshimoto, S. Murata, A. Chayahara, Y. Horino, J. Saraie, and K. Oe, Jpn. J. Appl. Phys., Part 2, **42**, L1235 (2003).

[8] S. Tixier, M. Adamcyk, T. Tiedje, S. Francoeur, A. Mascarenhas, P. Wei, and F. Schiettekatte, Appl. Phys. Lett., **82**, 2245 (2003)

[9] S. Francoeur, M.-J. Seong, A. Mascarenhas, S. Tixier, M. Adamcyk, and T. Tiedje, Appl. Phys. Lett., **82**, 3874 (2003).

[10] B. Fluegel, S. Francoeur, A. Mascarenhas, S. Tixier, E. C. Young, and T. Tiedje, Phys. Rev. Lett., **97**, 067205 (2006).

[11] V. Pačebutas et al, "*Terahertz time-domain-spectroscopy system based on femtosecond Yb:fiber laser and GaBiAs photoconducting components,"* Appl. Phys. Lett., **97**, 031111 (2010).

[12] V. Pacebutas *et al,* "*Molecular-beam-epitaxy grown GaBiAs for terahertz optoelectronic applications"* J Mater Sci: Mater Electron., **20**, 363 (2009).

[13] Krotkus, K. Bertulis, M. Kaminska, K. Korona, A. Wolos, J.Siegert, S. Marcinkevicˇius, J.-F. Roux, J.-L. Coutaz: IEEE Proc. Optoelectron., **149**, 111 (2002).

CHAPTER 5: APPLICATIONS OF THz SPECTROSCOPY

APPLICATIONS OF THz SPECTROSCOPY

I. INTRODUCTION

Terahertz radiation is corresponds to electromagnetic (EM) waves with frequencies in the range. 0.1 THz – 10 THz. In the EM spectrum, the THz range is placed in between the radio/microwave and infrared frequencies as shown in Fig. 5.1. Therefore THz frequencies are considered to fall between electronics and optics [1]. Radio/microwave frequencies can be accessed directly with electronics (up to 500 GHz), while long wavelength infrared radiation and beyond (say after 10 THz) can be introduced by 'photonics'. But, in order to generate or to detect THz radiation, both electronics and optics are necessary, which is a big challenge. Because of this technological difficulty and of the lack of devices, the region in between the microwave and radio waves is called the "THz Gap" [2].

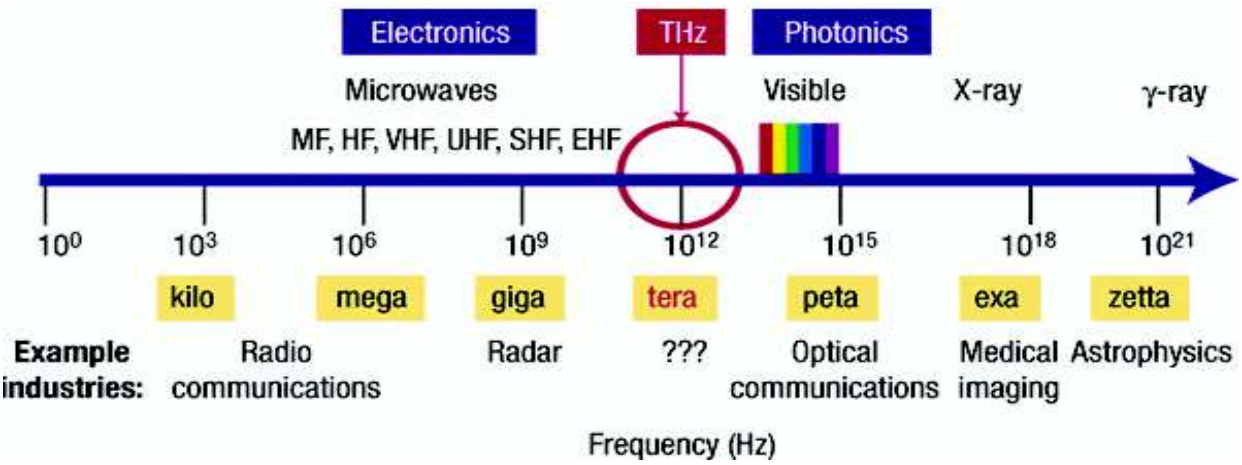

Fig. 5.1: Electromagnetic Spectrum

The excitation of matter by THz radiation allows to study many physical phenomena such as relaxation modes in liquids [3], propagation of surface plasmons [4], phonons in materials [6], spectral signature of organic molecules [7], rotational and vibration levels in gases [8,9], etc. In addition to these fundamentals, due its non-ionization property, THz radiation is safe for

the examination of human beings and also nondestructive for the samples which are analyzed [10]. Therefore many applications are foreseen in security (identification of explosives or drugs) [11], imaging (using THz radiation naturally emitted by the human body to reconstruct images) [12], telecommunications (secure at THz frequencies) [13], etc.

Terahertz time domain spectroscopy (THz-TDS) is a powerful technique for material studies over a wide range of frequencies from a few tens of GHz to a few THz. Within the past several years, numerous researchers have recognized the possibility of exploiting the broadband nature of the THz-TDS system for materials identification and characterization. Using ultra short electromagnetic pulses, THz-TDS gives access to study the far-infrared optical properties of many different materials, such as dielectrics [14], semiconductors [15], liquids [15a], and superconductors [15b]. Since few years, THz-TDS system allowed for imaging and can be used in package inspection [15c–e], biomedical diagnosis [15f], and gas sensing [1g].

In this chapter, the first part is about the description of the THz-TDS experimental bench and the method we used to extract the material parameters of a sample from the complex transfer function. The second part is devoted to the THz-TDS spectroscopy of samples (2D metallic devices, Carbon Nano-Tubes (CNTs), Graphene and Quantum Dots (QDs)) in the THz range. Finally, we present a carrier dynamics study in QDs samples using optical pump-THz probe spectroscopy and photoluminescence spectroscopy methods. We have performed these latter measurements at SPI, Vilnius.

II. Fundamental of THz-Time domain spectroscopy

In this section, we present the basic concepts of THz-TDS. The main properties of THz radiation will be discussed as well as the important mechanisms for generating and detecting THz radiation. Furthermore, THz-TDS will be utilized to determine the optical properties of solids.

The standard classical THz-TDS experimental setup is presented in the Fig. 5.2. In a THz-TDS system, both generation and detection of THz radiation occur. The THz-TDS system is driven by a pulsed femtosecond laser. A beam splitter divides the laser beam into two parts: one excites the THz emitter and the other one triggers the THz receiver. This probe beam explores amplitude of the THz pulse over time. Thus, THz waveform is obtained as a function of time. This waveform can be used as reference waveform. Then a sample is placed in the THz beam and another waveform is obtained. The ratio of the Fourier transform of these two

temporal wave forms gives the complex value of the transmission coefficient of the sample, which can be used to extract the optical properties (refractive index and absorption coefficient) of the sample.

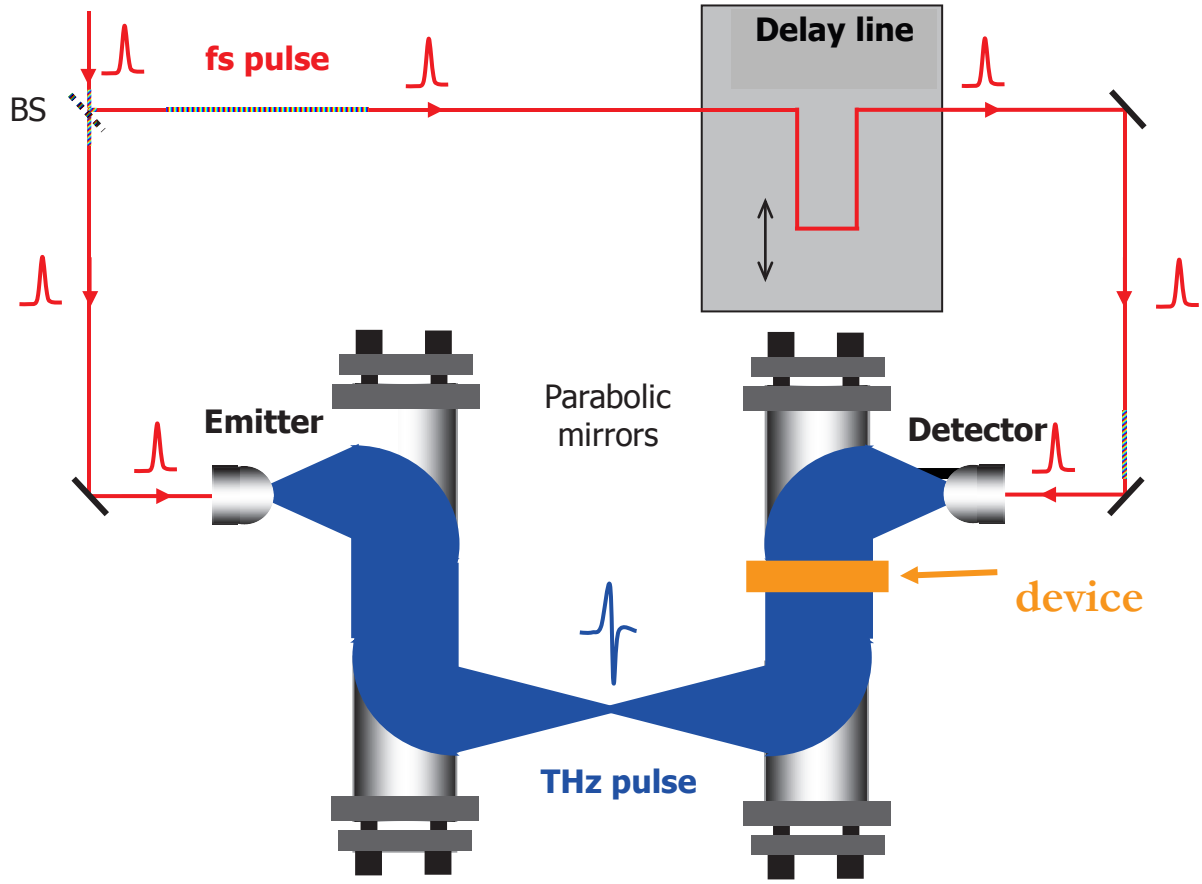

Fig. 5.2: Standard THz-TDS experimental setup

The frequency resolution (difference Δf between two neighboring points) depends on the total scan length as follows:

$$\Delta f = \frac{c}{2l} \tag{V-1}$$

where c is the velocity of light and l is the delay line displacement length. For, example a scan length l = 15 mm gives a frequency resolution of Δf =10 GHz.

II.1. Data Analysis in THz-TDS spectroscopy

THz TDS is used to determine the optical properties of the material (refractive index and absorption coefficient) through transmission (or reflection) measurement. In TDS measurement, one obtains an electric field trace with a temporal resolution in the range of several fs depending on the laser system used in the THz generation process. In principle, we record the temporal signal propagating through a sample (E_s) (Fig. 5.5) and in the absence of sample (E_{ref}) namely the reference signal, as shown in Fig. 5.3 and Fig. 5.4 [16]. Here we consider only materials (films) deposited over a substrate (Fig. 5.3), that will be effectively characterized in the experimental part of this chapter.

The Fast Fourier transformation (FFT) of those temporal traces gives the amplitude and phase information in the frequency domain (Fig. 5.6), that allows one to get information about the dielectric properties of the sample:

$$E(\omega) = \frac{1}{2\pi}\int_{-\infty}^{+\infty} e^{-i\omega t} E(t)\, dt \qquad \text{(V-2)}$$

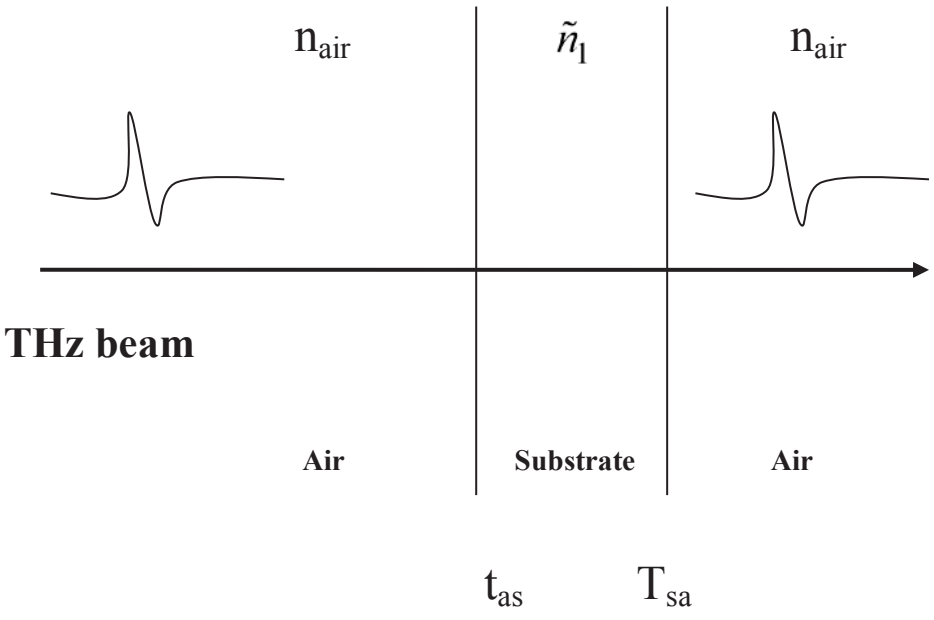

Fig. 5.3: The basic scheme of a THz-TDS transmission experiment for reference measurement

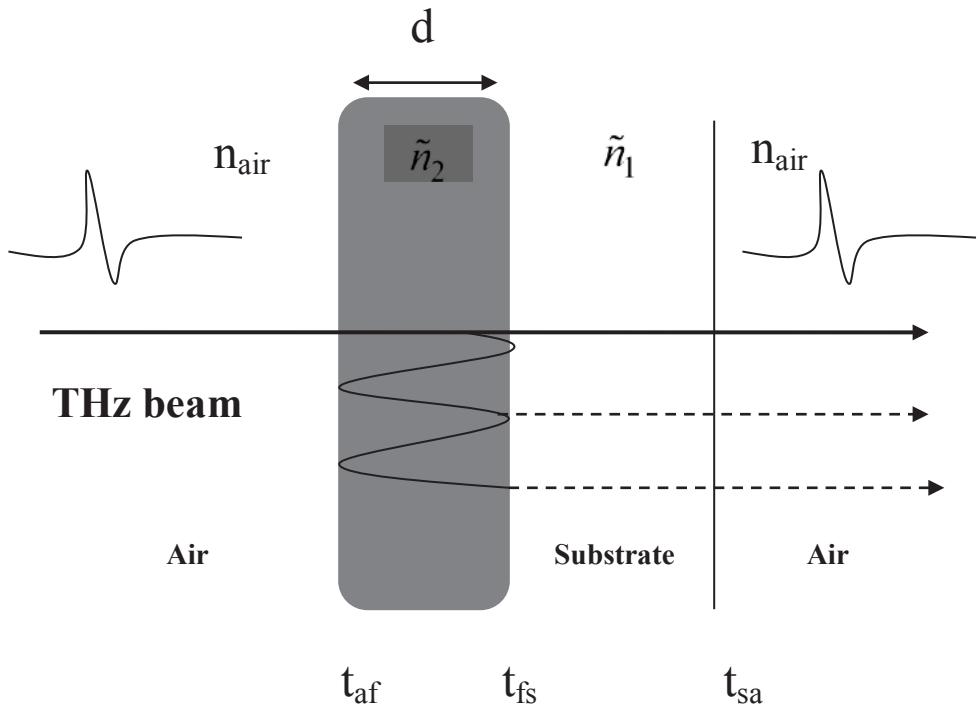

Fig. 5.4: The basic scheme of a THz-TDS transmission experiment, sample measurement. The sample is a parallel plate with thickness d and complex refractive index.

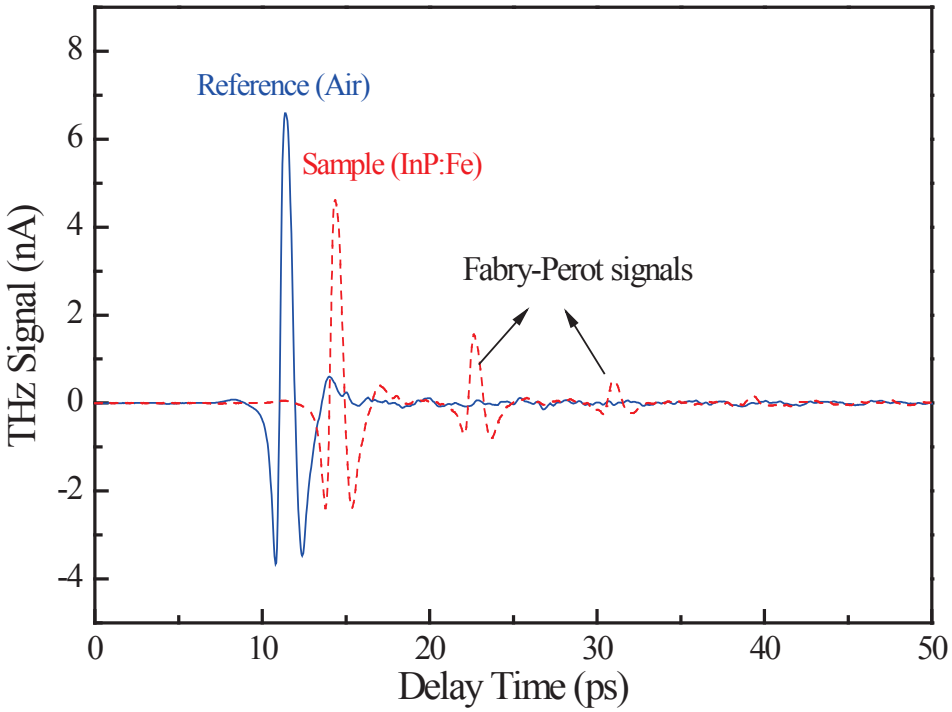

Fig. 5.5: Measured temporal signals of reference (blue) and sample (red) of 350 µm thick InP:Fe .

In a basic scheme, the sample (film) is a parallel plate with thickness d and a frequency dependent complex refractive index $\tilde{n}_2$. By passing through, the pulse gains a phase factor P_2.

$$E_{sample}(\omega) = E_0(\omega)t_{air\to 2}(\omega)P_2(\omega,d)t_{2\to 1}(\omega)t_{1\to air}(\omega)P_1(\omega,d_s) \times \sum_{k=0}^{+\infty}\left\{R_{21}(\omega)P_2^2(\omega,d)R_{2air}(\omega)\right\}^k \quad \text{(V-3)}$$

The reference electric field is:

$$E_{reference}(\omega) = E_0(\omega)t_{air\to 1}(\omega)P_{air}(\omega,d)t_{1\to air}(\omega)P_1(\omega,d_s) \quad \text{(V-4)}$$

where E_0 is the amplitude of the incoming signal, d_s is the thickness of substrate and $t_{air\to 2}$, $t_{2\to 1}$ and $t_{1\to air}$ are respectively the transmission at air-film interface, film-substrate interface and substrate-air interface. And $t_{air\to 1}$ and $t_{1\to air}$ are respectively the transmission at air-substrate interface and substrate-air interface. R_{21} and R_{2air} are reflection at interface film-substrate and film-air respectively. Hence we suppose that the substrate is thick enough to allow us time-window the transmitted signal and thus to select only the directly transmitted pulse through the substrate.

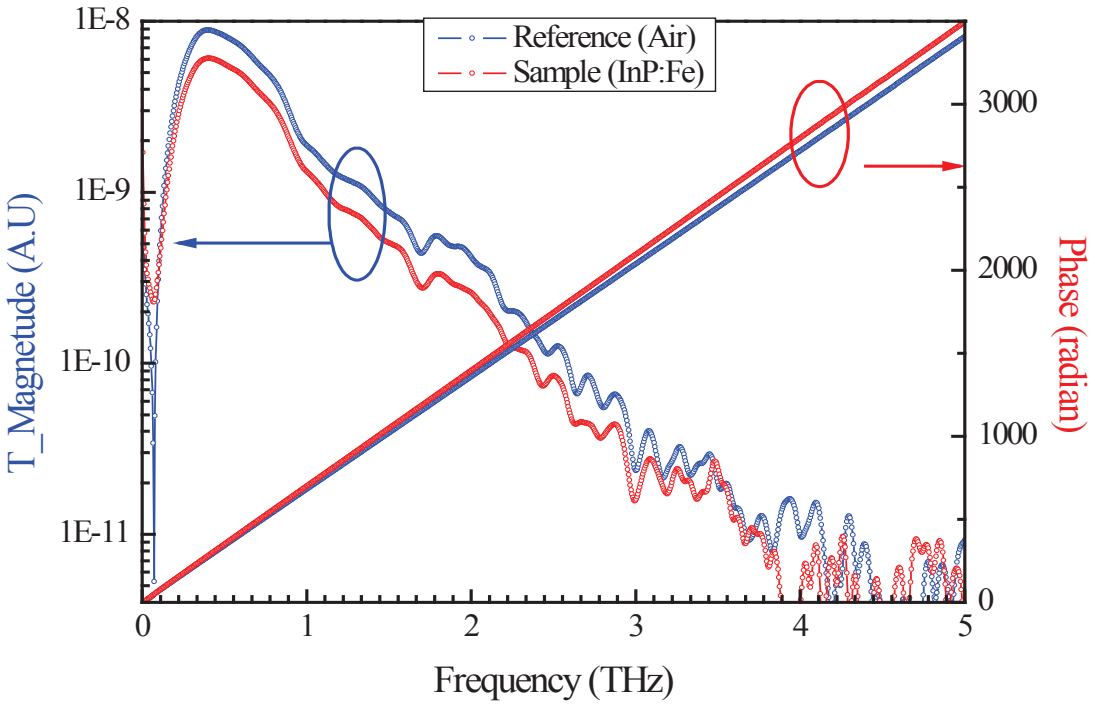

Fig. 5.6: Modulus and phase spectrum's of reference (in black) and sample (in red) of LiNbO3 1.1 mm thick.

Let us consider the reflection and transmission at the first and second interfaces (air-film and film-air, respectively). We assume an incident plane wave, at normal incidence and a planar surface without scattering. Thereby, we can use the Fresnel equations for the transmission and reflection coefficients for the interface *ab*:

$$\mathrm{T_{ab}} = \frac{2\tilde{n}_a}{\tilde{n}_a + \tilde{n}_b}; \quad R_{12} = \frac{\tilde{n}_a - \tilde{n}_b}{\tilde{n}_a + \tilde{n}_b} \tag{V-5}$$

Where $\tilde{n}_a$ and $\tilde{n}_b$ are complex refractive index ($\tilde{n} = n - ik$) of medium *a* and *b*.

The propagation coefficient in the medium *a* of thickness *d:*

$$P_a(\omega, d) = \exp\left[-i\frac{\tilde{n}_a \omega d}{c}\right] \tag{V-6}$$

Now we introduce the transfer function *T(ω)* of the sample as the complex ratio of the spectra $E_s(\omega)$ and $E_{ref}(\omega)$, described by the following equation:

$$T(\omega) = \frac{E_{Sample}(\omega)}{E_{reference}(\omega)} \tag{V-7}$$

From equations (V-3), (V-4), (V-5), (V-5), we obtain the transfer function:

$$T(\omega) = \frac{2\tilde{n}_2(1+\tilde{n}_1)}{(1+\tilde{n}_2)(\tilde{n}_2+\tilde{n}_1)} \exp\left[-i(\tilde{n}_2 - 1)\frac{\omega d}{c}\right] \times FP(\omega), \tag{V-8}$$

With

$$FP(\omega) = \frac{1}{1 - \frac{(\tilde{n}_2 - \tilde{n}_1)(\tilde{n}_2 - 1)}{(\tilde{n}_2 + \tilde{n}_1)(\tilde{n}_2 + 1)} \exp\left[-2i\tilde{n}_2 \frac{\omega d}{c}\right]}. \tag{V-9}$$

This last expression corresponds to the Fabry-Perot echoes in the sample with thickness *d.*

II.2. Description of the elements in the THz-TDS experimental bench

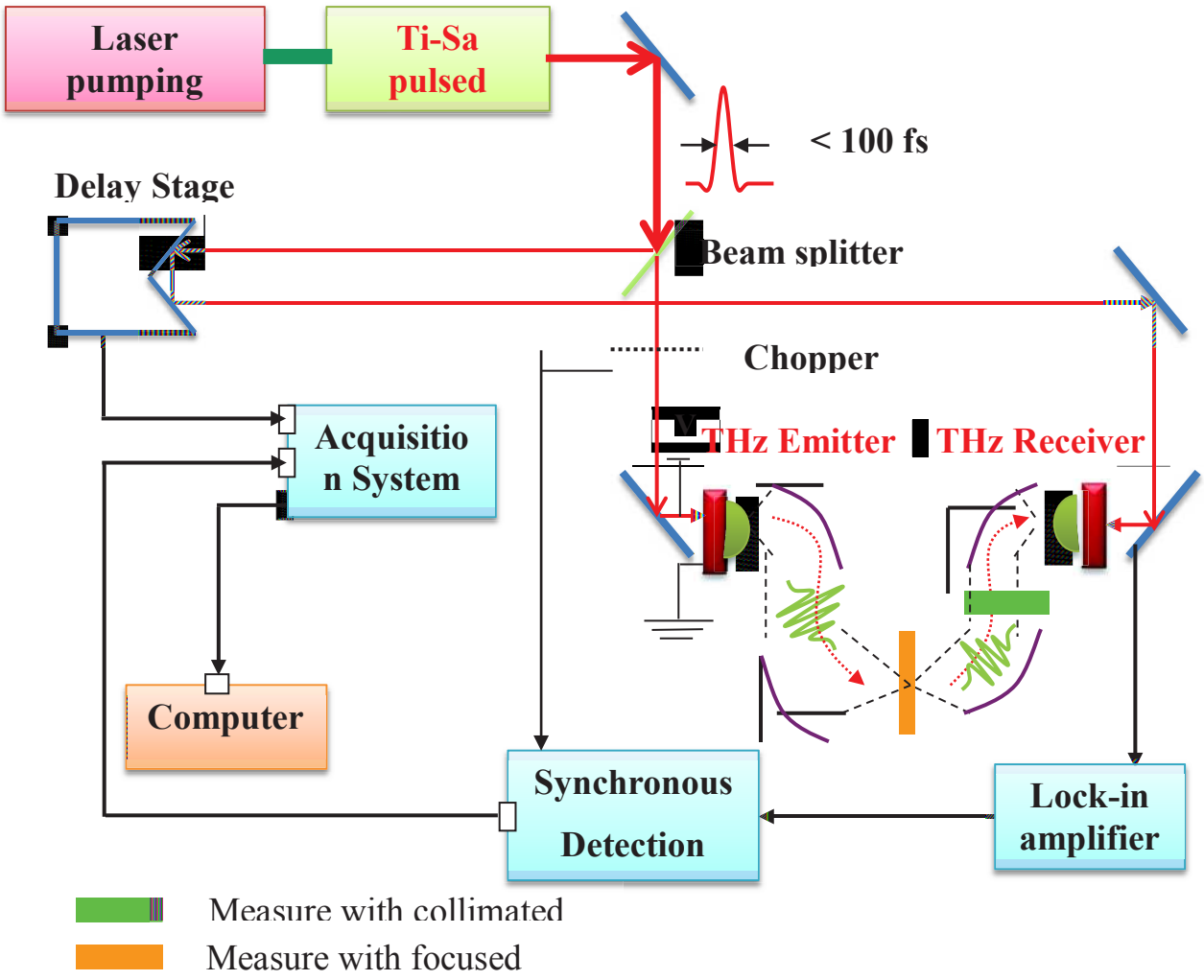

Fig. 5.7: THz-time domain spectroscopy bench used in our present study.

The THz-TDS experimental setup used in my research work is shown in Fig. 5.7. At the output of the pulsed laser, the optical beam has a diameter of about 1 mm and it is split into two by a beam splitter. The first optical beam passes through a delay line and illuminates the detector with an optical power of about 10 mW. The second beam is modulated by an optical chopper before illuminating the emitter. This latter is polarized by a static field of the order of 30 kV / cm. These two photoconductive antennas (emitter and detector) are separated by a distance of several tens of centimeters. THz radiation is shaped (collimated / focused) by hemispherical lenses (Si HR) associated with a set of four off-axis parabolic mirrors. The source of optical pulses used in our THz-TDS experiments is a titanium sapphire laser

(Tsunami, Spectra Physics @ 800 nm) pumped by a laser power of 3.82 W. The full width half maximum (FWHM) duration of the optical pulses, measured at the output of the laser cavity, is about 50 fs with a repetition rate of 82 MHz and an average optical power of about 400 mW. Two photoconductive LTG-GaAs antennas are used as THz emitter and detector. Each photoconductive antenna is made from LTG-GaAs layers deposited on an intrinsic GaAs substrate of 650 µm thickness [18]. Two metal (gold) electrodes (length 8 mm, width 40 µm) with a gap 6 µm gap at the center formed an antenna structure as show in Fig. 5.8.

II.2.1. Generation of THz radiation by photoconductive switching

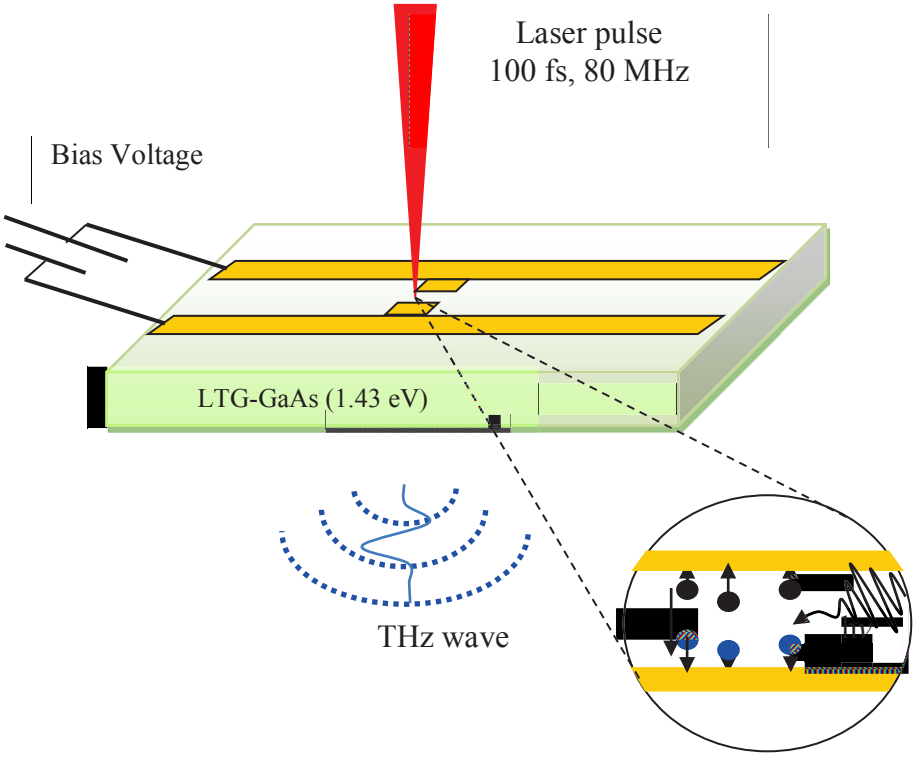

Fig. 5.8*: photoswitch on LT-GaAs substrate. Wire line length of 8 mm and a width of 30 microns, a distance of 30 to 40 microns, with a gap of 6 microns* [19]

The method of generation of THz radiation from ultrafast photoconductive devices was proposed by Auston *et al* [19] in the early 80s. The structure of a THz antenna is quite simple: two metal lines (gold) are deposited on a ultrafast semiconductor material (LTG-GaAs, InGaAs ...). These lines are biased by a voltage leading to a strong electric field at the gap

[20]. Photocarriers are generated when the interspace is illuminated by the laser photons, whose energy is bigger than the semiconductor gap (see Fig. 5.8). According to Maxwell's equations [21], the rapid variation of the density of the carriers and their acceleration by the electric field applied radiate a dipole signal, whose duration is typically 1 *ps* or less and whose spectrum spreads over the THz level.

II.2.2. Detection of THz radiation by photoconductive sampling

The photoconductive receivers are similar to the emitting (see Fig. 5.8.), the only difference is that the metal lines of the receiver will be polarized by the THz field emitted by the transmitter. The illumination of the optical radiation creates electron-hole pairs in the gap of the receiver antenna, which will then be accelerated by the incident THz field, hence the creation an average current whose mean value ranges from a few pico-amperes to a few nano-amperes. This current is proportional to the strength of the THz field that illuminates the receiver antenna. The temporal shape of the THz field is obtained by varying the delay in optical signal that illuminates the receiver antenna. The performance of these antennas is limited mainly by the duration of the optical pulse, the lifetime of the carriers in the photoconductive material (LTG-GaAs) as well as the THz field that illuminates the antenna.

III. CHARACTERIZATION OF DIFRACTIVE STRUCTURE PERIODIC HOLES IN A METALLIC SLAB

III.1. Introduction

The extraordinary transmission of electromagnetic waves through a periodic array of sub wavelength holes has attracted massive interest in both understanding of its physical origin and the fascinating interest in a variety of fields [22-24]. The physics of the far infrared response of such hole arrays was pioneering by R. Ulrich [25] in a remarkable and rather unknown paper, in which he already explained clearly the role of the different electromagnetic modes of the device that are resonantly excited by the incoming beam. More recently, the electromagnetic response of these devices in the terahertz (THz) frequency range has been reconsidered using new experimental tools, and this topic is subject to intense studies since the first reports by Miyamaru *et al.* [26] and by Cao and Nahata [27]. The reason originates in the easy manufacturing of the devices, which requires only mechanical tools like precise drilling machines, and also in the performance of the mostly used experimental

technique, namely THz-TDS [28]. Most of the amazing features of the electromagnetic response of metallic holes arrays have already been observed in the THz range, for example super-transmission [29], filtering [30], film sensing [31] and so on.

In this section, we focus on the study of THz wave diffraction by a network of two dimensional periodic hole array on metallic slab. This type of structure is interesting because it would excite the electrons at the surface of the metal. The resulting propagating wave is called a surface plasmon. We are interested particularly in the excitation of these surface plasmons in the structure. Here we first present theoretical results obtained by Rigorous Expansion Model (REM) and High Frequency Structure Simulator (HFSS) and compared with THz-TDS experimental results. And finally, we discussed about various phenomena observed in the reflection and transmission results.

III. 2. Surface plasmons

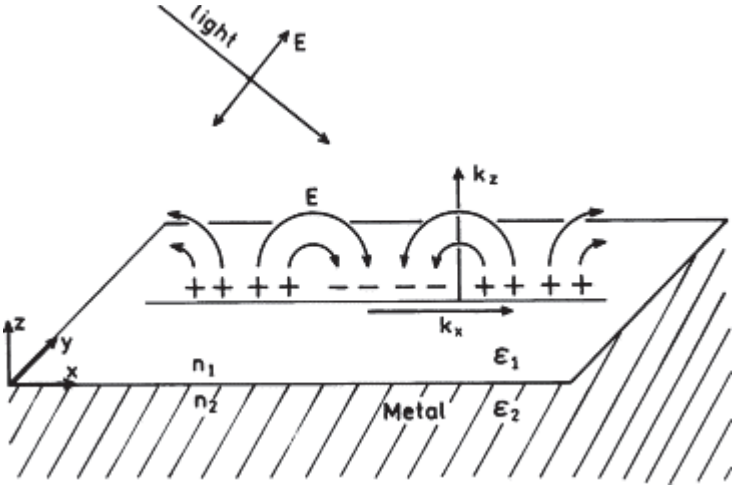

Fig. 5.9: Surface plasmons at air-metal interface

Surface plasmon (SP) is nothing but an electromagnetic wave propagating along the interface of two media, one of them is the inactive medium (dielectric, here air) and the other is active medium (conductor, here metal). A SP corresponds to the quantum of energy associated to a harmonic oscillation of the free charge carriers at the metal surface, which is mostly perpendicular to the surface and propagating along the interface. From Maxwell equations the dispersion condition of SP can be written as

$$k_{sp} = \frac{\omega}{c}\sqrt{\frac{\varepsilon_1 \varepsilon_2}{\varepsilon_1 + \varepsilon_2}} \qquad \text{(V-10)}$$

where c is the velocity of light in free space, ω is the angular frequency, ε_1 and ε_2 are respectively the complex dielectric constants of air and metal. As $k_{sp} > k_{air}$, SP are guided and thus a device is necessary to excite them using a incident plane wave. This could be a prism (ATR), a grating etc. Here the holes array plays the role of the coupler. Together some sub wavelength effects should be observed. Let us notice that, in the THz range, $\varepsilon_2 >> 1$, thus $k_{sp} \approx \frac{\omega}{c}$.

III.3. Two dimensional metallic device

Two dimensional grating was designed and manufactured with the geometrical properties shown in the table 5.1. THz-TDS is used to study the spectral characteristics of the 2D device. The device is placed in between the emitter and the detector (see in Fig. 5.7). We carried out both the transmission and reflection measurements with a 3 mm diameter (Φ = 3 mm) THz beam.

	Value	Precision
Material	Duraluminum (AZ5GU)	
Period (mm)	1,0	±0,01
Diameter (mm)	0,51	±0,01
Thickness (mm)	1,72	±0,01
Surface Flatness δe	1/100	

Table 5.1: Geometrical details of the device

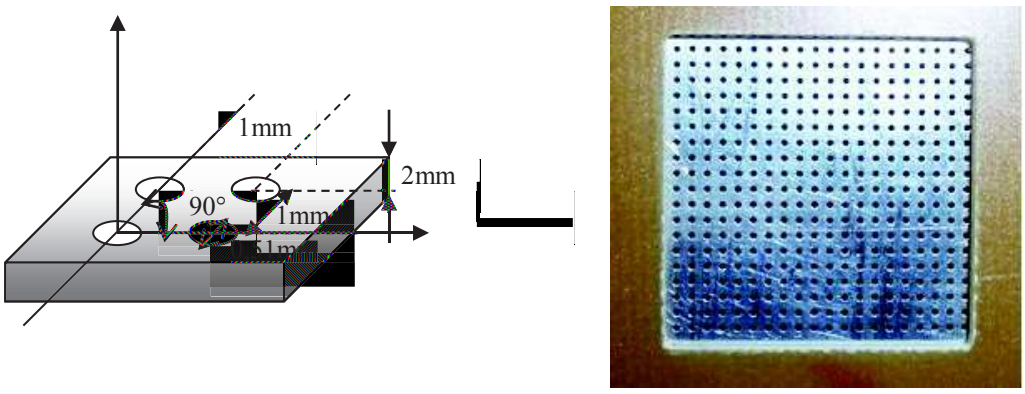

Fig. 5.10: (a) Geometrical dimensions of the device, and (b) Photograph of 2D metallic grating round holes with his diaphragm

III.3.1. Description of the device

The present device (*Fig. 5.10b)* is manufactured by micro-mechanical drilling method and the fabrication steps are:

• Cutting a mechanical material (duraluminum) (30 × 30 mm);

• Grinding and polishing of the surface (δe = 1/100);

• Drilling with a drill titanium carbide (ϕ = 0.51 mm) with lubrication, 7500 rev / min, 0.1 mm / sec. The drilling cycle starts from the inside to the outside of the network in the watch clockwise (to avoid problems of embrittlement of the material by shear). This device contains 20 × 20 holes.

• Grinding and polishing of the final surface.

• Ultrasonic Cleaning of manufacturing waste.

III.3.2. Theory

Let the equation of diffraction of a periodic structure:

$$\sin\theta_i + m\frac{c}{d\,f} = \sin\theta_m \qquad \text{(V-11)}$$

d is the period of the structure. θ_i and θ_m are incidence and diffracted angles. A new diffracted order propagates if θ_m <90°. For this limit θ_m = 90°, there is a redistribution of energy in the different diffracted orders, hence the appearance of rapid changes in the curve of transmission or reflection (Wood anomalies). We have:

$$\sin\theta_i + m\frac{c}{d\,f} = \pm\sin 90° = \pm 1 \qquad \Rightarrow \qquad f = m\frac{c}{d\left|1 \pm \sin\theta_i\right|} \tag{V-12}$$

d is the period in a 2D hole system, it depends on the direction as shown below. For a wave propagating in the direction (i, j), the period is:

$$d = a\sqrt{i^2 + j^2} \;\Rightarrow \qquad f = m\frac{c}{a\sqrt{i^2 + j^2}\left|1 \pm \sin\theta_i\right|} \tag{V-13}$$

It should be noted that these anomalies are independent of the polarization of light. When the incidence plane is not parallel to the holes (conical incidence), we have:

$$\vec{k}_i + m\vec{k}_g = \vec{k}_m \tag{V-14}$$

where the vectors are projected onto the surface. If ϕ is the angle between the direction normal to the plane of the holes and the direction k_i (same definition for the diffracted signal m, see drawing), we obtain:

$$\begin{cases} k_i \cos\varphi_i + m\,k_g = k_m \cos\varphi_m \\ k_i \sin\varphi_i = k_m \sin\varphi_m \end{cases} \tag{V-15}$$

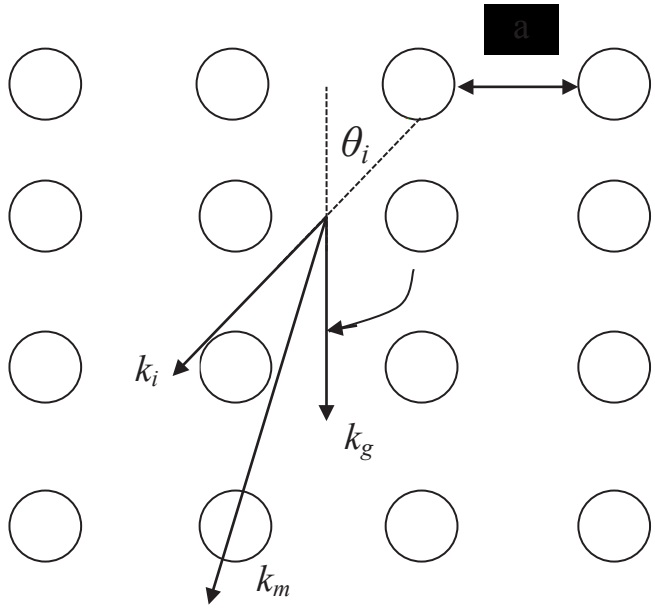

Fig. 5.15: Scheme of the wave vector conservation process.

Finally, with respect to the angles of incidence and diffraction, we have:

$$k_i = k \sin\theta_i \qquad k_m = k \sin\theta_m \quad k = \frac{2\pi}{\lambda} = \frac{2\pi f}{c} \tag{V-16}$$

Hence, for the appearance of a new diffraction order (θ_m = 90 °), equation (V-15) can be written as:

$$\begin{aligned} & k_i \sin\varphi_i = k_m \sin\varphi_m \qquad \Rightarrow \sin\theta_i \sin\varphi_i = \sin\varphi_m \\ & k_i \cos\varphi_i + m\,k_g = k_m \cos\varphi_m \qquad \Rightarrow \sin\theta_i \cos\varphi_i + m\frac{c}{d\,f} = \sqrt{1-\sin^2\theta_i \sin^2\varphi_i} \end{aligned} \tag{V-17}$$

Let us set:

$$x = m\frac{c}{df} \tag{V-18}$$

$$\begin{aligned} \Rightarrow \quad & \sin^2\theta_i \cos^2\varphi_i + 2x \sin\theta_i \cos\varphi_i + x^2 = 1 - \sin^2\theta_i \sin^2\varphi_i \\ \Rightarrow \quad & x = -\sin\theta_i \cos\varphi_i \pm \sqrt{\sin^2\theta_i \cos^2\varphi_i + \cos^2\theta_i} \end{aligned} \tag{V-19}$$

In the case of an incidence plane parallel to the holes, the wave is diffracted in a conical manner. The angle φ_i is given by:

$$\tan\varphi_i = \frac{i\,a}{j\,a} = \frac{i}{j} \qquad \Rightarrow \qquad \cos^2\varphi_i = \frac{1}{1+\frac{i^2}{j^2}} = \frac{j^2}{i^2+j^2} \tag{V-20}$$

We thus obtain:

$$f = \frac{c}{a}\left|\frac{m}{-\sin\theta_i \pm \sqrt{j^2 + i^2\cos^2\theta_i}}\right| \tag{V-21}$$

Let us comment about the redistribution of energy (Wood's anomalous) and excitation of a SP. We simplify here the explanation to a 1D structure. Redistribution of energy occurs when a new diffracted orders appears, i.e. $\theta_m = 90°$ in (V-16). Thus (V-11) writes simply:

$$\sin\theta_i + m\frac{c}{d\,f} = 1 \tag{V-22}$$

A SP is excited when the coupling equation is fulfilled:

$$\sin\theta_i + m\frac{c}{d\,f} = n_{SP} = \frac{k_{SP}}{\omega / c} \qquad \text{(V-23)}$$

As $n_{SP} \sim 1$ in the THz range, therefore (V-22) and (V-23) are similar. It means that both phenomena are superimposed and cannot be separated. Nevertheless for the s- polarization, SP cannot be excited and thus only Woods's anomalies are observed. By making the difference between p and s signals, SP excitation could be separated from Wood's anomalies. This is the goal of this study.

III.4. Rigorous expansion modal (REM)

Rigorous Expansion Model (RME) is a coding program prepared by L.C. Botten *et al* [32], from the University of Sydney. By using this code, one can study the transmission and reflection properties of certain materials (in ideal case) for desired frequency region. We use this code to study the phenomenon called Wood's Anomaly and the excitation of surface plasmons in 2D metallic grating. Our present device is metallic slab with period arrangement of holes (Fig. 5.10b). This model gives the transmission and reflection data for all the scattering orders, but we take only the 0^{th} order in order to compare with experimental data (because in experiment, we get only 0^{th} order data due to the lack of detectors for the detection of other orders data). In this model, we use the metal as perfect conductor (we cannot consider the metallic losses in this code), which means that the conductivity is infinite [33-34]. Therefore, to solve the problem with losses, we use the simulation software 'HFSS', where we can input the actual metallic losses.

III.5. High Frequency Structure Simulator (HFSS)

Numerous electromagnetic problems are not analytically solvable like scattering, radiation and transmission of energy because of the complexity of the studied structures. Consequently use of computational electromagnetic field is compulsory. It models the interaction of electric and magnetic fields with physical objects and their environment to find the numerical approximation of Maxwell's equations. These are few specific programs or software's that solve Maxwell's equations directly [39]. Here in our present work, we used HFSS software to solve the periodic structure electromagnetic response. HFSS stands for High Frequency Structure Simulator and is based on finite element method. HFSS automatically generates an appropriate and accurate mesh for solving the problem. HFSS delivers the S, Y, and Z parameters of the structure and 3D maps of the electromagnetic field (near- and far-field). The only drawback of this program is to be very CPU consuming because of its method of mesh

and the large bandwidth used in study (in our study around 1THz). Because of memory and time consuming, here we take only one unit cell and solve the problem with master-slave boundaries and Floquet ports. We have adjusted the conductivity of the material by two orders of magnitude to consider losses in the device. We summarize the HFSS results together with the experimental results and RME results in the following sections.

III.6. THz –TDS characterization of a two dimensional metallic grating

As already discussed in section (III.3), the sample (Fig. 5.10) is a 1.72-mm thick duraluminum slab, with cylindrical holes (diameter ϕ=0.51 mm) forming a square lattice whose cell length is a=1 mm. Thus the device filling factor is ~ 80 %. The holes are made by using a simple drill whose displacement is controlled by a computer. The transmission and reflection properties of the device are measured with a standard THz-TDS experiment, allowing us to measure the amplitude and the phase of the signal from 0.1 to 3 THz (presently up to 1 THz) [35].

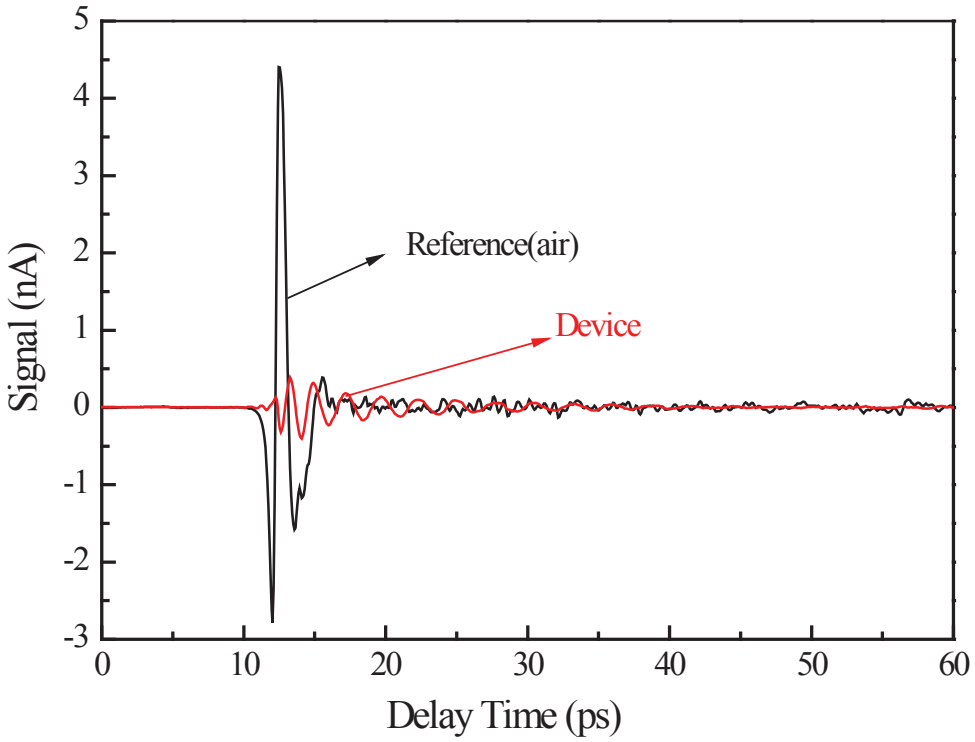

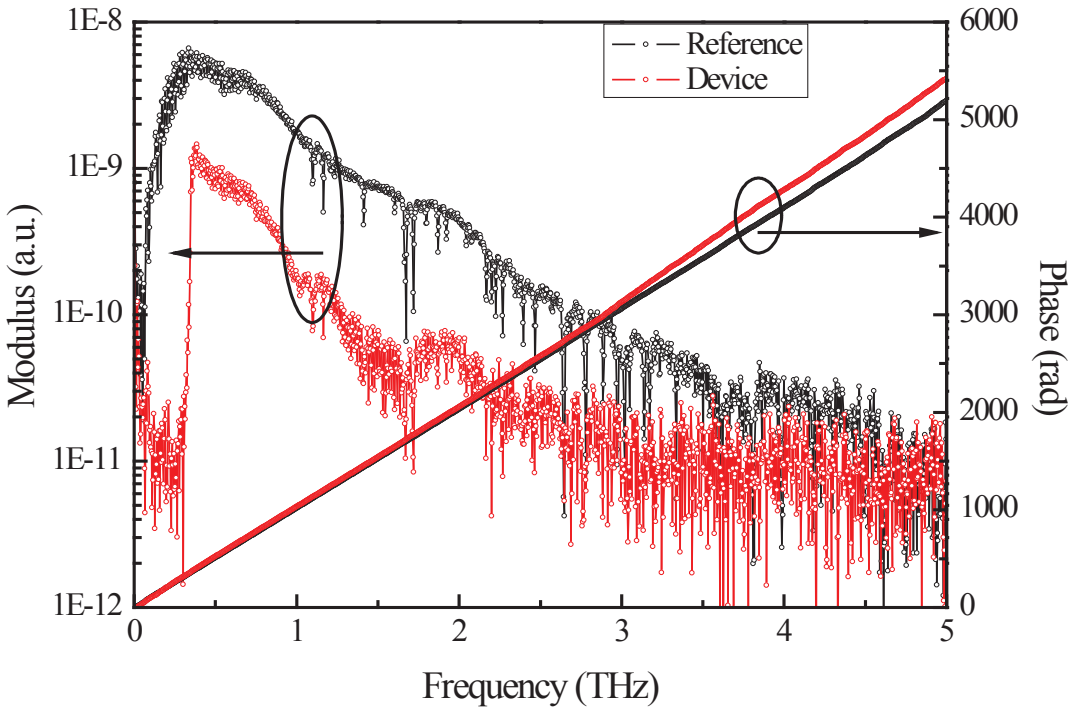

Fig. 5.11: (a) Temporal signal of the device at normal incidence, and (b) Fourier transform of the temporal signal.

The waveforms are recorded in an equivalent-time window of 100 ps duration, leading to a frequency resolution of 10 GHz. The incident and azimuthal angles can be adjusted with a precision better than 1°. The beam delivered by the emitting antenna (LT-GaAs photo conducting switch) is almost linearly polarized. Nevertheless, we improve the polarization of the beam by using a grid polarizer. The THz beam is made parallel thanks to a small high-resistivity Si spherical lens (diameter 2 mm) attached to the antenna and by a parabolic mirror. The optical arrangement of the receiving antenna is similar to the emitting one. At the sample location, the diameter of the THz beam at f = 1 THz is ~3 cm, while the device is 2×2 cm^2 wide. The metallic device holder serves as a 2×2 cm^2 diaphragm, leading to an angular resolution limited by diffraction to ~1° at 1 THz. Fig. 5.11a shows the waveform transmitted by the device and its corresponding FFT spectrum presented in the Fig. 5.11b.

III.7. Results and discussion

III.7.1. Experimental and modeling results of the transmission and reflection of the device in normal incidence

Our present device (periodic structure) is considered as diffractive structure and the light is diffracted into different orders. Fig. 5.12a shows the measured transmitted and reflected field amplitudes at normal incidence. The transmitted and reflected signals are measured in the direction perpendicular to the device surface, thus they correspond to not diffracted beams (m=0). If no energy is absorbed in the metal device through ohmic losses and if no energy is carried out by propagating orders of diffraction ($m \neq 0$), the sum of reflected and transmitted energies should be equal to 1. Fig. 5.12a reveals that, below the cutoff frequency f_{cutoff} (cutoff frequency is the minimum transmitted frequency, below this frequency no signal is propagated), 97 % of the incident energy is reflected. As, for this frequency range, no transmission occurs, the missing 3 % corresponds to light diffracted through the first m=1 order of diffraction and to light absorbed by the metal. Above f_{cutoff}, transmission is permitted and we observe the related decrease of the reflected amplitude. Typically, the field transmission (reflection) value is of the order of 20~30 % (70~80 %), i.e. 4~9 % (50~60 %) in energy. Therefore the missing energy is quite large (40~45 %). As below f_{cutoff}, only a very low percentage of energy is missing and above f_{cutoff}, the resonant features (m-lines) are feebly pronounced, the energy carrying by diffracted propagating orders or absorbed through SP losses remains relatively weak. This may be explained by the small relative hole area (large filling factor) of the structure. Thus the large lack of energy above f_{cutoff} may be explained mainly by absorption while the signal is passing through the holes. The roughness of the wall of the cylindrical holes, resulting from the drilling process, may be responsible for such losses. A short calculation of the propagation attenuation in a cylindrical waveguide shows that ohmic losses are not big enough to explain the observed lack of energy.

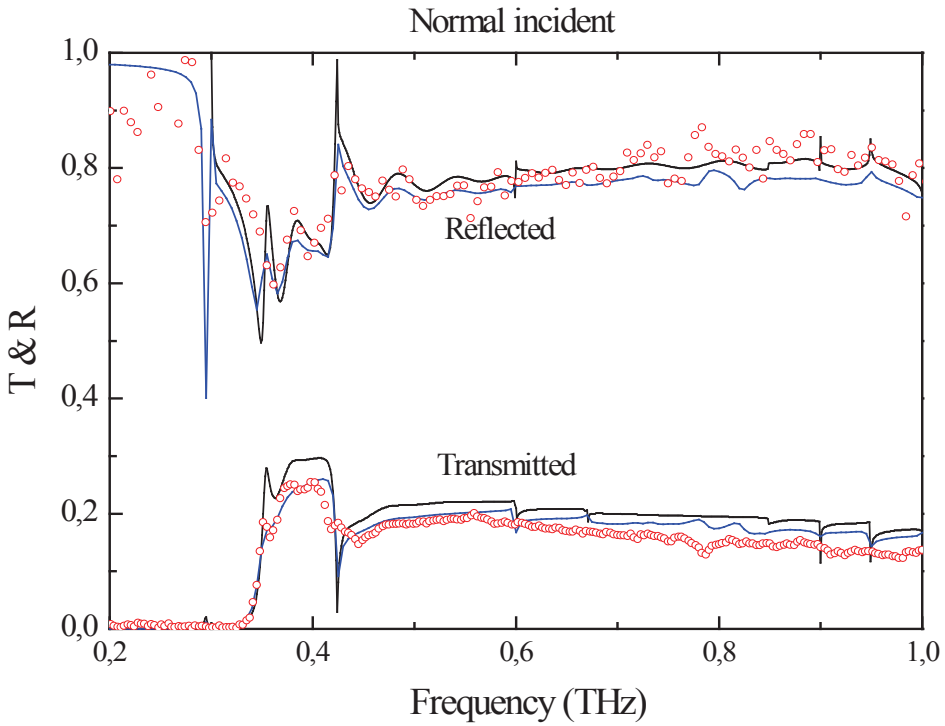

Fig. 5.12a: Transmitted and reflected field amplitude spectra recorded at normal incidence. The values are normalized to the incident field amplitude. Open circles are experimental data, Continues curves (in blue) are HFSS data, while continuous curves (in black) are calculated with the RME Method [32].

Fig. 5.12b represents the HFSS electric field mapping in unit cell before and after its cutoff frequency. As we discussed earlier, below the cutoff frequency, no signal is propagated through the unit cell. This is observed in Fig. 5.12b (left side) which was calculated at 3.34 THz. After cutoff frequency, the signal is propagated through the unit cell, this is clearly seen in right side picture calculated at 3.45 THz.

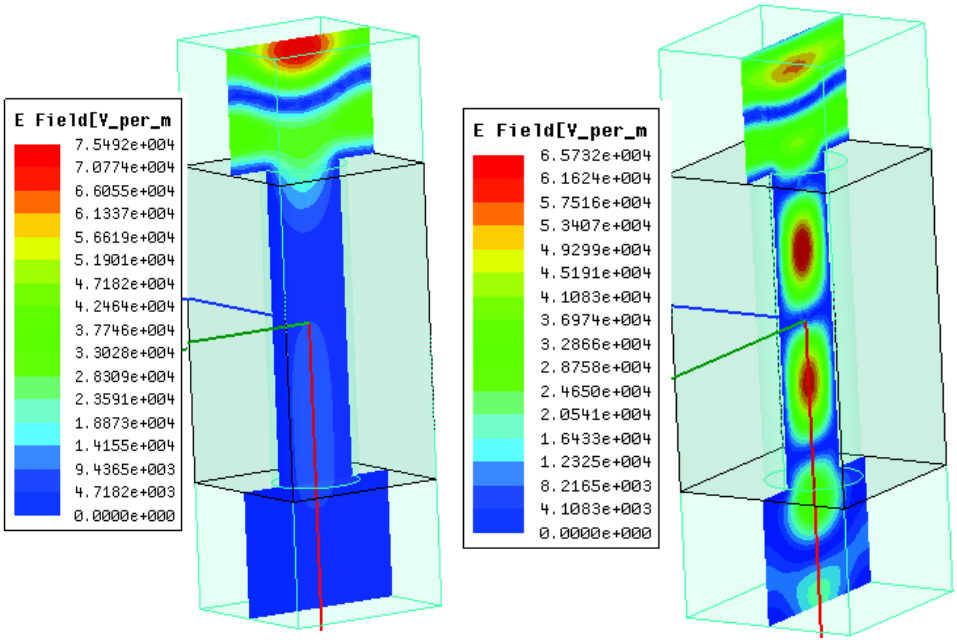

Fig. 5.12b: HFSS electrified mapping at 3.34 THz (left: bellow cutoff frequency f_c=3.45 THz) and at 0.4 THz (right: above cutoff) in unit cell.

III.7.2. Spectral properties of the device for different polarization of the incident THz field

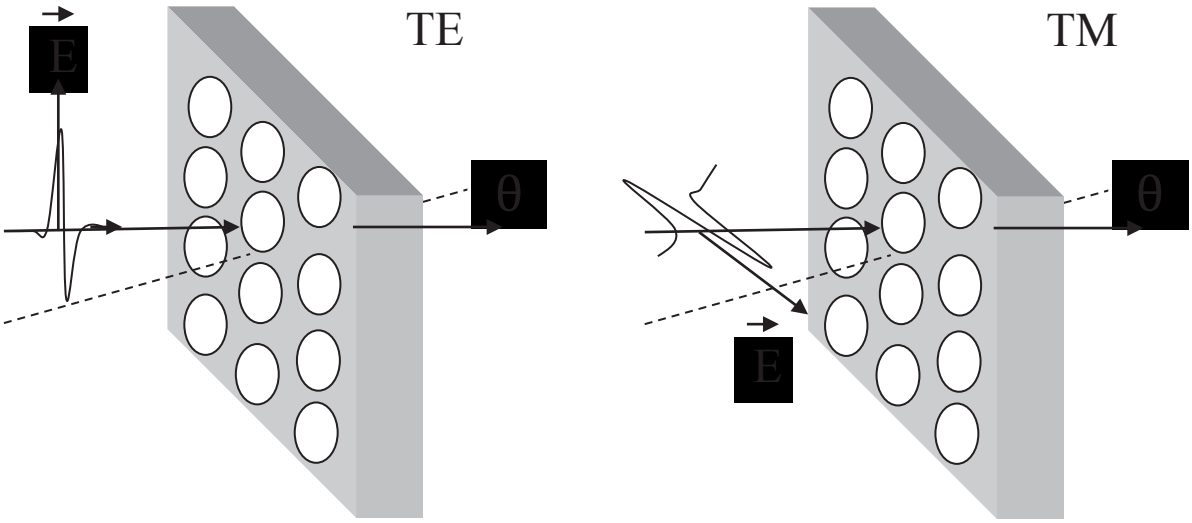

Fig. 5.13: Orientation of the device for TE and TM polarization in THz-TDS transmission experiment.

In this section, we study the transmission characteristics of the device depending on the polarization of the incident THz field. Fig. 5.13 shows the orientation of the device for two experimental cases studied. The TDS experimental results (open circles in red) and modeling results (HFSS (blue line), RME (black line)) of the device transmission coefficient for the THz energy, recorded for different angles of incidence θ ranging from 0° to 45° in both TE and TM polarizations presented in the Fig. 5.14 and Fig. 5.15 respectively.

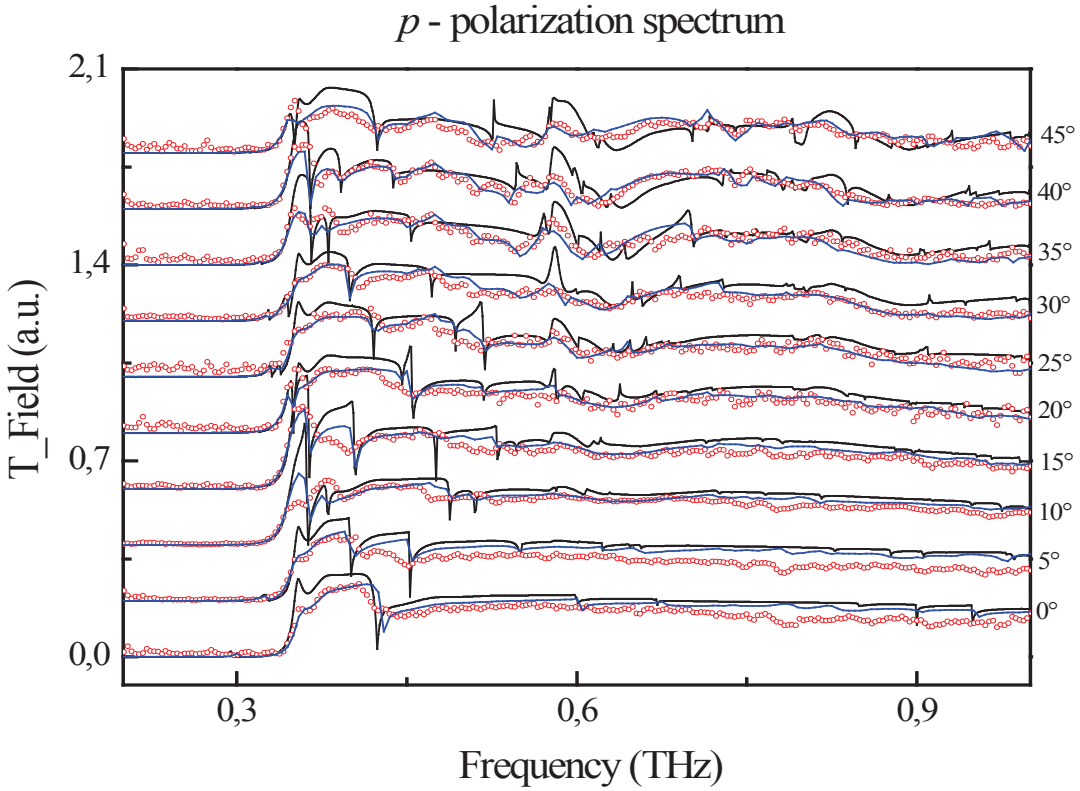

Fig. 5.14: p-polarization transmission spectra for different angles of incidence θ by step of Δθ=5°. Dots (in grey) are experimental data, Continues curves (in blue) are HFSS data, while continuous curves (in black) are calculated with the RME Method [32]. For sake of legibility, each curve is arbitrarily vertically shifted by 0.2.

Fig. 14 shows the frequency spectrum of the device transmission coefficient for the THz energy, recorded for different angles of incidence ranging from 0° to 45°. Here the plane of incidence is along the (1, 0) direction of the hole array, and the incident beam is *p*-polarized, *i.e.* the H-field is normal to the plane of incidence. We observe for each curve a threshold frequency (0.35 THz) below which no signal is transmitted. This corresponds to the cut-off

frequency of each hole which, owing to the sample thickness ($1.72\ \text{mm} \sim 2\times\lambda_{THz}$), can be considered as a circular waveguide ($f_{cutoff} = 1.841c/\pi\phi = 0.351$ THz). No direct coupling between evanescent waves at each side of the metal occurs, and thus no sub-cutoff frequency effect is observed. Above f_{cutoff}, different resonant features are seen, with a pronounced dispersion as the angle of incidence varies. The overall shape of each experimental curve is rather well described by the related modeling curves (continuous lines on Fig. 5.14), even if we do not use any adjustable parameter. Weak deviations between theory and experiment are seen at the sharper resonances. They could be attributed to the spectral resolution of our set up (16 GHz). Losses in metal or at the metal surface, even if their contribution to SP attenuation is still subject to controversy [36-38], may also broaden the resonances. The *s*-polarization spectra (Fig. 5.15) show an almost similar behavior, even if a few different resonance features appear.

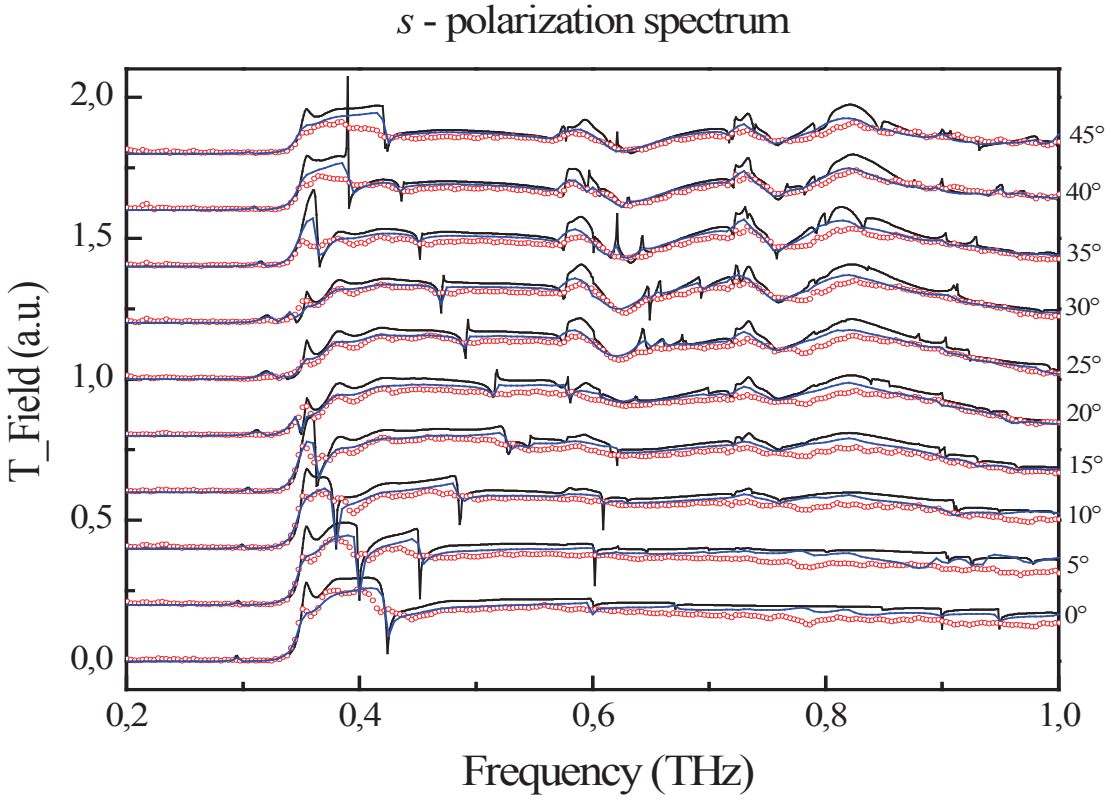

Fig. 5.15: S-polarization transmission spectra for different angles of incidence θ by step of Δθ=5°. Dots (in grey) are experimental data, Continues curves (in blue) are HFSS data, while continuous curves (in black) are calculated with the RME Method [32]. For sake of legibility, each curve is arbitrarily vertically shifted by 0.2.

As we mentioned earlier, there is an overall good agreement between the theory (solid lines)

and measurements (open circle), and for all the incident angles (Fig. 5.15).We observed that the black line (m-lines) are shifted with frequency based on variation in incidence.

III.7.3. Extraction of Woods anomaly and surface plasmons

Fig. 5.16 shows several dispersion curves (position of the Wood's anomalies in the θ-f plane) calculated using the relation (V-21). Each dispersion curve labeled by a capital letter is related to the (i,j) direction on the hole array and to the involved diffraction order m. Together, we plot the two main dips (not well pronounced) observed for each experimental transmission curve (s-polarization). They correspond to the excitation of a Wood anomaly for m=2 and (i,j)=(1,1) – curve B – for the second dips, and first to m=-2 and (i,j)=(1,1) – curve K – and then to m=-3 and (i,j)=(2,1) – curve I – for the first dips. A good agreement between theory and measured data (dips are not very clear) is observed, validating expression (V-21)

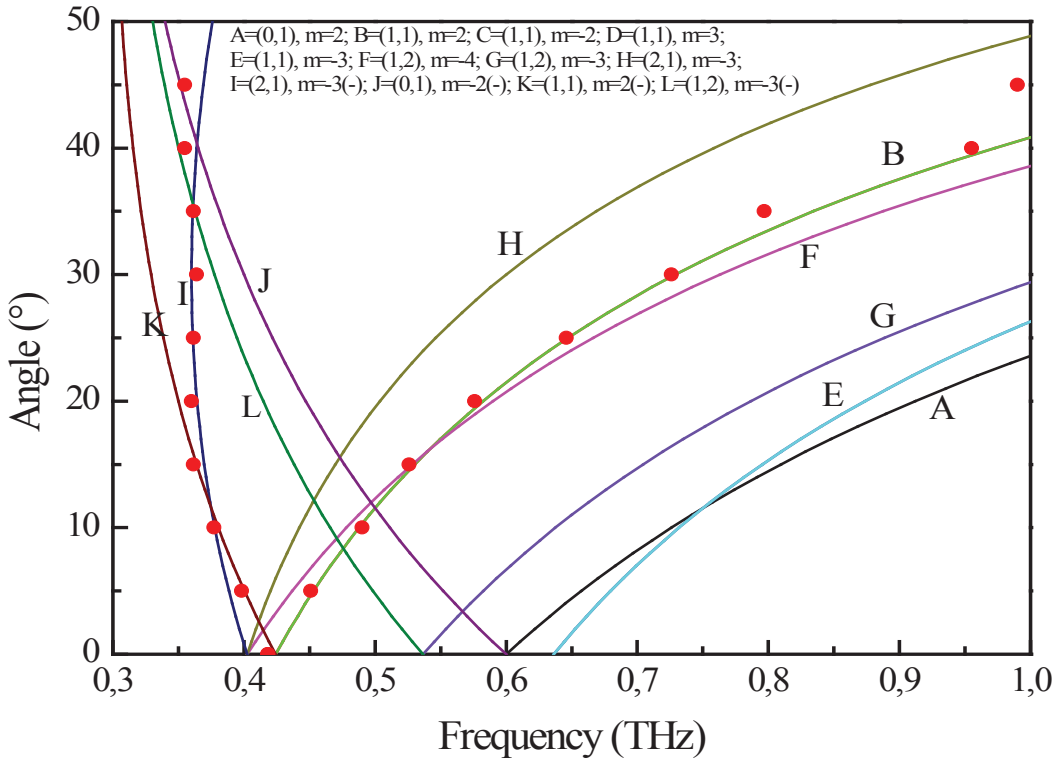

Fig. 5.16: Angle of incidence versus frequency for different directions (i,j) and diffracted orders m indicated as _m. Solid lines are calculated with (V-21), closed circles are measured data. 2 set of experimental data are plotted: the first set corresponds to (i,j)=(1,1) and m=2 – curve B –, and the second set to m=-2 and (i,j)=(1,1) – curve K – and then to m=-3 and (i,j)=(2,1) – curve I – .

When the incoming THz beam is p-polarized, both Wood's anomalies and propagating SP's

are excited under the same experimental conditions. On the other hand, if the THz beam is *s*-polarized, SP's are not excited. Thus the difference of the *p*-polarized and *s*-polarized spectra should exhibit features corresponding to only the excitation of SP's. Precisely, we expect to observe m-lines in the difference spectra, related to a lack of energy due to SP excitation. In Fig. 5.17, we plot the difference of the transmission modulus (*p*-polarization minus *s*-polarization) versus frequency for different angles of incidence. The continuous lines are calculated (HFSS and REM) while the open circles are measured data.

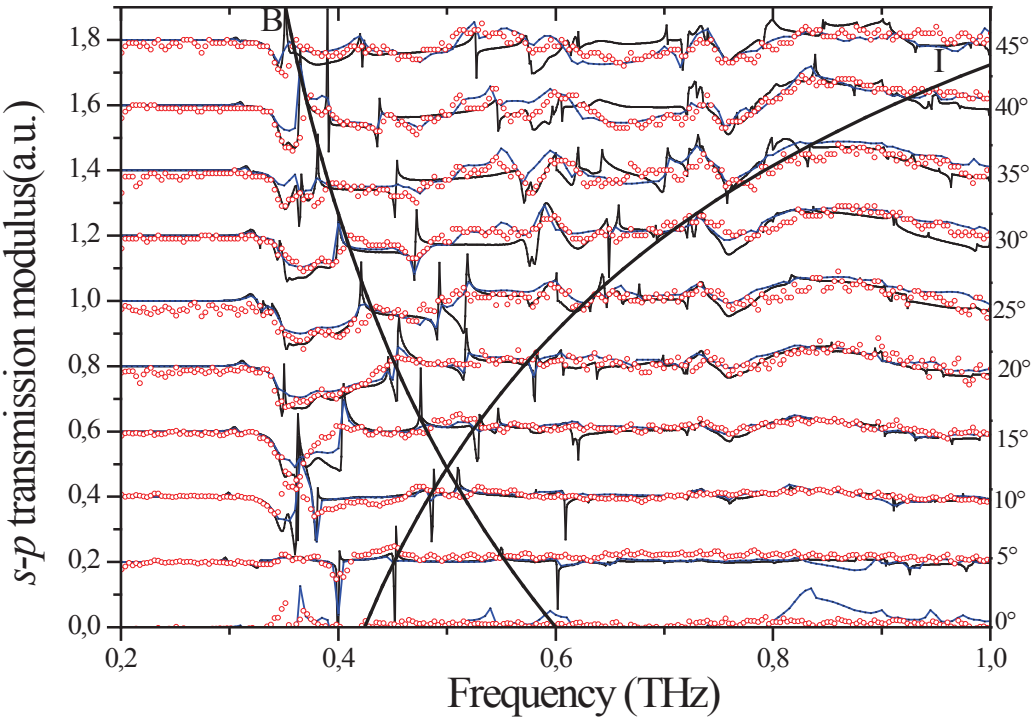

Fig. 5.17: Difference of p-polarization transmission and s-polarization transmission spectra for different angles of incidence θ by step of Δθ=5° (see Fig. 5.14). Circles are experimental data, Continues curves (in green) are HFSS data (in blue), while continuous curves are calculated with the RME Method [32]. For sake of legibility, each curve is arbitrarily vertically shifted by 0.4. To enlighten the SP dispersion effect, curves I ((i,j)=(0,1), m=-2) and B ((i,j)=(1,1), m=2) are plotted using relation (V-21) (each curve is shifted vertically by 0.2)

Let us examine the calculated curves. As compared to the transmission curves (Fig. 5.14b), some dips are located at the same frequencies (for example those along the line labeled B ((*i*,*j*)=(1,1), *m*=2)), but also many dips are missing, which are the ones only related to a Wood's anomaly, which occurs in both *s* and *p* polarization cases. On the contrary, the effect

of an efficient SP excitation is enlightened in the difference spectra. This is the case for the SP line labeled I ((*i*,*j*)=(0,1), *m*=-2), which was too weak to be clearly distinguish in the *p*-transmission curve (Fig. 5.14a). Let us notice that the continuous dispersion lines I and B in Fig. 5.17 are calculated with relation (V-21). Both erasing and enlightening effects are more clearly seen in Fig. 5.18.

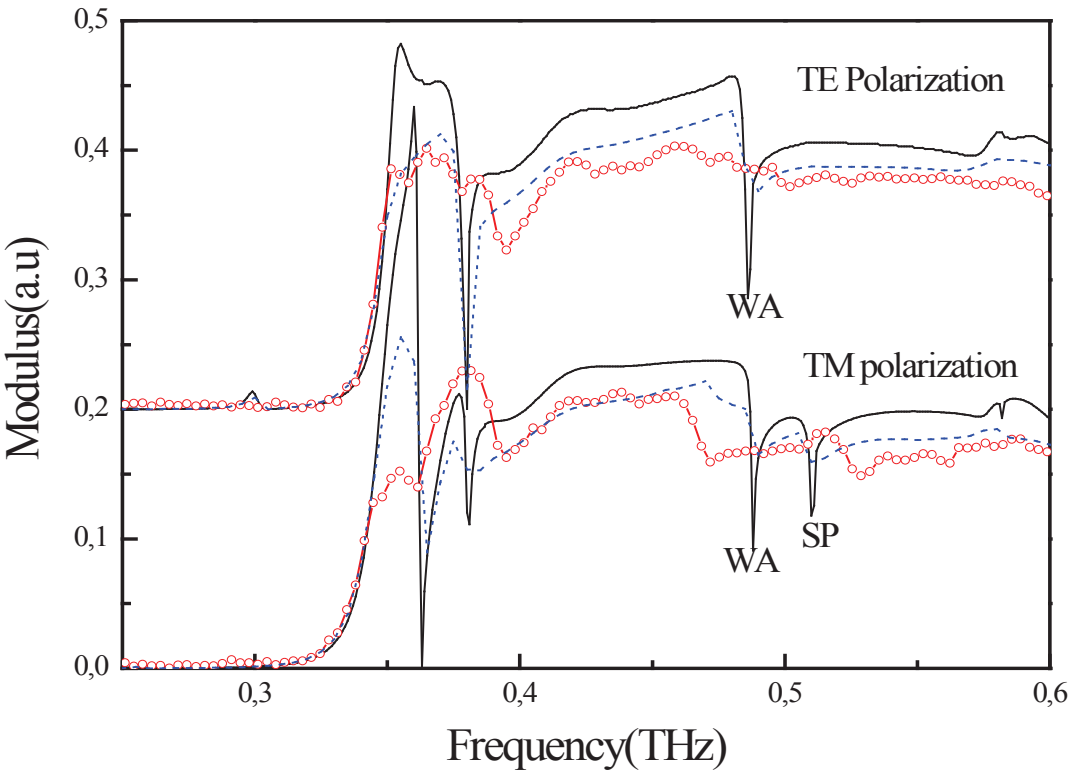

Fig. 5.18: p- and s-polarization transmission spectra for θ = 10°.

We draw both *p*- and *s*-transmissions spectra in the range 0.2-0.6 THz for θ=10°. The *p*-transmission plot shows no signal under the hole cut-off frequency (0.35 THz), then it roughly increases monotonously up to 25 % and remains more or less constant around 20 % for high frequencies. A pronounced dip is seen at 0.382 THz, and other ones at 0.49 THz and at 0.515 THz. The *s*-curve shows a similar behavior, but the transmission is much larger just above the cutoff frequency, i.e. around 0.36 THz, and the dip at 0.515 THz is not observed. So, the dip at 0.515 THz corresponds to the excitation of a SP. But unfortunately, due to ohmic losses, surface roughness of the metal and limit in frequency resolution (Δf = 16 GHz) of the experiment, we do not observed the m-lines (narrow dips) in experimental results. As we see in Fig. 5.18, the width of the each dip in RME data is about 2-3 GHz, and this is very small

compared to the experimental resolution.

III.8. Characterization of high pass filters

In this section, we present the THz characterization of a metallic mesh which is deposited on cyclic olefin copolymer (COC) films. COC [41] is a promising dielectric material with unique properties, such as low water absorption, low permittivity, flexibility, high chemical resistance, good metal adhesion, and high transparency in the visible, UV, and THz region (0.1–10 THz) [42-43]. More generally spreading, polymers are very attractive material for THz applications. Since a few years, polypropylene (PP) and benzocyclobutene (BCB) have been used in free-space THz devices [44-47] because of their low absorption coefficient in the THz region (α =2 cm^{-1} and 2.3 cm^{-1}, respectively, at 1 THz) [48-49]. But they also exhibit a few drawbacks like the lack of desired thickness of PP film and the drastic change in electrical properties of BCB during the process. COC seems to be a good candidate to replace PP and BCB. COC films can be obtained by spin coating of an appropriate commercial resin to achieve the desired thickness, while requiring a soft-bake at 140 °C for a few minutes [50]. Moreover, their absorption coefficient (α =2 cm^{-1} at 1 THz) is very close to the value of PP and BCB films.

The THz transmission measurements of the filters have been performed by classical THz-TDS using a setup shown in Fig. 5.7 and the details of its operation is discussed in section II.3. Here, our goal is to achieve higher THz transmission though the mesh filters by varying the parameters such as width (*w*) and period (*d*) for the application of high frequency pass filters. So, in our present study, we have used single layer and multi-layer filters with different parameters like width and period. We have measured the transmission spectra at normal incident. The experimental results together with the simulation results obtained with the Microwave CST Studio software are presented in our published article "*Broadband ultra-low-loss mesh filters on flexible cyclic olefin copolymer films for terahertz applications,* Appl. Phys. Lett. 102, 111114 (2013)," attached at the end of this manuscript.

A good agreement between simulation and measurements is observed for all devices. High values of transmittance, higher than the 76% is achieved between 1.5 and 2.5 THz with f_{-3dB} at 1.02 THz for single layer of *w*=0.5 µm. For single layer with *w*=2 µm, the transmittance at 1.5 THz is about 58%, which means that the width of the filter playing role in order to increase the transmittance. A rejection ration of 13 dB/decades is achieved for the frequency 0.25-2.5 THz. For double and triple layers, rejection ratio respectively is about 15 and 17 dB/decades for 0.25-2.5 THz.

III.9. Conclusion

In conclusion, we used 2D grating i.e. periodic holes array in metallic slab to study its electromagnetic response in the THz frequency region. We used three different methods for this study: RME, HFSS and THz-TDS. In this study, we have clearly assigned different resonant features in the transmission of a metallic hole array either to the excitation of a SP, or to the propagation in the surrounding medium (here air) of a new order of diffraction (Wood-Rayleigh anomaly). Unfortunately, certainly because of the ohmic losses and roughness scattering in the metal foil and also due to frequency resolution limit in experiment, surface plasmons were not definitively observed in THz-TDS experimental results. The application of the present device could be the spectroscopy of small amount of matter, taking benefit of the high sensitivity to any perturbation of the electromagnetic resonances of such devices. Finally, THz transmission measurement of metallic meshes deposited over cyclic olen copolymer films are studied with THz-TDS and compared with simulation result obtained with CST Studio. The analysis shows that COC is a promising candidate for the next generation of free-space devices for THz applications due to its particularly suitable dielectric properties at these frequencies. These features allow for the fabrication of robust, highly transparent broadband filters that can be integrated together with incoherent detection systems.

REFERENCE

[1] Jones, T. J. Rainsford, B. Fischer and D. Abbott, "*Towards T-ray spectroscopy of retinal isomers: A review of methods and modeling*", Vibrational Spectroscopy, **41**, 144 (2006).

[2] Y. S. Lee, "*Principles of Terahertz Science and Technology*" Springer Science Business Media, LLC, New-York (2009).

[3] M. Koeberga. et al, "*THz dielectric relaxation of ionic liquid:water mixtures,"* Chemical Physics Letters, **439**, 60 (2007).

[4] M. Nazarov. et al, "*Surface Plasmon THz waves in gratings,"* C.R. Physiques, Special Issue on Terahertz Optoelectronics, **9**, 232 (2008).

[5] D. F. Plusquellic, K. Siegrist, E. J. Heilweil, and O. Esenturk "*Applications of Terahertz Spectroscopy in Biosystems*" Chem. Phys. Chem., **8**, 2412 (2007).

[6] T. Kobayashi. et al, "*Phonon-polariton Based THz Spectroscopy,"* Ultrafast Phenomena XIV, Proceedings of the 14th International Conference, **79**, 254 (2005).

[7] K. Kawase, Y. Ogawa and Y. Watanabe, "*Non-destructive terahertz imaging of illicit drugs using spectral fingerprints,"* Optics Express, **11**, 20 (2003).

[8] B. L. Yu. et al, "*Direct observation of coherent rotational excitation, dephasing and depopulation of methanol and its isotopes using THz pulse radiation,"* Appl. Phys. Lett., **86**, 101108 (2005).

[9] D. Bigourd. et al, *"Multiple component analysis of cigarette smoke using THz spectroscopy, comparison with standard chemical analytical methods,"* Appl. Phys. B, **86**, 579 (2006) .

[10] Y. Ung, B. M. Fischer, H. Ng and D. Abbott, "*Towards Quality Control of Food Using Terahertz"* Proc. of SPIE 6799 (2007).

[11] M-C. Kemp et al, "*Security applications of terahertz technology,"* Proc. SPIE : Terahertz for Military and Security Applications I, **5070**, 44 (2003).

[12] W-L. Chan, J. Deibel and D. M. Mittleman. "*Imaging with terahertz radiation,"* Reports on Progress in Physics, **70**, 1325 (2007).

[13] R. Piesiewicz et al, "*Performance Analysis of Future Multigigabit Wireless Communication Systems at THz Frequencies With Highly Directive Antennas in Realistic*

Indoor Environment," IEEE Journal of Selected Topics in Quantum Electronics, **14**, 421 (2008).

[14] D. Grischkowsky, S. Keiding, M. van Exter, and Ch. Fattinger, "*Farinfrared time-domain spectroscopy with terahertz beams of dielectrics and semiconductors,"* J. Opt. Soc. Amer. B, **7**, 2006 (1990).

[15] M. van Exter, and D. Grischkowsky, "*Optical and electronic properties of doped silicon from 0.1 to 2 THz*," Appl. Phys. Lett., **56**, 1694 (1990).

[15a] J. E. Pedersen and S. R. Keiding, "*THz time-domain spectroscopy of nonpolar liquids,*" IEEE JQE., **28**, 2518 (1992).

[15b] J. F. Whitaker, F. Gao, and Y. Liu, "Terahertz-bandwidth pulses for coherent time-domain spectroscopy," in SPIE, **2145**, 168 (1994).

[15c] D. M. Mittleman, R. H. Jacobsen, and M. C. Nuss, "*T-ray imaging,*" IEEE Journal of Selected Topics in Quantum Electronics, **2**, 679 (1996).

[15d] B. B. Hu and M. C. Nuss, "*Imaging with terahertz waves,*" Opt. Lett., **20**, 1716 (1995).

[15e] D. M. Mittleman *et al*, ''*T-ray tomography*,'' Opt. Lett. **22**, 904 (1997).

[15f] D. M. Mittleman, M. Gupta, R. Neelamani, R. G. Baraniuk, J. V. Rudd, and M. Koch, "*Recent advances in terahertz imaging,"* Appl. Phys. B, **68**, 1085 (1999).

[15g] M. Mittleman, R. H. Jacobsen, R. Neelamani, R. G. Baraniuk, and M. C. Nuss, "*Gas sensing using terahertz time domain spectroscopy,*" Appl. Phys. B, **67**, 379 (1998).

[16] F. Garet, Thèse de doctorat *"Génération optoélectronique d'impulsions électromagnétiques ultra-courtes ; application à la spectroscopie THz," Grenoble INP (*1997).

[17] L.Duvillaret, F. Garet et J-L.Coutaz. "*Influence of noise on the characterization of materials by terahertz time-domain spectroscopy".* 3, JOSA B, **17**, 452(2000).

[18] J. F. Whitaker. "*Optoelectronic applications of LTMBE III-V materials,"* Mat. Sci . and Eng. B, **22**, 61 (1993).

[19] D. H, Auston, K. P. Cheng and P. R. Smith**,** *"Picosecond photoconducting hertzian dipoles,"* Applied Physics Letters, **45***,* 284 (1984).

[20] H, Eusèbe**.** doctoral thesis, INP-Grenoble "*Theoretical and experimental study of terahertz generation by photo switching components in low temperature GaAs,"* (2004).

[21] J. C. Maxwell. "*A treatise on electricity and magnetism"*. London : Oxford- at the clarendon press, **1** (1873).

[22] T. W. Ebbesen, H. J. Lezec, H. F. Ghaemi, T. Thio, and P. A. Wolff, *"Extraordinary optical transmission through sub-wavelength hole arrays,"* Nature, **301**, 667 (1997).

[23] H. F. Ghaemi, Tineke Thio, D. E. Grupp, T. W. Ebbesen and H. J. Lezec, *"Surface plasmons enhance optical transmission through subwavelength holes,"* Phys. Rev. B, **58**, 6779 (1998).

[24] L. Salomon, F. Grillot, A. V. Zayats, and F. Fronel, *"Near-field distribution of optical transmission of periodic subwavelength holes in a metal film,"* Phys. Rev. Lett., **86**, 1110 (2001).

[25] R. Ulrich, in *Optical and Acoustical Micro-Electronics*, Ed. J. Fox, Polytechnic Press, New York , 359 (1974)

[26] F. Miyamaru *et al,* Appl. Phys. Lett., **82**, 2568 (2003).

[27] H. Cao and A. Nahata, Opt. Express, **12**, 1004 (2004).

[28] M. Hangyo, M. Tani and T. Nagashima, Int. J. Infrared Millimeter Waves, **26**, 1661 (2005).

[29] F. Miyamaru and M. Hangyo, Appl. Phys. Lett., **84**, 2742 (2004).

[30] C. Winnewisser, F. Lewen, J. Weinzierl, and H. Helm, Appl. Opt., **38**, 3961 (1999).

[31] F. Miyamaru, S. Hayashi, C. Otani, K. Kawase, Y. Ogawa, H. Yoshida, and E. Kato, Opt. Lett., **31**, 1118 (2006).

[32] L. C. Botten, R. C. McPhedran, and G. H. Derrick, in *Electromagnetic Theory of Gratings*, Ed. R. Petit, Springer, Berlin, pp. 227-279 (1980).

[33] M. A. Ordal *et al*., Appl. Opt., **22**, 1099 (1983); *idem*, Appl. Opt., **26,** 744 (1987).

[34] F. Garet, L. Duvillaret and J.-L. Coutaz, IRMMW 2004, Karlsruhe (Germany), 27 Sept.-1 Oct. (2004).

[35] F. Aquistapace, L. Duvillaret, F. Garet, J. F. Roux, and J. -L. Coutaz, J. Appl. Phys., **94**, 7888 (2003).

[36] L. S. Mukina, M. M. Nazarov, A. P. Shkurinov. Surf. Sci., **600**, 4771 (2006).

[37] M. Nazarov, F. Garet, D. Armand, A. Shkurinov, and J.-L. Coutaz, C. R. Physique **9**, 32 (2008).

[38] M. Gong, Tae-In Jeon, and D. Grischkowsky, Optics Express, **17**, 17088 (2009).

[39] Mathew N. O. Sadiku, "*Elements of Electromagnetics*", Edition 4, Oxford University Press, (2010).

[40] D. C. Cook, *"Molecular epitaxy grown GaAs at low temperatures,"* Thin Solid Films, **231**, 61(1993).

[41] Synthesized by Topas Advanced Polymer GmbH under the trade name of Topas TM.

[42] K. Nielsen, H. K. Rasmussen, A. J. Adam, P. C. Planken, O. Bang, and P. U. Jepsen, Opt. Express, **17**, 8592 (2009).

[43] P. D. Cunningham, N. N. Valdes, F. A. Vallejo, L. M. Hayden, B. Polishak, X.-H. Zhou, J. Luo, A. K.-Y. Jen, J. C. Williams, and R. J. Twieg, J. Appl. Phys., **109**, 043505 (2011).

[44] M. Navarro, S. A. Kuznetsov, M. Aznabet, M. Beruete, F. Falcone, and M. S. Ayza, IEEE J. Quantum Electron., **47**, 375 (2011).

[45] C. Croenne, F. Garet, E. Lheurette, J.-L. Coutaz, and D. Lippens, Appl. Phys. Lett., **94**, 133112 (2009).

[46] P. Weis, O. Paul, C. Imhof, R. Beigang, and M. Rahm, Appl. Phys. Lett., **95**, 171104 (2009).

[47] C. Jansen, S. Wietzke, V. Astley, D. M. Mittleman, and M. Koch, Appl.Phys. Lett., **96**, 111108 (2010).

[48] Y.-S. Jin, G.-J. Kim, and S.-G. Jeon, J. Korean Phys. Soc., **49**, 513 (2006).

[49] E. Perret, N. Zerounian, S. David, and F. Aniel, Microelectron. Eng., **85**, 2276 (2008).

[50] E. Peytavit, C. Donche, S. Lepilliet, G. Ducournau, and J.-F. Lampin, Electron. Lett., **47**, 453 (2011).

1V. Characterization of InAs/InP: Fe multilayer QD's samples

1V.1. Introduction

The study of semiconductor quantum-dot (QD) nanostructures has attracted considerable interest in the last few decades. These nanostructures confine carriers in all three dimensions. As a consequence of this, QD's exhibit several important characteristics: atom-like density of states, large exciton binding energies, and enhanced oscillator strengths. Due to these unique properties, self assembled QD's offer lots of possibilities for new applications, e.g. in optoelectronic devices such as lasers [1,2,3], detector [13,14], amplifiers [15], high frequency optical devices [4,16,17], and single photon devices [5,6,18] as well as in electronics such as field effect transistors [7-9] or memory devices [8,10-12].

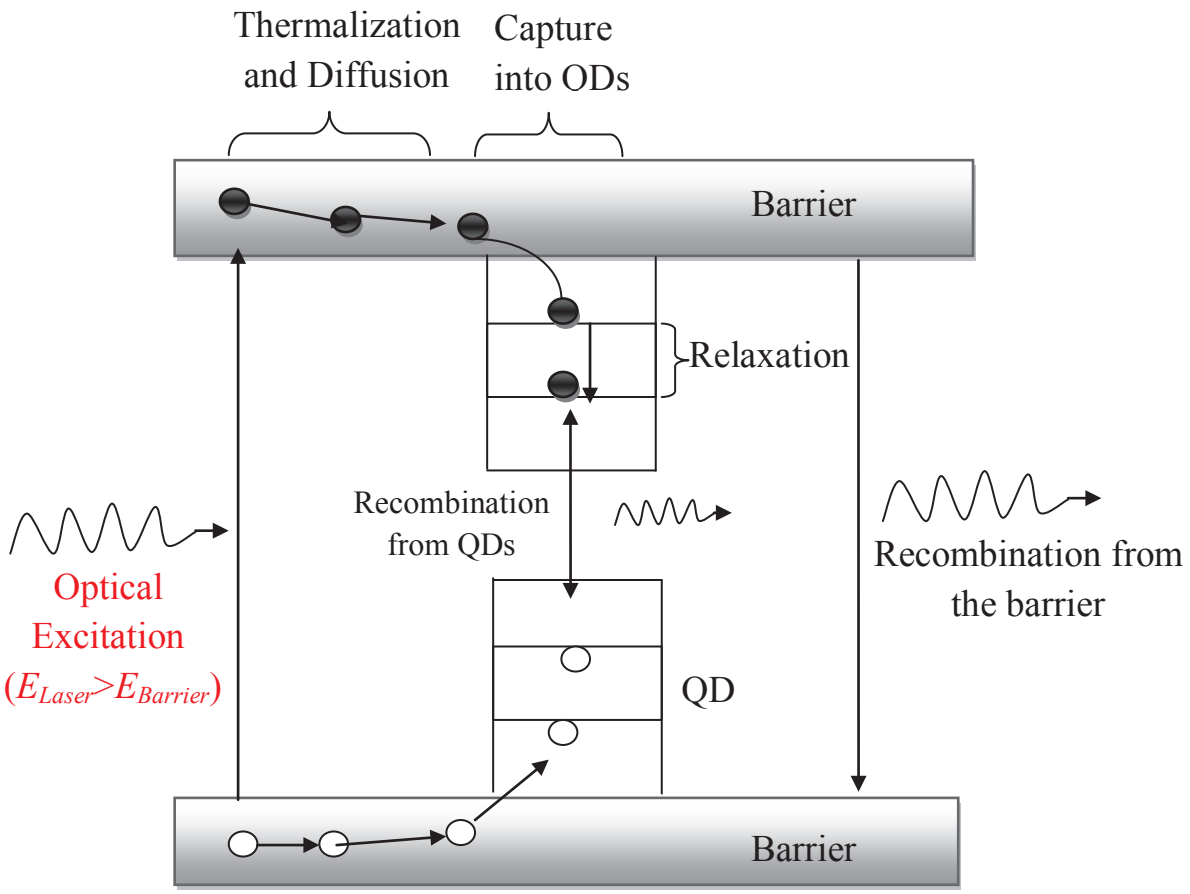

Fig. 5.19: Overview of the carrier capture and relaxation dynamics into a QD (if E_{Laser}>$E_{Barrier}$).

In this part of thesis, the carrier dynamics in QD's are studied using different ultrafast techniques CW photoluminescence (PL), optical pump-THz spectroscopy and THz excitation spectroscopy. In all these cases, the optical excitation energy is well above the QD energy levels within the InP:Fe layer continuum. Thus, the carrier dynamics from the initial excitation position and energy level within the barrier towards the QD ground state can be subdivided into five major steps mentioned below, which are schematically shown in Fig. 5.19.

- Carrier cooling and relaxation within the barrier layer.
- Carrier diffusion in the barrier towards the QD's.
- Carrier capture from the barrier continuum into the QD's.
- Carrier relaxation between the discrete energy levels within the QD's.
- Radiative and non-radiative recombination in the QD's.

1V.2. Details of InAs/InP:Fe quantum dots samples

In this study, we used five InAs/InP:Fe QD's thin film samples with different numbers of QD's layers. These films were grown by molecular beam epitaxy on iron doped InP (100) substrates (InP:Fe). Iron is employed to compensate the semiconductor, thus InP:Fe is highly resistive. For all these samples, a 100-nm InP buffer layer was grown on the substrate and then followed by a 100-nm $In_{0.528}Al_{0.238}Ga_{0.234}$ As layer. This was followed by 10, 20, 30, 40, 50 QD's layers respectively for B-0792, B-0846, B-0847, B-0850, B-0851 samples and each QD's layer was separated by a 10-nm $In_{0.528}Al_{0.238}Ga_{0.234}$ As barrier layer (Fig. 5.20). To avoid the strain effect in QD's layers, the height of QD's layers was reduced when the number of layers increases, in such a way all five QD's samples were designed with different QD's layer thicknesses: it means that a n QD's layer sample does not show a total QD's thickness n-times bigger than a single QD's layer. The thickness of each QD's layer is 5 mono layers (MLs) for B-0792, 4.5 MLs for B-0846, B-0847 samples and 4.2 MLs for B-0846, B-0847 samples as shown in Table 5.2.

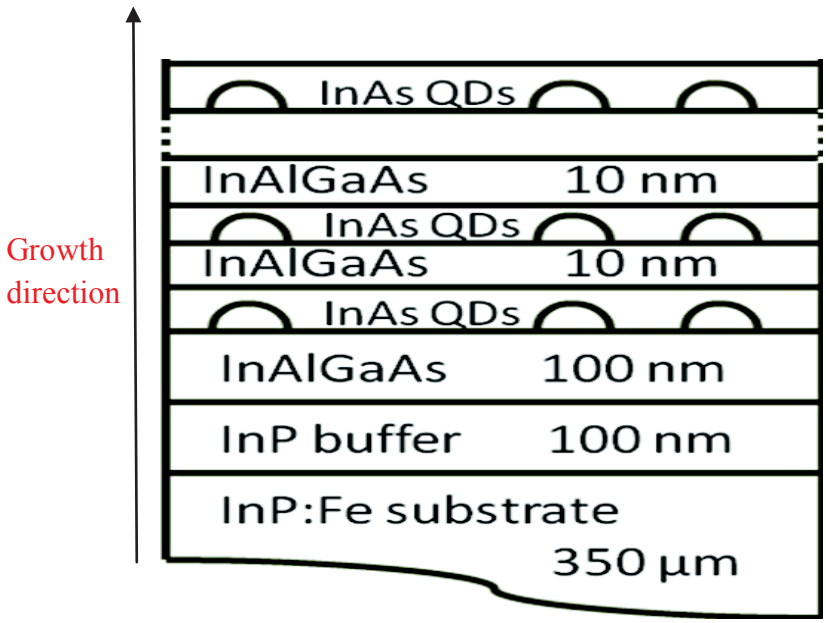

Fig. 5.20: QD's *layers growth process*

Device	Material	Nb. of Layers	Thickness
Substrate	InP:Fe	-	350 µm
B-0792	InAs	10	10×5.0 Monolayer's
B-0846	InAs	20	20×4.5 Monolayer's
B-0847	InAs	30	30×4.5 Monolayer's
B-0850	InAs	40	40×4.2 Monolayer's
B-0851	InAs	50	50×4.2 Monolayer's

Table 5.2: Details of different InAs QD samples. All samples have a 200 nm thick InAlGaAs buffer layer grown at 580 °C.

1V.2.1. Energy gap in semiconductor materials

At room temperature, the bandgap energies for different semiconductor materials used in our present devices are:

- InP – 1.344 eV (922 nm);
- $In_{0.528}Al_{0.238}Ga_{0.234}As$ – 1.088 eV (1139 nm);
- InAs QD's – 0.792 eV (1565 nm).

1V.3. Experimental Techniques to study carrier dynamics in InAs/InP:Fe multilayer QD's Samples

The carrier dynamics in semiconductor quantum dots are a key issue in understanding their behavior. Normally, the carrier dynamics are influenced by both the scattering between the photo-generated carriers and the available phonon modes within the semiconductor crystal, as well as by the scattering between photo-generated carriers among themselves such as electron-electron, electron-hole scattering and Auger scattering. In addition, the carrier dynamics are also influenced by the carrier trapping at free surfaces, interfaces and the defects present within the semiconductor material. To study the carrier dynamics in our present InAs QD's semiconductor material, three different experimental techniques are performed, namely photoluminescence spectroscopy, optical pump-THz probe spectroscopy and THz excitation spectroscopy. The details of all these experimental results are presented in the following sections.

1V.3.1. Photoluminescence (PL) Spectroscopy

PL spectroscopy is an important technique widely employed to reveal band structure and luminescence mechanism of self-assembled QD's. In optically illuminated QD's, there are three dynamic processes as shown in Fig. 5.19. First, electron-hole pairs are created by absorption of exciting radiation. Then, at thermal equilibrium, electrons and holes relax to the bottom of conduction band and the top of valence band respectively. Finally, photons are created by radiative recombination of electron-hole pairs. The intensity of light emitted from the QD's is measured as a function of wavelength or photon energy.

In our present photoluminescence experiment, samples are excited by a Nd-YAG laser doubled in frequency (wavelength 532 nm). The laser beam of 193 mW is focused on the centre of the sample (spot diameter~0.1 mm). A low noise detector is used to measure the fluorescent signal and the whole measurement was done at room temperature. Figs. 5.21a (vs energy) and 21b (vs wavelength) show the room-temperature PL spectra for all five QD's samples and the InP:Fe substrate alone. The peak around 0.8 eV (1.55 μm) in the QD's sample spectra corresponds to the inter-band recombination in the QD's. We observe a shift in the PL emission peak energy for samples with higher number of QD's layers (with reference to the 10 layers sample): this is due to a quantum size effect (energy gap in QD's increases when its size decreases) within the QD [19, 20]. The peak shape is almost similar for all the

samples as shown in Fig. 5.22 where we plot the normalized PL intensity. The 10-layers sample shows a slightly shifted spectrum. The inter-band recombination spectrum of the substrate appears as expected around 1.35 eV (~0.9 μm) due to its energy gap.

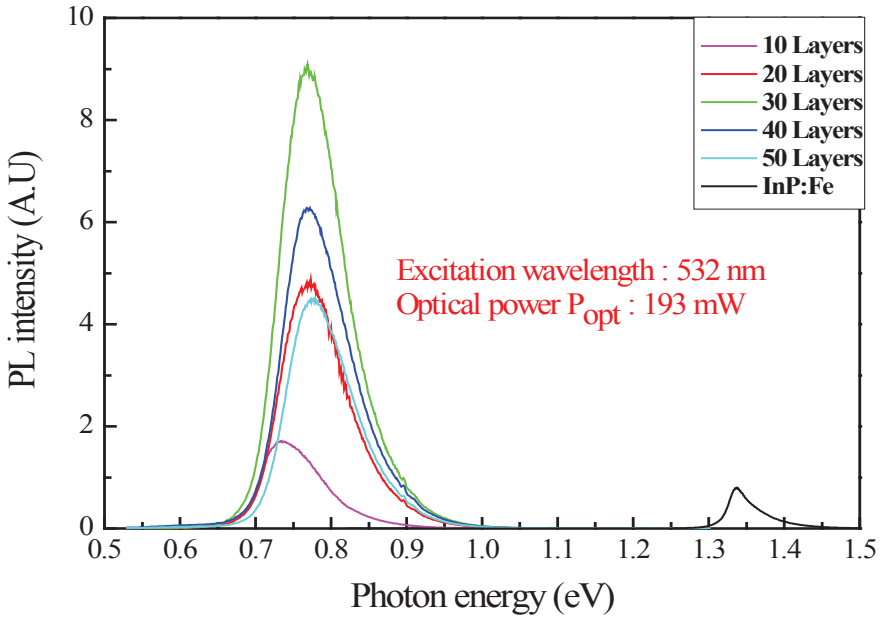

Fig. 5.21a: PL intensity spectra vs energy. The pump power is 193 mW.

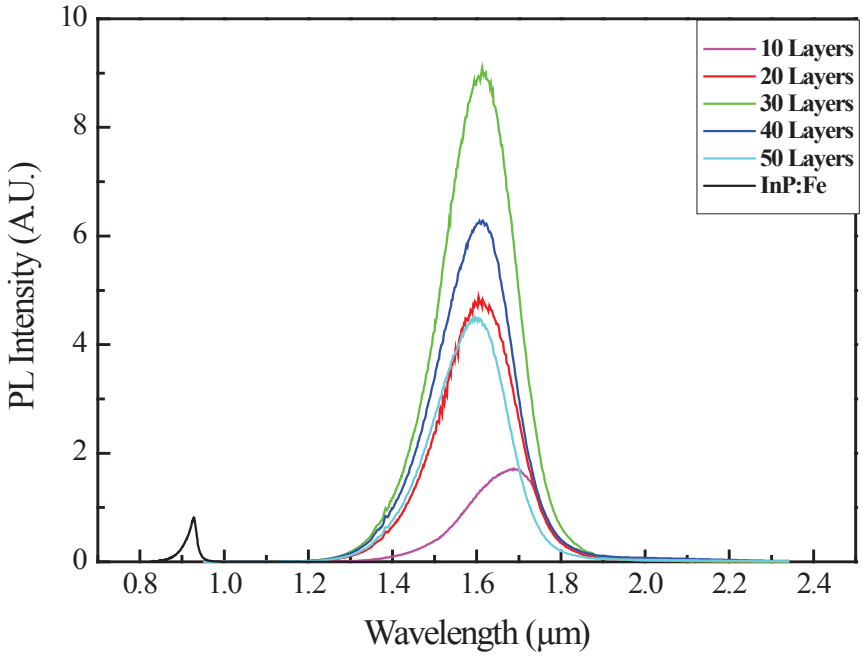

Fig. 5.21b: PL intensity spectra vs wavelength. The pump power is 193 mW.

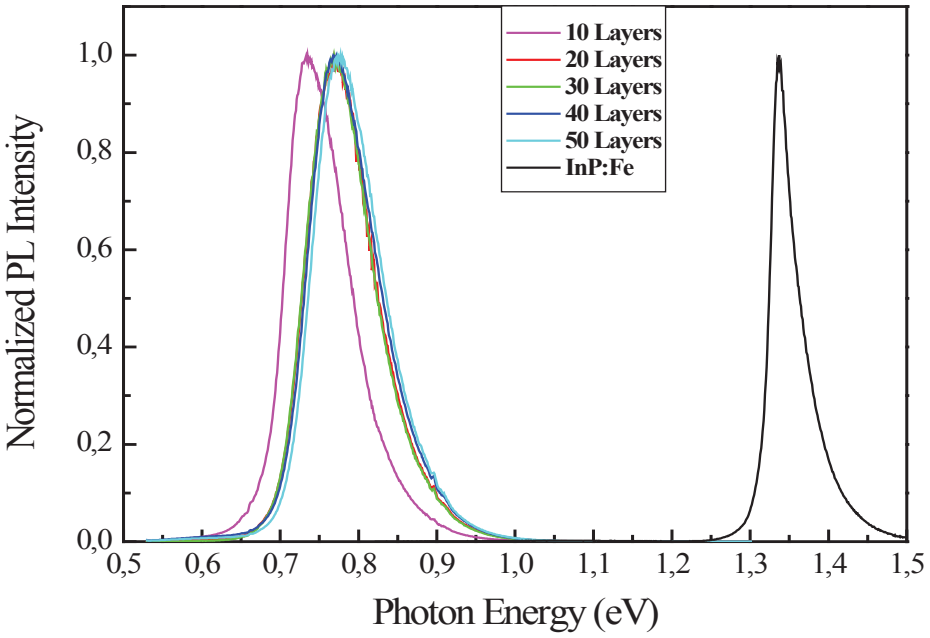

Fig. 5.22: Normalized PL intensity spectra.

PL intensities for B-0792, B-0846 and B-0850 samples increase linearly with the number of QD's layers (total thickness of QD's) as shown in Fig. 5.23, but it decreases for B-0847 and B-0851 samples. This could be attributed to a bad laser focusing on these last QD's samples.

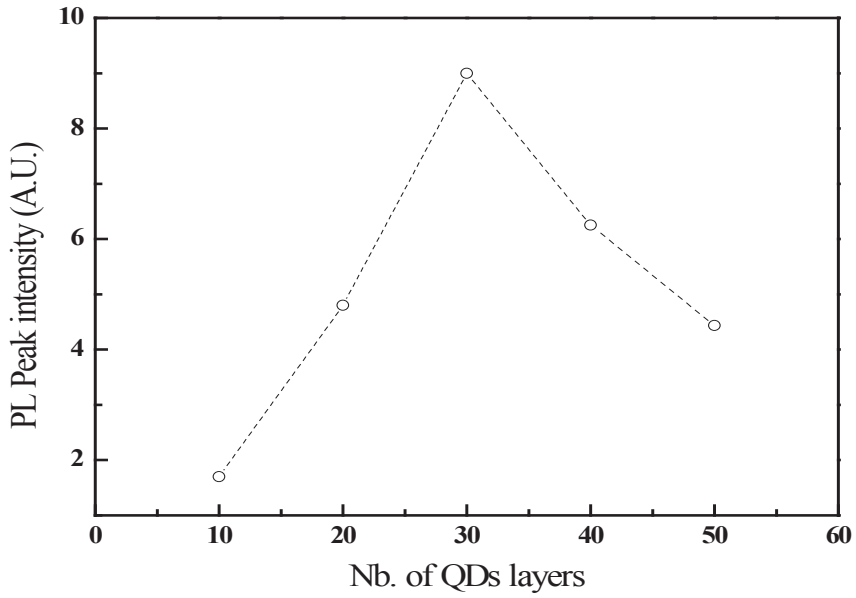

Fig. 5.23: PL peak intensity versus QD's total thickness. The pump power is 193 mW.

1V.3.2. Optical Pump -THz Probe Spectroscopy

1V.3.2.1. Optical pump-THz probe experimental setup

THz waves are strongly damped by free carriers in a material. Therefore, performing optical pump and THz probe experiment leads to a good determination of the photo-generated free carrier dynamics in the material without artefacts resulting from band to band excitation. The optical pump-THz probe experimental setup shown in Fig.5.24 is used to study the carrier dynamics in a InAs/InP:Fe QD's samples. This experimental setup is driven by fs laser pulses from a Ti: Sa oscillator (wavelength 800 nm, pulse duration 150 fs and repetition rate 76 MHz). One part of the optical beam is used for generation of THz probe pulse by photoconductive switching in LTG-GaAs switch. This THz pulse is guided by reflective optics through the sample and into the THz detector unit, where its temporal shape is detected and measured by photoconductive sampling in another LTG-GaAs switch. A second portion of the optical beam illuminates the THz detector (LTG-GaAs switch). A third portion of the optical beam is focused and overlapped with THz probe beam in the sample and a time delay is introduced between the optical pulse and the THz probe pulse. The diameter of the optical beam which is focused on the sample is limited by using a 2.29-mm diameter pinhole. To study the conductivity dynamics in the QD's samples, the amplitude of the THz transient at its maximum was measured as a function of the time delay between optical pulse and THz probe pulse. All measurements were performed at room temperature.

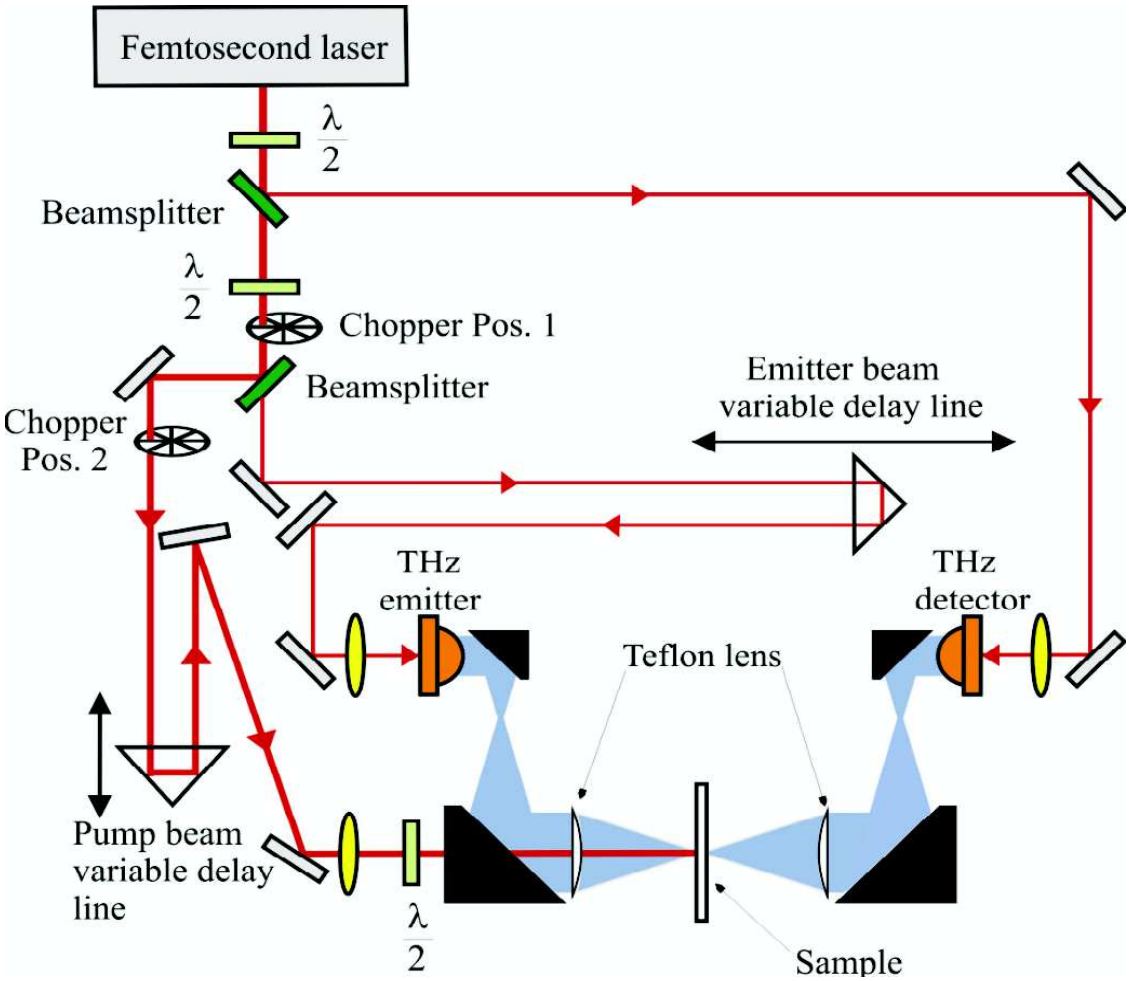

Fig. 5.24: Optical pump-THz probe experimental set up at 0.8 µm.

1V.3.2.2. Experimental Results

In this section, we present optical pump-THz probe experimental results obtained for all QD's samples. Here, the excitation laser wavelength (800 nm) corresponds to a 1.55-eV energy, which is higher than the bandgap of InAs; therefore all the carriers are excited over the barrier energy level (see Fig. 5.25). These excited carriers are thermalized in the barrier and afterward they are subject to either trapping into the QD's, recombination at the surface or band-to-band recombination.

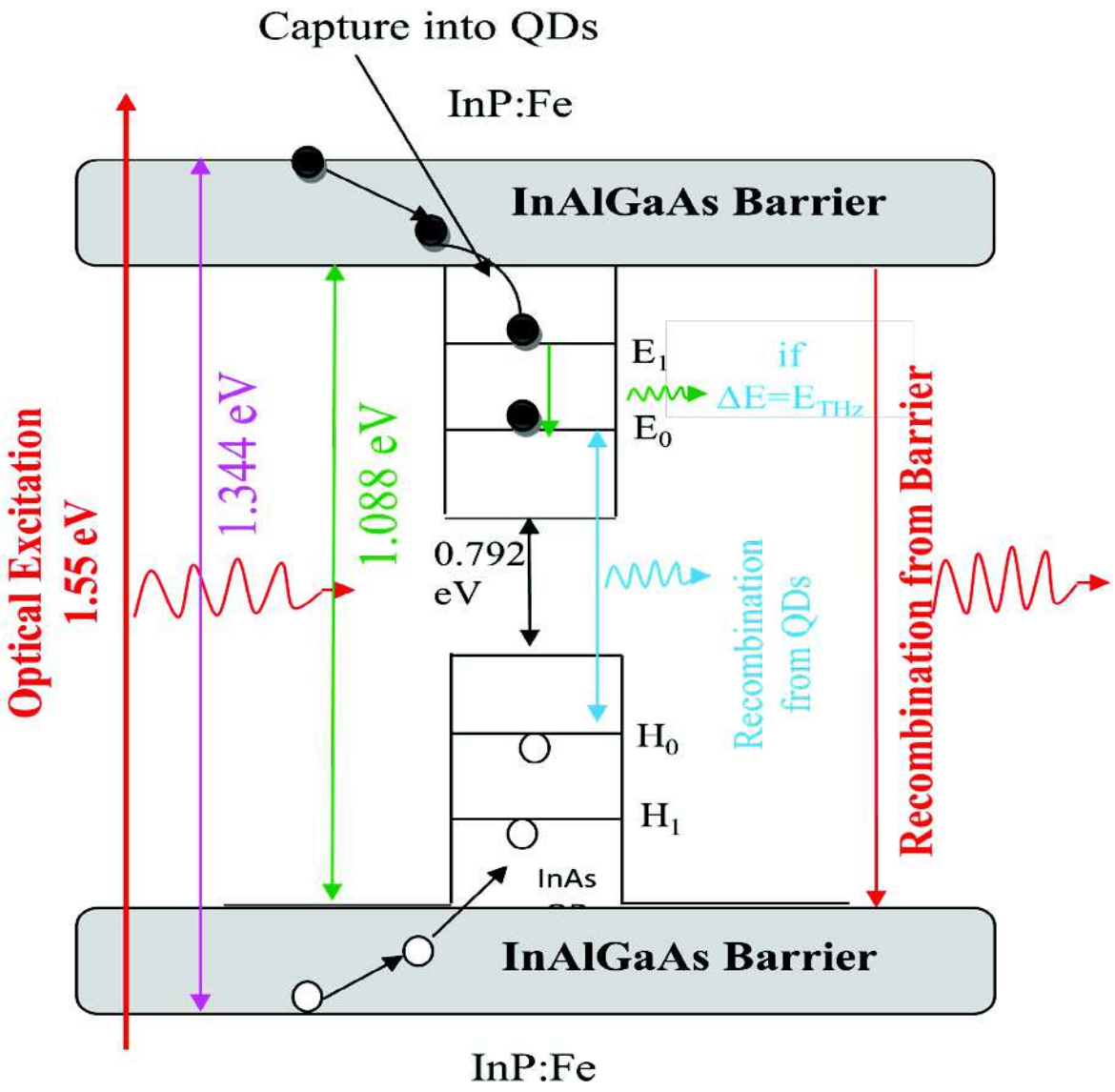

Fig: 5.25. Band diagram and electrons transition mechanism in InAs QD's.

The recorded temporal waveforms for substrate alone and for all QD's samples are presented in Fig. 5.26. We show two scan results for each sample: one is obtained when the sample was illumined by both optical pump and THz probe beams (grey line) and the other is obtained when the THz probe beam was absent (blue line), i.e. it is the THz signal generated by optical excitation of the samples.

For InP:Fe substrate, when the substrate is illuminated by the optical pump, carriers are photogenerated. These carriers are accelerated perpendicularly to the substrate by the intrinsic surface field due to the bending of the energy band at the surface or/and through the Dember effect. This leads to the radiation of a THz signal. When only the pump beam impinges on the

substrate, the measured variation of the THz signal corresponds exactly to the signal generated by photoexcitation (blue curves in Fig. 5.26a). When the sample is illuminated by both optical and THz beams, the photogenerated carriers generate the THz surface signal, but in addition these carriers absorb the impinging THz signal. The detected variation of the THz signal (grey curves) is thus the sum of the surface signal and of the transmission variation of the impinging signal. To better evaluate the carrier dynamics, we substract the THz photogenerated signal (blue lines) from the detected variation (grey curves): this leads to the corrected signal (red curves) that gives a better signature of the carrier dynamics.

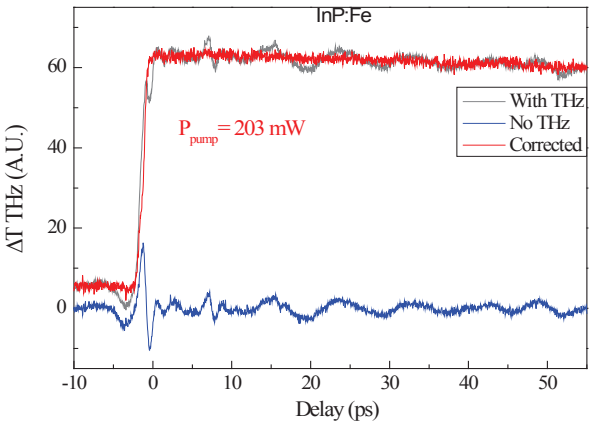

a

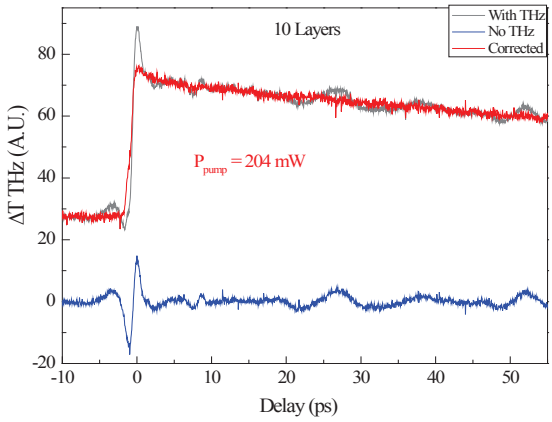

b

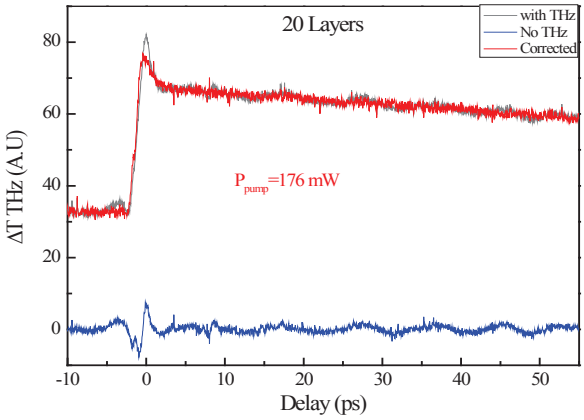

c

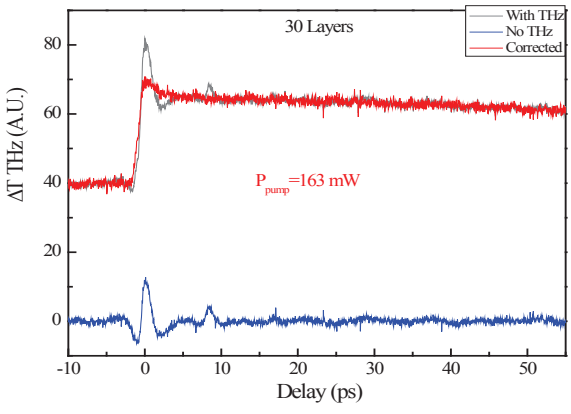

d

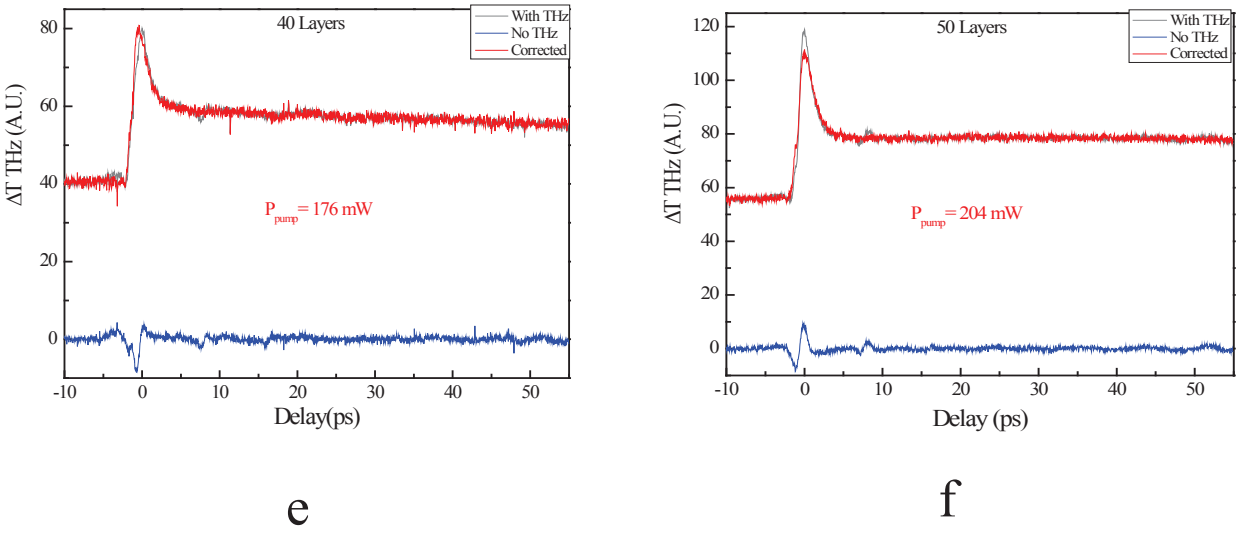

e f

Fig. 5.26*: Variation of THz transmission (raw curve in grey, corrected curve in red) and THz signal generated by optical excitation of the samples (blue).*

The so-corrected curves are presented in Fig. 5.27a (they are arbitrarily shifted vertically for seek of clarity). Each QD sample response includes a long plateau spreading over one hundred of ps, and a shorter feature. The long plateau decreases with time for small QD's layer numbers, while it is almost constant for the 50 layers one. As its duration is comparable with the carrier lifetime in the substrate and it seems to depend on the QD's layer number, it could originate in the excitation of electrons in the substrate or in the transfer of the photoexcited electrons from the QD's to the substrate. Also charges trapped at interfaces may explain such a behavior as well as interband recombination in the QD's, as already reported. The bottom plot in Fig. 5.27a presents a zoom of the shorter feature. We have subtract the plateau level by interpolating it at early times. The short peak increases with the number of QD's layers. Thus it could be attributed to carrier dynamics in the QD's. The duration of this pulse varies also with the number of QD's layers. This short pulse could be the signature of transfer of charges from the barriers to the QD's or of interband transition. Another explanation could be the density of trapping defects that could vary with the number of QD's layers.

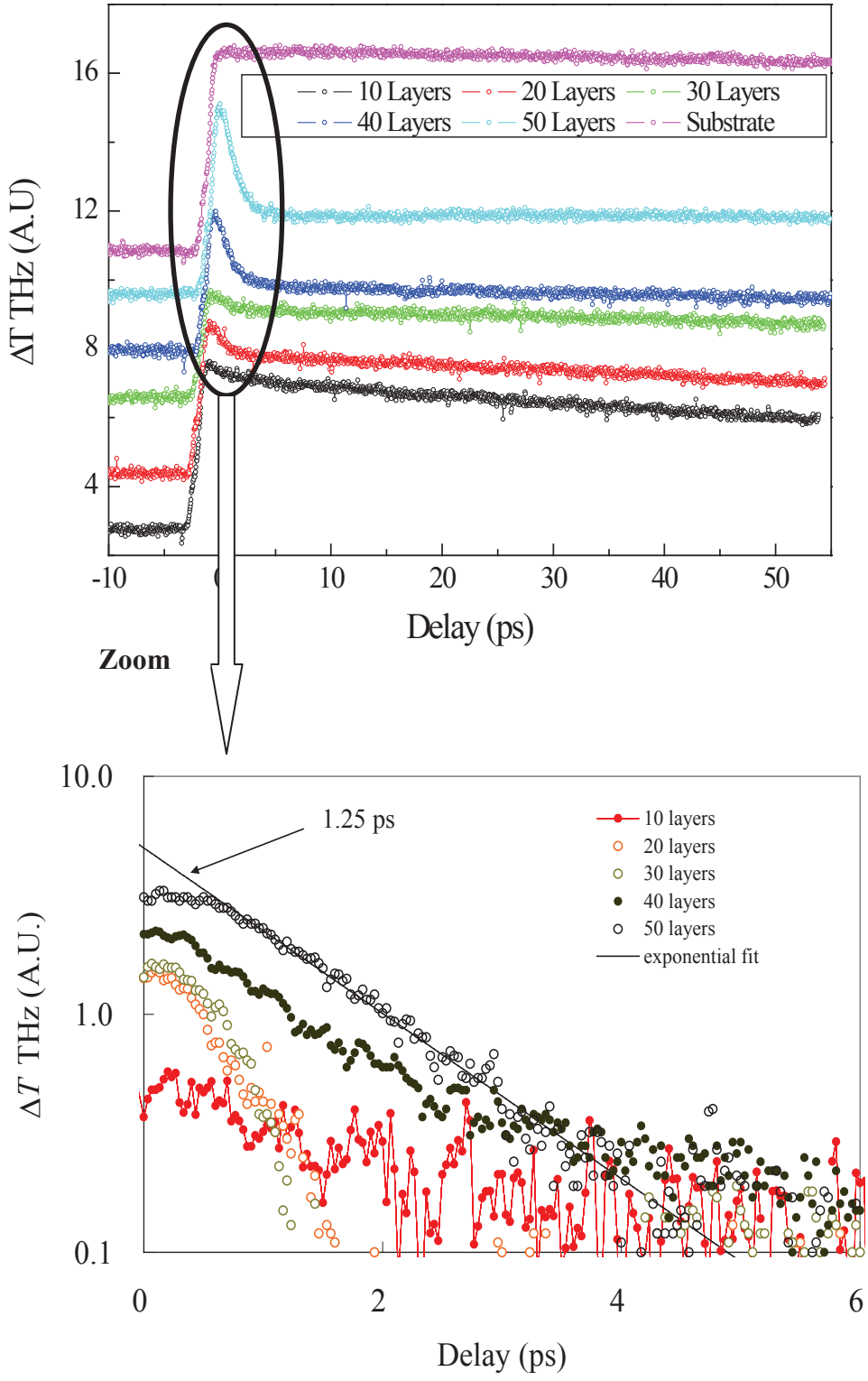

Fig. 5.27a: Corrected variation of THz transmission. The down plot is a zoom at early times, in which the plateau contribution has been removed.

Due to instability of the laser pump power, the previous measurements were performed at different pump powers for different layers samples. To confirm the exponential signature of the plots, we repeat the same measurement with another setup at constant pump power (120 mW) for all the samples, and we recorded the corrected THz waveforms together with previous curves are presented in Fig. 5.27b. New curves almost resemble with the previous ones, except some noise, which originates in the inclination of the incident pump beam (45°). In these two setups, the laser is operating at 800 nm with same repetition rate about 85 MHz, but the pulse duration is about 150 fs in the first setup and 100 fs in the second setup. The incident direction of the pump beam on the sample is normal in the first case, where as in second case it is 45°.

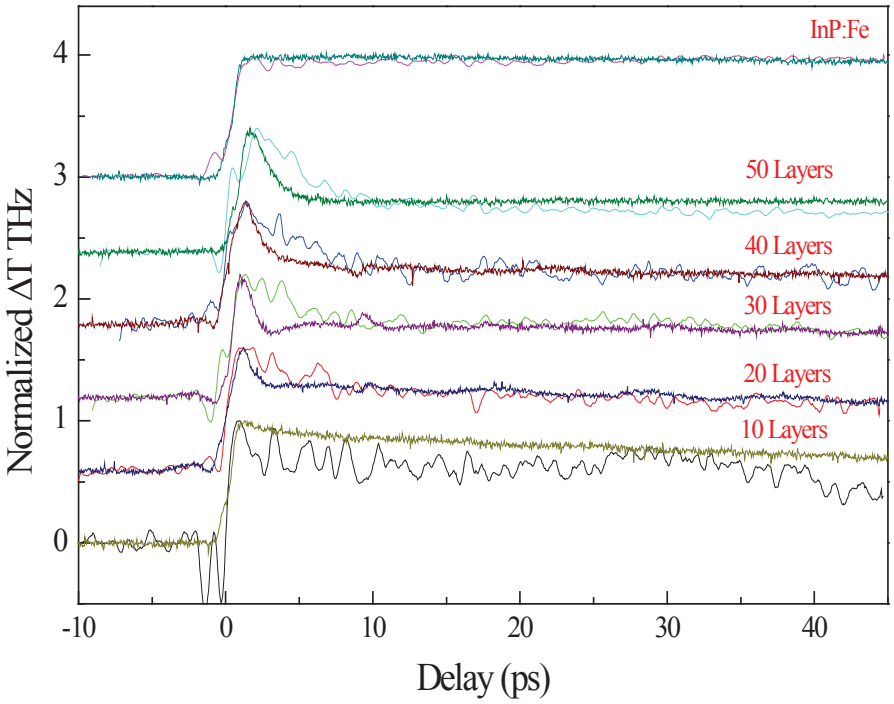

Fig. 5.27b: Corrected variation of THz transmission done for another setup at 0.8 μm.

Now, we do the pump-probe experiment for 30 layers sample for different optical pump power in order to observe the carrier saturation effect. The recorded curves for the optical powers of 165, 203 and 220 mW are presented in Fig. 5.28a, and the 3 curves exhibit an exponential behavior. The plateau shows a decay slope that varies slightly with the pump

power because, for higher pump power, more carriers are generated and occupied all intraband levels.

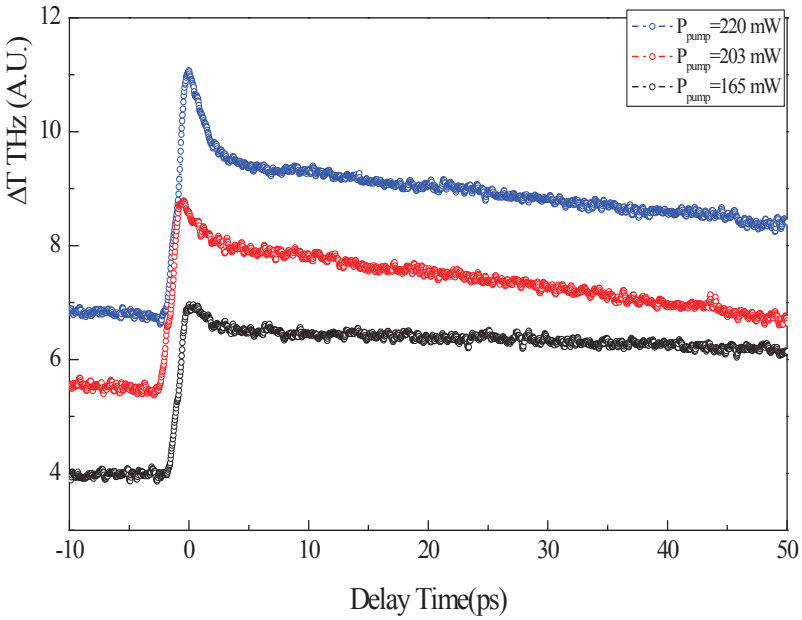

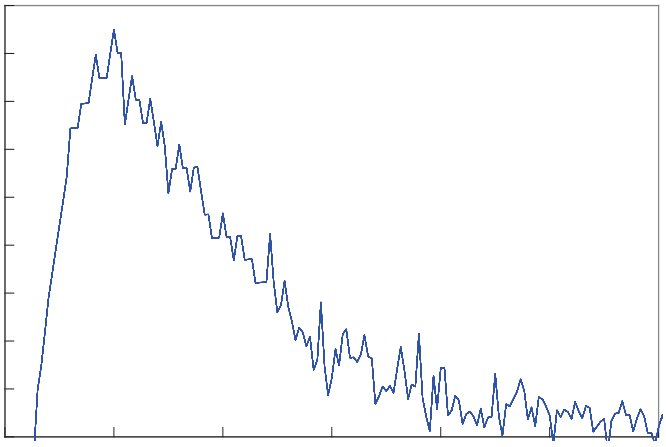

Fig. 5.28: Corrected variation of THz transmission of the 30-layers sample for different pump powers. The right plot is a zoom at early times, in which the plateau contribution has been removed.

So, the carrier in the higher intraband levels has to wait until the carriers in bottom of conduction band getting recombination, which implies a higher carrier relaxation time [21]. However, the short pulse shows a constant temporal shape Fig. 5.28b with duration of about

1.5 ps. It is clearly seen when the short pulses are normalized in amplitude (Fig. 5.29). Therefore, we do not observe any saturation effect with pump powers in the range 150-220 mW.

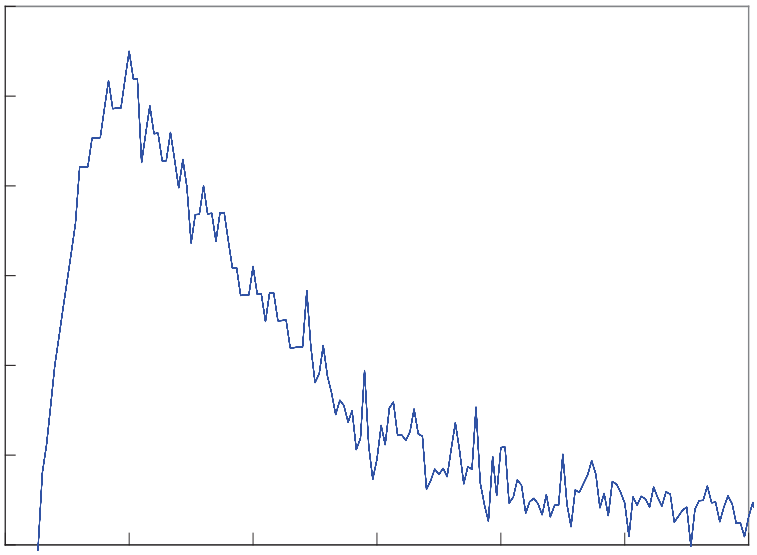

Fig. 5.29: Same as Fig. 5.28 but normalized to the peak amplitude.

IV.3.3. Optical Pump-THz probe experimental at 1030 nm

Here, we used optical pump-THz probe experimental at 1.03 µm wavelength to study carrier dynamics in InAs/InP:Fe QD's. The schematic used for this study is presented in Fig. 5.30a. Here, the pump wavelength is not able to excite carriers into the barrier material and we did not get any THz signal generated by photo-excitation of the samples. This means that the previous signals obtained with 0.8-µm wavelength are certainly due to the transfer of the electrons form the barriers to the QD's or through the Dember effect in the InP:Fe substrate. The recorded temporal curves, when the sample is optically pumped (350 mW, beam diameter 1.9 mm, pulse duration 70 fs) and probed with THz, are presented in Fig. 5.30b. The peaks at 10 ps that appears for all samples is due to a reflection of pump beam in the InP:Fe substrate, which is transparent at 1.03 µm. All the curves show almost exponential decay behavior, with

a decay time of 50~80 ps. Thus here this decay can only be related to the inter-band recombination in the QD's.

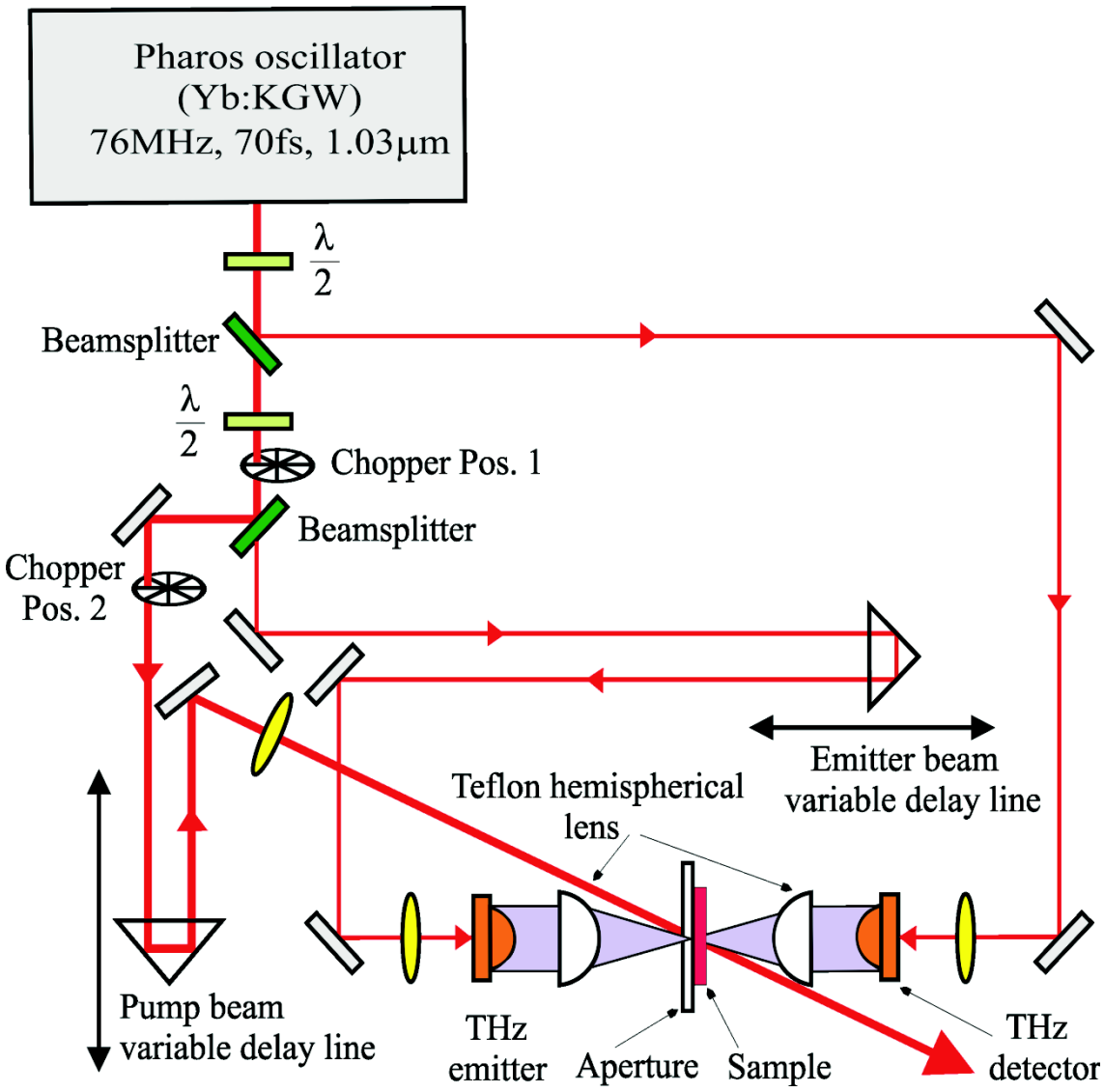

Fig. 5.30a: Optical pump-THz probe experimental setup at 1.03 μm

This allows us to attribute a part of the origin of the plateau observed at 0.8 μm (see preceding paragraph) to the inter-band transition. Here, the curves exhibit more noise compared to the previous curves at 0.8 μm; I think it may be due to delay line or laser.

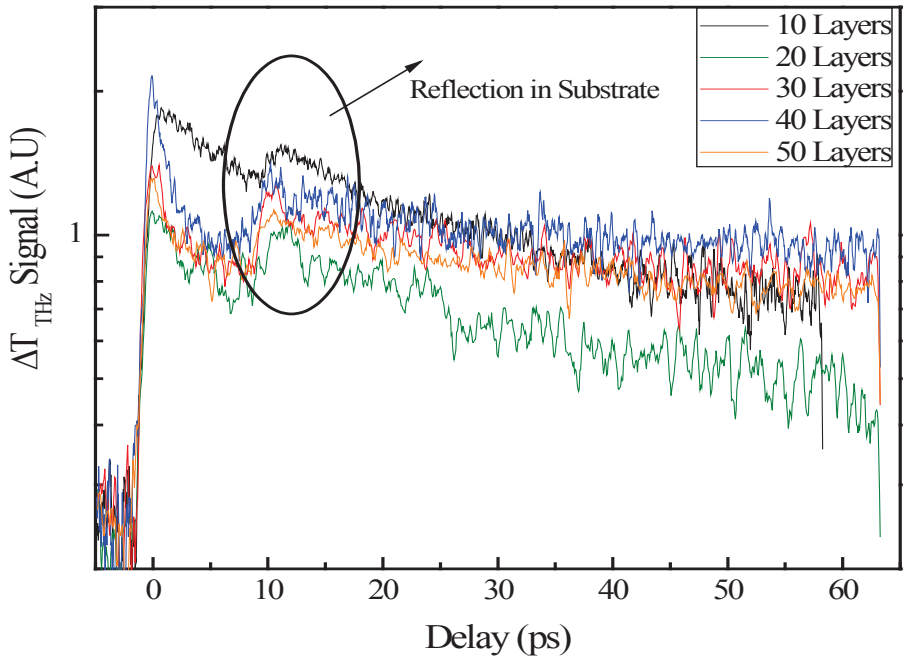

Fig. 5.30b: Variation of THz transmission for 1.03-µm pump wavelength.

1V.3.4. THz excitation Spectroscopy

As the optically excited samples radiate THz waves, we investigated this phenomenon. Fig. 5.31 shows the experimental set-up used for this study. This set-up includes an amplified Yb:KGW laser system which is operating at 1.03 µm with a pulse repetition rate of 200 kHz and a pulse duration of 160 fs. This laser beam supplies an optical parametric oscillator (OPO) that generates tunable wavelengths from 640 to 2600 nm with a pulse duration of about 140-160 ps. Here the samples are excited by the OPO beam, and the THz signal generated from the sample surface is detected by a GaBiAs photoconductive antenna which is triggered by a low-power delayed part of the Yb:KGW laser beam. For this study, we used only the 30 and 40 QD's layer samples (due to the lack time and availability of setup, we did not perform measurement for all the QD's samples). The THz waveform generated by the InAs QD's samples excited at 1.77 µm (0.7 eV) is shown in Fig. 5.32. With this pumping wavelength, no carriers are photo generated in the sample because of QD's energy gap (0.792 eV), thus the THz signal originates from pure non linear effects in the QD's. The spectra of the waveforms are given in Fig. 5.32a. They are quite chaotic because of the limited time-window. However, the FFT of these wave forms spread up to 5~6 THz (Fig. 5.32b).

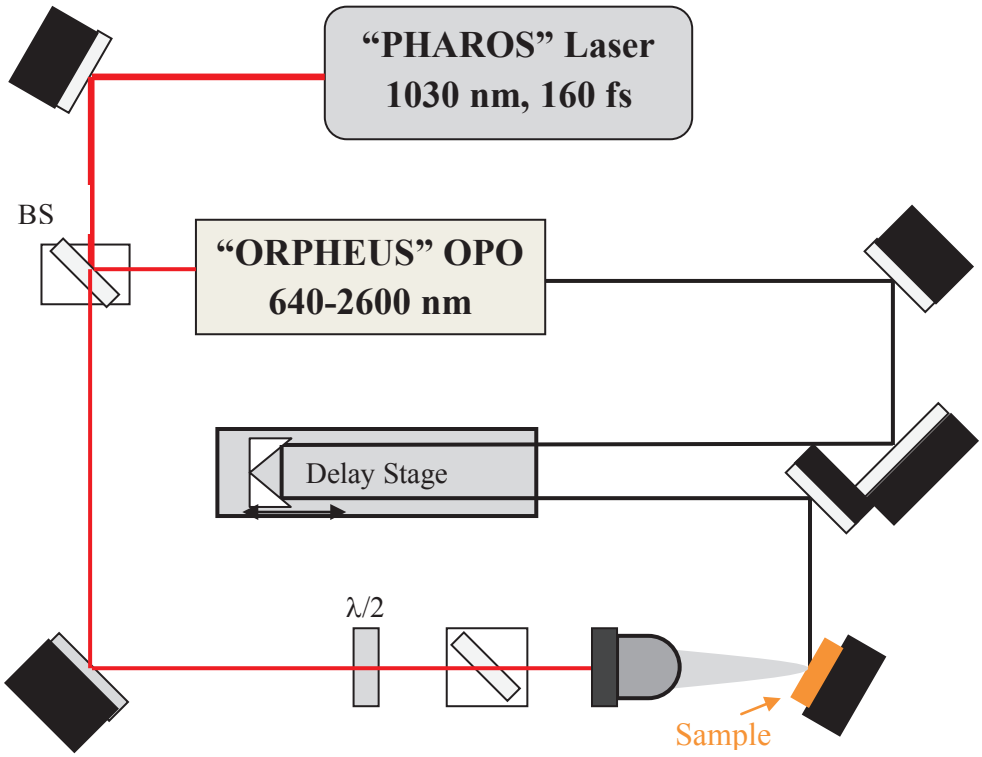

Fig. 5.31: Experimental setup for THz excitation spectroscopy. BS is beam splitter.

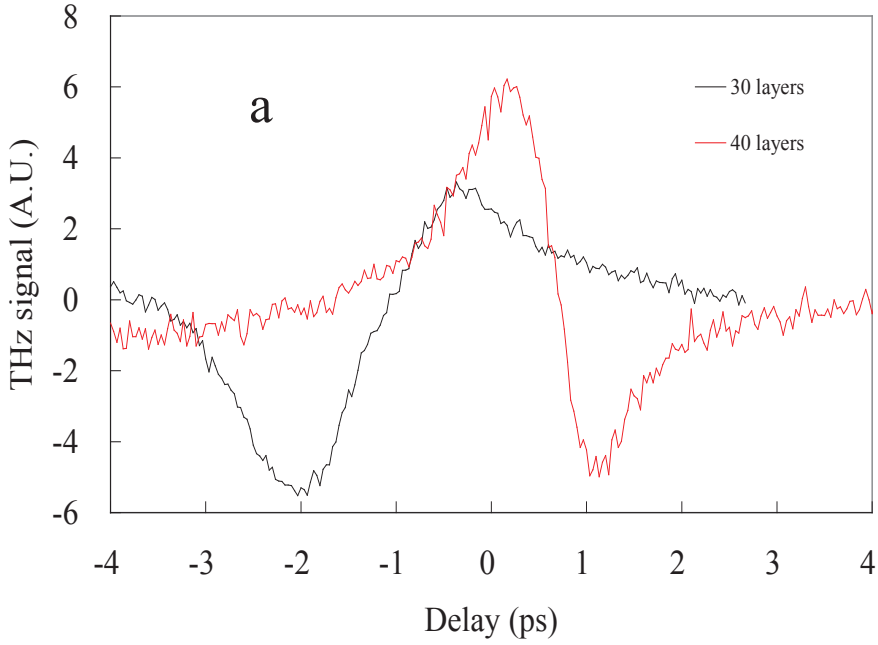

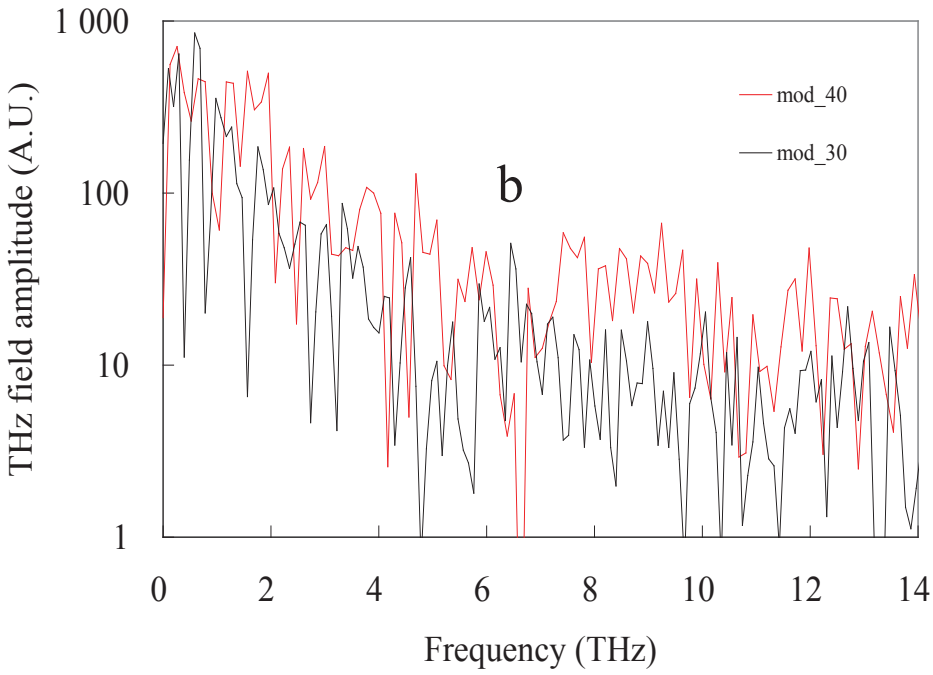

Fig. 5.32: THz waveform and its spectrum generated by the samples pumped at 0.7 eV.

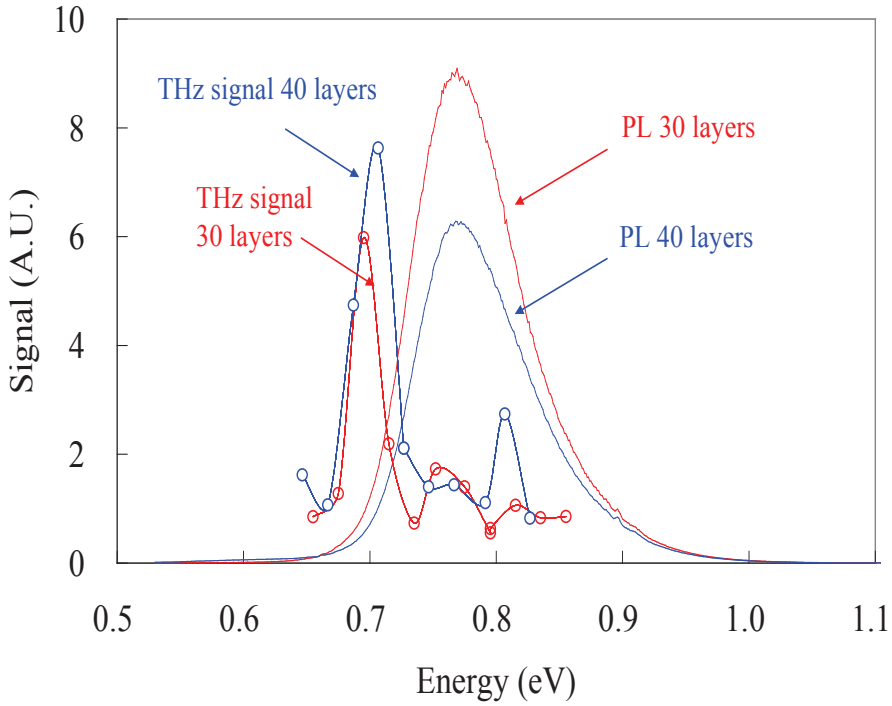

Fig. 5.33*: THz waveform and its spectrum generated by the samples pumped at 0.7 eV.*

Fig. 5.33 presents an interesting result, i.e. the THz signal amplitude versus the optical pumping photon energy (in eV, dashed curves) together with the photoluminescence spectrum

(continuous line). THz emission occurs at the lower limit of the luminescence spectrum, i.e. for photons whose energy is weaker that the bandgap energy of the QD's. Here again, this consolidates the idea of a nonlinear optical generation in the QD's.

IV.3.5. THz-TDS

In this section, we present the experimental results of THz-TDS characterization of InAs/InP:Fe multi layers QD's samples in the frequency range 0.1 – 3.5 THz. The experimental setup of TDS system is shown in Fig. 5.7. As discussed in earlier paragraphs, the TDS system utilizes a mode-locked Ti: Sa laser and LTG-GaAs photoconductive antennas for THz signal generation and detection. The laser produces optical pulses with a time width duration shorter than 100 fs and a wavelength of 800 nm at a repetition rate of 82 MHz.

Here, we measured three temporal signals with 35 ps time window during the THz-TDS experiment. The first one THz_{air} is measure when no sample is located in between the emitter and the detector. The second one THz_{sub} is measured when the InP:Fe substrate is placed in between the emitter and detector (the same substrate used to deposit QD's films on it). The third one THz_{QD} corresponds to the QD's film samples located in the THz beam. The measured temporal signal of free space, substrate and QD's sample are presented in Fig. 5.34a. The temporal wave forms for the bare and covered substrate samples are almost superimposed as regards to time. It means that the additional delay due to propagation in the QD's layers is almost negligible. In addition to that, the signals for the bare and covered samples are almost identical. The influence of QD's seems a priori weak. The signals around 22 ps and 31 ps are observed for both bare and covered substrates, thus it corresponds to the first and second rebounds in the substrate.

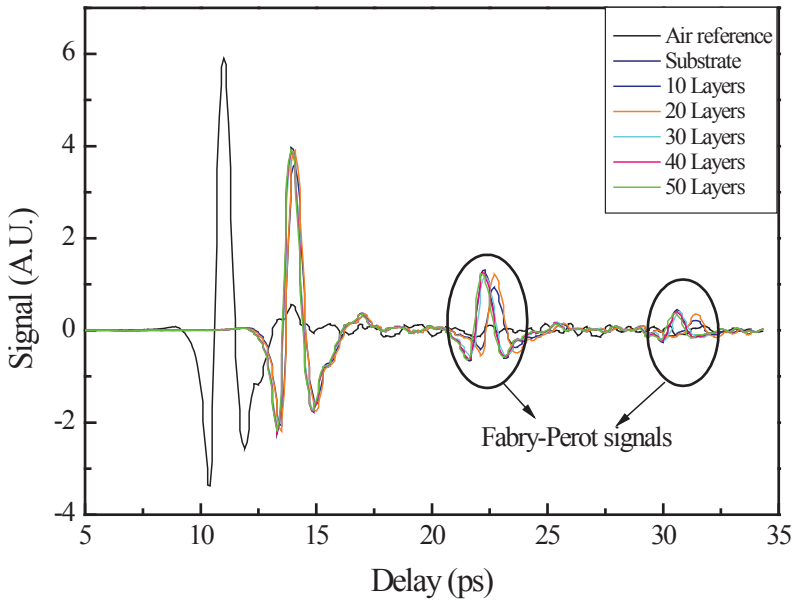

Fig. 5.34a: Temporal signals for air, substrate and substrate + QD's

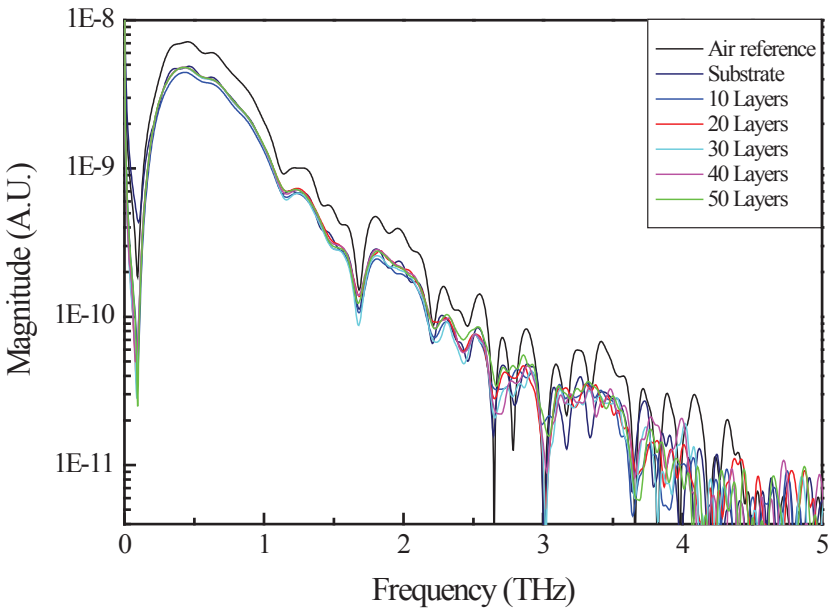

Fig. 5.34b: Transmission modulus for air, substrate and covered samples.

Fig. 5.34b represents the FFT spectrum of the temporal signal show Fig.5.34a. In this spectrum, we observe dips at 1.68, 2.64 and 3 THz which correspond to water absorption

lines. The difference in amplitude between the bare and covered substrates is very weak, and between the different covered samples is almost negligible. This is due to the very small QD layer thickness and the weak interaction between the QD's and the THz beam. So, it is really difficult to extract the refractive index and absorption parameters of QD's layers.

IV.4. Conclusion

In conclusion, we have used five QD's samples with different number QD's layers in this study and we have investigated the ultrafast carrier dynamics in InAs/InP:Fe self-assembled quantum-dot samples using four ultrafast techniques: standard femtosecond optical pump/probe reflectivity measurements, photoluminescence spectroscopy, terahertz excitation spectroscopy, and terahertz time domain spectroscopy. Quantum size confinement effect is clearly observed excitation PL emission spectrum i.e. the PL emission energy increases with decreasing the QD size. We have demonstrated carrier capture and relaxation processes in QD's by pump-probe technique. By analyzing the transient spectrum, the carrier capture times from InP:Fe substrate to InAs layers were obtained from 1.5 ps to several tens of ps. The capture time reduces when the number of QD's layers increases due to the large number of defects in higher order layers as compared to the lower ones. The normalized spectra of curves for all five QD's samples exhibit an almost similar exponential signature. The carrier relaxation time varies with pump power; this is observed when we record the transient curves for 30 layers at different pump powers.

References

[1] Y. Arakawa and H. Sakaki, "*Multidimensional quantum well laser and temperature dependence of its threshold current*", Appl. Phys. Lett., **40**, 939 (1982).

[2] N. Kirstaedter, N. N. Ledentsov, M. Grundmann, D. Bimberg, V. M. Ustinov, S. S. Ruvimov, M. V. Maximov, P. S. Kop'ev, Z. I. Alferov, U. Richter, P.Werner, U. Gosele, and J. Heydenreich, *"Low threshold, large T0 injection laser emission from (InGa)As quantum dots,"* Electron. Lett., **30**, 1416 (1994).

[3] F. Heinrichsdor, C. Ribbat, M. Grundmann, and D. Bimberg, *"High-power quantum-dot lasers at 1100 nm"*, Appl. Phys. Lett., **76**, 556 (2000).

[4] M. Kuntz, G. Fiol, M. Lämmlin, D. Bimberg, M. G. Thompson, K. T. Tan, C. Marinelli, R. V. Penty, I. H. White, V. M. Ustinov, A. E. Zhukov, Y. M. Shernyakov, and A. R. Kovsh, "*35 GHz mode-locking of 1.3 μm quantum dot lasers*", Appl. Phys. Lett., **85**, 843 (2004).

[5] P. Michler, A. Kiraz, C. Becher, W. V. Schoenfeld, P. M. Petro®, L. Zhang, E. Hu, and A. Imamo·glu, "*A quantum dot single-photon turnstile device*", Science, **290**, 2282 (2000).

[6] C. Santori, D. Fattal, J. Vu·ckovic, G. S. Solomon, and Y. Yamamoto, *"Indistinguishable photons from a single-photon device*", Nature, **419**, 594 (2002).

[7] S. Tiwari, F. Rana, H. Hana¯, A. Hartstein, E. F. Crabbe, and K. Chan, *"A silicon nanocrystal based memory",* Appl. Phys. Lett., **68**, 1377 (1996).

[8] K. Koike, K. Saitoh, S. Li, S. Sasa, M. Inoue, and M. Yano, *"Room-temperature operation of a memory-effect AlGaAs/GaAs heterojunction field-effect transistor with self-assembled InAs nanodots",* Appl. Phys. Lett., **76**, 1464 (2000).

[9] H. Kim, T. Noda, T. Kawazu, and H. Sakaki, *"Control of Current Hysteresis Effects in a GaAs/n-AlGaAs Quantum Trap Field Effect Transistor with Embedded InAs Quantum Dots",* Jpn. J. Appl. Phys., **39**, 7100 (2000).

[10] G. Yusa and H. Sakaki, *"Trapping of photogenerated carriers by InAs quantum dots and persistent photoconductivity in novel GaAs/n-AlAs field-effect transistor structures"*, Appl. Phys. Lett., **70**, 345 (1997).

[11] J.-E. Oh and J.-W. Kim, *"Room-temperature Memory Operation of Al-GaAs/GaAs High Electron Mobility Transistors with InAs Quantum Dots embedded in the Channel,"* in Proceedings of the International Electron Device Meeting 2000, IEDM, 106 (2000).

[12] C. Balocco, A. M. Song, and M. Missous, *"Room-temperature operations of memory devices based on self-assembled InAs quantum dot structures,"* Appl. Phys. Lett., **85**, 5911 (2004).

[13] J. C. Campbell, D. L. Hu®aker, H. Deng, and D. G. Deppe, *"Quantum dot resonant cavity phyotodiode with operation near 1.3 μm wavelength,"* Electr. Lett., **33**, 1337 (1997).

[14] L. Chu, A. Zrenner, M. Bichler, and G. Abstreiter, *"Quantum-dot infrared photo detector with lateral carrier transport,"* Appl. Phys. Lett., **79**, 2249 (2001).

[15] M. LÄammlin, G. Fiol, C. Meuer, M. Kuntz, F. Hopfer, A. R. Kovsh, N. N. Ledentsov, and D. Bimberg, *"Distortion-free optical amplification of 20-80 GHz mode locked laser pulses at 1.3 μm using quantum dots",* Electronics Lett., **42**, 697 (2006).

[16] X. D. Huang, A. Stintz, H. Li, L. F. Lester, J. Cheng, and K. J. Malloy, *"Passive mode-locking in 1.3 μm two-section InAs quantum dot lasers",* Appl. Phys. Lett., **78**, 2825 (2001).

[17] F. Hopfer, A. Mutig, M. Kuntz, G. Fiol, D. Bimberg, N. N. Ledentsov, V. A. Shchukin, S. S. Mikhrin, D. L. Livshits, I. L. Krestnikov, A. R. Kovsh, N. D. Zakharov, and P.Werner, *"Single-mode sub monolayer quantum-dot vertical-cavity surface-emitting lasers with high modulation bandwidth",* Appl. Phys. Lett., **89**, 141106 (2006).

[18] A. Lochmann, E. Stock, O. Schulz, R. Hopfer, D. Bimberg, V. A. Haisler, A. I. Toropov, A. K. Bakarov, and A. K. Kalagin, *"Electrically driven single quantum dot polarised single photon emitter",* Electronics Lett., **42**, 774 (2006).

[19] C. H. Wu et *al,* "*An Investigation of Quantum States in Ultra-Small InAs/GaAs Quantum Dots by Means of Photoluminescence*," Chinese Journal of Physics, **43**, 847 (2005).

[20] Charles A. Schmuttenmaer, "*Using Terahertz Spectroscopy to Study Nanomaterials*," Terahertz Science and Technology, **3**, 1941 (2010).

[21] D. A. Yarotski, R. D. Averitt, N. Negre, S. A. Crooker, and A. J. Taylor, "*Ultrafast carrier-relaxation dynamics in self-assembled InAs/GaAs quantum dots*," J. Opt. Soc. Am. B, **19**, 1480 (2002).

V. THz-TDS characterization of Carbon Nano Tubes (CNTs)

V.1. Introduction

Carbon nanotubes (CNT) are rolled-up graphene sheets (one atom thick graphite layer) with hollow cylindrical structures. CNTs are interesting as promising materials for polymer composites because of their excellent electrical, optical, thermal and mechanical properties [1]. The electrical conductivity of CNTs/polymer nano composites depends on many parameters like CNTs chirality, CNTs purity percentage, the aspect ratio of length to diameter of tubes [2]. CNTs are extremely attractive for a wide field of applications such as field emitters [3, 4], transistors [5, 6], chemical sensors [7] and unusual nano antennas [8] for communications between microscopic and macroscopic fields. CNTs are classified as single-walled Nano Tubes (SWNTs), which consist of only one graphene layer and Multi Walled Carbon Nano Tubes (MWNTs) which includes more than one graphene layer (Fig. 5.35). Single-walled carbon nanotubes SWNTs generally have higher electrical conductivity and higher aspect ratios, defined as length to diameter, than MWNTs. However MWNTs have higher mechanical strength and higher breakdown voltage than SWNTs. Hence, for CNT application to nanoelectronics, intermediate properties that have the advantages of both CNTs are required.

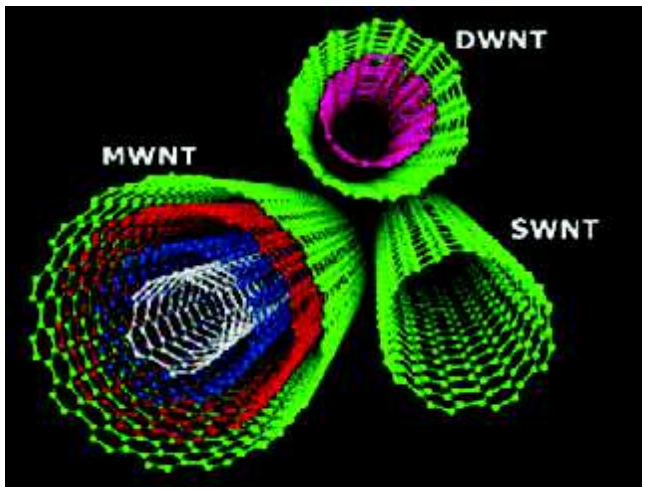

Fig. 5.35: Single Walled Nano Tubes (SWNT) and Multi Walled Nano Tubes (MWNT). (Picture is taken from internet).

To apply the CNTs properties to the new nano electronic devices, it would be essential to study the dispersion, absorption and conductivity of different CNTs structures. Although wide

studies have been done on CNTs at DC, low frequencies and optical frequencies, over the microwave and THz regimes, the electrical properties of CNTs have not yet been fully studied.

In this section, we present the study of optical and electrical properties of carbon nanotubes using a THz –TDS which is used as a non contact characterization technique. Here, we first perform transmission TDS measurement to record the temporal waveforms of the CNT devices, from which we can extract the amplitude and phase information. By using this information, we can calculate optical properties (refractive index, absorption) and electrical conductivity of the carbon nanotubes. Here, we do the TDS characterization for two different sets of carbon nanotube (SWNTs and MWNTs) and different thicknesses.

V. 2. First set of CNTs

The first set of CNTs samples includes SWNTs and MWNTs films. SWNTs and MWNTs films are prepared by vacuum filtration technique at the Department of Energy Science, Sungkyunkwan University, Korea. SWNTs and MWNTs films are deposited on a transparent fused quartz substrate whose dimensions are 2.5×2.5×0.215 cm^3. The thickness, length and diameter of SWNTs and MWNTs are presented in the table 5.3 below. The thickness of CNTs thin-films were measurement with a profilometer (1.09 µm for the SWNT film and 1.20 µm for the MWNT film) while the CNTs are 15-µm long (MWNT) and 5-µm long (SWNT). Their diameters are respectively 15 nm and 1.5 nm for MWNT and SWNT.

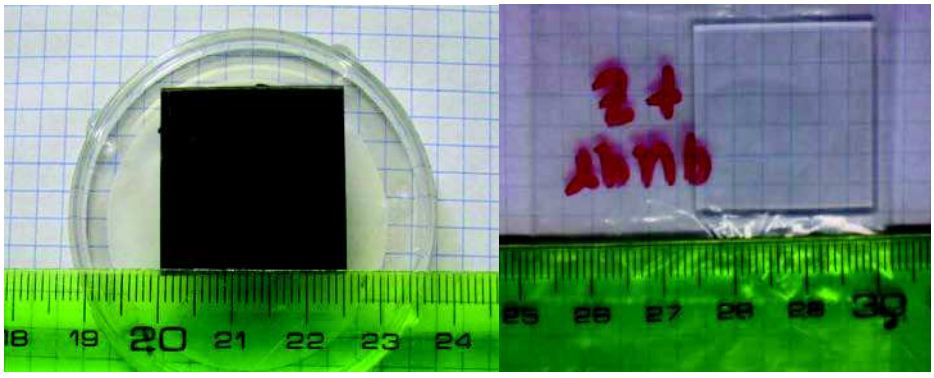

Fig. 5.36: (a) The CNT thin film deposited over a fused quartz substrate and (b) the bare fused quartz substrate.

	Length of CNT (μm)	*Diameter of CNT (nm)*	*Thickness of the film (μm)*
SWNT	15	15	1.09
MWNT	5	1.5	1.2

Table 5.3: Details of the SWNTs and MWNTs thin film samples

The THz TDS experimental chronology for transmission measurement is shown in Fig. 5.7. We measured three temporal waveforms for each CNTs sample as shown in Fig. 5.37, one is air reference signal, i.e. the signal measured without sample is in-between emitter and detector. The second one is the substrate reference signal which is measured by keeping the substrate in between the emitter and the detector. And finally, the third one is the sample signal measured by keeping the substrate covered with CNTs sample instead of the bare substrate. The measurements are done for SWNT and MWNTs samples and the recorded waveforms are presented in Fig. 5.38.

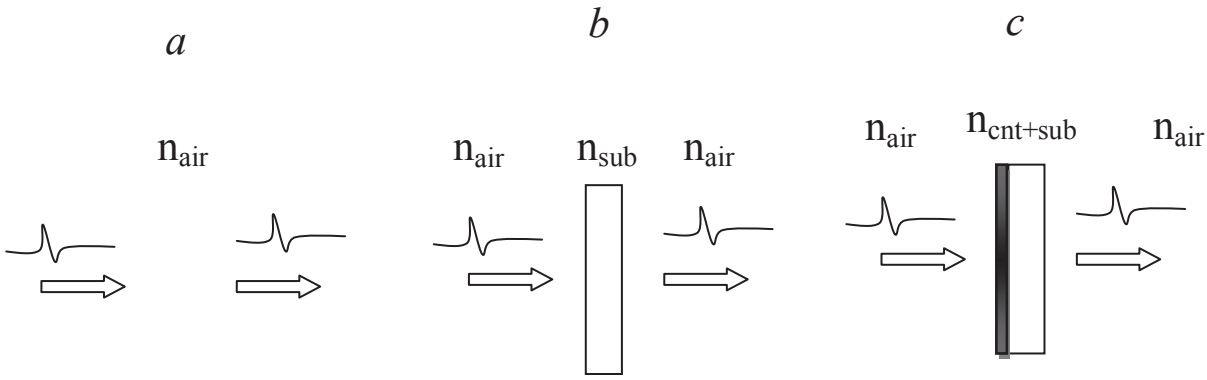

Fig. 5.37: *The scheme of a THz-TDS transmission experiment with a) Air reference, b) Substrate reference, and c) Substrate with CNTs.*

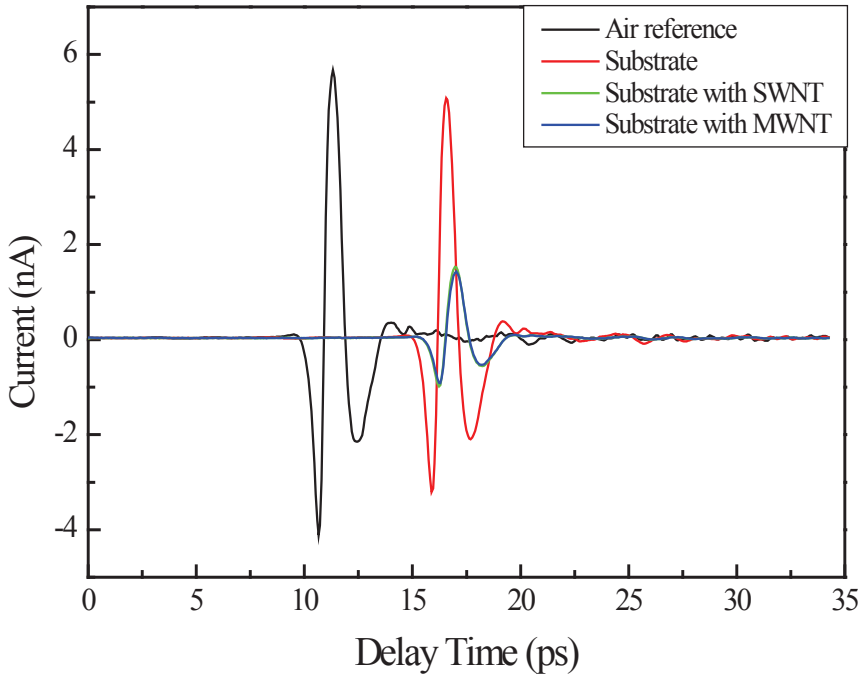

Fig. 5.38: Temporal waveforms for air reference, substrate and covered substrates.

The temporal waveforms for the SWNT and MWNT samples are almost superimposed as regards to time, which means that the delay due to propagation in the MWNT and SWNT is negligible. In contrast, the signals encounter losses as the peak value of the waveform is reduced for SWNT and MWNT. By making the FFT of these temporal signals, we get the phase and amplitude information (see Fig. 5.39). Here, we are mainly focused on to extract the absorption and dispersion parameters of the SWNTs and MWNTs in the frequency range 0.1 - 2 THz.

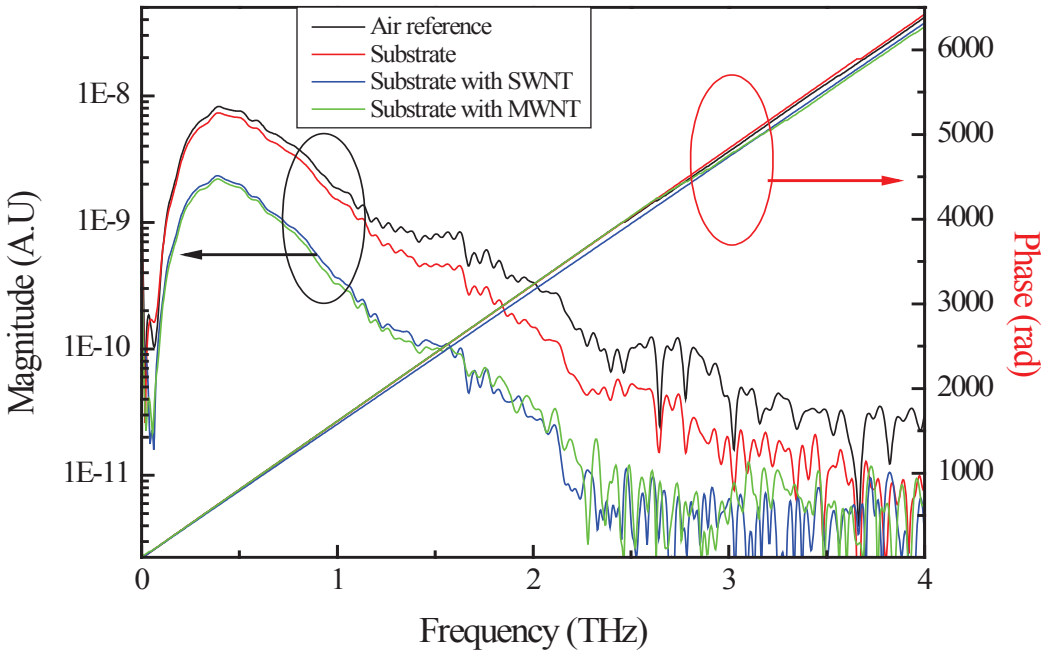

Fig. 5.39: Transmission modulus for air, substrate and CNT samples.

The extracted results for the refractive index and absorption coefficient of SWNT and MWNT are presented and discussed in the published article "*Carbon nanotube THz spectroscopy: study absorption and dispersion properties of SWNTs and MWNTs*" attached at the end of this thesis. We also extracted and studied the THz surface conductivity and transmission of SWNTs and MWNTs samples and the results are presented in article 2 "*THz time domain spectroscopy in different carbon nanotube thin films*". The experimental results show that the values of refractive index, power absorption, real conductivity and surface conductivity, are larger in SWNTs than in MWNTs due to smaller number of surface defects, and to more mobile carriers in SWNTs compared to MWNTs sample. When surface defects increases, the number of free electrons decreased, because the defects trap the free carriers [9].

V.3. Second Set of CNTs

	Diameter (mm)	*Film Thickness (nm)*	*Substrate thickness (mm)*
MF1	18.72	162.16	2.15
MF2	18.99	193.88	2.15

Table 5.4: Details of the MWNTs thin film samples

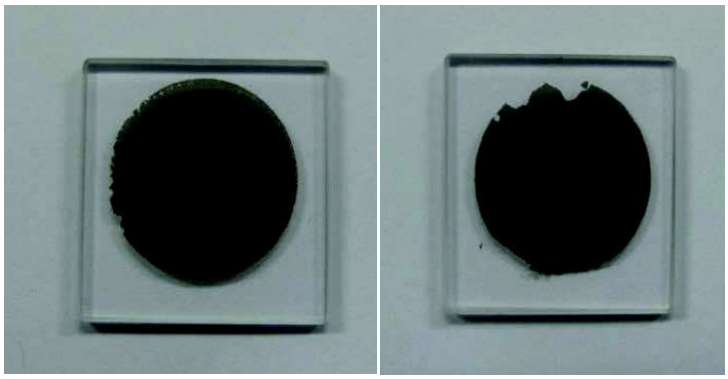

Fig. 5.39: Photograph of MWNTs samples MF1 and MF2

In the second set of CNTs samples, we used two MWNTs films named as MF1 and MF2, which are fabricated by the vacuum filtration method. These MWNTs were deposited on fused quartz substrate whose thickness is about 2.15 mm. The device picture and details are presented in Fig. 5.39 and table 5.4 respectively. Here, we focused to study on the AC and DC electrical conductivity responses of pure MWNTs films deposited on a fused quartz substrate. The study is performed by THz TDS (Fig. 5.7). We used a polynomial extrapolation method to extract the DC conductivity from the TDS experimental results and compare with classical electrical conductivity measured using the four-point probe technique. These results are published in the SPIE conference paper *"Terahertz Conductivity Studies in Carbon nanotube Networks prepared by the Vacuum Filtration Method"* is attached at the end of this manuscript. The results presented in this paper is summarize as follows, two sets of CNTs

were studied by THz-TDS. THz transmission is higher for SWNTs than the MWNTs. The experimental optical and electrical properties of SWNTs and MWNTs were determined up to 2 THz, and the results show that the refractive index, power absorption, surface conductivity are larger in SWNTs than in MWNTs due to the larger number of charge carriers and defects at the surface of SWNTs as compared to MWNTs. The power absorption and conductivity strongly depend on frequency, i.e. increase with frequency. However, the refractive index decreases slightly with frequency. All these results are then compared with the literature. The electrical conductivity of two MWNTs with different thickness as is measured by THz-TDS and by a four probe technique. The achieved conductivity from both the techniques is almost the same (≈ 70 S/m) for thin sample, while the conductivity of thick sample differs in both cases (37 S/m with THz-TDS and 67 S/m with a four probe method) and this difference may be due to an inhomogeneous sample.

V.4. Conclusion

We presented transmission THz-TDS experimental results for two different sets of CNT thin film samples (SWNTs and MWNTs) in the frequency range 0.1-2 THz. Experimental results show that the values of refractive index, power absorption, conductivity and filling factor are larger in SWNTs than in MWNTs because of a) the increased number of surface defects, and b) more mobile carriers at high filling factor in SWNTs compared to MWNTs sample. DC conductivity for MF1 and MF2 samples are calculated using TDS results and compared with four probe values, i.e. with DC value. For the MF1 sample, THz and DC conductivities are similar.

References

[1] V. Mittal, *"Polymer Nanotube Nanocomposites - Synthesis, Properties, and Applications,"* Wiley - Scrivener, (2010).

[2] S. Yellampalli, *"*Carbon Nanotubes - Polymer Nanocomposites*,"* InTech (2011).

[3] A. Nojeh, R. Fabian, and W. Pease, *"Field-Electron Emission from Single-Walled Carbon Nanotubes Lying on a Surface,"* Electrical and Computer Engineering, 1294 (2007).

[4] N. de Jonge, Y. Lamy, K. Schoots, and T. H. Oosterkamp, *"High brightness electron beam from a multi-walled carbon nanotube,"* Nature, **420**, 393 (2002).

[5] S. Heinze, J. Tersoff, R. Martel, V. Derycke, J. Appenzeller, and Ph. Avouris, *"Carbon nanotubes as Schottky barrier transistors,"* Phy Rev Lett., **89**, 106801 (2002)

[6] S. J. Tans, A. R. M. Verschueren, and C. Dekker, *"Room-temperature transistor based on a single carbon nanotube,"* Nature, **393**, 49 (1998)

[7] J. Kong, N. R. Franklin, C. W. Zhou, M. G. Chapline, S. Peng, K. J. Cho, and H. J. Dai, *"Nanotube molecular wires as chemical sensors,"* Science, **287**, 622 (2000)

[8] M. S. Dresselhaus. *"Nanotube antennas*,*"* Nature, **432**, 959 (2004)

[9] G. B. Jung, Y. Myung, Y. J. Cho *et al.*, "*Terahertz Spectroscopy of Nanocrystal-Carbon Nanotube and -Graphene Oxide Hybrid Nanostructures*," J. Phys. Chem. C*,* **114**, 11258 (2010)

VI. Characterization of Graphene Samples

VI.1. Introduction

Graphene is a two-dimensional (2D) lattice of carbon atoms arranged in a honeycomb crystal structure. Free electrons in graphene are mass less and show a gapless energy band structure [1-2]. Graphene exhibits unique optical and electrical properties, which make it a promising material for the development of high-speed electron devices, including field-effect transistors, pn-diodes, terahertz oscillators, and electronic and optical sensors [3-8]. Due to its gapless energy band structure, graphene devices may operate in the range of THz frequency [9].

VI.2. Sample Details

The epitaxial graphene samples used in our present study are grown on fused quartz substrate. We present here the optical properties (i.e. absorption and refractive index) of graphene layers determined using THz TDS. Compositions and dimensions of graphene samples are presented in the following table 5.5.

Sample	***material***	***Area (cm^2)***	***Thickness (nm)***	***Sheet resistance (Ω/sheet)***	***Conductivity (S/cm)***
QW1	Graphene	1.5×15	0.34	849.8	3.46×10^4
QW2	Graphene	1.5×15	0.34	4336.3	6.96×10^3
QW3	nAg+ Graphene	1.5×15	0.34	5989.6	5.19×10^3
Substrate	Fused Quartz	2×2	5×10^5	N/A	N/A

Table 5.5: Details of graphene samples

VI.3. Results and Discussion

As we explained in the earlier section, we measured 3 temporal waveforms for each sample: one is for free space (air reference), the second one is measured with bare substrate (substrate reference) and finally the third one is measured with the covered substrate. The recorded temporal waveforms for QW1, QW2, QW3 samples and bare substrate are presented in Fig. 5.40. The temporal waveforms for the bare and covered substrate samples almost superimposed as regards to time. It means that the additional delay due to propagation in the graphene layers is negligible. On the other hand, the signals encounter losses as the peak value of the waveform is reduced for covered samples. The second peak seen around 20 ps is observed for both bare and covered substrates, thus it corresponds to the first rebound in the substrate.

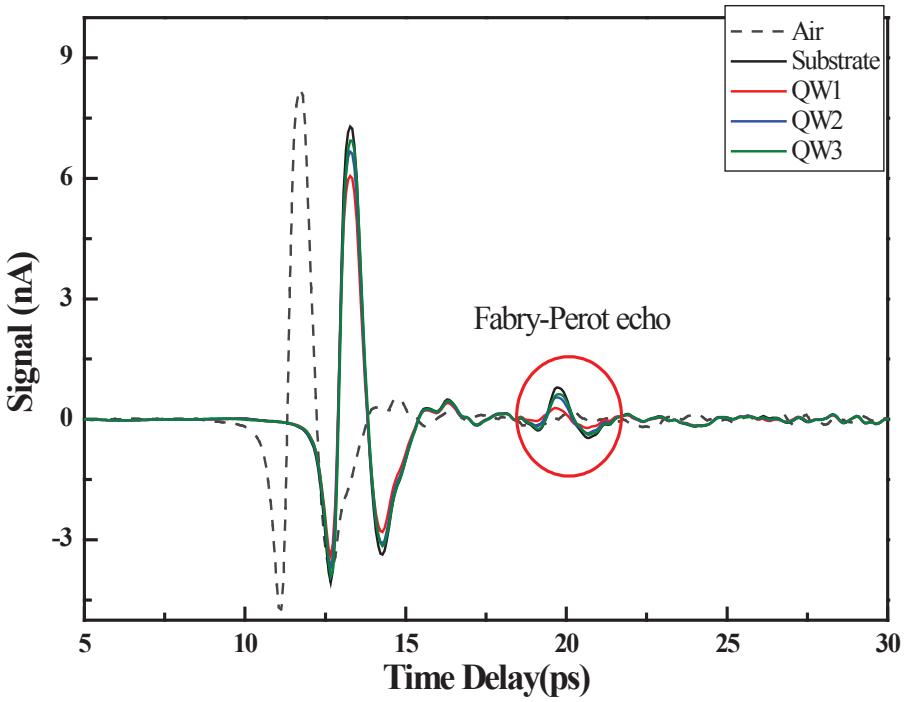

Fig. 5.40*: Temporal signals for reference, QW-1, QW-2 and QW-3 samples.*

The Fourier-transform of temporal waveforms is presented in Fig. 5.41. The difference in amplitude between the bare and covered substrates is weak, and between the different covered samples is even weaker.

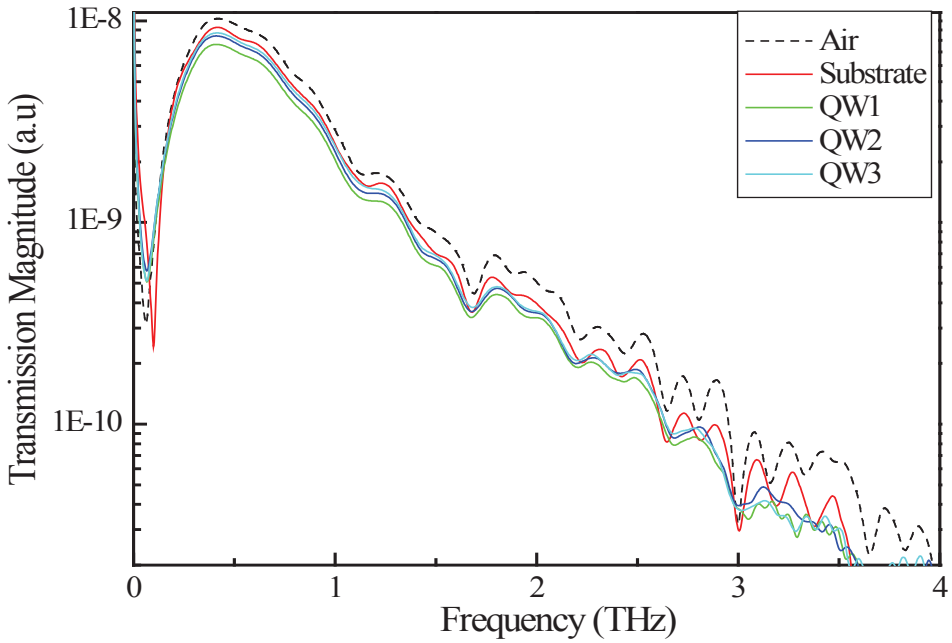

Fig. 5.41*: Transmitted spectra modulus for reference, QW-1, QW-2 and QW-3 samples.*

Fig. 5.42 shows the ratios of the spectra (modulus) of the covered samples and the bare substrate, i.e. the transmission of the covered samples relative to the bare substrate. At low frequencies up to 0.15 THz, because of the weak value of the THz-TDS signal magnitude and of the noise, transmission is higher than 1. Because of this experimental artifact, the curves are useful only above ~0.15 THz. Over 3.5 THz, the signal becomes noisy again, thus the readable range is 0.2~3.5 THz. The curves show a strong oscillatory behavior. This is due to the waveform rebound at 20 ps observed on Fig. 5.40. Consequently, it is useful to numerically time-window the waveform curves in order to get rid of this rebound. It will lead to more precise results, and in addition it will make easier the analysis of the results (extraction of graphene layer parameters). The so-filtered transmission is shown on *Fig. 5.43:* here the curves are almost flat up to 2.2 THz and after that little oscillation appear due to the noise. In Fig. 5.43, the observed transmission magnitude of QW1, QW2, and QW3 samples is respectively 82%, 91% and 95%, which means that the transmission increases with decreasing the conductivity (number of free carriers).

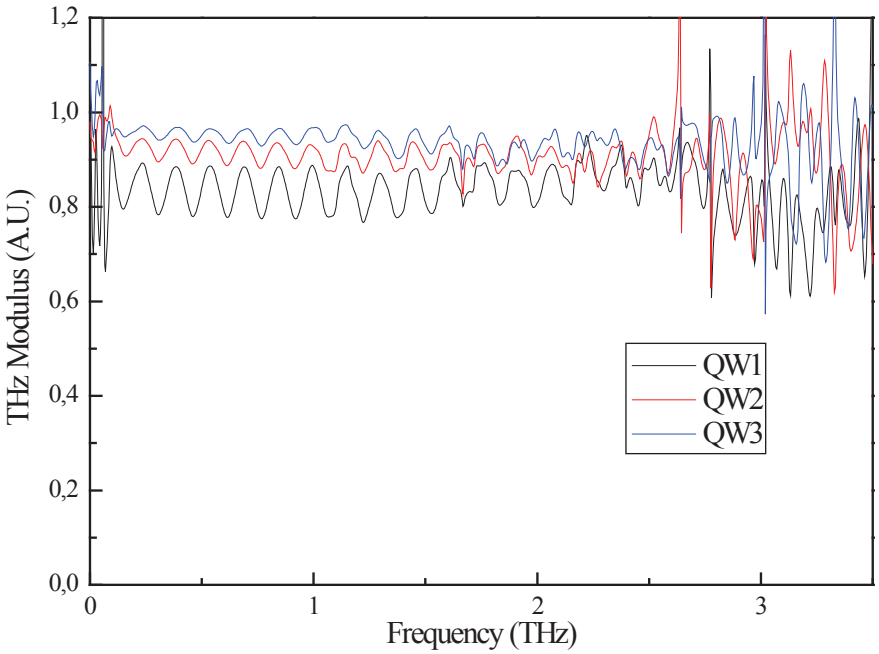

Fig. 5.42*: Transmission spectra modulus for QW-1, QW-2 and QW-3 samples.*

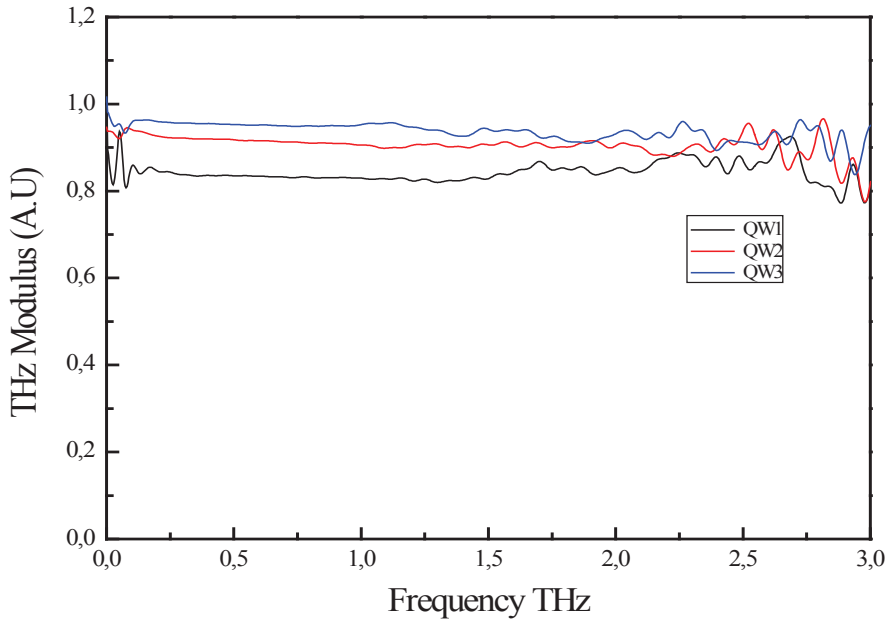

Fig. 5.43: Filtered transmission spectra modulus for QW-1, QW-2 and QW-3 samples.

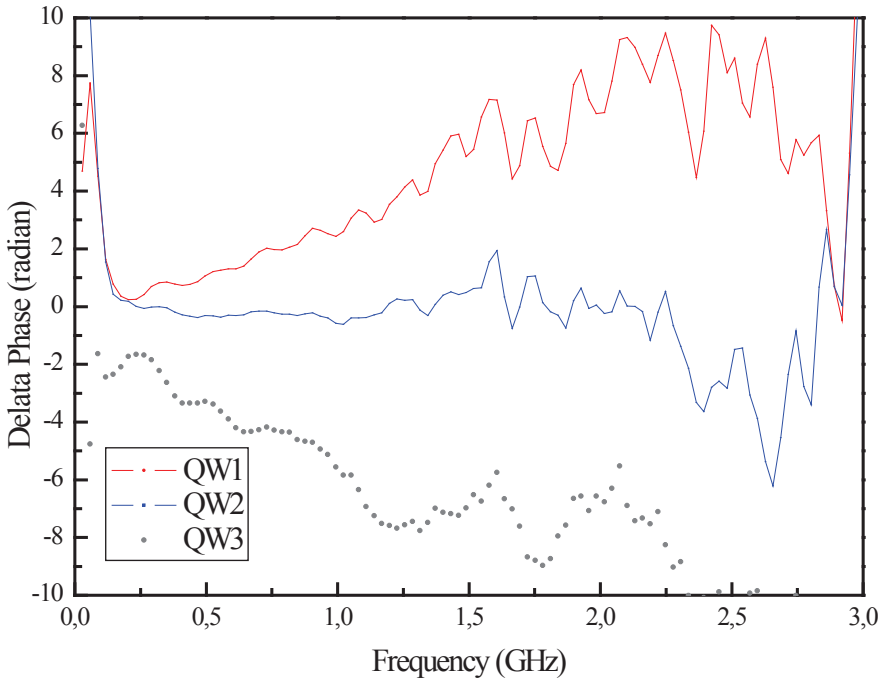

Fig. 5.44: Difference of phase, as regards to the substrate, for QW-1, QW-2 and QW-3 samples.

Fig. 5.44 shows the phase difference for the covered samples as compared to the bare substrate. In the useful 0.2~1.5 THz range, the phase difference increases or decreases depending on the sample: it means that there is some difference in the substrate thickness (≈10 μm), which is bigger than the film thickness (0.34 nm). Thus the phase difference is not exploitable and we cannot extract *n*. Nevertheless, we can exploit the modulus curves by making the hypothesis that the leak of energy in transmission through the layers is only due to absorption and not to the Fresnel losses at the interfaces.

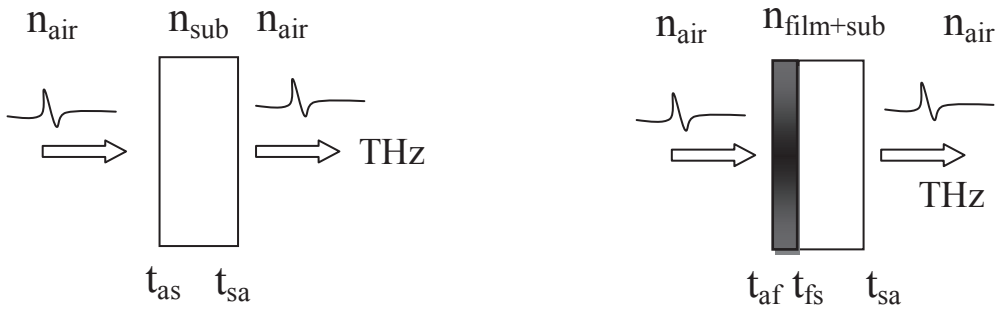

Fig. 5.45: Optical path of THz beam in the TDS for substrate and the sample (film with substrate) transmission measurement.

VI.3.1. Calculation for Index and Conductivity extraction

We consider a sample of thickness *d* with two flat and parallel faces, placed between the two media (Fig. 5.45). Let us write the expression for the transmissions through respectively the bare substrate and the covered substrate. We suppose the substrate is thick enough to allow us to remove the temporal rebounds in the substrate by an adequate time-windowing. But we take into account rebounds in the thin film [11].

$$\begin{aligned} S_{sub} &= t_{as} e^{-j\frac{\omega}{c}\tilde{n}_s d_s} t_{sa} \\ S_{cov} &= t_{af} \frac{e^{-j\frac{\omega}{c}\tilde{n}_f d}}{1 - r_{fa} r_{fs} e^{-2j\frac{\omega}{c}\tilde{n}_f d}} t_{fs} e^{-j\frac{\omega}{c}\tilde{n}_s d_s} t_{sa} \end{aligned} \qquad \text{(V-24a)}$$

Let us write the transfer function:

$$T = \frac{S_{cov}}{S_{sub}} = \frac{t_{af} t_{fs}}{t_{as}} \frac{e^{-j\frac{\omega}{c}\tilde{n}_f d}}{1 - r_{fa} r_{fs} e^{-2j\frac{\omega}{c}\tilde{n}_f d}}. \qquad \text{(V-24b)}$$

where the index *s* refers to substrate, *f* to film and *a* to air . t_{ij} and r_{ij} are the coefficients of transmission and reflection at the interface between media *i* and *j*:

$$t_{ij} = \frac{2n_i}{n_i + n_j}; \qquad r_{ij} = \frac{n_i - n_j}{n_i + n_j}. \qquad \text{(V-25)}$$

From equation (V-25), we re-write the transfer function:

$$T = \frac{1+\tilde{n}_s}{1+\tilde{n}_f} \frac{2\tilde{n}_f}{\tilde{n}_f + \tilde{n}_s} \frac{e^{-j\frac{\omega}{c}\tilde{n}_f d}}{1 - \frac{\tilde{n}_f - 1}{\tilde{n}_f + 1} \frac{\tilde{n}_f - \tilde{n}_s}{\tilde{n}_f + \tilde{n}_s} e^{-2j\frac{\omega}{c}\tilde{n}_f d}} \qquad \text{(V-27)}$$

We can simplify and re-write the above equation as:

$$T = \frac{2\left(1+\tilde{n}_s\right)\tilde{n}_f}{\left(\tilde{n}_f + 1\right)\left(\tilde{n}_f + \tilde{n}_s\right) e^{j\frac{\omega}{c}\tilde{n}_f d} - \left(\tilde{n}_f - 1\right)\left(\tilde{n}_f - \tilde{n}_s\right) e^{-j\frac{\omega}{c}\tilde{n}_f d}} \qquad \text{(V-28)}$$

We make the hypothesis that d is very small and thus $\frac{\omega}{c}\tilde{n}_f\, d << 1$ (at 1 THz, this means that $\tilde{n}_f\, d_{nm} << 10^5$):

$$T \approx \frac{2\left(1+\tilde{n}_s\right)\tilde{n}_f}{\left(\tilde{n}_f+1\right)\left(\tilde{n}_f+\tilde{n}_s\right)\left(1+j\frac{\omega}{c}\tilde{n}_f\, d\right)-\left(\tilde{n}_f-1\right)\left(\tilde{n}_f-\tilde{n}_s\right)\left(1-j\frac{\omega}{c}\tilde{n}_f\, d\right)} \tag{V-29}$$

The last expression simplifies into:

$$T \approx \frac{\left(1+\tilde{n}_s\right)}{\left(1+\tilde{n}_s\right)+j\frac{\omega}{c}d\left(\tilde{n}_f{}^2+\tilde{n}_s\right)} \tag{V-30}$$

We now introduce the conductivity σ of the film:

$$\sigma = j\omega\varepsilon_o\tilde{n}_f{}^2 \quad \text{, and } Z_o=\frac{1}{c\varepsilon_o} \qquad \Rightarrow \qquad j\frac{\omega}{c}=\frac{Z_o\sigma}{\tilde{n}_f{}^2} \tag{V-31}$$

Now, we introduce the conductivity in the transfer function:

$$T \approx \frac{\left(1+\tilde{n}_s\right)}{\left(1+\tilde{n}_s\right)+Z_o\sigma d\left(1+\frac{\tilde{n}_s}{\tilde{n}_f{}^2}\right)} \tag{V-32}$$

If the refractive index of the film is much bigger than that of the substrate, the preceding equation simplifies as:

$$T \approx \frac{1+\tilde{n}_s}{1+\tilde{n}_s+Z_o\sigma d} \qquad \left(\text{if } \frac{\tilde{n}_s}{\tilde{n}_f{}^2} << 1\right), \tag{V-33}$$

Then we write the expression for the electrical conductivity of the film from the transfer function:

$$\sigma \approx \frac{\left(1+\tilde{n}_s\right)\left(1-T\right)}{TZ_o d} \tag{V-34}$$

Experimentally, the observed transmission phase is very small ($\phi < 10° \rightarrow \phi(\text{rad}) < 0.16$). Thus, in a first approximation, we can suppose T is real:

$$\sigma \approx \frac{1}{Z_o d}\frac{1-T}{T}\left(1+n_s-j\kappa_s\right) \tag{V-35}$$

Therefore the real and imaginary conductivities are:

$$\sigma_r \approx \frac{1}{Z_o d}\frac{1-T}{T}\left(1+n_s\right)$$
$$\sigma_i \approx -\kappa_s \frac{1}{Z_o d}\frac{1-T}{T} \qquad \text{(V-36)}$$

The measured imaginary part κ_s of the substrate index is very small (see Fig. 5.48). Therefore, the conductivity is almost real and writes:

$$\sigma \approx \sigma_r \approx \frac{1}{Z_o d}\frac{1-T}{T}\left(1+n_s\right) \qquad \text{(V-37)}$$

Now we can extract the expression for the real and imaginary parts of index from relation (V-33), (V-37):

$$T \approx \frac{\left(1+\tilde{n}_s\right)}{\left(1+\tilde{n}_s\right)+j\frac{\omega}{c}d\left(\tilde{n}_f{}^2+\tilde{n}_s\right)} \Rightarrow \tilde{n}_f{}^2 \approx -n_s - j\frac{1-T}{T}\left(1+n_s\right)\frac{c}{\omega d} = n_f{}^2-\kappa_f{}^2-2jn_f\kappa_f \qquad \text{(V-38)}$$

We compare real and imaginary parts in the above equation and write:

$$n_f{}^2-\kappa_f{}^2 \approx -n_s$$
$$2n_f\kappa_f \approx \frac{1-T}{T}\left(1+n_s\right)\frac{c}{\omega d} \qquad \text{(V-39)}$$

By simplifying the above expressions, the real and imaginary parts of film refractive index are:

$$n_f{}^2 \approx \frac{-n_s \pm \sqrt{n_s{}^2+\left(\frac{\sigma}{\omega\varepsilon_o}\right)^2}}{2} \Rightarrow n_f{}^2 \approx \frac{\frac{\sigma}{\omega\varepsilon_o}-n_s}{2} \qquad , (\sigma >> n_s \rightarrow \sigma^2 >> n_s{}^2) \qquad \text{(V-40a)}$$

$$\kappa_f{}^2 \approx \frac{n_s \pm \sqrt{n_s{}^2+\left(\frac{\sigma}{\omega\varepsilon_o}\right)^2}}{2} \Rightarrow \kappa_f{}^2 \approx \frac{\frac{\sigma}{\omega\varepsilon_o}+n_s}{2} \approx n_f{}^2 \qquad \text{(V-40b)}$$

As the substrate index is very small compared to film, the real and imaginary parts film indexes are almost equal. (V-40a) and (V-40b) are the final expressions we can use to calculate the experimental index of graphene films.

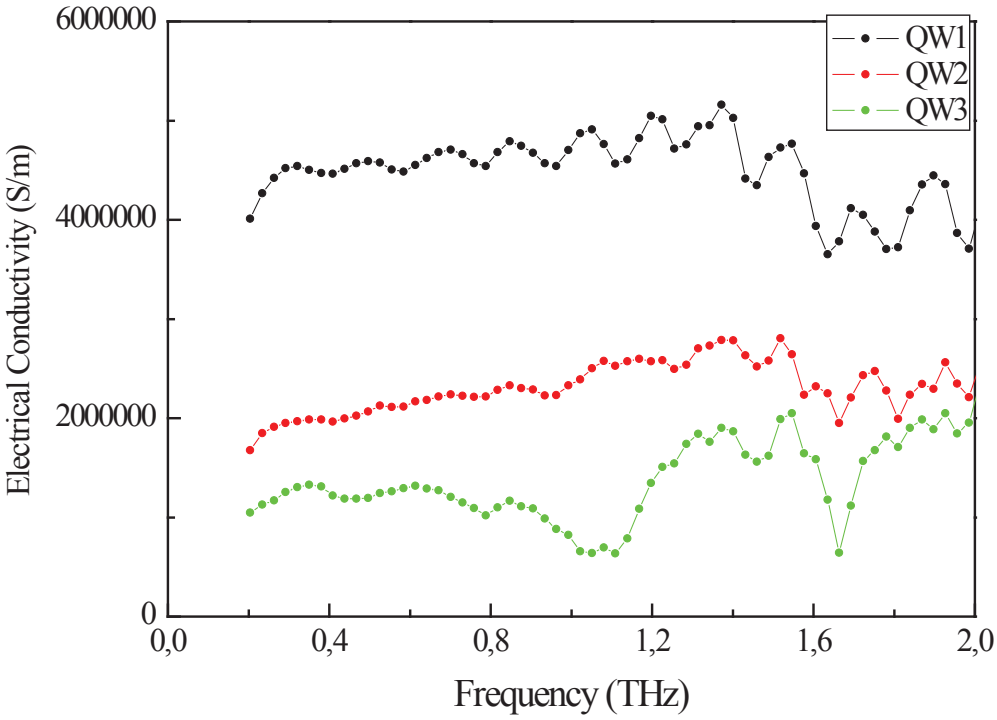

Fig. 5.46: Frequency dependence electrical conductivity of QW1, QW2 and QW3 samples.

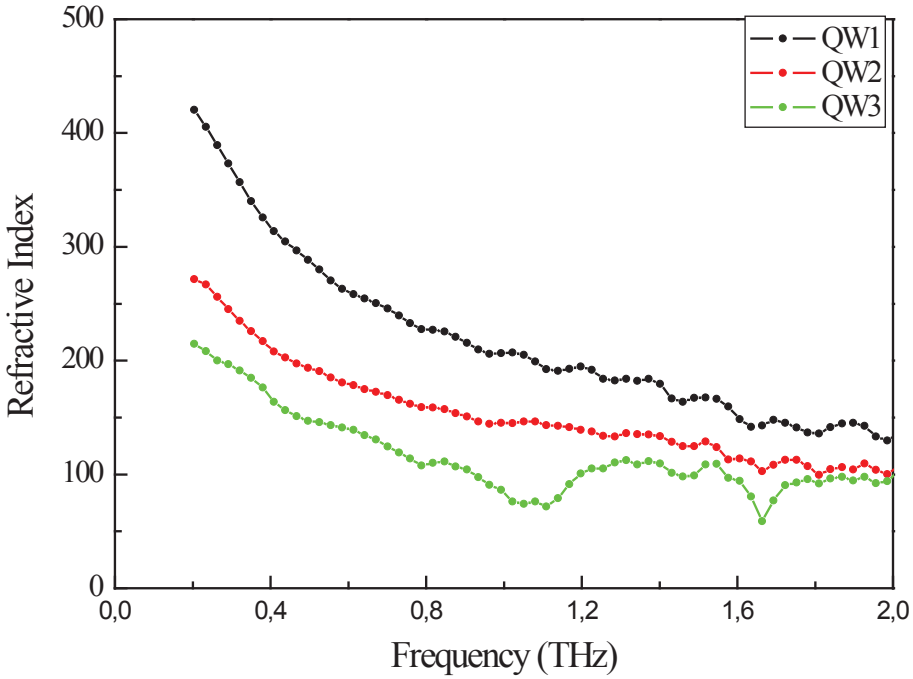

Fig. 5.47: Frequency dependence refractive index of the QW1, QW2 and QW3 sample.

From the experimental transmission data, the electrical conductivity of graphene layers are calculated using relation (V-37) and the results are presented in Fig. 5.46. The magnitude of the conductivity is higher for QW1 than QW2 and QW3 as expected, because the sheet resistance is lower for QW1 than for QW2 and QW3. The conductivity increases slightly with frequency upto 1.6 THz, after that it reduced weakly (I think it may be due to noise). We also calculated the experimental refractive index of graphene films using the relation (V-40) and results are presented in Fig. 5. 47. Refractive index of graphene layers increases with conductivity. So, refractive index of QW1 sample is larger compared to the two other samples QW2 and QW2. Also the refractive index decreases with frequency strongly up to 1.6 THz, and then remains almost stable. Here, the thickness of all graphene layers is equal, so the conductivity and refractive index strongly depend on the sheet resistance. If the conductivity is high, the THz transmission through the sample is low due to larger absorption by free carriers at the surface of the sample (see Fig. 5.43).

Finally, Fig. 5.47 presents the parameters of the substrate material. The index is almost constant and equal to ~1.95 in the useful THz range. The absorption is weak, at the limit of determination of our set up (~1 cm^{-1}). Thus all the absorption features observed in Fig. 5.47 are due to noise; only the tendency of increase is relevant. The material is certainly fused quartz, when we compare our results to the ones by D. Grischkowsky [10]

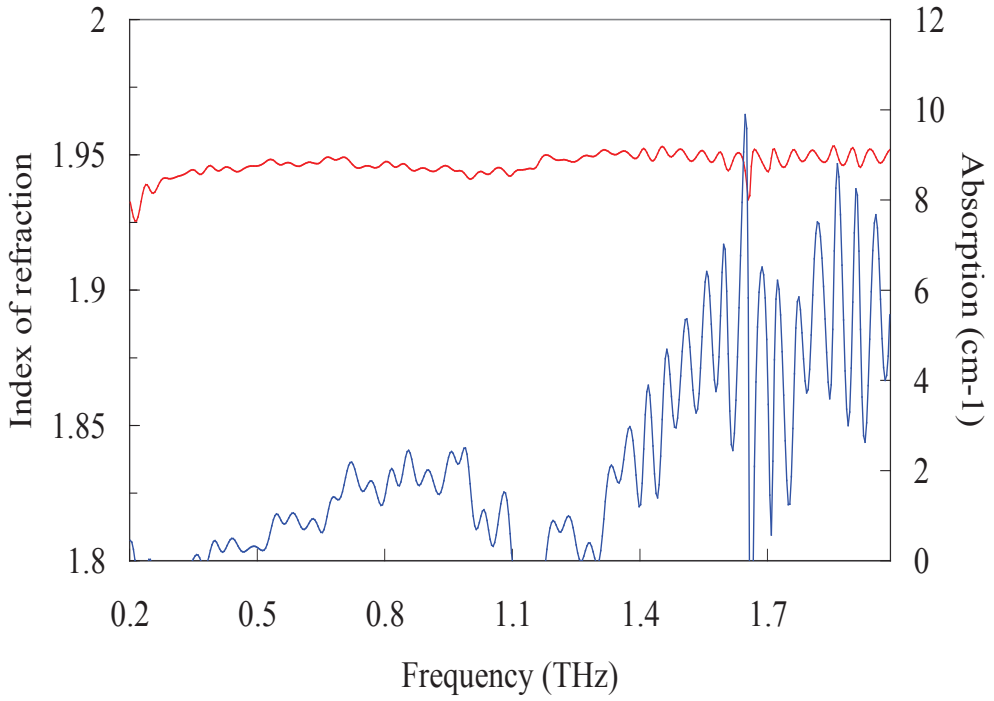

Fig. 5.48: Index of refraction (red line) and absorption (blue line) spectra of the substrate material.

VI.4 Conclusion

In conclusion, we have studied optical and electrical properties of three different graphene layers QW1, QW2 and QW3 using THz-TDS. The THz transmission coefficient for QW1 is higher than other two samples. The electrical conductivity and refractive index of graphene layers are extracted from the experimental amplitude and phase information. The results shows that electrical conductivity is varying as QW1> QW2>QW1, due to larger free carrier concentration in QW1 than others. It also increases slightly with frequency. The refractive index is also higher for QW1 than the two other layers. This change in refractive index is very strong in lower frequency region upto 1.5 THz. Finally, the analysis shows that, the transmission, electrical conductivity and refractive index of graphene layers are strongly depending on its sheet resistance. In any case, graphene layers behave as almost ideal conductor of high conductivity.

References

[1] K. Geim, and K. S. Novoselov, *"The rise of graphene",* Nat. Mater., **6**, 183 (2007).

[2] K.S. Novoselov et al, "*Two-dimensional gas of massless Dirac fermions in graphene";* Nature, **438**, 197 (2005).

[3] A. H. Castro Neto, F. Guinea, N. M. R. Peres, K. S. Novoselov, A. K. Geim, arXiv : con-mat/0709.1163 (2007).

[4] K. S. Novoselov, A. K. Geim, S. V. Morozov, D. Jian, M. I. Katsnelson, I. Grigorieva, S. V. Dubonos, A. A. Firsvo, Nature, **438**, 197 (2005).

[5] C. Berger, Z. Song, X. Li, X. Wu, N. Brown, C. Naud, D. Mayou, T. Li, J. Hass, A. N. Marchenkov, E. H. Conrad, P. N. Frist, W. A. de Heer, Science, **213**, 1191 (2006)

[6] Y. Zhang, Y. Tan, H. L. Stormer, P. Kim, Nature, **438**, 201 (2005).

[7] G. Liang, N. Neophytou, D. E. Nikonov, M. S. Lundstrom, IEEE Trans. Electron Devices, **54**, 657 (2007).

[8] *F. Rana,* IEEE Trans. Nanotechnol., **7**, 91 (2008).

[9] V. Ya. Aleshkin et al, "*THz laser based on optically pumped graphene: model and feasibility of realization,"* JETP Lett., **89**, 70 (2009).

[10] D. Grischkowsky, *"Far Infrared time-domain spectroscopy with terahertz beams of dielectrics and semiconductors,"* JOSA B7, 2006 (1990).

[11] Feng Gao *et al*, "*High frequency Surface Impedance and Penetration Depth of* $YBa_2Cu_3O_7$ *Film: Coheren Time-Domain Spectroscopy Method*," IEEE Transactions on applied super conductivity, **5**, 1970(1995).

ANNEXE I

Broadband ultra-low-loss mesh filters on flexible cyclic olefin copolymer films for terahertz applications

Fabio Pavanello,[1,a)] Frédéric Garet,[2] Mohan-Babu Kuppam,[2] Emilien Peytavit,[1] Mathias Vanwolleghem,[1] François Vaurette,[1] Jean-Louis Coutaz,[2] and Jean-François Lampin[1]
[1]*IEMN, UMR CNRS 8520, Avenue Poincaré, CS 60069, 59652 Villeneuve d'Ascq cedex, France*
[2]*IMEP-LAHC, UMR CNRS 5130, Université de Savoie, Site de Chambery Bâtiment Chablais, 73376 Le Bourget du Lac cedex, France*

(Received 1 February 2013; accepted 14 March 2013; published online 22 March 2013)

The cyclic olefin copolymer (COC) has recently demonstrated promising properties for THz applications due to its extremely high transparency in the THz region. Here, we prove that COC can be efficiently used as substrate material for free-space THz devices through the design, fabrication, and characterization of high-pass metal mesh filters. Measurements are in good agreement with calculations, and a transmittance higher than 75% has been measured between 1.5 THz and 2.5 THz for a single-layer filter. In addition, we prove that stacked meshes can be easily embedded to improve their rejection ratio in the stop-band, while preserving a high transparency in the pass-band. The broadband behavior of these filters should extend up to their diffraction limit estimated at around 6.3 THz for the single-layer filter. © *2013 American Institute of Physics*. [http://dx.doi.org/10.1063/1.4798522]

The cyclic olefin copolymer (COC)[1] is a promising dielectric material with unique properties, such as low water absorption, high chemical resistance, good metal adhesion, flexibility, low permittivity, and high transparency in the visible, UV, and THz region (0.1–10 THz).[2,3] All these properties are very attractive for various THz applications, added to the fact that polymers can be processed using standard photolithographic techniques.

Until now, polypropylene (PP) and benzocyclobutene (BCB) have been widely employed for free-space THz devices[4–7] due to their low absorption coefficient in the THz region ($\alpha = 2\,\mathrm{cm}^{-1}$ and $2.3\,\mathrm{cm}^{-1}$, respectively, at 1 THz).[8,9] Nevertheless, they present various drawbacks associated to some of their processing steps. On one side, PP films are only commercially available under specific film thicknesses, thus introducing design constraints. In addition, as recently observed for the fabrication of 3-D metamaterials, they may present a rough surface (granule size of 6–10 μm) that limits the maximal pattern resolution.[4] On the other side, spin-on BCB films require a hard-bake at 250 °C for 1 h under nitrogen atmosphere.[9] Induced stresses due to a different thermal expansion coefficient between BCB film and carrier substrate can affect the mechanical properties of the film, once removed from the host substrate.[10] Furthermore, it has been shown that a slight oxygen contamination during the hard-bake changes drastically BCB electrical properties.[9] In contrast, COC films can be obtained by spin coating of an appropriate commercial resin to achieve the desired thickness, while requiring a soft-bake at 140 °C for a few minutes.[11] Moreover, their absorption coefficient ($\alpha = 0.2\,\mathrm{cm}^{-1}$ at 1 THz) is nearly an order of magnitude lower than in the case of PP and BCB films.

COC has been already employed in several applications like THz fibers, low-loss interconnects, microfluidic devices, and waveguides.[2,11–13] However, despite these encouraging results, there is still no application of COC thin films (order of μm) as substrates for free-space THz devices. Mesh filters, metamaterials, and photonic band gap structures are only a few examples of applications where a low-loss substrate is essential to improve the overall performances.[14–16]

In this Letter, we investigate COC films as substrates for free-space THz devices through the fabrication of high-pass mesh filters with a cut-off frequency $f_{-3\mathrm{dB}}$ at 1 THz and a transmittance (referred to the power) higher than 75% over a broad range above 1.5 THz. This type of filters can be for instance placed in front of a bolometric detection system to filter out unwanted low frequency-harmonic signals that could arise from multiplier based THz frequency source or amplified spontaneous emission that could arise from photomixer based THz frequency source.[17,18] It can also be used to improve the sideband suppression ratio of a receiver system.[19] The low levels of power generated by photomixers at THz frequencies (order of μW) imply that such filters need to be transparent and broadband enough to maintain the source tenability.[20]

Mesh filters have been extensively investigated since the pioneering work by Ulrich due to their application as infrared filters for astronomy.[21] They have also been employed as polarizers, beam splitters, and reflectors in several domains like imaging, detection, or sensing.[16,21,22] In particular, high-pass filters can be free-standing (only the metal mesh) or substrate-based (the metal mesh lies on a substrate) crossed-mesh metallic patterns as shown in Fig. 1. Free-standing filters are characterized by a considerable thickness (tens of μm) for mechanical reasons, whereas substrate-based ones have metal thicknesses as small as hundreds of nm.[23] The EM response of these filters can be described in the framework of a coupled-mode theory.[24] Free-standing mesh filters cannot be highly transparent for evanescent modes due to their thickness t (a few μm thick is already detrimental

[a)]Electronic mail: fabio.pavanello@ed.univ-lille1.fr

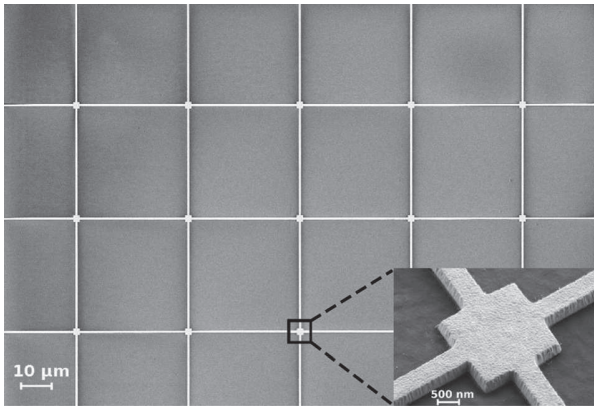

FIG. 1. SEM image of a single-layer filter before Si wafer removal. The lattice homogeneity (period of 38 μm) is well-maintained over the whole mesh surface. Inset: close-up of a mesh-cross, squares have been added to improve the adhesion and stability of the mesh wires (width of 500 nm) without influencing the EM response.

because of the exponential decay). The only solution is to make each aperture working as a classical waveguide, but the mesh aperture a has to be larger than 150 μm to allow transmission at frequencies higher than 1 THz. This reasoning implies that a high transparency over a broad bandwidth (larger than the mesh period d in wavelength) can be only achieved by a substrate-based filter. However, the substrate has to present low losses and permittivity and, at the same time, be well-suited to be processed by microelectronics techniques. In particular, the wire width w has to be as small as possible in order to decrease the reflection at the metal surface. Finally, a trade-off between all of these parameters has to be chosen to achieve f_{-3dB} at 1 THz. These considerations are also valid for a stacked structure but, due to a higher rejection ratio in the stop-band, d has to be larger than in the case of a single-layer filter. Here, the transmission properties of single-layer and double-layer filters are presented.

In order to obtain an accurate design taking into account effects like Fabry-Pérot fringes and/or losses in the substrate, a 3-D full-wave field simulation software (MICROWAVE STUDIO from CST) based on finite integration technique has been used.[14] Floquet's modes and infinite periodic boundary conditions have been chosen for the design to optimize the computing time and accuracy. The unit cells of the simulated structures are reported in Fig. 2. A lossy model (DC conductivity) for the metal mesh and an approximate 1st order Debye

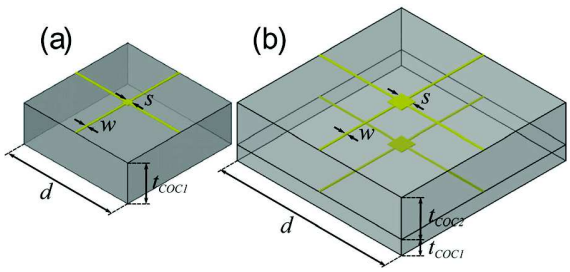

FIG. 2. Unit cells of the mesh-filters used for the simulations. Figs. 2(a) and 2(b) show the structures of the single-layer and double-layer filters, respectively. The structures are in scale and their dimensions are reported in Table I.

TABLE I. Parameters used in the design of the single-layer, the double-layer, and the triple-layer (only simulated) filters with f_{-3dB} at 1 THz (units are μm).

	d	w	s	t_{COC1}	t_{COC2}	t_{COC3}	t_{metal}
Single	38	0.5	2	13	…	…	0.31
Double	59	0.5	5	5	13	…	0.31
Triple	70	0.5	5	5	13	13	0.31

model for the substrate have been applied. In particular, the substrate permittivity is modeled by an algorithm using as input values a relative permittivity $\epsilon_r = 2.34$ and a tangent loss dielectric factor $\tan\delta = 2.3 \times 10^{-3}$ at 2.5 THz.[25] These parameters have been obtained by previous measurements of COC samples. The typical design of mesh filters has been slightly modified by adding a square block of side s at each mesh-cross (see Fig. 1). This element has no influence on the transmission properties for small s, but it is mechanically useful to keep the mesh well-aligned during the fabrication process, in particular when a new COC layer is deposited on top of it. In Table I, we summarize the parameters optimized by simulations for the fabricated single-layer and double-layer filters and the triple-layer (only simulated) filter.

The fabrication consists in COC[26] deposition by spin coating over an aluminum sacrificial layer onto a silicon substrate. Then, COC is cured at 140 °C for 2 min to obtain low stress films. Electron beam lithography is used for pattern definition due to the size of the smallest element ($w = 0.5$ μm).The size of w is a trade-off between the design and the fabrication constraints associated to the mesh stability and the possibility to use deep-UV lithography for cost effective fabrication process. Chrome (10 nm) and gold (300 nm) films are deposited by thermal evaporation followed by a lift-off technique. In the case of the double-layer structure, all of the fabrication steps are repeated. Finally, the filter is removed from the host substrate through a wet etching of the sacrificial layer and placed onto an annular holder as illustrated in Fig. 3. This fabrication process leads to high-quality lattices over large film surfaces (up to 2×2 cm^2 area) with metallic patterns characterized by a high definition as underlined in the inset of Fig. 1.

The measurements of the filters have been performed by THz time domain spectroscopy (THz-TDS) using a setup

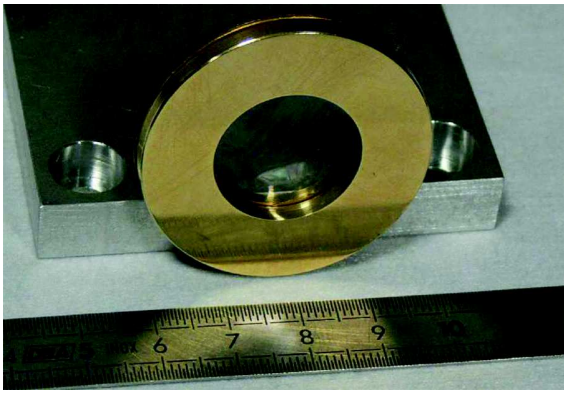

FIG. 3. Photograph of the single-layer filter mounted onto an annular holder. COC high transparency and sub-μm mesh wires width make the filter hardly visible.

based on low-temperature grown GaAs photoconductive switches illuminated by 100 fs-800 nm laser pulse for the emission and the detection of the signal. All of our spectra have been recorded under normal incidence, and no preferential polarization has been used due to the filter symmetry. Details of our setup and of the data post-processing can be found elsewhere.[27] A good agreement between simulation and measurements is observed for all devices. In particular, Fig. 4(a) underlines the key role of w in achieving high values of transmittance above 1.5 THz. A transmittance higher than 76% is obtained between 1.5 and 2.5 THz in the case of $w = 0.5\ \mu$m with $f_{-3\text{dB}}$ at 1.02 THz. A rejection ratio of 13 dB/decade is achieved in the frequency range 0.25-2.5 THz. Main loss mechanisms in these filters are input and output coupling between plan wave and waveguide modes and destructive Fabry-Pérot fringes (for comparison, the film without the mesh presents a calculated transmittance of 90% at 2 THz). Metal reflections are negligible for $w = 0.5\ \mu$m because of the extremely thin mesh wires (the metal covers less than 3% of the overall surface). Finite metal conductivity at these frequencies is not a major cause of losses (for instance, a value of 0.12 dB higher can be obtained computationally for $w = 0.5\ \mu$m in a perfect electric conductor approximation at 2 THz).

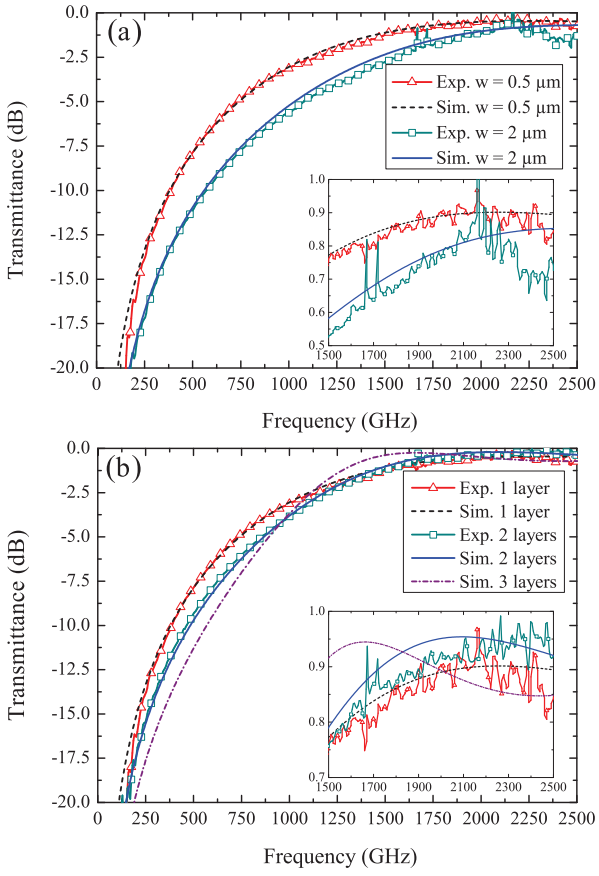

FIG. 4. Transmission properties of the mesh filters. Insets are in linear scale. Fig. 4(a) shows the comparison between two single-layer filters with different width w and same period $d = 38\ \mu$m. The inset reveals a higher transmittance above 1.5 THz for the filter with $w = 0.5\ \mu$m. Fig. 4(b) shows that multi-layer filters are able to increase the rejection ratio in the stop-band while keeping a high transmittance above 1.5 THz. The red curve (up triangle) and the black curve (dashed) have been reported as a reference and correspond to the same curves of Fig. 4(a). The inset emphasizes the role of Fabry-Pérot fringes in the pass-band.

Fig. 4(b) shows that a higher rejection ratio can be achieved in the stop-band when a stacked structure is used. Here, only two layers are considered but, as reported in the computational results, a structure with three layers would increase this effect. The double-layer filter has a measured rejection ratio of 15 dB/decade, while the 3-layers filter has a calculated rejection ratio of 17 dB/decade in the frequency range 0.25-2.5 THz. Computational results have shown that a larger dielectric spacing can be used to increase the rejection ratio, but a 13 μm thick dielectric spacing is used to achieve an accurate electronic alignment during the lithographic process. In all cases, the properties of COC are certainly critical to have low absorption in the substrate and low Fabry-Pérot fringes amplitudes.[14] It is worth noticing that the addition of layers to the structure forces to increase the mesh period to keep an $f_{-3\text{dB}}$ at the same frequency due to the higher rejection ratio of stacked meshes. However, a larger period causes the diffraction to shift to lower frequencies, and thus, a low refractive index (effective for a thin substrate compared to the wavelength) is convenient to limit the amount of this shift.

In conclusion, we have shown that COC is a promising candidate for the next generation of free-space devices for THz applications due to its particularly suitable dielectric properties at these frequencies and to the possibility of fabricating accurate and reliable sub-μm metallic patterns, as demonstrated in this Letter. These features allow for the fabrication of robust, highly transparent broadband filters that can be integrated together with incoherent detection systems.

This work received financial support from the Seventh Framework Program for Research of the European Commission FP7/2007-2013 (Grant Agreement 238393—Marie-Curie initial training network "MITEPHO").

[1]Synthesized by Topas Advanced Polymer GmbH under the trade name of Topas™.
[2]K. Nielsen, H. K. Rasmussen, A. J. Adam, P. C. Planken, O. Bang, and P. U. Jepsen, Opt. Express **17**, 8592 (2009).
[3]P. D. Cunningham, N. N. Valdes, F. A. Vallejo, L. M. Hayden, B. Polishak, X.-H. Zhou, J. Luo, A. K.-Y. Jen, J. C. Williams, and R. J. Twieg, J. Appl. Phys. **109**, 043505 (2011).
[4]M. Navarro-Cía, S. A. Kuznetsov, M. Aznabet, M. Beruete, F. Falcone, and M. S. Ayza, IEEE J. Quantum Electron. **47**, 375 (2011).
[5]C. Croenne, F. Garet, E. Lheurette, J.-L. Coutaz, and D. Lippens, Appl. Phys. Lett. **94**, 133112 (2009).
[6]P. Weis, O. Paul, C. Imhof, R. Beigang, and M. Rahm, Appl. Phys. Lett. **95**, 171104 (2009).
[7]C. Jansen, S. Wietzke, V. Astley, D. M. Mittleman, and M. Koch, Appl. Phys. Lett. **96**, 111108 (2010).
[8]Y.-S. Jin, G.-J. Kim, and S.-G. Jeon, J. Korean Phys. Soc. **49**, 513 (2006).
[9]E. Perret, N. Zerounian, S. David, and F. Aniel, Microelectron. Eng. **85**, 2276 (2008).
[10]S. Bothra, M. Kellam, and P. Garrou, J. Electron. Mater. **23**, 819 (1994).
[11]E. Peytavit, C. Donche, S. Lepilliet, G. Ducournau, and J.-F. Lampin, Electron. Lett. **47**, 453 (2011).
[12]P. S. Nunes, P. D. Ohlsson, O. Ordeig, and J. P. Kutter, Microfluid. Nanofluid. **9**, 145 (2010).
[13]P. I. Okagbare, J. M. Emory, P. Datta, J. Goettert, and S. A. Soper, Lab. Chip **10**, 66 (2010).
[14]H. A. Smith, M. Rebbert, and O. Sternberg, Appl. Phys. Lett. **82**, 3605 (2003).
[15]H. Tao, A. C. Strikwerda, K. Fan, C. M. Bingham, W. J. Padilla, X. Zhang, and R. D. Averitt, J. Phys. D: Appl. Phys. **41**, 232004 (2008).

[16]S. Gupta, G. Tuttle, M. Sigalas, and K.-M. Ho, Appl. Phys. Lett. **71**, 2412 (1997).
[17]W. Li and J. Yao, IEEE Trans. Microwave Theory Tech. **58**, 3259 (2010).
[18]H. Song, N. Shimizu, T. Furuta, A. Wakatsuki, and T. Nagatsuma, Appl. Phys. Lett. **93**, 241113 (2008).
[19]I. S. Gregory, T. D. Drisdale, W. R. Tribe, D. R. S. Cumming, M. J. Evans, M. Missous, and E. H. Linfield, in *Joint 29th Int. Conf. on Infrared and Millimeter Waves and 12th Int. Conf. on Terahertz Electronics*, 27 September-1 October 2004, pp. 587–588.
[20]S. Preu, J. Appl. Phys. **109**, 061301 (2011).
[21]R. Ulrich, Infrared Phys. **7**, 37 (1967).
[22]S. Yoshida, E. Kato, K. Suizu, Y. Nakagomi, Y. Ogawa, and K. Kawase, Appl. Phys. Express **2**, 012301 (2009).
[23]P. A. R. Ade, G. Pisano, C. Tucker, and S. Weaver, Proc. SPIE **6275**, 62750U (2006).
[24]F. J. Garcia-Vidal, L. Martin-Moreno, T. W. Ebbesen, and L. Kuipers, Rev. Mod. Phys. **82**, 729 (2010).
[25]A. R. Djordjević, R. M. Biljić, V. D. Likar-Smiljanić, and T. K. Sarkar, IEEE Trans. Electromagn. Compat. **43**, 662 (2001).
[26]Grade T8007—Spin-on resin: mr-I T85-5.0 XP by micro resist technology.
[27]L. Duvillaret, F. Garet, and J. L. Coutaz, IEEE J. Sel. Top. Quantum Electron. **2**, 739 (1996).

ANNEXE II

Carbon Nanotube Terahertz Spectroscopy: Study of Absorption and Dispersion Properties of SWNT and MWNT

Horacio Lamela[a*], Ehsan Dadrasnia[a],
Frédéric Garet[b], Mohan Babu Kuppam[b], and Jean-Louis Coutaz[b]

[a] Optoelectronic and Laser Technology Group (GOTL), Carlos III de Madrid University, 28911 Leganes, Madrid, Spain.
[b] IMEP-LAHC, UMR CNRS 5130, Université de Savoie, 73376 Le Bourget du Lac Cedex, France.

ABSTRACT

In this paper, we report on the optical and electrical properties of single-walled (SWNT) and multi-walled (MWNT) carbon nanotube thin-films investigated by terahertz time-domain spectroscopy. Our study focuses on the absorption and dispersion properties of the single-walled and multi-walled carbon nanotubes in frequency range of 0.1-2 THz. The results show that the single-walled carbon nanotubes thin-films have the great frequency-dependent of the power absorption coefficient, the index of the refraction and conductivity compared to the multi-walled carbon nanotubes thin-films because more mobile carries of carbon nano-structure as well as effective of carbon nanotubes length and diameter.

Keywords: terahertz, time-domain spectroscopy, carbon nanotube, conductivity.

1. INTRODUCTION

Terahertz time-domain spectroscopy (THz-TDS) is a well-established technique for characterizing the electromagnetic response of materials in the far infrared. For example, this technique has been used for studying the properties of carbon nanostructures, like carbon nanotubes (CNT) [1]. As compared to Fourier transform far infrared spectroscopy (FTIR) used previously to determine the CNT response [2], THz-TDS exhibits many advantages, namely the coherence of the THz radiation leading to get directly the magnitude and phase of the signals, the very good signal over noise ratio (more than 60 dB), the extremely large achievable bandwidth and the possibility of performing time-resolved measurements, for example through pump-and-probe techniques [3]. This allows one to derive both the refractive index and the coefficient of absorption of materials, using samples with flat and parallel faces. The precision could be as good as 0.01 on the refractive index and less than 0.1 cm^{-1} on the absorption coefficient, without the need of employing the Kramers-Kronig relationship. Nevertheless, the frequency resolution of THz-TDS is of the order of a few GHz, worst than the one of FTIR, but which is sufficient to study most of common materials that show broadband spectral features. Especially, THz-TDS is well adapted to characterize the doping level and the free carrier dynamics of conducting and semi-conducting samples.

CNTs and graphene structures and their properties have been studied by several means such as photonic emission, scanning, microscopy and tuning fields. It appears that several physical parameters of CNT's have characteristic resonant frequencies within the THz range [4-8]. Since the first report on THz-TDS study of CNT published in the late 90's [4], CNT samples have been subject to intense research in the THz range and more recent papers have permit to define precise physical models to describe the THz properties of CNTs films [5-7,11-13].

In this paper, we present an experimental THz-TDS characterization of single-walled carbon nanotubes (SWNTs) and multi-walled carbon nanotubes (MWNTs) thin film samples. As compared to previous studies, we use pure CNT films, i.e. the CNTS are not embedded in a hosting material. This study aims us to compare the power absorption, refractive

* horacio@ing.uc3m.es.

Carbon Nanotubes, Graphene, and Associated Devices IV, edited by Didier Pribat, Young-Hee Lee, Manijeh Razeghi,
Proc. of SPIE Vol. 8101, 81010G · © 2011 SPIE · CCC code: 0277-786X/11/$18 · doi: 10.1117/12.895221

index, conductivity and free carrier density of these CNTs thin film samples. In section 2, we express the CNTs thin-films dimensions and characterizations. Finally, the results in terms of comparing the optical and electrical properties of these CNTs films will be analyzed and discussed in section 4.

2. CNTS SAMPLES AND THZ-TDS EXPERIMENTAL SETUP

Since the deposition of the carbon nanotube thin-film on the high permittivity gate insulator does not degrade the perfect high speed carrier transport of CNT, we use two SWNT and MWNT thin films which were deposited on a transparent fused quartz substrate whose size is 2.5×2.5×0.215 cm^3 as shown in Figure 1. The thickness of these two CNTs thin-films under measurement has been measured with a profiler (1.09 µm for the SWNT film and 1.20 µm for the MWNT film) while the CNTs are 15-µm long (MWNT) and 5-µm long (SWNT). Their diameters are respectively 15 nm and 1.5 nm for MWNT and SWNT. The substrate is almost transparent as compared to the CNT-covered sample, as 60~80 % of the THz signal is absorbed in the CNT films. The THz characterization of the sample is performed using a classical THz time-domain spectroscopy (TDS) set up shown in Figure 2 [9]. The samples are located at the waist of the THz beam that could be considered as an almost perfect Gaussian beam, whose section at the waist is much smaller than the 2.5×2.5 cm^2 sample surface. The Rayleigh length of the THz beam, throughout the whole 0.1-3 THz experimental range, is much bigger than the sample thickness. Therefore, the samples can be considered as illuminated by a plane THz wave. The experimental frequency resolution is set at 30 GHz, which is sufficient for characterizing the samples as their spectra do not show any sharp or narrow feature.

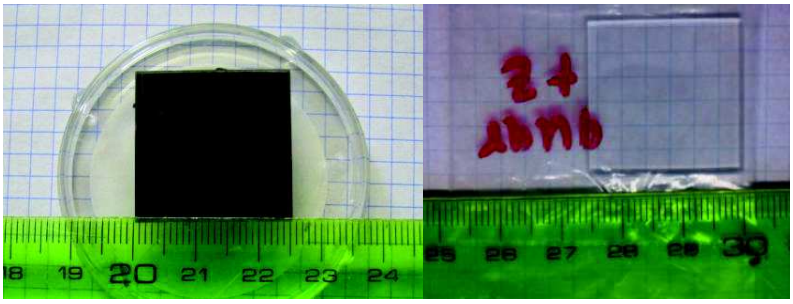

Figure 1. (a) The CNT thin-film deposited over the fused quartz substrate and (b) the stand alone fused quartz substrate.

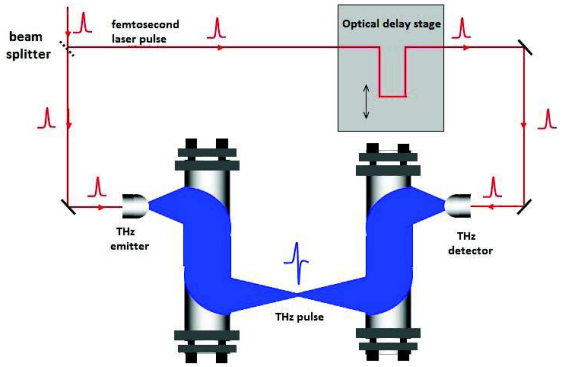

Figure 2. Schematic of the THz-TDS set up. The sample is located at the THz beam waist.

3. TERAHERTZ SIGNAL ANALYSIS

The THz-TDS characterization procedure of the CNT film is performed as follows. We measure 3 temporal waveforms, firstly a reference signal without samples in between the antennae, then a signal with the quartz substrate in the set up, and finally the signal with the substrate covered by the CNT film. Figure 3 shows the recorded THz pulses in time-domain (a) and their spectra –modulus– (b) for the reference, the quartz substrate, and the MWNT and SWNT samples. Let us notice that the samples are located at the waist of the THz beam in between two parabolic mirrors (Fig. 2), and that the Rayleigh length of the THz beam is much bigger than the sample thickness.

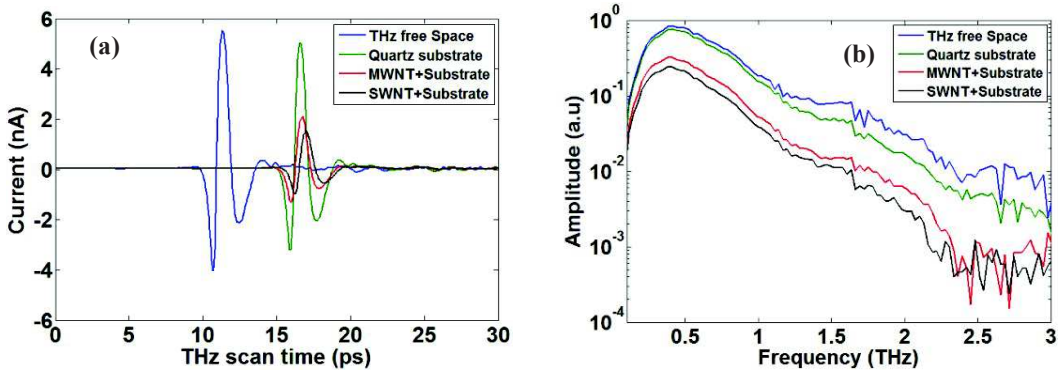

Figure 3. (a) THz pulses in time-domain and (b) corresponding spectrums of the THz free space, quartz substrate, MWNT and SWNT samples (thin-film deposited on quartz substrate).

Therefore, the beam can be considered as parallel throughout the sample, and we can use classical extracting technique to calculate both the refractive index and the absorption coefficient of the films [10]. Let us recall the principle of the extraction technique proposed by L. Duvillaret *et al.* in [10].

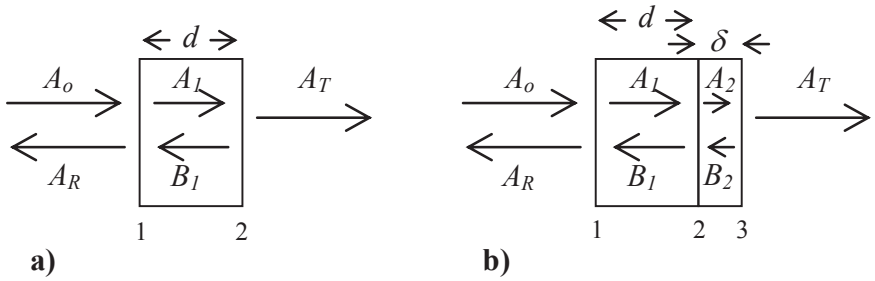

Figure 4. Schematic of the THz field reflected and transmitted by the samples. Left: Single slab with parallel faces; Right: Slab covered with a film.

A sample, with flat and parallel faces whose thickness is d and the complex refractive index is $\tilde{n}$, is illuminated under normal incidence by a parallel THz beam of pulsation ω (Fig. 4a). A simple analysis of the electromagnetic response of the slab gives the expression T of the transmission coefficient:

$$T(\omega) = \frac{A_T}{A_o} = \frac{t_1 t_2 e^{j(k_1 - k_3)d}}{1 - r_1 r_2 e^{2jk_1 d}} \qquad (1)$$

where A_o and A_T are respectively the incoming and transmitted amplitudes, c is the velocity of light in vacuum, r_1 (t_1) and r_2 (t_2) are the reflection (transmission) coefficients at respectively the first and second interfaces, and k_1 and k_3 are the

wavevector moduli respectively in the slab and in the surrounding medium. When the sample is located in air (or in vacuum), (1) simplifies into:

$$T(\omega) = \frac{4\tilde{n}}{(\tilde{n}+1)^2} \frac{e^{-j\frac{\omega}{c}(\tilde{n}-1)d}}{1 \mp \left(\frac{\tilde{n}-1}{\tilde{n}+1}\right)^2 e^{-2j\frac{\omega}{c}\tilde{n}d}} \tag{2}$$

The extracting method is based on finding the zeros of the function $T_{meas} - T(\omega)$ in the complex plane whose axes are the real and imaginary parts of $\tilde{n}$, where T_{meas} is the measured signal. Because of the oscillatory behavior of $T(\omega)$, an error function is defined and used to determine $\tilde{n}$. As an example, Figure 5 shows the so-determined index of refraction and coefficient of absorption of the fused quartz substrate versus frequency. Both the relatively high value of the index of refraction and the increase of absorption with frequency demonstrate that the substrate material is not a pure fused quartz as indicated by the supplier, but certainly a silicate glass with a low doping concentration.

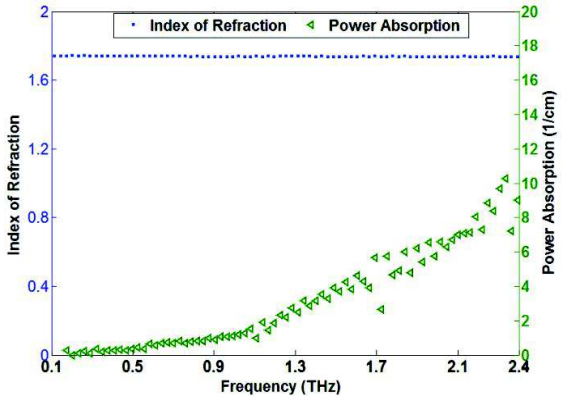

Figure 5. The power absorption and the refractive index of quartz substrate.

When the slab of known complex refractive index $\tilde{n}$ is covered by a film (Fig. 4b) of complex refractive index $\tilde{n}_f$ and thickness δ, the transmitted field takes a more complicated expression than (1):

$$A_T = \frac{t_1 t_2 t_3 e^{j2k_2(\delta-d)} e^{-jk_3\delta} e^{jk_1 d} A_o}{1 - r_2 r_3 e^{j2k_2(\delta-d)} - r_1\left[r_2 + r_3\left(t_2^{\,2} - r_2^{\,2}\right)e^{j2k_2(\delta-d)}\right]e^{2jk_1 d}} \tag{3}$$

r_1 (t_1), r_2 (t_2), and r_3 (t_3) are the coefficients of reflection (transmission) at the first, second and third interfaces, and $k_1 = \frac{\omega}{c}\tilde{n}$, $k_2 = \frac{\omega}{c}\tilde{n}_f$ and $k_3 = \frac{\omega}{c}$. One uses the bare substrate as the reference. Then the differential signal becomes:

$$\frac{A_T}{A_{Tref}} = \frac{t_2 t_2^{*-1} t_3 e^{jk_2\delta} e^{-jk_3\delta} e^{-jk_2 d} e^{jk_3 d}\left(1 - r_1 r_2^* e^{2jk_1 d}\right)}{1 - r_2 r_3 e^{j2k_2\delta} e^{-2jk_2 d} - r_1\left[r_2 + r_3\left(t_2^{\,2} - r_2^{\,2}\right)e^{-2jk_2 d} e^{j2k_2\delta}\right]e^{2jk_1 d}} \tag{4}$$

where r_2^* (t_2^*) are the reflection and transmission coefficient at the sample-air interface. Extracting $\tilde{n}_f$ from (4) is a difficult task. However, if the substrate is much thicker than the film, one can time-window the recorded waveform in order to get rid of the temporal echoes that reflect back and forth in the substrate. Thus, the incoming field A_1 at the interface 2 between the substrate and the film simply writes $A_1 = t_1 A_o e^{jk_1 d}$ and the transmitted field is:

$$A_T = \frac{t_1 t_2 t_3 e^{j(k_2-k_3)(\delta-d)} e^{j(k_1-k_3)d}}{1 - r_2 r_3 e^{2jk_2(\delta-d)}} A_o \tag{5}$$

with $r_2 = \frac{\tilde{n} - \tilde{n}_{\blacksquare}}{\tilde{n} + \tilde{n}_{\blacksquare}}$ and $r_3 = \frac{\tilde{n}_{\blacksquare} - 1}{\tilde{n}_{\blacksquare} + 1}$. Then one uses, as the reference signal, the signal A_S transmitted through the substrate, with the same time-window as the signal transmitted through the covered sample. The ratio of both gives:

$$\frac{A_{T,film}}{A_{T,substrate}} = \frac{t_2 t_3}{t_2^*} \frac{e^{jk_2(\delta-d)} e^{-jk_3\delta}}{1 - r_2 r_3 e^{2jk_2(\delta-d)}} \tag{6}$$

with $r_{S2} = \frac{\tilde{n} - 1}{\tilde{n} + 1}$. This expression is similar to the one (1) obtained for the single slab case. Thus the classical extraction procedure may be used in the case of thin films, as soon as the refractive index $\tilde{n}$ of the substrate is known. Practically, it is requested to measure the reference signal (without any sample in the set up), and then the substrate alone. The classical extraction procedure gives $\tilde{n}$. Then the signal is measured with the covered sample in the set up. From the experimental T_{f-meas} and using both (5) and the extraction procedure, $\tilde{n}_{\blacksquare}$ is easily obtained. Let us notice that, provided the substrate is thick enough to reject all the rebounds in the substrate, this method does not need any simplification, such as a small optical thickness of the film or a transparent substrate.

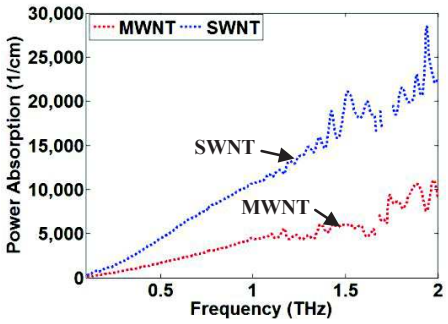

Figure 6. Power absorption of the SWNT**s** and MWNT**s** thin films.

4. RESULTS AND DISCUSSION

The extraction of the CNTs film parameters is performed as explained in paragraph 3. Figures 6 and 7 present the results of power absorption and refractive index of these two CNTs samples. We remove some points in the curves around 1.7 THz corresponding to artefacts due to residual water vapour absorption lines (the water vapour rate remaining in the experimental chamber is about several percents). The measured power absorption of the SWNTs thin films is higher than the MWNTs one at higher frequencies. This can be attributed to the larger length and diameter of MWNTs (length of 15 µm and diameter of 15 nm) as compared to SWNTs (length of 5 µm and diameter of 1.5 nm). The order of magnitude of the absorption and refractive index of both MWNTs and SWNTs are about 10 times bigger than those reported by Jeon *et al.* [11]. This difference originates certainly in a bigger nanotube density within our CNT films than in the samples studied by Jeon *et al*. Also we did not perform a post-treatment to remove residual metallic particles from the film as done by Jeon *et al.*

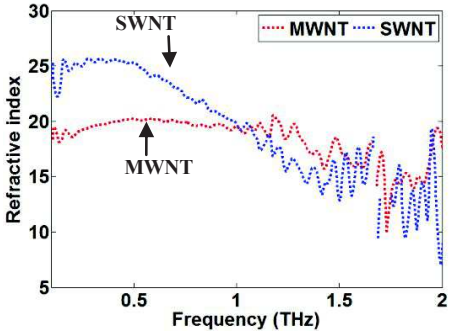

Figure 7. Refractive index of the SWNT and MWNT thin-films.

The frequency response curves for both refractive index and absorption look more or less like the one of a metallic layer (Drude model) with a plasma frequency at several THz. This is validated by extracting the conductivity of the material from its electromagnetic response. In fact, for conducting materials, the imaginary part ε_i of the dielectric constant writes:

$$\varepsilon_i = \varepsilon_{bound} - \frac{\sigma}{\omega \varepsilon_o}, \tag{7}$$

where ε_{bound} accounts for the bound electron contribution (displacement current), σ is the conductivity (conduction current), ω the pulsation and ε_o the permittivity of vacuum. In ideal metals obeying the Drude model, the displacement current contribution may be neglected and thus σ increases proportionally to the frequency. The conductivity of the CNT determined from the results shown in Figures 6 and 7 is plotted in Figure 8. We observe the expected overall increase of σ with the frequency. Nevertheless, the curves show additional features and deviations from the Drude model that can be attributed to the already reported excitation of 2 phonons along the CNT chain [12]. One should notice that the CNT films have not a dense crystalline structure, but they are a random arrangement of tubes. Thus they should be treated, from an electromagnetic point-of-view, as an effective medium made of CNT embedded in air. The important point is that the SWNT sample has a greater conductivity compared to the MWNT one because of low surface defects in single-walled CNTs which can be verify by recent results by Jung *et al.* [2]. As power absorption, refractive index and conductivity are dependant parameters, the difference in the SWNT and MWNT films response can also be explained by surface defects of carbon nano-structure.

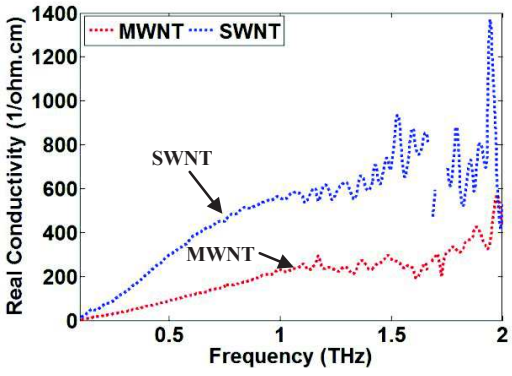

Figure 8. Real conductivity of the SWNT and MWNT thin films.

5. CONCLUSION AND FUTURE WORK

THz electromagnetic signals will certainly push the border in science and technology (sensing, imagery, telecoms…) to higher performance. Thus high technology devices and systems are more and more compulsory. They request new technologies and materials, among which CNTs are promising due to their unique conductivity behaviour. This paper is a contribution to the effort of developing new CNT devices for the THz range. We presented experimental THz-TDS results for two different CNT thin-samples (e.g., SWNT and MWNT) in frequency range of 0.1-2 THz. Even if our samples are not the same as those previously studied by other teams, the obtained measurement data in this study confirm the results published in the literature. They show that the values of refractive index, power absorption, conductivity and filling factor are larger in SWNTs than in MWNTs because of a) the increased number of surface defects, and b) more mobile carriers at high filling factor in single-walled carbon nanotube compared to multi-walled carbon nanotube sample. In a next stage, we will investigate and compare the THz optical and electrical properties of CNTs thin film with graphene thin film.

ACKNOWLEDGEMENT

This work is supported by the European Community (project FP7 ITN Marie Curie MITEPHO number 238393) [14], in order to develop compact tunable dual-mode diode lasers for THz spectroscopy in sensing and biomedical applications.

REFERENCES

[1] C. Kang, I. H. Maeng, S. J. Oh *et al.*, "Characterization of carbon nanotubes utilizing terahertz electromagnetic waves," Proceedings of ISAP 2005, vol.3, 1173-6, Seoul, Korea.

[2] G. B. Jung, Y. Myung, Y. J. Cho *et al.*, "Terahertz Spectroscopy of Nanocrystal-Carbon Nanotube and -Graphene Oxide Hybrid Nanostructures," J. Phys. Chem. C, 114(25), 11258-11265 (2010).

[3] See for example *Sensing with Terahertz Radiation*, edited by D. Mittleman, Spinger (2003); *TeraHertz Optoelectronics*, edited by K. Sakai, Springer (2005).

[4] A. Ugawa, A. G. Rinzler, and D. B. Tanner, "Far-infrared gaps in single-wall carbon nanotubes," Physical Review B, 60(16), R11305 (1999).

[5] T.-I. Jeon, J.-H. Son, K. H. An *et al.*, "Terahertz absorption and dispersion of fluorine-doped single-walled carbon nanotube," Journal of Applied Physics, 98(3), 034316-034316-4 (2005).

[6] C. Kang, I. H. Maeng, S. J. Oh *et al.*, "Terahertz optical and electrical properties of hydrogen-functionalized carbon nanotubes," Physical Review B, 75(8), 085410 (2007).

[7] E. P. J. Parrott, J. A. Zeitler, J. Mc Gregor *et al.*, "The Use of Terahertz Spectroscopy as a Sensitive Probe in Discriminating the Electronic Properties of Structurally Similar Multi-Walled Carbon Nanotubes," Advanced Materials, 21(38-39), 3953 (2009).

[8] O. Hilt, H. B. Brom, and M. Ahlskog, "Localized and delocalized charge transport in single-wall carbon-nanotube mats," Physical Review B, 61(8), R5129 (2000).

[9] described in: L. Duvillaret, F. Garet, J.-F. Roux, and J.-L. Coutaz, "Analytical Modeling and Optimization of Terahertz Time-Domain Spectroscopy Experiments Using Photoswitches as Antennae," IEEE J. Sel. Topics in Quant. Electron. 7, 615-623 (2001).

[10] L. Duvillaret, F. Garet, and J. L. Coutaz, "A reliable method for extraction of material parameters in terahertz time-domain spectroscopy," Selected Topics in Quantum Electronics, IEEE Journal of, 2(3), 739-746 (1996).

[11] T.-I. Jeon, J.-H. Son, G. H. An *et al.*, "Characterization of carbon nanotubes by THz time-domain spectroscopy," 39, (2001).

[12] T. I. Jeon, K. J. Kim, C. Kang *et al.*, "Optical and electrical properties of preferentially anisotropic single-walled carbon-nanotube films in terahertz region," Journal of Applied Physics, 95(10), 5736-5740 (2004).

[13] X. Y. He, and X. N. Fu, "Simulation Investigation on Optical and Electrical Properties of Carbon Nanotube in Terahertz Region," Communications in Theoretical Physics, 51(1), 161-164 (2009).

[14] http://www.uc3m.es/portal/page/portal/grupos_investigacion/optoelectronics/european_projects/mitepho, [MITEPHO], (2010).

ANNEXE III

THz Time-Domain Spectroscopy in Different Carbon Nanotube Thin-Films

Ehsan Dadrasnia[1], Horacio Lamela*[1], Mohan-Babu Kuppam[2], Frédéric Garet[2] and Jean-Louis Coutaz[2]

[1]Optoelectronic and Laser Technology Group (GOTL), Carlos III de Madrid University, 28911Leganes, Madrid, Spain

[2] IMEP-LAHC, Université de Savoie - F73376 Le Bourget du Lac Cedex, France.

Corresponding author: horacio@ing.uc3m.es

ABSTRACT

The direct metallic or semiconducting characterization of carbon nanotubes (CNTs) in the high-frequency is one of the key issues to use them in the different state-to-the-art applications. In this work, the terahertz surface conductivity and transmission of carbon nanostructures thin-film utilizing terahertz time-domain spectroscopy (THz-TDS) have been studied. We have also compared the achieved results of single-walled carbon nanotubes thin-film surface conductivity with pervious study as a function of frequency. However, we have improved the obtained conductivity of carbon nanostructures from the microwave to terahertz range by THz-TDS technique with high signal-to-noise ratio.

Keywords: Terahertz spectroscopy, Carbon nanotubes, CNTs, Surface conductivity, Transmission.

1. INTRODUCTION

Over the past decade, terahertz (THz) electromagnetic signals have been intensively considered in nanoscience and wide range of nanotechnology because of their high performance [1]. Analyzing and signal processing of coherent THz-TDS measurements lead to the precise determination of the complex permittivity of materials and for example to study the properties of different thin-films from 0.1 to 3 THz [2]. THz-TDS allows us to derive the absorption and dispersion of different materials if the sample typically exhibits flat and parallel faces [3]. An atomically thin layer of carbon nanotubes (CNTs) is the forefronts of research into one dimensional of nanoscience state-of-the-art [4]. CNTs can be the one of excellent candidates in nanoengineering because of their interesting properties in many range of applications, for example in biomedical, security [5] and photonic emission due to the high mobility and electron transfer in terahertz frequency [6]. Finding the CNTs electrical and optical properties is one of the key elements in order to apply them to the aforementioned applications. The CNTs properties can be measured without fabrication and pattering of electrical contact by THz time-domain spectroscopy.

CNTs thin-films are consisted of both metallic and semiconducting carbon nanotubes network embedded in air. As THz waves are very absorbing by free carriers, the terahertz surface conductivity characterization using TDS is then well adapted to focus the metallic content in such thin-films of carbon nanostructure and material-liked. Following our recent research work [7], this paper will investigate the THz-TDS surface conductivity properties of single-walled carbon nanotubes (SWNTs) and multi-walled carbon nanotubes (MWNTs) thin-films. In section 2, we describe the THz-TDS set-up and the CNT samples characterization method. The results in terms of comparing the terahertz surface conductivity and transmission properties of the carbon nanostructure films is analyzed and discussed in section 3. In section 4, we finally conclude and describe the perspectives of such studies for future works.

.

Terahertz Technology and Applications V, edited by Laurence P. Sadwick, Créidhe M. O'Sullivan,
Proc. of SPIE Vol. 8261, 82610Y · © 2012 SPIE · CCC code: 0277-786X/12/$18 · doi: 10.1117/12.910099

2. THZ EXPERIMENTAL SET-UP AND CNT THIN-FILMS

The THz characterization of the CNT samples is performed using a classical THz-TDS set-up in transmission (see Figure 1(a)) [8] as it is much simple to use compare to reflection and to prevent any phase error because of any misalignment of the film position and also to the one of mirror commonly used for the reference measurement. Moreover, THz-TDS is well adapted to characterize moderated absorbing material like carbon nanostructure thin-films because of its high signal-to-noise ratio [9]. Figure 1(b) shows the spectra of four recorded measurements of Fast Fourier Transform (FFT) waveforms: the reference signal without any sample in between the THz antennas, the signal transmitted by the fused-quartz substrate, and finally the signal transmitted by the substrate covered by the CNT film (MWNT and SWNT).

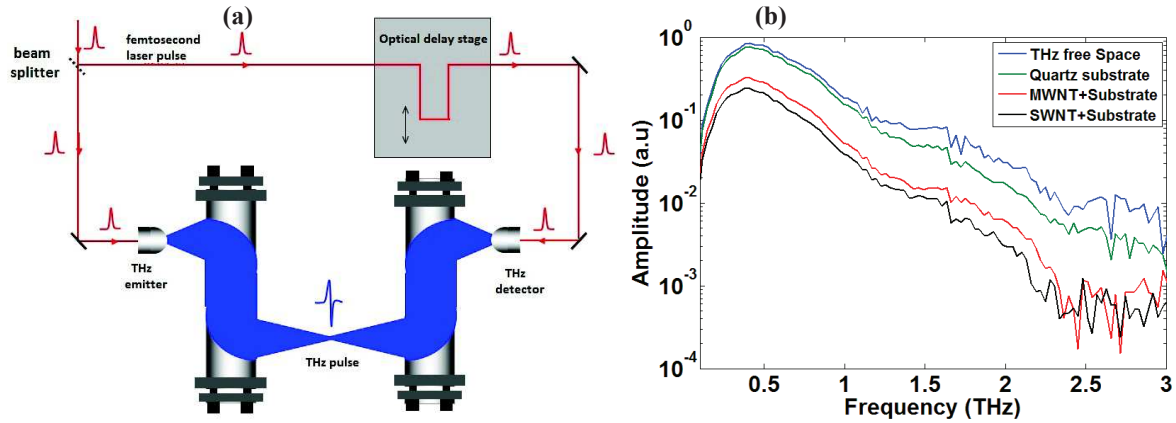

Figure 1: (a) Schematic of the THz-TDS set-up. (b) Spectrums of the THz free space, quartz substrate, MWNT and SWNT samples (thin-film deposited on quartz substrate).

Figure 2 shows a zoom of the CNT film which is deposited on fused-quartz substrate (2.5×2.5×0.215 cm^3) with the power absorption less than 10 cm^{-1} at 2 THz. The CNTs are 15-µm long for MWNT and 5-µm long for SWNT. Their diameters are respectively 15 nm and 1.5 nm for MWNT and SWNT. As compared to previous studies, we have used pure CNT films, i.e. not embedded in a hosting material. To find the thickness of CNT films, a profiler measurement leading to a value of 1.09µm and 1.2µm thick for respectively the thickness of the SWNT and MWNT films. To be characterized, the samples are located at the waist of the THz beam that could be considered as an almost perfect Gaussian beam, whose section at the waist which is very much smaller than the 2.5×2.5 cm^2 sample surface - no diaphragm is need to resize the THz beam size to the sample one. Moreover, we can notice that the Rayleigh length of the THz beam is much longer than the sample thickness throughout the whole 0.1-3 THz experimental range. Therefore, the samples can be considered as illuminated by a plane THz wave and no defocusing of the THz beam which is noticed because of the sample.

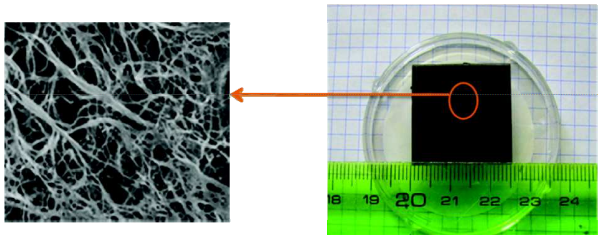

Figure 2: The CNT thin-film deposited over the fused quartz substrate.

3. RESULTS AND DISCUSSION

One should notice that the CNT films do not have a dense crystalline structure, but they exhibit random arrangement of tubes. Thus they should be treated, from an electromagnetic point-of-view, as an effective medium made of pure CNTs embedded in air. The THz-TDS measurements aim us to characterize the conductivity properties of the carbon nanostructure films. Figure 3 demonstrates our recent experimental results on analyzing the THz response conductivity of single-walled and multi-walled CNTs as results of the power absorption and refractive index (calculated from the ratio of the complex spectra of the input and transmitted signal) [7]. The difference power absorption between SWNT and MWNT can be explained by the carrier density of carbon nanostructures which is proportional to the power absorption coefficient. The Raman spectroscopy analysis indicates the different surface defects in carbon nanostructures. The higher terahertz conductivity responses of SWNT compared to MWNT is because of the lower surface defects [10].

The conductivity of carbon nanotube samples by THz frequency is relayed on two carrier specifications: concentration and distribution energy. To achieve the terahertz surface conductivity of carbon nanotubes sample, whose thickness is d, we derive the real surface conductivity σ_s from the real conductivity σ ($\sigma_s=d\sigma$). The SWNT and MWNT conductive film layers were deposited with thickness of 1.09μm and 1.2μm, respectively on the bare fused-quartz substrate which is considered as an optically thick dielectric medium with refractive index of 1.73 (n_s) that permits time windowing of the multiple echoes. The transmission through the first interface (air-sample) and internal reflection from the SWNT (or MWNT) interface with the vacuum impedance of 377Ω (Z) are given:

$$T(\sigma_s)=\frac{2}{1+n_s+\sigma_s Z} \tag{3}$$

$$R(\sigma_s)=\frac{n_s-1-\sigma_s Z}{1+n_s+\sigma_s Z} \tag{4}$$

In this case, the incident, reflection and transmission angles are equal to zero (normal incidence). The Fresnel's coefficients of the electrical field that is parallel to the incident sample are $t_{ij}=\frac{2n_i}{n_i+nj}$ and $r_{ij}=\frac{n_i+nj}{n_i+nj}$. The refractive indices are $n_1=n_4=n_{air}$ and $n_3=n_{substrate}$. t_{13} is the transmission through the second interface from air to substrate, r_{34} and r_{31} are the internal reflections inside the fused-quartz substrate (see Figure 4). Since the thickness of CNT samples (μm range) is much smaller in comparison to the bare substrate (mm range), the approximation ratio of total (relative) transmission of the CNT sample to the fused-quartz substrate can be derived by:

$$T_{total}(\sigma_s)=\frac{T_{CNTsample}}{T_{Substrate}}=\left(\frac{T(\sigma_s)}{t_{13}}\right)^2.\left(\frac{1-(r_{34}r_{31})^2}{1-(r_{34}R(\sigma_s))^2}\right) \tag{5}$$

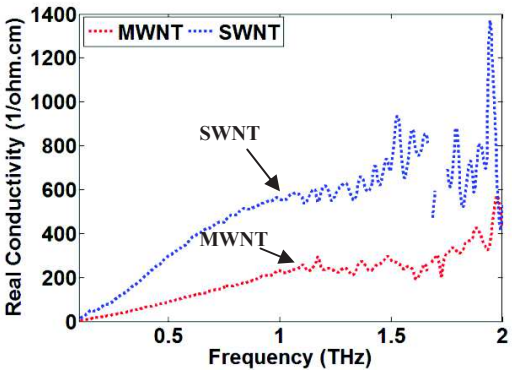

Figure 3. Real conductivity of the SWNT and MWNT thin films.

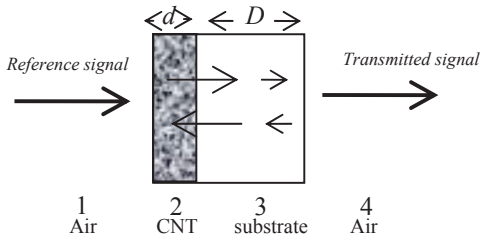

Figure 4. Schematic of the THz signal reflected and transmitted by the samples (slab covered with the CNT film).

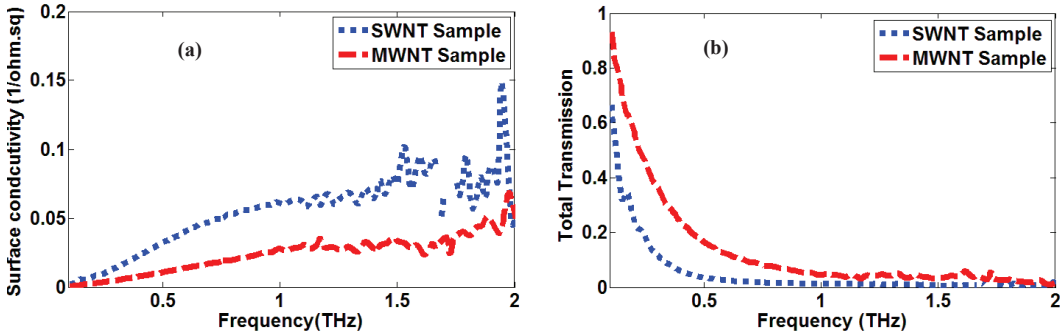

Figure 5. (a) Surface conductivity and (b) Total transmission of the SWNT and MWNT thin films.

The direct metallic or semiconducting characterization of carbon nanotubes in the high-frequency can be done by using THz-TDS contactless and nondestructive technique. In this study, the terahertz surface conductivity of carbon nanostructure films including SWNT and MWNT deposited on the fused-quartz bare have been characterized by THz-TDS which can be applied as a possible method to find the SWNT and MWNT metallic properties up to 2 THz. As the studied films in this work had more metallic treats (with high conductivity as shown in Figure 3), the real part of surface conductivity dominates the imaginary part.

The surface conductivity and the total transmission of SWNT and MWNT samples are demonstrated in Figure 5 as functions of frequency. The surface conductivity of SWNT is much higher in comparison to MWNT because of the less surface defects and high conductivity values in SWNT structure (the CNT samples have thickness on the order of 1μm). Equation (5) have exhibited that the total transmission is relevant to the surface conductivity. The relative transmission (through CNT/fused-quartz substrate) results are demonstrated in Figure 5(b) where with increasing frequency from the microwave to terahertz range, the total transmission significantly decreases as the carrier density and power absorption of carbon nanostructures increase.

We have compared our SWNT thin-film terahertz conductivity with very recently published study, referred to the results reported by Liang *et al*., that they characterized the surface conductivity of a single-walled film (with thickness on the order of 100nm) on different glass substrates in the microwave frequency range (0.1-0.5 THz) [9], we have calculated the real conductivity based on the surface conductivity of SWNT with thickness of 100nm in Liang *et al*. work over 0.3-0.4THz. The results in Figure 3 show similar value of conductivity (350 1/Ω.cm) of our SWNT sample with thickness of 1.09μm as Liang *et al*. obtained for a SWNT sample with thickness of 100nm. However, we have improved the spectrum measurement from the microwave range to terahertz range using THz-TDS with high signal-to-noise ratio. The results indicate that the real conductivity is strongly dependent on the crystallinity of the graphitic layers and the number of surface defects in carbon nanostructures. Eventually, the carbon nanostructure conductivity values can be ordered by SWNT > MWNT.

4. CONCLUSIONS AND FUTURE WORK

In summary, due to the smaller thickness of CNT films compared to the THz wavelength, carbon nanostructure networks at the air-bare substrate interface show a finite surface conductivity boundary condition. This work studied the terahertz surface conductivity and total transmission of carbon nanostructure thin-films utilizing the THz-TDS to show the metallic content. The future work of our research is to carry out in collaboration with Korean (Advanced Institute of Nanotechnology, University of Sungkyunkwan) research group in order to find the effect of atomic interaction on the number of surface defects and consequently the possibility of increasing the conductivity of MWNT samples for further nanoscience applications.

ACKNOWLEDGEMENT

This work is supported by the European Community (project FP7 ITN Marie Curie MITEPHO number 238393) [11], in order to develop compact and integrated tunable dual-mode diode lasers for THz spectroscopy in sensing and biomedical applications.

REFERENCES

[1] M. Tonouchi, "Cutting-edge terahertz technology," Nature Photonics, 1(2), 97-105 (2007).

[2] M. Naftaly, and R. E. Miles, "Terahertz Time-Domain Spectroscopy for Material Characterization," Proceedings of the IEEE, 95(8), 1658-1665 (2007).

[3] L. Duvillaret, F. Garet, and J. L. Coutaz, "A reliable method for extraction of material parameters in terahertz time-domain spectroscopy," Selected Topics in Quantum Electronics, IEEE Journal of, 2(3), 739-746 (1996).

[4] M. S. Dresselhaus, A. Jorio, and R. Saito, [Characterizing Graphene, Graphite, and Carbon Nanotubes by Raman Spectroscopy] Annual Reviews, Palo Alto(2010).

[5] L. Dai, [Carbon Nanotechnology:Recent Developments in Chemistry, Physics, Materials Science and Device Applications] ELSEVIER, (2006).

[6] T.-I. Jeon, J.-H. Son, K. H. An *et al.*, "Terahertz absorption and dispersion of fluorine-doped single-walled carbon nanotube," Journal of Applied Physics, 98(3), 034316-034316-4 (2005).

[7] H. Lamela, E. Dadrasnia, F. Garet *et al.*, "Carbon Nanotube Terahertz Spectroscopy: Study of Absorption and Dispersion Properties of SWNT and MWNT," Proceedings of SPIE. 8101-16,(2011).

[8] A. Ugawa, A. G. Rinzler, and D. B. Tanner, "Far-infrared gaps in single-wall carbon nanotubes," Physical Review B, 60(16), R11305 (1999).

[9] M. Liang, Z. Wu, L. Chen *et al.*, "Terahertz Characterization of Single-Walled Carbon Nanotube and Graphene On-Substrate Thin Films," Microwave Theory and Techniques, IEEE Transactions on, 59(10), 2719-2725 (2011).

[10] G. B. Jung, Y. Myung, Y. J. Cho *et al.*, "Terahertz Spectroscopy of Nanocrystal-Carbon Nanotube and -Graphene Oxide Hybrid Nanostructures," Journal of Physical Chemistry C, 114(25), 11258-11265 (2010).

[11] http://www.uc3m.es/portal/page/portal/grupos_investigacion/optoelectronics/european_projects/mitepho, [MITEPHO], (2010).

ANNEXE IV

Invited Paper

Terahertz Conductivity Studies in Carbon Nanotube Networks Prepared by the Vacuum Filtration Method

Horacio Lamela*[1], Ehsan Dadrasnia[1], Dong-Mok Lee[2], Seunghyun Baik[2,3], Mohan Babu Kuppam[4], Frédéric Garet[4] and Jean-Louis Coutaz[4]

[1]*Optoelectronic and Laser Technology Group (GOTL), Carlos III de Madrid University, 28911 Leganes, Madrid, Spain*
[2]*Department of Energy Science, Sungkyunkwan university, Suwon, 440-746, Korea*
[3]*School of Mechanical Engineering, Sungkyunkwan university, Suwon, 440-746, Korea.*
[4] *IMEP-LAHC, Université de Savoie - F73376 Le Bourget du Lac Cedex, France.*

**Corresponding author: horacio@ing.uc3m.es*

ABSTRACT

The electrical properties of carbon nanostructures have been greatly stimulating to use in the nanotechnology for electronic components. In this paper, we study the AC and DC electrical conductivity responses of multi-walled carbon nanotube films, prepared by the vacuum filtration methods, with noncontact terahertz time-domain spectroscopy (THz-TDS) approach utilizing the extrapolation analysis as well as probe-in line technique.

Keywords: Terahertz, Spectroscopy, Conductivity, Carbon nanotubes devices, Multi-walled carbon nanotubes.

1. INTRODUCTION

The new generations of nanoelectronic-polymer devices have been fabricating by using hybrid composites. The excellent electrical properties of molecular-scale carbon nanotubes (CNTs) are considered as an interesting research area in producing nanocomposites samples. CNTs and graphene have been considered as an alternative material to Indium-Tin Oxide (ITO) for flexible transparent conductive films since it has unique electrical, optical and mechanical properties[1, 2]. CNTs are promising new materials because of their excellent electrical, thermal and mechanical properties [3,4,5]. The electrical conductivity of CNT/polymer nanocomposites is relevant to many parameters of CNTs like chirality, purity content, concentration and the aspect ratio of length to diameter of tubes [6]. CNT films are networks of carbon nanotubes. CNTs networks can be used to form metal–semiconductor, semiconductor–semiconductor or metal–metal junctions [7]. Multiwalled carbon nanotubes (MWNTs) are composed of annular shells of nanotubes and exhibit metallic properties. MWNTs typically have larger diameters and longer lengths compared with singlewalled carbon nanotubes.

Using coherent terahertz time-domain spectroscopy (THz-TDS) provides a precise approach to measuring the response of a material to electromagnetic absorption and dispersion over the frequency range 0.1− 3THz of flat parallel faces of thin-film samples [8, 9]. Due to the unique CNT electronic and mechanic properties in terahertz range [5] and because of high signal-to-noise (SNR) ratio , recent works have permitted to define and describe the CNT film properties [10] to demonstrate those properties of CNTs compared with conventional structures in a range of industries, such as biomedicine and security [11].
In this work, THz and DC conductivity responses of MWNT thin-films are studied. In section 2, we illustrate the physical characterization of MWNT samples under this work. In section 3, the THz-TDS set-up to get temporal waves is shown. We describe the main approach to achieve the electrical DC and AC conductivity responses of MWNT thin-films

Carbon Nanotubes, Graphene, and Associated Devices V, edited by Didier Pribat, Young-Hee Lee, Manijeh Razeghi,
Proc. of SPIE Vol. 8462, 84620C · © 2012 SPIE · CCC code: 0277-786/12/$18 · doi: 10.1117/12.931511

in the section of results and discussion. In section 5, we finally conclude the perspectives of this study and also future work.

2. CNTS DEVICES IN NANOENGINEERING

Besides developing process of carbon nanotube and controlling methods for the fabrication of tubes in nanotechnology [12], there are some recent examples to use carbon nanotubes in the nanoengineering applications. *Cha et al.* primarily reviewed the nanotechnologies with CNTs for RF and terahertz technology like field-effect and flexible thin-film transistors [13]. There is one very recent result in terms of THz-TDS measurement and conductivity control of carbon nanostructure to study the field-effect transistors as a high speed electronic device. The electron-density-dependence characteristics by a simple Drude model showed the measured frequency-dependent optical sheet conductivity of graphene in the terahertz frequency range for the nanoelectronic devices [14].

In this line of investigation, we are preliminary studying the THz electrical properties of pure MWNTs films prepared by the vacuum filtration methods. We have two pure and homogenous surface MWNT samples deposited over quartz substrate with thicknesses of 162.16nm (MF1) and 193.88nm (MF2). The size of reference quartz substrate for both samples is about 2.5×2.5 cm^2. The diameters of films are 18.72mm and 18.99mm respectively for MF1 and MF2 (See Fig. 1). MF1 and MF2 have different concentrations of MWNTs. The nanotube suspension was prepared by mixing and ultrasonicating (380W, 20 min) deionized water (10 ml), SDS (Sigma Aldrich, 71725, 0.1g) and MWNTs (Hanwha nanotech, CMP-330F, 10mg). The nanotube suspension was deposited on the filter paper (Whatman, Anodisc 25) by the vacuum filtration method. Then we removed SDS surfactants by rinsing with deionized water. Finally, the MWNT films were transferred on quartz substrates (Figure 1).

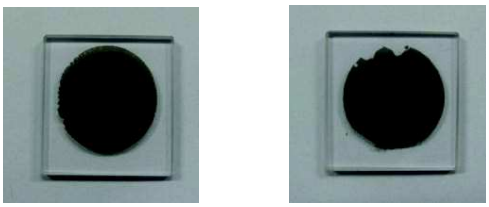

(a) (b)

Fig. 1: MWNT films with thicknesses of (a) 162.16nm and (b) 193.88nm deposited on the quartz substrate.

3. THZ-TDS OPTOELECTRONIC SET-UP FOR CNTS[15].

The THz-TDS optoelectronic configuration is consisted of a femtosecond (fs) laser, beam splitter, optical time delay device, chopper, paraboloidal mirrors, optical lens, THz source and detector antennas and optical lens. The generated fs laser beam is split into two optical pulses, pumped and probe. The pumped and probe beams respectively go to the THz emitter and THz detector antennas using lens. Two optical paths from the beam splitter to the THz emitter and THz detector have the same length as the receiver antenna is gated synchronously with an excitation of the transmitter. Off-axis paraboloidal mirrors with focal length *f* are used to guide the THz pulse with output power on the range of mW from the emitter, through a sample onto the detector. The mirrors are arranged in order of *f-2f-2f-2f-f* and the distance between two parabolic mirrors is *2f*. The sample exactly is located on the focal point of these mirrors with distance of *f* of each mirror which makes the THz emission focus through the sample before being collimated again. When thin films, made from MWNTs, are exposed to electromagnetic radiation up to 2.5 THz, the response reveals the effects on optical and electrical properties of carbon nanostructures [15].

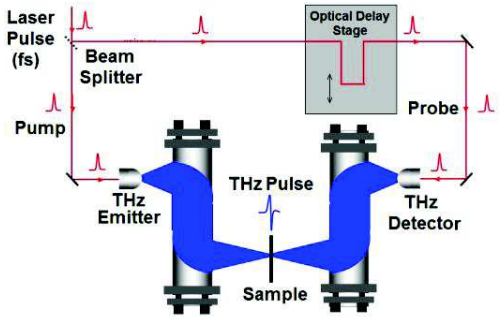

Fig. 2: Schematic of the free contact THz-TDS configuration and position of sample under measurement [15].

Three THz temporal waveform measurements have been done for each MWNTs sample (reference air, reference substrate and self-sample pulses) as shown in Figure 3. The first measurement has recorded the reference signal without any sample in between the THz emitter and detector antennas. The second has measured the THz signal with the reference substrate, and the third has measured the signal with the substrate covered by MWNT films. All THz signals have been measured several times to reduce the percentage of error and show good repeatability for each sample then the average amplitude of each THz waveform is calculated.

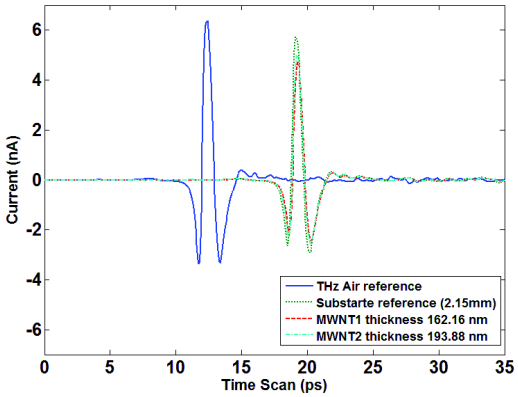

Fig. 3: THz temporal signals of free space, reference substrate, and MWNTs samples.

The substrate thickness and MWNT structure absorption make to change the phase delay and transmission field after passing the incident THz air reference signal through the sample. To transfer those THz temporal signals into the frequency spectrum, we have used the fast Fourier transform (FFT) technique. The time window is about 35ps with sampling number of 1024 and time step of several femtoseconds for all THz measurements. The terahertz spectra give the responses in arbitrary units (a.u.) of free space, reference substrate, and MWNT thin-films deposited on substrate.
This is obvious that by decreasing the time windowing in FFT analysis we have smoother THz spectrum. But, we lose some data and information in the THz signals by reducing the time window especially once the edge of time window is close to the THz temporal signals. Furthermore, there are inconsistent values of the THz signal in the low frequencies (less than 0.1 THz). Those ripples are because of the sampling time which is very small and not enough to recover the equivalent low frequencies below 0.1 THz. Figure 4 shows the THz signals in frequency domain where we have used the extrapolation technique to find more precise and smooth information at lower frequencies. The rest ripple effect at higher frequencies can be cause of noise in system and the absorption lines of atmospheric water vapor (e.g., around 1.7 THz and 2.6 THz).

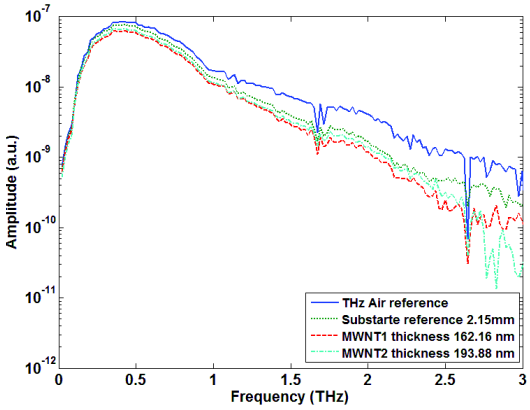

Fig. 4: THz spectrum of free space, references substrate, and MWNT samples for time-window 35ps.

4. RESULTS AND DISCUSSION

Figure 5 illustrates a schematic of the MWNT devices. The thick reference substrate is covered with the high dense CNT films. When the slab of known complex refractive index n_s is covered by a MWNT film of complex refractive index n_f and thickness *d*, the transmitted field takes a more complicated expression than equation compared to a stand-alone slab [16]. The THz beam can be considered as parallel throughout the sample, and we can use classical extracting technique to calculate both the refractive index and the absorption coefficient of the films. Since the substrate is much thicker than the film, one can time-window the recorded waveform in order to get rid of the temporal echoes that reflect back and forth in the substrate. To calculate the optical constants, we have used the terahertz time-domain differential method [17, 18]. The electrical transmitted THz signal through the film with thickness of *d* and considering multi-reflections within MWNTs film can be written in frequency domain as follows (Figure 5b)

$$E_f(\omega) = E_0 t_{12} t_{23} t_{31} \exp(\frac{i\omega d n_f}{c}) \exp(\frac{i\omega D n_s}{c}).FP(\omega) = E_0 t_{12} t_{23} t_{31} \exp(\frac{i\omega d n_f}{c}) \exp(\frac{i\omega D n_s}{c}).\frac{1}{1 - r_{21} r_{23} \exp(\frac{i2\omega d n_f}{c})} \quad (1)$$

According to the transmitted electromagnetic wave through the different layers of materials, the reference electrical field is (Figure 5a)

$$E_r(\omega) = t_{13} t_{31} \exp(\frac{i\omega d}{c}) \exp(\frac{i\omega D n_s}{c}) E_0 \quad (2)$$

By knowing that the incident angle THz beam to sample is zero (normal incidence), the transmission and reflection Fresnel's coefficients of the electrical field inside the sample respectively are $t_{ij} = \frac{2n_i}{n_i + nj}$ and $r_{ij} = \frac{n_i - nj}{n_i + nj}$. To study the optical and electrical properties of MWNT composite thin-films, it would be necessary in the first step to find the absorption and dispersion properties of reference substrate.

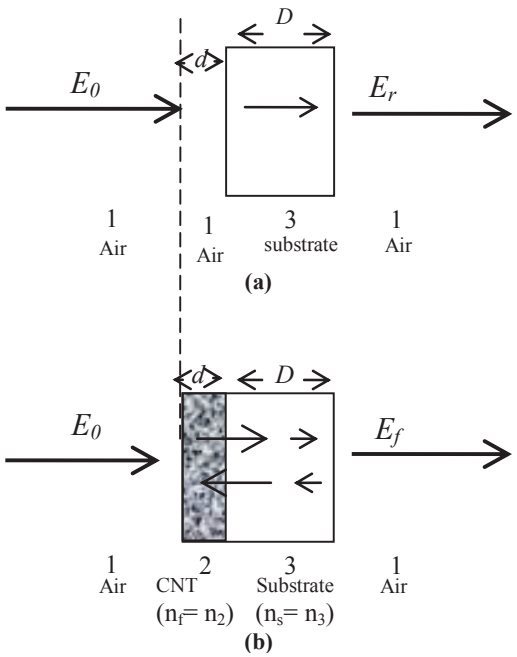

Fig. 5: Schematic of the THz signal reflected and transmitted (a) with only stand alone reference substrate and (b) with MWNT films deposited on a substrate.

Through the equation (1) and by having THz air space as reference, the average refractive index of quartz reference substrate with thickness of 2.15mm is 1.95 and it shows the low power absorption coefficient 8 cm^{-1} at 2 THz (see Figure 6). By taking into account that the refractive index of air n_1 and the complex dielectric function which is equal to the complex refractive index square $\varepsilon = \varepsilon_1 + i\varepsilon_2 = n_f^2 = (n+ik)^2$, the electrical conductivity as a function of frequency for both MWNT thin-films in the frequency range of 0 THz -2.5 THz are illustrated in Figure 7. Since there were the inconsistence values of electrical conductivity at low frequencies, we have applied to the extrapolation with polynomial functions to find DC conductivity and compare them with the classical electrical conductivity measurement using the four-point probe method [19, 20] with a current source (Keithley 6221) and a nanovoltmeter (Keithely 2182A). The average DC conductivities for MF1 and MF2 have been demonstrated in 70.6 S/cm and 66.6 S/cm, respectively. The achieved conductivity using the extrapolation technique in THz -TDS method at zero frequency respectively are about 74 S/cm and 37 S/cm for MF1 and MF2. To get close results with the probe-in line DC measurement, we have been working on more precise DC results using free contact THz-TDS method, by having accurate details of MWNTs samples (e.g., geometry) and also physical understanding of MWNT properties within Drude-Lorentz model which allows us to obtain similar results of 74 S/cm and 37 S/cm for MF1 and MF2.

Table 1. Electrical conductivity of MF1 and MF2 measured by the four-point probe and THz-TDS methods.

	Four-point probe method (S/cm)	*THz-TDS method (S/cm)*
MF1	**70.6**	**74**
MF2	**66.6**	**37**

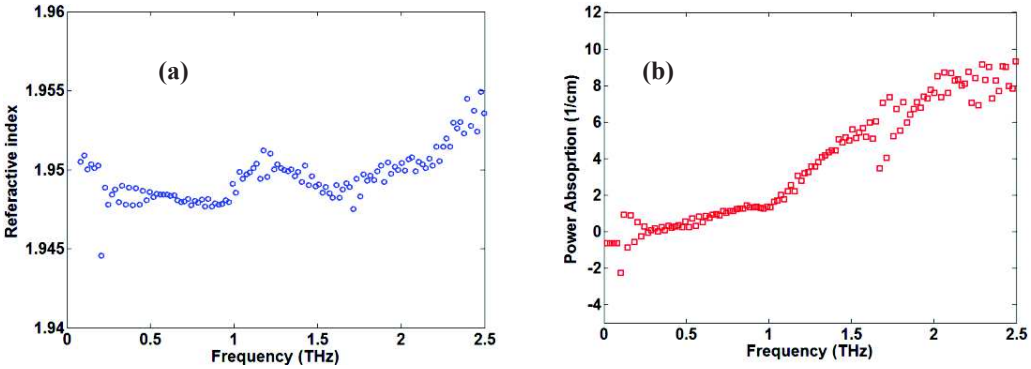

Fig. 6: Refractive index (a) and power absorption (b) of reference quartz substrate.

In summary, the results show the high level of electrical properties inside the MWNT samples. Those conductivity properties can be ascribed to relevant of the carrier density. Furthermore, the damping rate is proportional to the free-electron density. Then the higher damping rate indicates the large numbers of the electrons are available in a bonded regime. The high density of free-electron gives the possibility to make highly conductive nanocomposite films.

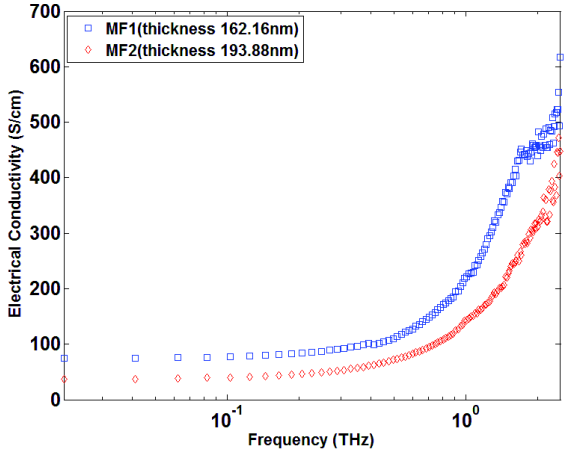

Fig. 7: Frequency-dependent THz conductivity of MWNT thin-films with thicknesses of 162.16nm (MF1) and 193.88nm (MF2).

5. CONCLUSIONS AND FUTURE WORK

Studying conductivity of the carbon-like material has been greatly stimulating to use in the nanotechnology and nanodevices like fast transistors. In this study, we have studied the pure MWNT thin-films in order to find the uncontaminated conductivity for MWNT thin-films. It will be interesting to investigate the properties of carbon nanotube – metal hybrids at DC and THz regimes in the future. Graphene-based composites can also be explored. To cover these issues and find more precise results, we will use the high efficient tools for spectroscopy in the THz and sub-millimeter regimes with THz-TDS and continuous wave THz.

ACKNOWLEDGEMENTS

This work is supported by the European Community (project FP7 ITN Marie Curie MITEPHO number 238393) [21] to develop compact and integrated tunable dual-mode diode lasers for THz spectroscopy in sensing and biomedical applications. We also acknowledge the World Class University program (R31-2008-000-10029-0) funded by the Ministry of Education, Science and Technology, Korea.

REFERENCES

[1] Z. Wu, Z. Chen, X. Du, J. M. Logan, J. Sippel, M. Nikolou, K. Kamaras, J. R. Reynolds, D. B. Tanner, A. F. Hebard, and A. G. Rinzler, "Transparent, Conductive Carbon Nanotube Films," Science, 305(5688), 1273-1276 (2004).

[2] S. Bae, H. Kim, Y. Lee, X. Xu, J.-S. Park, Y. Zheng, J. Balakrishnan, T. Lei, H. Ri Kim, Y. I. Song, Y.-J. Kim, K. S. Kim, B. Ozyilmaz, J.-H. Ahn, B. H. Hong, and S. Iijima, "Roll-to-roll production of 30-inch graphene films for transparent electrodes," Nat Nano, 5(8), 574-578 (2010).

[3] V. Mittal, [Polymer Nanotube Nanocomposites - Synthesis, Properties, and Applications] Wiley - Scrivener, (2010).

[4] S. Iijima, "Helical microtubules of graphitic carbon", Nature, 354(7), 56-58 (1991).

[5] R. Saito, G. Dresselhaus and M.S. Dresselhaus, "Physical properties of carbon nanotubes", Imperial college press, (1998).

[6] S. Yellampalli, [Carbon Nanotubes - Polymer Nanocomposites], (2011).

[7] M. S. Dresselhaus, G. Dresselhaus, and P. Avouris, [Carbon Nanotubes: Synthesis, Structure, Properties and Applications] Springer, (2001).

[8] D. Mittleman, [Sensing with Terahertz Radiation] Springer Series in Optical Sciences, (2003).

[9] L. Duvillaret, F. Garet, and J. L. Coutaz, "A reliable method for extraction of material parameters in terahertz time-domain spectroscopy," Selected Topics in Quantum Electronics, IEEE Journal of, 2(3), 739-746 (1996).

[10] M. Liang, Z. Wu, L. Chen, L. Song, P. Ajayan, and H. Xin, "Terahertz Characterization of Single-Walled Carbon Nanotube and Graphene On-Substrate Thin Films," Microwave Theory and Techniques, IEEE Transactions on, 59(10), 2719-2725 (2011).

[11] L. Dai, [Carbon Nanotechnology:Recent Developments in Chemistry, Physics, Materials Science and Device Applications] ELSEVIER, (2006).

[12] Y. Nakayama, and S. Akita, [Nanoengineering of carbon nanotubes and the status of its applications] Materials Research Society, Warrendale(2002).

[13] C. SeungNam, C. Jung Han, B. Chan Wook, S. Hyung Bin, C. Joonhyock, K. Ohyun, and K. Jong Min, "Perspectives on Nanotechnology for RF and Terahertz Electronics," Microwave Theory and Techniques, IEEE Transactions on, 59(10), 2709-2718 (2011).

[14] I. Maeng, S. Lim, S. J. Chae, Y. H. Lee, H. Choi, and J.-H. Son, "Gate-Controlled Nonlinear Conductivity of Dirac Fermion in Graphene Field-Effect Transistors Measured by Terahertz Time-Domain Spectroscopy," Nano Letters, 12(2), 551-555 (2012).

[15] H. Lamela, E. Dadrasnia, F. Garet, M. B. Kuppam, and J. L. Coutaz, "Carbon Nanotube Terahertz Spectroscopy: Study of Absorption and Dispersion Properties of SWNT and MWNT," Proceedings of SPIE. 8101-16,(2011).

[16] M. Born, and E. Wolf, [Principles of Optics] Cambridge University Press, Cambridge(1999).

[17] L. Kwang-Su, L. Toh-Ming, and X. C. Zhang, "The measurement of the dielectric and optical properties of nano thin films by THz differential time-domain spectroscopy," Microelectronics Journal, 34(1), 63-6969 (2003).

[18] L. Kwang-Su, L. Toh-Ming, and X. C. Zhang, "Tera Tool [terahertz time-domain spectroscopy]," Circuits and Devices Magazine, IEEE, 18(6), 23-28 (2002).

[19] F. M. Smits, "Measurement of sheet resistivities with the four-point probe," Bell System Technical Journal, 34, 711-718 (1958).

[20] K.-Y. Chun, Y. Oh, J. Rho, J.-H. Ahn, Y.-J. Kim, H. R. Choi, and S. Baik, "Highly conductive, printable and stretchable composite films of carbon nanotubes and silver," Nat Nano, 5(12), 853-857 (2010).

[21] MITEPHO, [Microwave and Terahertz Photonics]

http://www.uc3m.es/portal/page/portal/grupos_investigacion/optoelectronics/european_projects/mitepho, (2010).